



THÈSE EN COTUTELLE

Pour obtenir le grade de

Docteur en «Chimie des Matériaux»

Délivré par l'Université de Lille

ET

Docteur en «Chimie»

Délivré par l'Université de Gand

Présentée par

Lama HAMDOUNA

**Caractérisation RMN et activité antimicrobienne de complexes
organométalliques préparés par mécanosynthèse**

**NMR characterization and antimicrobial activity of mechanically
synthesized organometallic complexes**

Soutenance prévue le 20 novembre 2023

Composition du Jury :

Mme Catherine SJ CAZIN	Professeure, Université de Gand	<i>Co-directeur de thèse</i>
M. Christophe COPÉRET	Professeur, ETH Zurich	<i>Président du jury</i>
M. Fady NAHRA	Professeur, Université de Gand	<i>Examineur</i>
M. Franck FAYON	Directeur de Recherche, CEMHTI Orléans	<i>Rapporteur</i>
M. Olivier LAFON	Professeur, Université de Lille	<i>Directeur de thèse</i>
Mme Sharon ASHBROOK	Professeure, Université de St Andrews	<i>Rapporteur</i>



This research was supported by the French government through the “Programme d’Investissements d’Avenir” (I-SITE ULNE / ANR-16-IDEX-0004 ULNE) managed by the “Agence Nationale de la Recherche”. In addition, this project has received funding from the European Union’s Horizon 2020 research and innovation programme “Marie Skłodowska-Curie grant” (agreement No 847568). Financial support for the Centre National de la Recherche Scientifique (CNRS) is acknowledged in addition.

Dedicated to my parents, Ali Hamdouna and Amal Hayek

It has always been so hard to find the words, Dad, but now I am proud to say that your daughter did all this for you! To my strong Mom, THANK YOU.

Abstract

The extensive use of solvents in modern chemical synthesis has posed significant economic and environmental challenges. To address these concerns, it is crucial to reduce solvent usage and embrace eco-friendly synthesis methods. One promising solution to these challenges is mechanochemical synthesis, which employs mechanical forces to drive chemical reactions without traditional solvents. However, many aspects of the reaction mechanisms involved in mechanochemistry remain poorly understood. Solid-state nuclear magnetic resonance (ssNMR) spectroscopy, capable of providing atomic-level resolution, holds great promise in unraveling the mechanisms of mechanochemical reactions. In this dissertation, we applied ssNMR spectroscopy to investigate the mechanochemical synthesis of transition metal-N-heterocyclic carbene (NHC) complexes through the weak base approach. These complexes, such as [Cu(Cl)(NHC)], [Ag(Cl)(NHC)], and [Rh(acac)(CO)(NHC)], have applications in catalysis and as anti-infective coatings for medical devices. Our research primarily focuses on exploring the impact of different workup protocols used during the preparation of these complexes. To explore these processes, we conducted a series of multinuclear ssNMR experiments, involving spin-1/2 (^1H , ^{13}C , ^{15}N , ^{109}Ag) and quadrupolar (^{35}Cl , ^{63}Cu) nuclei, at static magnetic field strengths of 9.4, 18.8, and 28.2 T. This approach allowed us to monitor the consumption of reactants and the formation of intermediate and final products across various synthetic routes and workup protocols. We leveraged the high resolution and sensitivity offered by a 1.2 GHz NMR magnet to observe isotopes subject to substantial quadrupolar interactions, such as ^{35}Cl and ^{63}Cu . Signal assignment in the NMR spectra was achieved through 2D heteronuclear correlation techniques in conjunction with Density Functional Theory (DFT) calculations of NMR parameters. Additionally, we complemented our ssNMR studies with techniques such as powder X-ray diffraction (XRD) and vibrational spectroscopy. Moreover, we extended our investigation to the mechanochemical synthesis of chalcogen-NHC derivatives, specifically thioureas (NHC=S) and selenoureas (NHC=Se), known for their unique electronic properties and biological activities. Using multinuclear ssNMR experiments, including spin-1/2 (^1H , ^{13}C , ^{15}N , ^{77}Se) and quadrupolar (^{33}S) nuclei at static magnetic fields of 9.4 and 18.8T, along with DFT calculations of NMR parameters, we unveiled the mechanisms underlying these transformations. Our findings unequivocally confirm that the studied transition metal-NHC complexes and chalcogen-NHC derivatives are indeed formed in the solid-state during ball milling, dispelling any doubts regarding solvent-driven reactions during subsequent workup or characterization. However, this assertion does not apply to the [Rh(acac)(CO)(NHC)] complexes, where mechanical forces during ball milling facilitated the

reaction but necessitated the presence of solvents to complete it. Moreover, our study identified intermediate compounds, unreacted reagents, and by-products, providing a comprehensive understanding of the reaction outcomes. Additionally, this dissertation also explores the antimicrobial potential of mechanochemically synthesized Cu(I)-NHC complexes against a broad spectrum of bacterial and fungal strains, particularly those commonly associated with infections linked to medical devices like catheters. Significantly, demonstrating their effectiveness against *Staphylococcus aureus* and *Candida* strains, these complexes exhibit promise as potential treatments for urinary tract infections associated with catheter use.

Résumé

L'utilisation de solvants dans les méthodes de synthèse chimique modernes pose un problème économique et environnemental. Pour répondre à ces préoccupations, il est crucial de réduire leur utilisation et d'adopter des méthodes de synthèse plus respectueuses de l'environnement. Une solution prometteuse à ces défis est la synthèse mécanochimique, qui utilise des forces mécaniques pour déclencher des réactions chimiques sans recourir aux solvants traditionnels. Cependant, de nombreux aspects des mécanismes réactionnels impliqués en mécanochimie demeurent encore mal compris. La spectroscopie de résonance magnétique nucléaire à l'état solide (RMN des solides), qui est capable de fournir des informations structurales avec une résolution atomique, présente un potentiel considérable pour élucider les mécanismes des réactions mécanochimiques. Dans ce manuscrit, nous avons utilisé la RMN des solides pour étudier la synthèse mécanochimique en utilisant des bases faibles de complexes de métaux de transition comprenant des ligands carbène N-hétérocyclique (NHC). Ces complexes, tels que $[\text{Cu}(\text{Cl})(\text{NHC})]$, $[\text{Ag}(\text{Cl})(\text{NHC})]$, et $[\text{Rh}(\text{acac})(\text{CO})(\text{NHC})]$, ont des applications, à la fois, en catalyse et pour les revêtements anti-infectieux de dispositifs médicaux. Notre étude se concentre principalement sur l'exploration de l'impact de divers protocoles de post-traitement utilisés lors de la préparation de ces complexes. Pour explorer ces processus, nous avons mené une série d'expériences par RMN des solides multinucléaires, impliquant des noyaux de spin-1/2 (^1H , ^{13}C , ^{15}N , ^{109}Ag) mais également quadripolaires (^{35}Cl , ^{63}Cu), à des différents champs magnétiques, 9,4, 18,8 et 28,2 T. Cette approche nous a permis de suivre la consommation des réactifs et la formation des produits intermédiaires et finaux au travers de différentes voies de synthèse et de divers protocoles de post-traitement. Nous avons exploité le gain en résolution à 28,2 T pour observer les isotopes soumis à des interactions quadripolaires élevées, tels que le chlore-35 et le cuivre-63. L'attribution des signaux dans les spectres RMN a été réalisée grâce à des techniques de corrélation hétéronucléaire 2D combinées avec des calculs de paramètres RMN basés sur la théorie de la fonctionnelle de la densité (DFT). Nous avons complété nos études en RMN des solides par des techniques telles que la diffraction des rayons X (XRD) sur poudre et la spectroscopie vibrationnelle. En outre, nous avons étendu nos recherches à la synthèse mécanochimique de dérivés de dérivés chalcogène-NHC, en particulier les thiourées ($\text{NHC}=\text{S}$) et les sélénourées ($\text{NHC}=\text{Se}$), connus pour leurs propriétés électroniques uniques et leur activité biologique. À l'aide d'expériences de RMN des solides multinucléaires, incluant des noyaux de spin-1/2 (^1H , ^{13}C , ^{15}N , ^{77}Se) et quadripolaires (^{33}S) à des champs magnétiques statiques de 9,4 et 18,8 T, ainsi que des calculs DFT des paramètres RMN, nous avons mis en évidence les

mécanismes sous-jacents à ces transformations. Nos résultats confirment sans équivoque que les complexes de cuivre et d'argent ainsi que les dérivés chalcogène-NHC étudiés se forment effectivement à l'état solide lors de l'étape de broyage. À l'inverse, les complexes de $[\text{Rh}(\text{acac})(\text{CO})(\text{NHC})]$ ne se forment pas à l'état solide. Pour ces composés, les forces mécaniques exercées pendant le broyage contribue uniquement à faciliter la réaction en mélangeant les réactifs et en réduisant la taille des particules. La réaction, elle-même, nécessite la présence d'un solvant. De plus, notre étude a permis d'identifier des composés intermédiaires, des réactifs n'ayant pas réagi et des sous-produits, permettant ainsi une meilleure compréhension des réactions de mécanosynthèse. En outre, cette thèse explore également le potentiel antimicrobien des complexes Cu(I) -NHC préparés par mécanosynthèse contre un large spectre de souches bactériennes et fongiques, en particulier celles communément associées aux infections liées aux dispositifs médicaux tels que les cathéters. En démontrant leur efficacité contre les souches de *Staphylococcus aureus* et de *Candida*, ces complexes sont prometteurs en tant que traitements potentiels des infections urinaires associées à l'utilisation de cathéters.

Samenvatting

Het uitgebreide gebruik van oplosmiddelen in moderne chemische syntheses heeft aanzienlijke economische en ecologische uitdagingen met zich meegebracht. Om deze problemen aan te pakken, is het cruciaal om het gebruik van oplosmiddelen te verminderen en milieuvriendelijke synthesesmethoden te omarmen. Een veelbelovende oplossing voor deze uitdagingen is mechanochemische synthese, waarbij gebruik wordt gemaakt van mechanische krachten om chemische reacties aan te sturen zonder traditionele oplosmiddelen. Veel aspecten van de reactiemechanismen die betrokken zijn bij mechanochemie worden echter nog slecht begrepen. Solid-state nuclear magnetic resonance (ssNMR) spectroscopie, die resolutie op atomair niveau kan bieden, is zeer beloftevol voor het ontrafelen van de mechanismen van mechanochemische reacties. In dit proefschrift hebben we ssNMR spectroscopie toegepast om de mechanochemische synthese van transitietaal-N-heterocyclische carbeenen (NHC) complexen te onderzoeken via de zwakke base benadering. Deze complexen, zoals $[\text{Cu}(\text{Cl})(\text{NHC})]$, $[\text{Ag}(\text{Cl})(\text{NHC})]$, en $[\text{Rh}(\text{acac})(\text{CO})(\text{NHC})]$, hebben toepassingen in katalyse en als anti-infecterende coatings voor medische apparatuur. Ons onderzoek richt zich voornamelijk op het onderzoeken van de invloed van verschillende bewerkingsprotocollen die gebruikt worden tijdens de bereiding van deze complexen. Om deze processen te onderzoeken hebben we een serie multinucleaire ssNMR-experimenten uitgevoerd met spin-1/2 (^1H , ^{13}C , ^{15}N , ^{109}Ag) en quadrupolaire (^{35}Cl , ^{63}Cu) kernen bij statische magnetische veldsterktes van 9,4, 18,8 en 28,2 T. Met deze aanpak konden we het verbruik van reagentia en de vorming van tussen- en eindproducten over verschillende syntheseroutes en opwerkingsprotocollen volgen. We maakten gebruik van de hoge resolutie en gevoeligheid van een 1,2 GHz NMR-magneet om isotopen te observeren die onderhevig zijn aan substantiële quadrupolaire interacties, zoals ^{35}Cl en ^{63}Cu . Signaaltoewijzing in de NMR spectra werd bereikt door 2D heteronucleaire correlatietechnieken in combinatie met Density Functional Theory (DFT) berekeningen van NMR parameters. Daarnaast vulden we onze ssNMR-studies aan met technieken zoals poederröntgendiffractie en vibratiespectroscopie. Bovendien hebben we ons onderzoek uitgebreid naar de mechanochemische synthese van chalcogeen-NHC derivaten, met name thioureas ($\text{NHC}=\text{S}$) en selenoureas ($\text{NHC}=\text{Se}$), bekend om hun unieke elektronische eigenschappen en biologische activiteiten. Met behulp van multinucleaire ssNMR experimenten, waaronder spin-1/2 (^1H , ^{13}C , ^{15}N , ^{77}Se) en quadrupolaire (^{33}S) kernen bij statische magneetvelden van 9,4 en 18,8 T, samen met DFT berekeningen van NMR parameters, hebben we de mechanismen onthuld die ten grondslag liggen aan deze transformaties. Onze bevindingen bevestigen ondubbelzinnig dat de

bestudeerde transitiemetaal-NHC complexen en chalcogeen-NHC derivaten inderdaad in vaste toestand worden gevormd tijdens het kogelmalen, waardoor alle twijfels over oplosmiddelgestuurde reacties tijdens de daaropvolgende bewerking of karakterisering worden weggenomen. Deze bewering geldt echter niet voor de $[\text{Rh}(\text{acac})(\text{CO})(\text{NHC})]$ complexen, waar mechanische krachten tijdens het kogelmalen de reactie vergemakkelijkten, maar de aanwezigheid van oplosmiddel nodig is om de reactie te voltooien. Bovendien identificeerde onze studie intermediaire verbindingen, reagentia die niet reageerden, en bijproducten, waardoor een uitgebreid inzicht werd verkregen in de reactie-uitkomsten. Daarnaast onderzoekt dit proefschrift ook het antimicrobiële potentieel van mechanisch gesynthetiseerde Cu(I) -NHC-complexen tegen een breed spectrum van bacteriële en schimmelstammen, met name stammen die vaak geassocieerd worden met infecties in verband met medische hulpmiddelen zoals katheters. Door hun effectiviteit tegen *Staphylococcus aureus* en *Candida* stammen aan te tonen, zijn deze complexen veelbelovend als potentiële behandelingen voor urineweginfecties die geassocieerd worden met het gebruik van katheters.

Acknowledgements

This thesis would not have been complete without the support and encouragement of my supervisors, family members, colleagues, and friends. I am honored to acknowledge the contributions of these individuals who have, in various ways, made this journey an unforgettable and meaningful experience.

I begin by expressing my gratitude to the members of the jury, Prof. Christophe Copéret, Prof. Fady Nahra, Dr. Franck Fayon, and Prof. Sharon Ashbrook, who kindly agreed to evaluate my doctoral work.

My foremost gratitude goes to Prof. Olivier Lafon, my supervisor, whose constant support and guidance have been invaluable throughout my doctoral journey. His belief in my abilities has been a source of inspiration, driving me to reach higher and strive for excellence. I am grateful for the opportunities he provided to me to participate in workshops, as well as national and international conferences, which broadened my horizons, and allowed me to gain knowledge and experience that is indispensable to my academic and professional growth. Moreover, I am deeply appreciative of his understanding and respect for my personal life, helping me to balance my professional and personal responsibilities. Prof. Lafon has not only been a mentor in academia but also a guide in life. I have learned from him the invaluable skill of prioritization, an art that has enriched my life both inside and outside the academic sphere. In Prof. Olivier Lafon, I have had the privilege of an exceptional supervisor, and I could not have asked for a better mentor to accompany me on this journey.

I also extend my heartfelt appreciation to Prof. Catherine Cazin, my co-supervisor, for her guidance and support throughout my journey. Prof. Cazin's availability for discussions and her invaluable insights shared through frequent meetings, have significantly contributed to the success of my research. Additionally, I would like to extend my gratitude to Dr. Christel Neut, my co-supervisor, for the expertise she shared with me.

My gratitude extends to the RMN2I team at the University of Lille. I want to express my sincere thanks to Dr. Laurent Delevoye for his expertise, motivation, and support. His ability to bring a smile to my face during corridor conversations is evidence of his positive influence on my research experience. I am also grateful to Dr. Julien Trébosc for his invaluable assistance in overcoming practical NMR-related challenges. His insights into NMR experiments and analysis

have been indispensable in the progress of my work. Thanks to Dr. Andrew Rankin for assisting with the NMR experiments, sharing his knowledge, offering support, and encouraging me throughout my research. I would also like to thank Bertrand Doumert and Bertrand Revel for maintaining the exceptional NMR facility in Lille. My appreciation extends to Dr. Manjunatha Reddy for his insightful scientific discussions and invaluable advice, which have further enriched my academic journey.

I would like to express my gratitude to all my current and former colleagues from the RMN2I team for their continuous support, insightful discussions, shared laughter, and cherished moments. Special thanks to Dr. Jennifer Gomez, Dr. Racha Bayzou, and Dr. Parth Raval for warmly welcoming me to the UCCS laboratory and sharing their knowledge and experiences. I'm also thankful to my colleagues Diane, Céline, Athulya, Neethu, Pierre, and Raphael for creating a positive and motivating atmosphere that made my journey smoother.

Lastly, I would like to dedicate a special acknowledgement to my family, whose support, love, encouragement, and belief in me, have made this achievement possible. To my dad, your invaluable lesson that education is life's greatest achievement and the gateway to boundless opportunities will forever guide me. Your relentless dedication to ensuring our education and pushing us to excel academically have been the driving force throughout my journey. Even though you are no longer with us, I always feel your presence, your motivation, and your pride in my accomplishments. You will forever be my inspiration. To my incredible mom, your boundless love, tenderness, faith, prayers, late-night companionship during dissertation writing, delicious meals, attentive ear to both my achievements and failures, and continuous encouragement have been the driving force that has pushed me forward.

My gratitude extends to my wonderful siblings, Samah, Nour, and Houssein, who have always been there for me, offering support and love, even from afar. Your presence in my life has been a constant source of motivation and strength. I would also like to thank my nephews Fadel, Mohammad, Talia, and Ali, for being the most adorable part of my life.

A heartfelt special thanks extend to my fiancé, Hussein Darwich, who has been my unconditional support throughout this journey. Without him, I could not have achieved what I have. His love, understanding, patience, positivity, and encouragement have always motivated me to pursue my dreams. I am profoundly grateful for having him in my life.

Table of Contents

Abstract.....	i
Résumé	iii
Samenvatting	iv
Acknowledgements.....	vii
Table of Contents	ix
List of Figures	xiv
List of Schemes	xxiii
List of Tables	xxv
List of Abbreviations.....	xxvi
List of Symbols.....	xxvii
General Introduction.....	1
Chapter 1. Literature Review	8
1.1 Introduction.....	8
1.2 Overview of Mechanochemical Synthesis	8
1.2.1 Principle of Mechanochemical Synthesis	8
1.2.2 Historical Background	8
1.2.3 Equipment	10
1.2.4 Milling Parameters	11
1.2.5 Advantages of Mechanochemical Synthesis over Traditional Methods	13
1.2.6 Advancements in Mechanochemical Synthesis of Organometallic Complexes	14
1.2.7 Developments and Challenges in Monitoring Milling Reactions	14
1.2.7.1 In situ monitoring of milling reactions	15
1.2.7.2 Ex situ monitoring of milling reactions	17
1.3 SSNMR Spectroscopy	19
1.3.1 Challenges of ssNMR Spectroscopy	19

ix

1.3.2	Resolution and Sensitivity Enhancement	22
1.3.3	Challenges and Advances in Computing NMR Parameters.....	24
1.3.4	Potential Applications of ssNMR in Mechanochemical Synthesis	27
1.4	Organometallic Complexes Bearing NHC Ligands	34
1.4.1	Overview of NHCs	34
1.4.1.1	Structural properties of NHCs	34
1.4.1.2	Stability of NHCs.....	36
1.4.1.3	Classification of NHCs	36
1.4.1.4	Attractive features of NHCs.....	37
1.4.2	Applications of Transition Metal-NHC Complexes	38
1.4.3	Conventional Synthesis of Transition Metal-NHC Complexes	38
1.4.4	Mechanochemical Synthesis of Transition Metal-NHC Complexes	40
1.5	References	45
Chapter 2. Understanding the Mechanochemical Synthesis of Transition Metal-NHC Complexes using ssNMR Spectroscopy		66
2.1	Introduction.....	66
2.2	Cu(I)-NHC Complexes	67
2.2.1	Results and Discussion.....	68
2.2.1.1	Mechanochemical synthesis	68
2.2.1.2	¹ H ssNMR spectroscopy	70
2.2.1.3	¹³ C ssNMR spectroscopy	74
2.2.1.4	¹⁵ N ssNMR spectroscopy	79
2.2.1.5	⁶³ Cu ssNMR spectroscopy	81
2.2.1.6	³⁵ Cl ssNMR spectroscopy	86
2.2.2	Experimental Details	88
2.2.2.1	Samples preparation.....	88
2.2.2.2	ssNMR spectroscopy	89

2.2.2.3	DFT calculations of NMR parameters	95
2.2.3	Conclusion	96
2.2.4	Statement of Contribution	96
2.3	Ag(I)-NHC Complexes	97
2.3.1	Results and Discussion.....	98
2.3.1.1	Mechanochemical synthesis	98
2.3.1.2	^1H ssNMR spectroscopy	99
2.3.1.3	^{13}C ssNMR spectroscopy	101
2.3.1.4	^{15}N ssNMR spectroscopy	103
2.3.1.5	^{109}Ag ssNMR spectroscopy	105
2.3.2	Experimental Details	107
2.3.2.1	Samples preparation.....	107
2.3.2.2	ssNMR spectroscopy	108
2.3.3	Conclusion	110
2.3.4	Statement of Contribution	110
2.4	Rh(I)-NHC Complexes	110
2.4.1	Results and Discussion.....	112
2.4.1.1	Mechanochemical synthesis	112
2.4.1.2	^1H ssNMR spectroscopy	114
2.4.1.3	^{13}C ssNMR spectroscopy	115
2.4.1.4	^{15}N , ^{19}F , and ^{11}B ssNMR spectroscopy	117
2.4.1.5	ATR-FTIR spectroscopy.....	118
2.4.1.6	PXRD	119
2.4.1.7	In situ ATR-FTIR spectroscopy.....	120
2.4.2	Experimental Details	121
2.4.2.1	Samples preparation.....	121
2.4.2.2	ssNMR spectroscopy	123

2.4.2.3	PXRD	124
2.4.2.4	ATR-FTIR spectroscopy.....	124
2.4.2.5	In-Situ ATR-FTIR spectroscopy.....	125
2.4.3	Conclusion.....	125
2.4.4	Statement of Contribution	126
2.5	References	126
Chapter 3. Understanding the Mechanochemical Synthesis of Chalcogen-NHC Derivatives using ssNMR Spectroscopy		138
3.1	Introduction.....	138
3.2	Results and Discussion.....	139
3.2.1	Mechanochemical Synthesis.....	139
3.2.2	ssNMR Spectroscopy of IPr=S.....	141
3.2.2.1	¹ H ssNMR spectroscopy	141
3.2.2.2	¹³ C ssNMR spectroscopy	143
3.2.2.3	¹⁵ N ssNMR spectroscopy	146
3.2.2.4	³³ S ssNMR spectroscopy	147
3.2.3	ssNMR Spectroscopy of IPr=Se.....	148
3.2.3.1	¹ H ssNMR spectroscopy	148
3.2.3.2	¹³ C ssNMR spectroscopy	150
3.2.3.3	⁷⁷ Se ssNMR spectroscopy	151
3.3	Experimental Details	153
3.3.1	Samples Preparation	153
3.3.1.1	Materials	153
3.3.1.2	General procedure.....	153
3.3.1.3	Synthesis of IPr=S	153
3.3.1.4	Synthesis of IPr=Se	154
3.3.1.5	Workup	154

3.3.2	ssNMR Spectroscopy	154
3.3.2.1	ssNMR experiments at $B_0 = 9.4$ T	154
3.3.2.2	ssNMR experiments at $B_0 = 18.8$ T	156
3.3.2.3	ssNMR experiments at $B_0 = 28.2$ T	157
3.3.3	DFT Calculations of NMR Parameters	157
3.4	Conclusion	157
3.5	Statement of Contribution	158
3.6	References	158
Chapter 4. Antimicrobial Activity of Cu(I)-NHC Complexes against Catheter-Associated Pathogens		166
3.1	Introduction	166
3.2	Results and Discussion	167
3.2.1	Synthesis of the Cu(I)-NHC Complexes	167
3.2.2	Antimicrobial Properties of the Cu(I)-NHC Complexes	168
3.3	Experimental Details	169
3.3.1	Microorganism Strains	169
3.3.2	Minimum Inhibitory Concentration of the Microorganisms	169
3.4	Conclusion	170
3.5	Statement of Contribution	171
3.6	References	171
General Conclusion		176
Perspectives		178
Curriculum Vitae		179

List of Figures

Figure 1.1. Chronological timeline of the historical development of mechanochemistry.	10
Figure 1.2. Pictures of (a) modern mixer mill (Retsch MM 400) and (b) planetary mill (Fritsch, Pulverisette 5/4). Each mill is equipped with unique sets of jars and grinding balls with varying volumes and compositions. The schematic diagram illustrates the operational modes of both the mixer mill and the planetary mill.	11
Figure 1.3. (a) Vibrational ball mill integrated into a static ssNMR probe. The main image presents a comprehensive view of the complete probe, excluding the aluminum shield, while the inset provides a closer look at the upper section where the ball mill is placed. (b) The upper section featuring schematics illustrating the working principle of the ball mill, demonstrating the translation of rotational motion into transversal shaking through the eccentric wheel. The colored parts are 3D-printed using polylactic acid. ⁵³	16
Figure 1.4. Schematic representation highlighting the key advantages and disadvantages associated with analytical techniques commonly utilized for the ex situ monitoring of mechanochemical reactions.	19
Figure 1.5. Summary of anisotropic interactions in NMR.	20
Figure 1.6. Comparison between solution ^{13}C NMR and solid-state ^{13}C NMR spectra.	20
Figure 1.7. Schematic representation of the principal components of chemical shift tensor and line shape dominated by CSA.	21
Figure 1.8. (a) Schematic illustration of MAS. Pulse sequences of (b) CP, (c) ^1H detection and indirect detection of X ($^1\text{H}\{\text{X}\}$) DCP HETCOR, (d) QCPMG, and (e) WURST-QCPMG. These sequences represent the primary NMR techniques employed in my doctoral research.	24
Figure 1.9. 1D $^1\text{H} \rightarrow ^{13}\text{C}$ CP-MAS spectra of samples collected at different time intervals from the milling jar during the bromination reaction of cyclic sulfoximine (shown above the spectra). Resonances associated with the sulfoximine starting material are shaded in grey. Complete conversion of the starting material is observed after 30 minutes of ball milling. The MAS spinning sidebands are denoted by (*). ⁷⁴	28
Figure 1.10. 1D $^1\text{H} \rightarrow ^{13}\text{C}$ CP-MAS NMR spectra of benzoic acid (a), EDC·HCl (b), and crude mixture formed after 1 h grinding (c). The spinning sidebands are denoted by asterisks (*), and the signals of unreacted EDC·HCl are indicated by red arrows.	29

Figure 1.11. Real time in situ study of co-crystallization between Ph_3PO and $p\text{-C}_6\text{F}_4\text{I}_2$ without milling via 1D ^{31}P CP-MAS ssNMR spectroscopy. (a) Chemical structures of the halogen acceptor and donor, along with the crystallographic structures of cocrystals **1**¹⁰³ and **2**. Cocrystal **1** exhibits a single crystallographically identified halogen bond while cocrystal **2** displays three crystallographically distinct halogen bonds. (b) In situ 1D $^1\text{H} \rightarrow ^{31}\text{P}$ CP-MAS NMR spectra conducted at 35 °C, with a magnetic field strength of $B_0 = 9.4$ T, and a MAS frequency, $\nu_R = 10$ kHz. The inset displays isotropic peaks corresponding to Ph_3PO , pure **1**, and pure **2**. (c) Corresponding normalized peak integrals plotted over time. The sum of all peak integrals (black) remains constant, indicating the absence of an amorphous intermediate.⁷¹31

Figure 1.12. In situ ^{13}C MAS NMR spectra of the mechanochemical reaction co-crystallization between caffeine and malonic acid recorded over 84 hours. The ^{13}C NMR spectra as function of time are displayed as a surface, while the contour maps at the bottom left show enlargement of regions corresponding to high, moderate and low isotropic chemical shifts. On the right, five representative spectra display the corresponding regions. Each spectrum was observed after 1 hour.¹⁰⁴32

Figure 1.13. In situ $^1\text{H} \rightarrow ^{13}\text{C}$ CP-MAS NMR spectra of the mechanochemical bromination reaction conducted over a time range of 0 to 100 hours (bottom). Resonances attributed to the reaction products are identified using insets and red-colored rectangles. A plot of the normalized intensity of the NMR resonances for the two products as a function of time is presented (top). The solid lines depict a first-order kinetics fit.⁷⁴33

Figure 1.14. Schematic illustration of the centrifugal force exerted on the inner rotor wall is shown as inset. The plot displays the estimated centrifugal pressure as function of the MAS frequency, taking into account different MAS rotor sizes.⁷⁴34

Figure 1.15. General structural features of NHCs.35

Figure 1.16. The first isolated stable NHC.35

Figure 1.17. Ground state electronic structure of NHCs.36

Figure 1.18. Structures of some of the most commonly applied classes of NHCs.37

Figure 1.19. Overview of the major applications of NHCs in modern chemistry, categorized into three distinct areas. The figure highlights the diverse applications of transition metal-NHC complexes.....38

Figure 1.20. Mechanochemical synthesis of transition metal-NHC complexes.^{129,131–142}41

Figure 2.1. 1D ^1H MAS NMR spectra of (a) pure and (b) crude **2** (green), **3^{OP}** (blue), and **3^{SW}** (orange) acquired at $B_0 = 18.8$ T with a MAS frequency, $\nu_R = 60$ kHz. The spectrum of compound **1** is also shown in black in panel (a) for the sake of comparison. The shaded area denotes the region where the $^1\text{H}_2$ signal of **1** and $[\text{CuCl}_2][\text{IPr}\cdot\text{H}]$ resonates. The ^1H signal denoted by the black box corresponds to KHCO_3 . The signal resonating near 5 ppm in 1D ^1H NMR spectrum of crude **3^{OP}** and **3^{SW}** is assigned to water.71

Figure 2.2. (a) 1D ^1H MAS NMR spectra of **1** and pure **2** and **3^{OP}** acquired at $B_0 = 28.2$ T with $\nu_R = 60$ kHz, along with the assignment of the ^1H signals. Im and Ph denote the signals of the imidazole and phenyl ring, respectively. These spectra exhibit slightly higher resolution than those shown in **Figure 2.1a** recorded at $B_0 = 18.8$ T. The atom numbering of the imidazole ring is indicated on the structure shown as an inset. (b) Correlation between DFT-calculated ($\delta_{\text{iso}}^{\text{calc}}$) and experimental ($\delta_{\text{iso}}^{\text{exp}}$) isotropic chemical shifts for the ^1H sites of $[\text{CuCl}_2][\text{IPr}\cdot\text{H}]$ and $[\text{Cu}(\text{Cl})(\text{IPr})]$ crystal structures. The $\delta_{\text{iso}}^{\text{exp}}$ values were measured from the 1D ^1H MAS NMR spectra of pure **2** and **3^{OP}** shown in panel (a).72

Figure 2.3. 2D $^1\text{H}\{^{13}\text{C}\}$ DCP HETCOR NMR spectra of (a) **1** and (b) pure **2** acquired at $B_0 = 18.8$ T with $\nu_R = 60$ kHz.73

Figure 2.4. 1D ^1H MAS NMR spectra of crude and pure **2** prepared by ball milling $\text{IPr}\cdot\text{HCl}$ (1 eq.) in the presence of CuCl (1 eq.) for 10 min. The 1D ^1H MAS NMR spectra are acquired at $B_0 = 18.8$ T with $\nu_R = 60$ kHz. The shaded area denotes the region where the $^1\text{H}_2$ signal resonates. 74

Figure 2.5. 1D $^1\text{H}\rightarrow^{13}\text{C}$ CP-MAS NMR spectra of (a) pure and (b) crude **2** (green), **3^{OP}** (blue), and **3^{SW}** (orange) samples acquired at $B_0 = 9.4$ T with $\nu_R = 12.5$ kHz. The spectrum of compound **1** is also shown in black in panel (a) for the sake of comparison. The multiplet assigned to the $^{13}\text{C}^2$ site for samples **3^{OP}** and **3^{SW}** is shown as an inset in panels (a) and (b). The isotropic chemical shifts of the $^{13}\text{C}^2$ nucleus are indicated on the spectra. Furthermore, the vertical dashed line in panel (b) denotes the isotropic chemical shift of the $^{13}\text{C}^2$ nucleus in compound **1**.75

Figure 2.6. (a) 1D $^1\text{H}\rightarrow^{13}\text{C}$ CP-MAS NMR spectra of **1** and pure **2** and **3^{OP}** acquired at $B_0 = 9.4$ T with $\nu_R = 12.5$ kHz, along with the assignment of the ^{13}C signals. The spectral assignment is based on ^{13}C isotropic chemical shifts measured in solution^{32,33} as well as 2D $^1\text{H}\{^{13}\text{C}\}$ DCP HETCOR NMR spectra and DFT calculations of the isotropic chemical shifts. (b) Correlation between $\delta_{\text{iso}}^{\text{exp}}$ and $\delta_{\text{iso}}^{\text{calc}}$ for the ^{13}C sites of **1** and pure **2** and **3^{OP}** crystals (blue squares) and isolated

molecules (black circles). The $\delta_{\text{iso}}^{\text{exp}}$ values were measured from the 1D $^1\text{H} \rightarrow ^{13}\text{C}$ CP-MAS spectra of **1** and pure **2** and **3^{OP}** shown in panel (a).76

Figure 2.7. 1D $^1\text{H} \rightarrow ^{13}\text{C}$ CP-MAS spectra of pure **3^{OP}** at the $^{13}\text{C}^2$ central line recorded at magnetic fields of (a) 9.4 T (MAS rate, $\nu_R = 12$ kHz) and (b) 18.8 T (MAS rate, $\nu_R = 18$ kHz): experimental (blue) and simulated (black).78

Figure 2.8. 2D $^1\text{H}\{^{13}\text{C}\}$ DCP HETCOR spectra of crude (a) **2**, (b) **3^{OP}**, and (c) **3^{SW}** acquired at $B_0 = 18.8$ T with $\nu_R = 60$ kHz. The cross peak ascribed to the $^{13}\text{C}^2$ site in IPr·HCl and $[\text{CuCl}_2][\text{IPr}\cdot\text{H}]$ compounds are denoted by red and green arrows, respectively.79

Figure 2.9. 1D $^1\text{H} \rightarrow ^{15}\text{N}$ CP-MAS NMR spectra of **1** and pure **2** and **3^{OP}** acquired at $B_0 = 9.4$ T with $\nu_R = 8$ kHz, along with the assignment of the ^{15}N signals.80

Figure 2.10. Experimental (blue) and simulated (black) 1D $^1\text{H} \rightarrow ^{15}\text{N}$ CP-MAS NMR spectra of crude (a) **3^{SW}**, (b) **3^{OP}**, and (c) **2** and (d) **1** acquired at $B_0 = 9.4$ T with $\nu_R = 8$ kHz. The simulated spectra are the sum of up to three components: the blue, green, and gray-filled peaks are ^{15}N components associated with $[\text{Cu}(\text{Cl})(\text{IPr})]$, $[\text{CuCl}_2][\text{IPr}\cdot\text{H}]$, and IPr·HCl compounds, respectively. The relative integrated intensity of $[\text{Cu}(\text{Cl})(\text{IPr})]$ signal is indicated in the figure for samples **3^{SW}** and **3^{OP}**.81

Figure 2.11. Experimental and simulated (black) static 1D ^{63}Cu VOCS-QCPMG NMR spectra of pure (a, d) **2** (green), (b, e) **3^{OP}** (blue), and (c, f) **3^{SW}** (orange) acquired at room temperature and two magnetic field strengths: (a, b, c) $B_0 = 28.2$ T and (d, e, f) $B_0 = 18.8$ T. These spectra are generated by performing a Fourier transform of the sum of QCPMG echoes. The asterisk symbol (*) indicates the NMR signals from copper parts inside the probe including the sample coil (see **Figure 2.13**).83

Figure 2.12. (a) Static 1D VOCS-QCPMG and (b) MAS ^{63}Cu NMR spectra of crude **2**, **3^{OP}**, and **3^{SW}** acquired at $B_0 = 18.8$ T and $T = 298$ K. The spectra in panel (a) are reconstructed by the co-addition of two sub-spectra and are the Fourier transform of the sum of QCPMG echoes. The gray-shaded regions denote the ^{63}Cu signals from the probe (see **Figure 2.13**). The spectra in panel (b) are acquired with $\nu_R = 10$ kHz.85

Figure 2.13. Background ^{63}Cu NMR signals from the 4 mm double-resonance HX probe acquired at $B_0 = 18.8$ T. The spectrum is reconstructed by the co-addition of three individual pieces acquired using the QCPMG pulse sequence.86

Figure 2.14. Experimental (blue) and simulated (black) 1D WURST-QCPMG ^{35}Cl NMR spectra of (a) **1** and pure (b) **2**, (c) **3^{OP}**, and (d) **3^{SW}** acquired at two magnetic field strengths, $B_0 = 18.8$ T

(bottom) and 28.2 T (top), under static conditions at $T = 298$ K. Line width (LW) information is included. These spectra are generated by performing a Fourier transform of the sum of QCMPG echoes. VOCS technique was employed to record the ^{35}Cl NMR spectra of pure **2**, **3^{OP}**, and **3^{SW}** at $B_0 = 18.8$ T (see acquisition details in **Table 2.7**).....87

Figure 2.15. 1D ^1H wDUMBO-decoupled MAS NMR spectra of (a) pure (**4**, **5**) and (b) crude (**4***, **5***) samples acquired at $B_0 = 9.4$ T with a MAS frequency, $\nu_R = 12.5$ kHz. The spectrum of compound **1** is also shown in black in panel (b) for the sake of comparison. The shaded area denotes the region where the $^1\text{H}^2$ signal of compounds **1** and **4** resonates.100

Figure 2.16. 1D ^1H wDUMBO-decoupled MAS NMR spectra of compounds **4** and **5** acquired at $B_0 = 9.4$ T with a MAS frequency, $\nu_R = 12.5$ kHz, along with the assignment of the ^1H signals. Im and Ph denote the signals of the imidazole and phenyl ring, respectively.....101

Figure 2.17. 1D $^1\text{H} \rightarrow ^{13}\text{C}$ CP-MAS NMR spectra of (a) pure (**4**, **5**) and (b) crude (**4***, **5***) samples acquired at $B_0 = 9.4$ T with $\nu_R = 12.5$ kHz. The spectrum of compound **1** is also shown in black in panels (a) and (b) for the sake of comparison. The signals assigned to the $^{13}\text{C}^2$ site for compound [Ag(Cl)(IPr)] are shown as an inset in panels (a) and (b). The vertical dashed line in panel (b) denotes the isotropic chemical shift of the $^{13}\text{C}^2$ nucleus in compound **1**.102

Figure 2.18. (a) 1D $^1\text{H} \rightarrow ^{13}\text{C}$ CP-MAS NMR spectra of compounds **4** and **5** acquired at $B_0 = 9.4$ T with $\nu_R = 12.5$ kHz, along with the assignment of the ^{13}C signals. The spectral assignment of **5** is based on ^{13}C isotropic chemical shifts measured in solution⁷⁴ as well as the 2D $^1\text{H}\{^{13}\text{C}\}$ DCP HETCOR NMR spectrum. (b) 2D $^1\text{H}\{^{13}\text{C}\}$ DCP HETCOR NMR spectrum of **5** acquired at $B_0 = 18.8$ T with $\nu_R = 60$ kHz.103

Figure 2.19. Experimental (blue) and simulated (black) 1D $^1\text{H} \rightarrow ^{15}\text{N}$ CP-MAS NMR spectra of (a) **5**, (b) **4**, (c) **5***, and (d) **4*** acquired at $B_0 = 9.4$ T with $\nu_R = 8$ kHz. The simulated spectra are the sum of up to three components: the blue, green, and gray-filled peaks are ^{15}N components associated with [Ag(Cl)(IPr)], [AgCl₂][IPr·H], and IPr·HCl compounds, respectively.....104

Figure 2.20. The 1D $^1\text{H} \rightarrow ^{109}\text{Ag}$ CP-MAS pulse sequence with flip-back recovery and no ^1H decoupling.105

Figure 2.21. 1D $^1\text{H} \rightarrow ^{109}\text{Ag}$ CP-MAS NMR spectra of (a) **5**, (b) **4**, (c) **5***, and (d) **4*** acquired at $B_0 = 9.4$ T with MAS frequency, $\nu_R = 12.5$ kHz. The simulated spectra of **5** and **4*** are represented as black dashed lines. The isotropic resonances are indicated by *.106

Figure 2.22. 1D static ^{109}Ag CPMG NMR spectra of (a) **AgCl**, (b) **4***, (c) **4**, (d) **5***, and (e) **5** acquired at $B_0 = 9.4$ T with MAS frequency, $\nu_R = 12.5$ kHz. The gray-shaded region denotes the signal corresponding to AgCl resonating at 390 ppm..... 107

Figure 2.23. 1D ^1H wDUMBO-decoupled MAS NMR spectra of **IPr·HBF₄** (black), **[Rh(acac)(CO)₂]** (green), **6a*** (red), and **6a** (olive), acquired at $B_0 = 9.4$ T with a MAS frequency, $\nu_R = 12.5$ kHz. Peak assignment of the ^1H signals of **IPr·HBF₄**, **[Rh(acac)(CO)₂]**, and **6a** is based on their solvent-based ^1H NMR counterpart.^{33,86} The atom numbering of the imidazole ring is indicated on the structure shown as an inset..... 115

Figure 2.24. 1D $^1\text{H} \rightarrow ^{13}\text{C}$ CP-MAS of **IPr·HBF₄** (black), **[Rh(acac)(CO)₂]** (green), **6a*** (red), and **6a** complex (olive), acquired at $B_0 = 9.4$ T with a MAS frequency, $\nu_R = 12.5$ kHz. An expansion of the $^1\text{H} \rightarrow ^{13}\text{C}$ CP-MAS spectrum of **6a**, shown as an inset, displays the doublet assigned to the $^{13}\text{C}^2$ nucleus of the imidazolylidene ring split by the J -coupling constant $^1J(^{13}\text{C}-^{103}\text{Rh}) = 73$ Hz. 116

Figure 2.25. 1D $^1\text{H} \rightarrow ^{13}\text{C}$ CP-MAS spectra of **IPr·HBF₄**, **[Rh(acac)(CO)₂]**, **6a***, and **6a**, acquired at $B_0 = 9.4$ T with a MAS frequency, $\nu_R = 12.5$ kHz. Peak assignment of the ^{13}C signals of **IPr·HBF₄**, **[Rh(acac)(CO)₂]**, **6a**, and K_2CO_3 is based on their solvent-based ^{13}C NMR counterpart.^{31,86,87} 117

Figure 2.26. 1D (a) $^1\text{H} \rightarrow ^{15}\text{N}$ CP-MAS, (b) ^{19}F MAS, and (c) ^{11}B MAS NMR spectra of **IPr·HBF₄** (black), **[Rh(acac)(CO)₂]** (green), **6a*** (red), and **6a** (olive) acquired at $B_0 = 9.4$ T with a MAS frequency, $\nu_R = 12.5$ kHz for ^{15}N and ^{11}B and, $\nu_R = 20$ kHz for ^{19}F 118

Figure 2.27. ATR-FTIR spectra of the carbonyl stretching region for (a) **[Rh(acac)(CO)₂]**, (b) **6a***, and (c) **6a**. All spectra were recorded directly on solids..... 119

Figure 2.28. (a) PXRD patterns for **6a**, **6a***, **[Rh(acac)(CO)₂]**, **IPr·HBF₄**, and K_2CO_3 . (b) An expansion of the PXRD patterns between $2\theta = 8$ and 15.5° of **6a*** (black) and physical mixture of the reagents (**IPr·HBF₄**, **[Rh(acac)(CO)₂]**, and K_2CO_3) (red) with the proportions used for the reaction (see **Scheme 2.6**). The simulated PXRD patterns of **IPr·HBF₄** (blue), **[Rh(acac)(CO)₂]** (red), and $\text{K}_2\text{CO}_3 \cdot 1.5\text{H}_2\text{O}$ (pink) are also displayed. The PXRD pattern of the **6a*** mixture does not exhibit reflection of the **6a** complex, in particular at $2\theta = 9^\circ$ 120

Figure 2.29. (a) Synthesis of compound **6a** involving a solvent-based workup process initiated with (i) pre-ground (**6a***) and (ii) non-pre-ground reagents. (b) Kinetic profiles of reactions with pre-ground (red) and non-pre-ground (blue) reagents. The progress of the reaction was tracked by monitoring the changes in the intensity of absorption of $\nu_{(\text{co})}$ corresponding to compound **6a** at

1961 cm^{-1} after the addition of solvent addition for the pre-ground treated solids in comparison to the non-pre-ground solids.121

Figure 3.1. 1D ^1H MAS NMR spectra of **1** (black), **7*** (green), and **7** (blue) acquired at $B_0 = 9.4$ T with MAS frequency, $\nu_R = 60$ kHz. The shaded area denotes the region where the imidazolium proton ($^1\text{H}^2$) signal of compound **1** resonates.142

Figure 3.2. 1D ^1H MAS NMR spectra of compound **7**, acquired at $B_0 = 9.4$ T with $\nu_R = 60$ kHz, along with the assignment of the ^1H signals. The signals of the imidazole and phenyl ring are denoted by Im and Ph, respectively. The assignment of the ^1H signals is based on their ^1H solution-state NMR spectra and DFT calculations of the isotropic chemical shifts, as shown in panels (b). The atom numbering of the imidazole ring is indicated on the structure shown as an inset in panel (a). The asterisk symbol (*) denotes the impurity signal from water. (b) Correlation between DFT-calculated ($\delta_{\text{iso}}^{\text{calc}}$) and experimental ($\delta_{\text{iso}}^{\text{exp}}$) isotropic chemical shifts for the ^1H sites of IPr=S crystal structure. The δ_{isoexp} values were measured from the 1D ^1H MAS spectrum of compound **7** shown in panel (a).142

Figure 3.3. 1D $^1\text{H} \rightarrow ^{13}\text{C}$ CP-MAS NMR spectra of **1** (black), **7*** (green), and **7** (blue) samples acquired at $B_0 = 9.4$ T and $T = 298$ K with MAS frequency, $\nu_R = 12.5$ kHz. The isotropic chemical shifts of the C^2 carbon nucleus is indicated by gray shading. A magnified view of the $^{13}\text{C}^2$ signal in **7*** and **7** is presented as an inset.144

Figure 3.4. 1D $^1\text{H} \rightarrow ^{13}\text{C}$ CP-MAS NMR spectra of compound **7** acquired at $B_0 = 9.4$ T with $\nu_R = 12.5$ kHz, along with the assignment of the ^{13}C signals. The spectral assignment is based on ^{13}C isotropic chemical shifts measured in solution¹⁸ and DFT calculations of the isotropic chemical shifts, as shown in panel (b) and **Table 3.2**. (b) Correlation between DFT-calculated ($\delta_{\text{iso}}^{\text{calc}}$) and experimental ($\delta_{\text{iso}}^{\text{exp}}$) isotropic chemical shifts for the ^{13}C sites of IPr=S crystal structure. The δ_{isoexp} values were measured from the 1D $^1\text{H} \rightarrow ^{13}\text{C}$ CP-MAS spectrum of compound **7** shown in panel (a).144

Figure 3.5. Experimental (blue) and simulated (black) 1D $^1\text{H} \rightarrow ^{13}\text{C}$ CP-MAS NMR spectra of ^{33}S -enriched IPr=S at the $^{13}\text{C}^2$ central line recorded at static magnetic fields $B_0 = 9.4$ T (top) (MAS frequency, $\nu_R = 12.5$ kHz), 18.8 T (middle) (MAS frequency, $\nu_R = 12.5$ kHz), and 28.2 T (bottom) (MAS frequency, $\nu_R = 20$ kHz), and $T = 300$ K. The vertical red dotted lines are drawn to highlight the narrowing of the $^{13}\text{C}^2$ as the magnetic field strength increases.145

Figure 3.6. Experimental (red) and simulated (black) 1D $^1\text{H} \rightarrow ^{15}\text{N}$ CP-MAS NMR spectra of (a) **7**, (b) **7***, and (c) **1** acquired at a static magnetic field of $B_0 = 9.4$ T with MAS frequency, $\nu_R = 10$ kHz. The simulated spectra are the sum of up to two components: the gray and blue-filled lines are ^{15}N signals associated with $\text{IPr}\cdot\text{HCl}$ and $\text{IPr}=\text{S}$, respectively. The relative integrated intensity of compound $\text{IPr}=\text{S}$ in the crude mixture is indicated in panel (b). 146

Figure 3.7. Experimental (blue) and simulated (red) 1D ^{33}S VOCS-QCPMG NMR spectrum of ^{33}S -enriched $\text{IPr}=\text{S}$ acquired at $B_0 = 18.8$ T and $T = 300$ K under static conditions. The spectrum is generated by performing a Fourier transform of the sum of QCPMG echoes. The simulated spectrum was generated using $C_Q(^{33}\text{S}) = 27.4$ MHz and $\eta_Q(^{33}\text{S}) = 0.12$ as the main parameters. The asterisk (*) symbol denotes the NMR signal from the probe. 148

Figure 3.8. 1D ^1H MAS NMR spectra of **8*** (green) and **8** (blue) acquired at $B_0 = 9.4$ T with a MAS frequency, $\nu_R = 60$ kHz. The spectrum of compound **1** is also shown for the sake of comparison. The shaded region indicates the chemical shift region where the imidazolium proton ($^1\text{H}^2$) signal of compound **1** resonates. 149

Figure 3.9. 1D ^1H MAS NMR spectra of compound **8**, acquired at $B_0 = 9.4$ T with $\nu_R = 60$ kHz, along with the assignment of the ^1H signals. The assignment of the ^1H signals is based on their ^1H solution-state NMR spectra. The asterisk symbol (*) denotes the impurity signal from water. 149

Figure 3.10. 1D $^1\text{H} \rightarrow ^{13}\text{C}$ CP-MAS NMR spectra of **8*** (green) and **8** (blue) acquired at $B_0 = 9.4$ T with a MAS frequency, $\nu_R = 12.5$ kHz. The spectrum of compound **1** is also shown for the sake of comparison. The isotropic chemical shift of the $^{13}\text{C}^2$ site is indicated by gray shading. A magnified view of the $^{13}\text{C}^2$ signal in **8*** and **8** is presented as an inset. In **8**, the $^{13}\text{C}^2$ signal exhibits a 1:2 asymmetric splitting pattern owing to the quadrupolar-dipolar cross-term interaction with the ^{14}N nucleus ($I = 1$). The ^{13}C signals in **8*** at 161.5 ppm and 169.0 ppm are assigned to KHCO_3 and K_2CO_3 , respectively. 150

Figure 3.11. 1D $^1\text{H} \rightarrow ^{13}\text{C}$ CP-MAS spectra of compound **8** acquired at $B_0 = 9.4$ T with $\nu_R = 12.5$ kHz, along with the assignment of the ^{13}C signals. The spectral assignment is based on ^{13}C isotropic chemical shifts measured in solution.³⁶ 151

Figure 3.12. 1D ^{77}Se ssNMR spectra of (a) **8**, (b) **Se₈**, and (c, d) **8*** acquired at $B_0 = 9.4$ T with MAS frequency, $\nu_R = 10$ kHz, and $T = 298$ K. The spectra are acquired using (a,c) CPMAS and (b, d) CPMG pulse sequences. Isotropic resonances are indicated by *. The inset in panel (a)

shows an expanded view of the isotropic resonance. The structure of compound Se_8 is shown as inset in panel (b). 152

Figure 4.1. The chemical structure of the investigated copper-NHC complexes. 168

List of Schemes

Scheme 1.1. Solution-based synthetic access to transition metal-NHC complexes. ¹²⁹	40
Scheme 1.2. General weak base approach toward the mechanochemical synthesis of transition metal-NHC complexes.	41
Scheme 1.3. Transition metal-NHC complexes synthesized mechanochemically through the weak base approach. “Ph” and “Mes” denote the phenyl and 2,4,6-trimethylphenyl aromatic groups, respectively. The NHC ligands used are IPr, <i>N,N'</i> -bis-[2,6-(di-iso-propyl)phenyl]imidazolyliidene; SIPr, <i>N,N'</i> -bis-[2,6-(di-iso-propyl)phenyl]imidazolinyliidene; IMes, <i>N,N'</i> -bis-(2,4,6-trimethylphenyl) imidazolyliidene; SIMes, <i>N,N'</i> -bis-[2,6-bis(diphenylmethyl)-4-methylphenyl]imidazolinyliidene; IPr*, <i>N,N'</i> -bis-[2,6-bis(diphenylmethyl)-4-methylphenyl]imidazolyliidene; I ^t Bu, <i>N,N'</i> -bis-(tert-butyl)imidazolyliidene; ICy, <i>N,N'</i> -bis-(cyclohexyl)imidazolyliidene; and MIC, 1-(2,6-diisopropylphenyl)-3-(methyl)-4-(4-tertbutylphenyl)-1,2,3-triazolyliidene.	42
 Scheme 2.1. Weak base approach towards the mechanochemical synthesis of [Cu(Cl)(IPr)]. ²⁹ The gray sphere denotes the ¹³ C ² carbon of the imidazolyliidene moiety in the different compounds.	68
Scheme 2.2. (A) Schematic outline of the mechanosynthesis: (i) two-step one-pot (SW) synthesis and (ii) one-step one-pot (OP) synthesis. (B) Pure and crude samples collected after (i) solvent-based and (ii) solvent-free workup procedures, respectively.	70
Scheme 2.3. Mechanochemical synthesis of [Ag(Cl)(NHC)] complexes through the weak base approach. ⁷²	98
Scheme 2.4. Mechanochemical synthesis of (a) 4 and (b) 5 complexes. The gray circle denotes the ¹³ C ² carbon of the imidazolyliidene moiety.....	99
Scheme 2.5. Mechanochemical synthesis of [Rh(acac)(CO)(NHC)] (6a-f) complexes. Reaction conditions: NHC·HBF ₄ (100 mg), [Rh(acac)(CO) ₂] (1 eq.), and K ₂ CO ₃ (3 eq.) in a planetary ball mill at 400 rpm for 30 min. ^a Isolated yield (%).	113
Scheme 2.6. Mechanochemical synthesis of [Rh(acac)(CO)(IPr)] 6a complex. Reaction conditions: i) A mixture of IPr·HBF ₄ (100 mg, 0.21 mmol), [Rh(acac)(CO) ₂] (54 mg, 0.21 mmol), and K ₂ CO ₃ (87 mg, 0.63 mmol) is subjected to mechanochemical milling in a planetary ball mill at 400 rpm for 30 min, resulting in the formation of the crude reaction mixture 6a* as the initial product; ii) Subsequent solvent-based workup is employed to process the crude reaction mixture,	

yielding to the isolation and purification of the desired pure product $[\text{Rh}(\text{acac})(\text{CO})(\text{IPr})]$ **6a** in 74% yield. The gray circle denotes the $^{13}\text{C}^2$ carbon of the imidazolylidene moiety in both $\text{IPr}\cdot\text{HBF}_4$ and **6a**. The bottom scheme denotes the distinct color of the samples involved. The blue circle depicts the CO ligand and represents the substitution of one CO ligand in $[\text{Rh}(\text{acac})(\text{CO})_2]$ with IPr to form the desired complex. 114

Scheme 3.1. Mechanochemical weak base approach for the synthesis of chalcogen-NHC derivatives. Reaction conditions: $\text{NHC}\cdot\text{HCl}$ (100 mg), S_8/Se_8 (1.1 equiv.), and K_2CO_3 (3 equiv.), and ball milling time of 30 min ($\text{NHC}=\text{S}$) or 8 h ($\text{NHC}=\text{Se}$). Isolated yield in parentheses. 140

Scheme 3.2. Mechanochemical synthesis of (a) $\text{IPr}=\text{S}$ (**7**) and (b) $\text{IPr}=\text{Se}$ (**8**) compounds. The gray circle denotes the C^2 carbon of the imidazolylidene moiety in the different compounds... 141

List of Tables

Table 2.1. Experimental and computed $\delta_{\text{iso}}(^1\text{H})$ shifts in ppm for crystal structures (DFT ^C) of 1 and pure 2 and 3^{OP} .	73
Table 2.2. Experimental and calculated $\delta_{\text{iso}}(^{13}\text{C})$ shifts in ppm for the crystals (DFT ^C) and isolated molecules (DFT ^I) of 1 and pure 2 and 3^{OP} .	77
Table 2.3. Experimental and computed $\delta_{\text{iso}}(^{15}\text{N})$ shifts in ppm for the crystals (DFT ^C) and isolated molecules (DFT ^I) of 1 and pure 2 and 3^{OP} .	80
Table 2.4. Experimental and DFT calculated ^{63}Cu NMR parameters for pure forms of 2 , 3^{OP} , and 3^{SW} samples.	84
Table 2.5. ^{35}Cl NMR parameters of 1 and pure 2 , 3^{OP} , and 3^{SW} determined by the simulation of the 1D ^{35}Cl NMR spectra of Figure 2.14 and calculated for the periodic crystal structures using DFT (DFT ^C).	88
Table 2.6. Experimental NMR details for the static ^{63}Cu QCPMG measurements of the pure samples 2 , 3^{OP} , and 3^{SW} .	94
Table 2.7. Experimental NMR details for the static ^{35}Cl WURST-QCPMG measurements of compound 1 and the pure samples 2 , 3^{OP} , and 3^{SW} .	95
Table 3.1. Experimental and calculated $\delta_{\text{iso}}(^1\text{H})$ values of compound 7 measured experimentally and calculated for the periodic crystal structure.	143
Table 3.2. $\delta_{\text{iso}}(^{13}\text{C})$ values of compound 7 measured experimentally and calculated for the periodic crystal structure.	145
Table 4.1. In vitro minimum inhibitory concentration assessment of the mechanochemically synthesized Cu(I)-NHC complexes (a-d) against catheter-associated microorganisms.	169

List of Abbreviations

ATR-FTIR: attenuated total reflectance-Fourier transform infrared spectroscopy

CAAC: Cyclic (Alkyl)(Amino)Carbene

CP: cross-polarization

CPMG: Carr-Purcell-Meiboom-Gill

CSA: chemical shift anisotropy

CT: central transition

DCP: double CP

DFT: density functional theory

EFG: electric field gradient

EPR: electron paramagnetic resonance

HETCOR: heteronuclear correlation

IPr: *N,N'*-bis-[2,6-(di-iso-propyl)phenyl]imidazolylidene

IUPAC: International Union of Pure and Applied Chemistry

LAG: liquid-assisted grinding

MAS: magic angle spinning

MIC: minimum inhibitory concentration

NHC: N-heterocyclic carbene

NHCs: N-heterocyclic carbenes

PXRD: powder X-ray diffraction

QCPMG: Quadrupolar CPMG

QUEST: QUadrupolar Exact SoftWare

rf: radio frequency

SNR: signal-to-noise ratio

ssNMR: solid-state Nuclear Magnetic Resonance

VOCS: variable offset cumulative spectroscopy

WURST: wideband uniform-rate smooth truncation

List of Symbols

C_Q : quadrupolar coupling constant

h : Planck constant

Q : nuclear quadrupole moment

γ : gyromagnetic ratio

δ : chemical shift tensor

δ_{aniso} : reduced anisotropy

δ_{iso} : isotropic chemical shift

ν_1 : nutation frequency

ν_R : MAS frequency

T_{RD} : recovery delay

η_{CS} : chemical shift asymmetry

η_Q : quadrupolar coupling asymmetry

GENERAL INTRODUCTION

General Introduction

The extensive utilization of solvents in modern chemical synthesis processes, with an annual consumption exceeding 20 million tons,¹ has raised significant concerns regarding their environmental and economic impacts. These concerns extend beyond solvent production, as the purification and recycling processes often require substantial energy consumption.² Consequently, there is an urgent need to significantly reduce the use of solvents to minimize the footprint of chemical production. One highly promising approach to achieve this goal is through the application of mechanochemical synthesis.³

Mechanochemical synthesis, often conducted using ball mills, harnesses mechanical forces such as grinding, shearing, or milling to drive chemical transformations in the absence of conventional liquid solvents. This approach offers environmentally friendly and sustainable solutions for chemical synthesis, effectively addressing the challenge of solvent waste management.⁴ In addition, it offers several advantages, including simplified workup procedures,⁵ increased product yields within shorter reaction times,⁶ and the ability to access compounds that are elusive through traditional solution-based methods due to solubility constraints.⁷ Mechanochemical synthesis finds application in various chemical science disciplines, including organic,^{8,9} organometallic,^{10,11} main group,¹² and supramolecular chemistry,¹³ as well as metal-mediated¹⁴ and enzymatic transformations.¹⁵ However, within the promise of mechanochemistry lies a complex challenge. Predicting the outcomes of mechanochemical reactions remains a formidable task, partly due to the influence of solvents during the workup phase, which can modify the final product's structure.¹⁶ Therefore, gaining a deeper understanding of the mechanochemical reaction mechanism requires comprehensive structural characterization of chemical species in the solid-state, before any workup procedures.

While techniques like powder X-ray diffraction (PXRD) and vibrational spectroscopy are conventionally employed for this purpose,¹⁷ recent studies have highlighted the potential of solid-state nuclear magnetic resonance (ssNMR) spectroscopy as a superior method for monitoring mechanochemical reactions.¹⁸ Unlike other techniques, ssNMR offers the advantage of characterizing both crystalline and amorphous structures without necessitating the dissolution of powder samples in solvents.

The application of mechanochemical methods for the synthesis of important discrete organometallic complexes has gained momentum only in recent years.^{10,11} Despite the importance of such compounds in homogeneous catalysis, their preparation generally does not rely on sustainable routes. Therefore, providing operationally simple, sustainable synthetic routes to these complexes is highly desirable. Among the arsenal of well-defined organometallic complexes, transition metal complexes bearing N-heterocyclic carbene (NHC) ligands play a prominent role. With their modifiable steric and electronic properties, and the ability to stabilize highly reactive metallic centers, NHC ligands have enabled a plethora of developments in homogeneous catalysis,¹⁹ materials science,²⁰ and medicinal chemistry.²¹ Although synthetic routes to these compounds traditionally revolve around solution chemistry, over the past eight years several groups have been able to translate these synthetic approaches into mechanochemical ones.²²

Among the various synthetic strategies available, one that particularly stands out is the mechanochemical weak base approach to transition metal-NHC complexes. This method, reported concomitantly in 2020 by the Cazin²³ and Udvardy²⁴ groups, stands out not only for the fact that it employs readily available starting materials in an operationally simple way and makes use of an inexpensive base (e.g., K_2CO_3 , Cs_2CO_3) but also because of its wide applicability to different metal centers (i.e., Cu(I), Ag(I), Au(I), Rh(I), Pd(II)), in combination with a variety of NHC ligands [benzimidazolium, imidazol(in)ium, as well as Cyclic (Alkyl)(Amino)Carbene (CAAC)].^{23–25} However, in all documented cases, the mechanical treatment of the solid reactants was followed by the subsequent addition of solvents for the workup and purification of the products, and/or the processed samples were dissolved in solvents for characterization. Consequently, little evidence is provided to confirm that the observed reactions occur solely during the mechanical processing and not as a result of subsequent treatments. Acquiring this information is crucial for gaining a deeper understanding of the origin of reactivity in a mechanochemical synthetic approach.

In Chapter 2, we delve into a comprehensive exploration of the mechanochemical synthesis of distinct transition metal-NHC complexes, highlighting the mechanisms underlying these reactions. This chapter is organized into distinct sections, each section dedicated to unraveling the synthesis of specific complexes: $[Cu(Cl)(NHC)]$, $[Ag(Cl)(NHC)]$, and $[Rh(acac)(CO)(NHC)]$. To achieve this goal, we employed ssNMR spectroscopy as the primary analytical technique, complemented by computational simulations of NMR parameters and other solid-state analytical tools. Our primary objective is to elucidate whether the desired compounds are indeed formed in the solid-state during ball milling or arise later in solution during the subsequent workup protocol.

Additionally, our study seeks to explore the potential formation of intermediate compounds that might arise during these processes.

Expanding our scope beyond transition metal-NHC complexes, Chapter 3 introduces a straightforward mechanochemical synthesis of chalcogen-NHC derivatives, specifically thioureas and selenoureas. These compounds have gained significant attention due to their unique electronic properties and biological activities. The application of mechanochemistry in this context overcomes the limitations and drawbacks inherent in conventional solution-based methods, offering a more sustainable, eco-friendly, and practical alternative. To comprehensively understand the underlying mechanisms of these transformations, we conduct thorough ssNMR analysis in conjunction with density functional theory (DFT) calculations of NMR parameters. Our investigation encompasses determining whether the desired compounds are formed in the solid-state during ball milling or in solution during the subsequent workup protocol.

Furthermore, our study delves into assessing the antimicrobial activity of metal-NHC complexes, focusing particularly on copper-NHCs, against a spectrum of resistant microorganisms associated with catheter-based infections. Synthesized through a mechanochemical approach, these complexes were evaluated for their antimicrobial activity through the determination of the minimum inhibitory concentration (MIC).

References

- (1) Kerton, F.; Marriott, R. Alternative Solvents for Green Chemistry. *R. Soc. Chem.* **2013**. <https://doi.org/10.1039/9781849736824>.
- (2) Capello, C.; Hellweg, S.; Badertscher, B.; Hungerbühler, K. Life-Cycle Inventory of Waste Solvent Distillation: Statistical Analysis of Empirical Data. *Environ. Sci. Technol.* **2005**, 39 (15), 5885–5892. <https://doi.org/10.1021/es048114o>.
- (3) Ball Milling Towards Green Synthesis: Applications, Projects, Challenges. *R. Soc. Chem.*, **2014**. <https://doi.org/10.1039/9781782621980>.
- (4) Clarke, C. J.; Tu, W.-C.; Levers, O.; Bröhl, A.; Hallett, J. P. Green and Sustainable Solvents in Chemical Processes. *Chem. Rev.* **2018**, 118 (2), 747–800. <https://doi.org/10.1021/acs.chemrev.7b00571>.

- (5) James, S. L.; Adams, C. J.; Bolm, C.; Braga, D.; Collier, P.; Frišćić, T.; Grepioni, F.; Harris, K. D. M.; Hyett, G.; Jones, W.; Krebs, A.; Mack, J.; Maini, L.; Orpen, A. G.; Parkin, I. P.; Shearouse, W. C.; Steed, J. W.; Waddell, D. C. Mechanochemistry: Opportunities for New and Cleaner Synthesis. *Chem. Soc. Rev.* **2011**, *41* (1), 413–447. <https://doi.org/10.1039/C1CS15171A>.
- (6) Howard, J. L.; Cao, Q.; Browne, D. L. Mechanochemistry as an Emerging Tool for Molecular Synthesis: What Can It Offer? *Chem. Sci.* **2018**, *9* (12), 3080–3094. <https://doi.org/10.1039/C7SC05371A>.
- (7) Hernández, J. G.; Bolm, C. Altering Product Selectivity by Mechanochemistry. *J. Org. Chem.* **2017**, *82* (8), 4007–4019. <https://doi.org/10.1021/acs.joc.6b02887>.
- (8) Stolle, A.; Szuppa, T.; Leonhardt, S. E. S.; Ondruschka, B. Ball Milling in Organic Synthesis: Solutions and Challenges. *Chem. Soc. Rev.* **2011**, *40* (5), 2317–2329. <https://doi.org/10.1039/C0CS00195C>.
- (9) Tan, D.; Frišćić, T. Mechanochemistry for Organic Chemists: An Update. *Eur. J. Org. Chem.* **2018**, *2018* (1), 18–33. <https://doi.org/10.1002/ejoc.201700961>.
- (10) Rightmire, N. R.; Hanusa, T. P. Advances in Organometallic Synthesis with Mechanochemical Methods. *Dalton Trans.* **2016**, *45* (6), 2352–2362. <https://doi.org/10.1039/C5DT03866A>.
- (11) Beillard, A.; Bantreil, X.; Métro, T.-X.; Martinez, J.; Lamaty, F. Alternative Technologies That Facilitate Access to Discrete Metal Complexes. *Chem. Rev.* **2019**, *119* (12), 7529–7609. <https://doi.org/10.1021/acs.chemrev.8b00479>.
- (12) Tan, D.; García, F. Main Group Mechanochemistry: From Curiosity to Established Protocols. *Chem. Soc. Rev.* **2019**, *48* (8), 2274–2292. <https://doi.org/10.1039/C7CS00813A>.
- (13) Frišćić, T. Supramolecular Concepts and New Techniques in Mechanochemistry: Cocrystals, Cages, Rotaxanes, Open Metal–Organic Frameworks. *Chem. Soc. Rev.* **2012**, *41* (9), 3493–3510. <https://doi.org/10.1039/C2CS15332G>.

- (14) Porcheddu, A.; Colacino, E.; De Luca, L.; Delogu, F. Metal-Mediated and Metal-Catalyzed Reactions Under Mechanochemical Conditions. *ACS Catal.* **2020**, *10* (15), 8344–8394. <https://doi.org/10.1021/acscatal.0c00142>.
- (15) Bolm, C.; Hernández, J. G. From Synthesis of Amino Acids and Peptides to Enzymatic Catalysis: A Bottom-Up Approach in Mechanochemistry. *ChemSusChem* **2018**, *11* (9), 1410–1420. <https://doi.org/10.1002/cssc.201800113>.
- (16) Koby, R. F.; Doerr, A. M.; Rightmire, N. R.; Schley, N. D.; Brennessel, W. W.; Long, B. K.; Hanusa, T. P. Mechanochemical Formation, Solution Rearrangements, and Catalytic Behavior of a Polymorphic Ca/K Allyl Complex. *Chem. – A Eur. J.* **2021**, *27* (31), 8195–8202. <https://doi.org/10.1002/chem.202100589>.
- (17) Lukin, S.; Germann, L. S.; Frišćić, T.; Halasz, I. Toward Mechanistic Understanding of Mechanochemical Reactions Using Real-Time In Situ Monitoring. *Acc. Chem. Res.* **2022**, *55* (9), 1262–1277. <https://doi.org/10.1021/acs.accounts.2c00062>.
- (18) Silva, I. d'Anciães A.; Bartalucci, E.; Bolm, C.; Wiegand, T. Opportunities And Challenges in Applying Solid-State Nmr Spectroscopy in Organic Mechanochemistry. *Adv. Mater.* **2023**, 2304092. <https://doi.org/10.1002/adma.202304092>.
- (19) Díez-González, S.; Nolan, S. P. Copper, Silver, and Gold Complexes in Hydrosilylation Reactions. *Acc. Chem. Res.* **2008**, *41* (2), 349–358. <https://doi.org/10.1021/ar7001655>.
- (20) Mercks, L.; Albrecht, M. Beyond Catalysis: N-Heterocyclic Carbene Complexes as Components for Medicinal, Luminescent, and Functional Materials Applications. *Chem. Soc. Rev.* **2010**, *39* (6), 1903–1912. <https://doi.org/10.1039/B902238B>.
- (21) Oehninger, L.; Rubbiani, R.; Ott, I. N-Heterocyclic Carbene Metal Complexes in Medicinal Chemistry. *Dalton Trans.* **2013**, *42* (10), 3269–3284. <https://doi.org/10.1039/C2DT32617E>.
- (22) Aleksanyan, D. V.; Kozlov, V. A. Mechanochemical Tools in the Synthesis of Organometallic Compounds. *Mendeleev Commun.* **2023**, *33* (3), 287–301. <https://doi.org/10.1016/j.mencom.2023.04.001>.

- (23) Pisanò, G.; J. Cazin, C. S. Mechanochemical Synthesis of Cu(I)-N-Heterocyclic Carbene Complexes. *Green Chem.* **2020**, *22* (16), 5253–5256. <https://doi.org/10.1039/D0GC01923B>.
- (24) De, S.; Joó, F.; Horváth, H.; Udvardy, A.; Czégéni, C. E. Stirring or Milling? First Synthesis of Rh(I)-(Di-N-Heterocyclic Carbene) Complexes Both in Solution and in a Ball Mill. *J. Organomet. Chem.* **2020**, *918*, 121308. <https://doi.org/10.1016/j.jorganchem.2020.121308>.
- (25) Pisanò, G.; Cazin, C. S. J. General Mechanochemical Synthetic Protocol to Late Transition Metal–NHC (N-Heterocyclic Carbene) Complexes. *ACS Sustain. Chem. Eng.* **2021**, *9* (29), 9625–9631. <https://doi.org/10.1021/acssuschemeng.1c00556>.

CHAPTER 1.

Literature Review

Chapter 1. Literature Review

1.1 Introduction

This thesis chapter provides a comprehensive exploration of mechanochemical synthesis, encompassing its fundamental principles, diverse applications, and the equipment utilized in the process. It delves into the challenges encountered and the advancements achieved in monitoring milling reactions, with a specific emphasis on in situ and ex situ measurements, as well as the application of ssNMR spectroscopy. Additionally, the chapter investigates recent developments in the mechanochemical synthesis of organometallic complexes bearing NHC ligands. It examines various aspects, including the structural properties of these ligands, their applications, and a comparative analysis of conventional and mechanochemical synthesis methods for transition metal complexes bearing NHC ligands, with a special focus on highlighting the weak base approach.

1.2 Overview of Mechanochemical Synthesis

1.2.1 Principle of Mechanochemical Synthesis

A mechanochemical reaction is a chemical reaction that is induced by the direct absorption of mechanical energy. This definition was established by the IUPAC in 2004.¹ In mechanochemical reactions, mechanical actions such as shearing, compression, and grinding play a crucial role in providing the required energy to initiate and promote chemical transformations. Typically, these reactions are carried out using ball mills, which are specifically designed to efficiently transfer energy from the milling balls to the materials being ground, thereby enhancing their chemical reactivity. In 2019, IUPAC recognized mechanochemistry as one of the top ten innovative chemical technologies for sustainable development.²

1.2.2 Historical Background

The history of mechanochemistry can be traced back to ancient times, specifically to 315 B.C., when Theophrastus, a student of Aristotle, described a mechanical-assisted reaction in his book "On Stones". In this work, Theophrastus detailed the reduction of cinnabar (HgS) to mercury (Hg⁰) using a copper vessel and a copper pestle filled with vinegar containing acetic acid.^{3,4} However, after this early discovery, there was a gap of approximately 2000 years with no further reports on mechanical-assisted protocols.

The resurgence of mechanochemistry occurred in 1820 when Michael Faraday conducted grinding experiments using a mortar and pestle to reduce AgCl with active metals such as zinc, iron, copper, or tin.⁵ Although not all of Faraday's results can be reliably replicated today, his work marked one of the earliest systematic investigations into mechanochemical processes.

In 1893, M. Carey Lea conducted groundbreaking studies that revolutionized the understanding of mechanochemical reactions.⁶ Lea's experiments distinguished between the effects of grinding and pressure from thermal influences, elucidating their unique impacts on chemical systems. He demonstrated that grinding silver halides led to the formation of elemental silver, whereas heating alone caused them to melt without decomposition. This emphasized the role of mechanical activation in inducing chemical transformations.

In 1919, Wilhelm Ostwald recognized mechanochemistry as a distinct subdiscipline of chemistry and coined the term "mechanochemistry".⁷ Later in 1984, Gerard Heinicke provided a formal definition of mechanochemistry as the discipline that focuses on physical-chemical modifications of solids induced by mechanical factors (**Figure 1.1**).^{8,9}

Significant advancements have been made in the field of mechanochemical synthesis of organometallic complexes over the past two decades. Initial reports in the early 1990s documented successful synthesis of various complexes,¹⁰ but interest remained relatively low. However, recent studies have reignited enthusiasm for this approach. Researchers have demonstrated the feasibility and advantages of mechanochemical synthesis for a wide range of organometallic complexes, including transition metal complexes with N-heterocyclic carbenes (NHCs), arene and cyclopentadienyl ligands, monometallacyclic and pincer derivatives, as well as main group metal compounds.¹¹ These developments have highlighted the potential of mechanochemical synthesis as an efficient and environmentally friendly method for the synthesis of complex organometallic compounds.

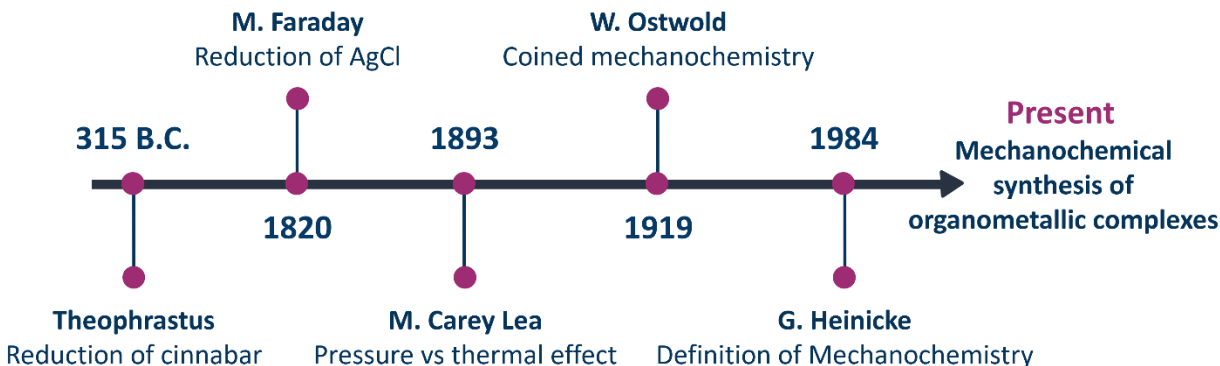


Figure 1.1. Chronological timeline of the historical development of mechanochemistry.

1.2.3 Equipment

Mechanochemical synthesis requires specialized equipment capable of efficiently transferring mechanical energy to the solid reactants. The energy transfer can be achieved manually using a mortar and pestle or automatically through a mortar grinder or various mill devices, such as tumbling mills, planetary mills, mixer (shaker) mills, etc. Among these, planetary mills and mixer mills are widely recognized as highly effective equipment for laboratory mechanochemical synthesis (**Figure 1.2**).

- *Mortar and pestle*

Grinding with a mortar and pestle is a simple and cost-effective method applied in mechanochemical synthesis. It involves grinding solid reactants, typically on a small scale (milligram level), for a specific duration, usually a few minutes, with or without a catalyst. However, the use of mortar and pestle poses certain challenges. These challenges include the difficulty of accurately measuring the energy input, as it solely relies on the operator's strength and technique. Additionally, maintaining consistent and reproducible reaction conditions can be problematic.

- *Mixer mill*

A typical mixer mill setup consists of a clamp securely holding two jars, often made of steel. In a mixer mill, the milling jar is positioned horizontally and swings back and forth. The jars experience vigorous vibrations multiple times per minute, typically at a frequency ranging from 3 to 25 Hz. Throughout the vibration process, the milling balls, usually steel spheres, collide with one another, as well as with the sample and the jar walls, generating impact-related forces.¹² Consequently, the sample absorbs mechanical energy in the form of short pulses.

- *Planetary mill*

The term “planetary mill” is derived from the motion of the milling jars, which resembles the movement of the planets. In a planetary mill, 2 or more milling jars are placed on a rotating disk and rotate around their axis, either in the same or the opposite direction of the rotating disks, with a maximum rotation frequency of 400 rpm. As the disk and jars rotate, the grinding balls inside the jars collide with the jar walls, resulting in a combination of shear, friction, and impact forces.^{13–}

¹⁵ The milling jars used in a planetary mill are typically spherical and are available in various compositions, such as zirconia, agate, chrome-steel, etc.

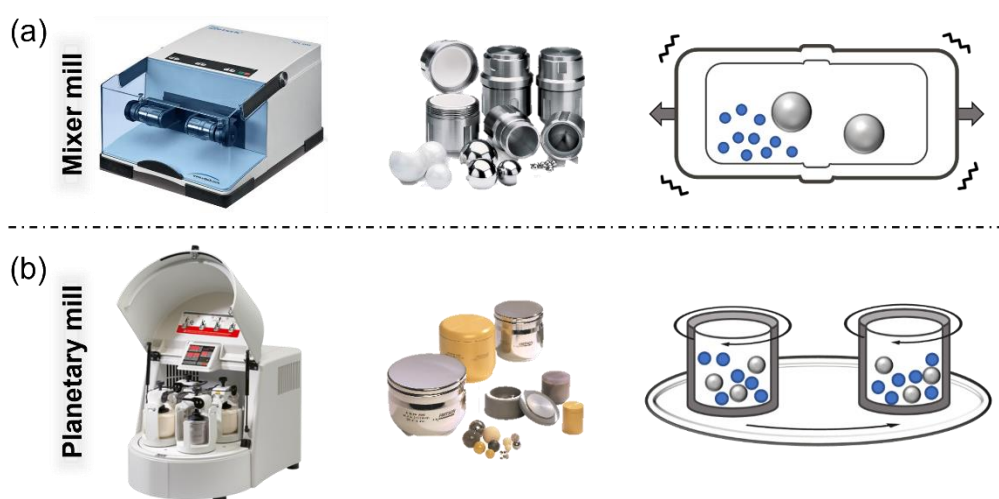


Figure 1.2. Pictures of (a) modern mixer mill (Retsch MM 400) and (b) planetary mill (Fritsch, Pulverisette 5/4). Each mill is equipped with unique sets of jars and grinding balls with varying volumes and compositions. The schematic diagram illustrates the operational modes of both the mixer mill and the planetary mill.

1.2.4 Milling Parameters

When conducting a mechanochemical reaction, several important parameters should be considered in addition to the mill design and its mode of action. These parameters include the composition of the milling jars and balls, the size and quantity of the milling balls, the milling speed, temperature, and milling time.

- *Composition of milling jars and balls*

The composition of the milling jars and balls used in a mechanochemical reaction greatly influences its success. The density of the milling material directly impacts its moment of inertia, which in turn affects the amount of kinetic energy transferred to the sample. Generally, higher-density milling materials tend to enhance the reaction yields. Apart from density, chemical resistance also plays a significant role in material selection. For laboratory-scale synthesis, tungsten carbide and zirconia are commonly preferred due to their chemical resistance. On the other hand, stainless steel, despite its potential for contamination and degradation,¹⁶ is often chosen for large-scale industrial applications due to its cost-effectiveness.

- *Size and quantity of milling balls*

In laboratory-scale synthesis, the size of the milling balls typically falls within the range of 0.1 to 30 mm. It is important to select a milling ball size that maintains coherence between mass and energy while keeping the overall mass constant. Additionally, maintaining the filling degree is essential. In laboratory-scale milling jars, which usually have volumes ranging between 1 and 500 mL, a proportional distribution should be followed. The distribution involved filling one-third of the jars with milling balls, one-third with reactants, and leaving one-third with void space.

- *Milling speed*

The milling frequency, in the case of mixer mills, or rotation rate, in the case of planetary mills, is a crucial parameter in ball milling. Generally, higher agitation frequencies result in faster ball movement and thus increased kinetic energy supplied to the system.¹⁷ However, adjusting the milling frequency can also lead to temperature changes that may be challenging to regulate. Therefore, careful consideration should be given to the temperature changes when adjusting the milling frequency.

- *Temperature*

Temperature can impact factors such as diffusion processes and defect concentrations.¹⁸ In the case of a shaker mill, the temperature can rise to 60 °C due to the impacts generated by the milling balls against the milling jar. While increased temperature can enhance the kinetics of certain reactions, it is important to note that some reactions may be negatively affected by

elevated temperatures. Therefore, careful consideration should be given to the temperature condition to optimize the reaction outcome.

- *Milling time*

Milling time determines the duration required for the process to reach completion. Several factors, including the type of mill used, milling speed, and ball-to-powder ratio, influence the milling time. However, it's important to note that longer milling times can have negative effects on the reaction. Extended durations increase the risk of contamination from the milling balls or jar and may result in the formation of undesirable phases, such as a transition to the amorphous state when the milling process is carried out excessively.

1.2.5 Advantages of Mechanochemical Synthesis over Traditional Methods

Mechanochemical synthesis provides numerous advantages when compared to traditional synthesis methods. One major advantage is that solid-state synthesis eliminates the need for heating, expensive or hazardous reagents, and complex multi-step processing, making it a simpler and more cost-effective option.^{19–21} Additionally, mechanochemical reactions exhibit enhanced reactivity of reactants under grinding or milling, enabling the synthesis of novel or modified compounds and materials.^{22,23}

Solvent-related issues commonly encountered in solution-based synthesis are effectively avoided in solvent-free mechanochemical reactions. These issues include the impact of solvent quality on reaction outcomes and the labor-intensive solvent conditioning process, such as distilling, degassing, and drying. By circumventing these challenges, mechanochemical synthesis offers a more efficient approach.

Furthermore, solid-state synthesis expands the range of available reactants by enabling the use of typically inert or highly insoluble reagents, which may not be suitable for solution-based methods.²⁴ Moreover, mechanochemical synthesis demonstrates higher reaction yields and shorter reaction times, providing time and resource efficiencies.¹⁹

It is important to note that liquid-assisted grinding (LAG) is a specific mechanochemical synthesis methodology that incorporates certain advantages of traditional solution-based methods. LAG involves the use of a catalytic amount of liquid to facilitate the milling process. This approach combines the strengths of both mechanochemical and solution-based methods, enhancing the overall synthesis process.²⁵

1.2.6 Advancements in Mechanochemical Synthesis of Organometallic Complexes

In recent years, the field of mechanochemical synthesis has witnessed significant progress in the synthesis of a wide range of compounds, including organic,^{20,26–29} inorganic,³⁰ and hybrid materials, such as main group elements,^{21,31} metal complexes,^{32,33} organometallic compounds,^{22,34} polymers,³⁵ supramolecular complexes,³⁶ energy materials,³⁷ and nanomaterials.^{38,39}

Owing to the prominence of organic and inorganic compounds, organometallic compounds have often received less attention. However, groundbreaking studies have emerged, demonstrating the feasibility of synthesizing organometallic complexes under mechanochemical conditions.¹¹ These studies have shed light on the potential of mechanochemical methods in this realm.

A key driving force behind the recent advancements in the mechanochemical synthesis of organometallic complexes is the rapid development of solvent-free organic transformations. These transformations are catalyzed or mediated by transition metal complexes, offering an impetus for the exploration of novel synthetic routes and sustainable synthesis methodologies. This progress has unlocked new possibilities for designing and synthesizing organometallic complexes with tailored properties, offering exciting prospects for further innovation and applications in this field.

1.2.7 Developments and Challenges in Monitoring Milling Reactions

Extensive research has been dedicated to unraveling the complex chemical transformations occurring in mechanochemical processes. Scientists have explored a wide range of factors contributing to these processes, including the reduction of particle size, creation of surface defects, mass transfer, and diffusion of surface molecules. Furthermore, various theories have been proposed to shed light on the underlying mechanisms driving these chemical reactions.

One prominent theory, known as the hot-spot theory, was initially proposed by Bowden and co-workers in 1952.⁴⁰ This theory suggests that the impact and friction forces generated during mechanochemical processes result in the production of thermal energy, leading to localized temperature increases. These elevated temperatures, in turn, can trigger crucial processes such

as crystallization or amorphization. However, despite its initial recognition, the hot-spot theory has faced substantial criticism and scrutiny.

Another theory that has been proposed is based on the collision theory. This perspective highlights the role of kinetic energy generated during mechanical treatment as a key factor in initiating phenomena such as fracture and abrasion. The collision theory emphasizes the significance of kinetic energy as the driving force behind mechanochemical reactions.

In addition to these theories, Smekal made an important observation regarding the reactivity of solids during mechanochemical processes.⁴¹ He discovered that even if an immediate chemical reaction does not occur, the reactivity of solids can still be enhanced through mechanical deformation. This phenomenon, known as “mechanical activation”, holds the potential to significantly improve the efficiency of subsequent processing steps.

Nevertheless, the ultimate source of reactivity in mechanochemical processes remains a mystery that researchers are actively investigating. The lack of knowledge in this field can be attributed to practical constraints. Mechanochemical processes often take place in closed systems, where the milling process is intermittently halted, and mechanistic information is obtained through ex situ analysis. These analysis typically involve the dissolution of a compound in a liquid medium, which deviates from the non-equilibrium conditions present during mechanochemical reactions. To overcome these limitations, real-time in situ monitoring analysis can be employed to probe the chemical composition of the reaction mixture.

1.2.7.1 In situ monitoring of milling reactions

In recent years, significant progress has been made in the development of advanced techniques to enable real-time in situ monitoring of mechanochemically-induced reactions. These techniques allow for probing short-lived or unstable products and monitoring the reactions without interruption. Among the most commonly utilized methods are synchrotron powder X-ray diffraction and X-ray absorption spectroscopy, which have been refined to track changes occurring within the milling jar during the transformations.^{42–46} Additionally, Raman spectroscopy has provided valuable insights into the kinetics of these reactions during ball-milling.^{47,48} Moreover, the synergistic combination of these techniques has shown significant promise in advancing our understanding of mechanochemical synthesis.^{49–51}

In addition to these techniques, non-destructive and atom-selective ssNMR spectroscopy has emerged as a promising tool for gaining atomic-level insights into mechanochemical reactions.⁵² For instance, Wüllen and co-workers developed an innovative setup integrating a ball milling device into a static ssNMR probe (**Figure 1.3**), allowing for the monitoring of mechanochemical synthesis in real-time. They successfully employed this setup to observe the mechanochemical synthesis of zinc phenylphosphonate from zinc acetate and phenylphosphonic acid.⁵³ However, it is important to note that these ssNMR experiments are conducted on static samples, which limits the acquisition of high-resolution NMR spectra.

Despite the significant progress made, current real-time in situ analysis still has some limitations. One of the primary reasons for these limitations is the experimental setup involved in these reactions. The nature of mechanochemical reactions, occurring in sealed and rapidly moving milling jars, makes it challenging to directly observe and track the progress of the reaction. The high-speed and violent motion of the milling balls further complicates the monitoring process. Additionally, the sampling that can be monitored in the mechanoreactor is limited, and the home-built devices used for analysis are not yet commercially accessible.

As a result, understanding mechanochemical synthesis through real-time in situ analysis is challenging and remains an open line of research, with much to be investigated. Consequently, it becomes necessary to employ ex situ analytical techniques that can capture and preserve as much information as possible about the milling process.

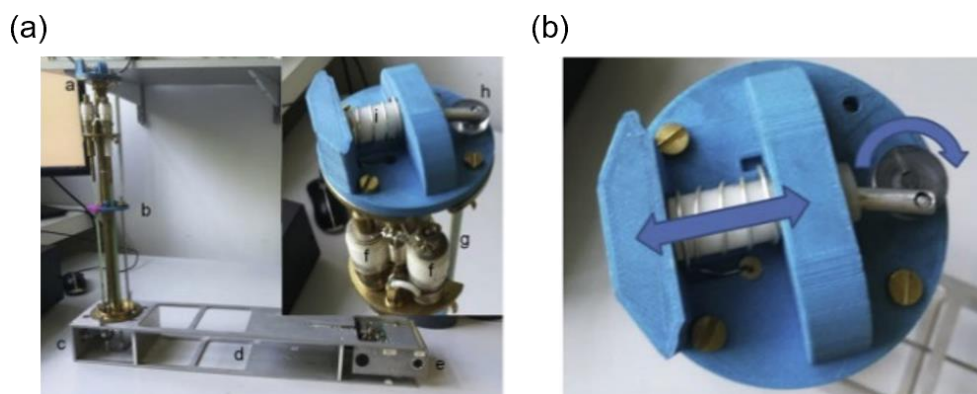


Figure 1.3. (a) Vibrational ball mill integrated into a static ssNMR probe. The main image presents a comprehensive view of the complete probe, excluding the aluminum shield, while the inset provides a closer look at the upper section where the ball mill is placed. (b) The upper section featuring schematics illustrating the working principle of the ball mill, demonstrating the translation

of rotational motion into transversal shaking through the eccentric wheel. The colored parts are 3D-printed using polylactic acid.⁵³

1.2.7.2 Ex situ monitoring of milling reactions

Ex situ monitoring of milling reactions involves the collection of samples at different time intervals during the milling process and subsequent analysis using various analytical techniques. The careful selection and utilization of appropriate ex situ methods can provide valuable insights into the progress of the reaction, intermediate species formed, and final products obtained. **Figure 1.4** summarizes the commonly employed analytical techniques in mechanochemical studies, along with their respective advantages and limitations.

One widely used technique in the analysis of solid materials in mechanochemical reactions is powder X-ray diffraction (PXRD).^{54,55} PXRD proves highly effective in providing valuable structural information, such as phase identification, purity assessment, crystallite size determination, and morphology analysis. It is particularly useful for detecting transformations occurring during these reactions. Additionally, PXRD can be employed for quantitative purposes, particularly through advanced techniques such as Rietveld analysis, which can refine crystal structures. However, achieving quantitative results with PXRD often requires careful calibration, data processing, and validation. Despite its notable advantages, PXRD is limited to studying crystallites within a specific size range. This limitation poses challenges when attempting to characterize fully amorphous materials resulting from mechanochemical processes.

Raman spectroscopy is another valuable technique that offers insights into the chemical composition of the reaction by tracking functional groups.⁵⁶ Unlike PXRD, Raman spectroscopy is not dependent on the crystallinity, making it applicable to non-crystalline materials. Furthermore, it is characterized by its high sensitivity and relatively low cost compared to other analytical techniques such as PXRD, NMR, and electron paramagnetic resonance (EPR) spectroscopy. However, one significant limitation of Raman spectroscopy is its poor repeatability, making it challenging to obtain reliable quantitative data. Another limitation arises when analyzing materials that are not Raman-active or exhibit high fluorescence. Additionally, the radiation used in Raman spectroscopy can generate heat in samples, potentially altering their composition or degrading compounds.

Infrared (IR) spectroscopy is a technique that provides structural information by probing the vibrational modes of functional groups in molecules. It is often used in conjunction with Raman

spectroscopy to complement the analysis of mechanochemical processes. IR spectroscopy is versatile, offering insights into molecular composition and structural characteristics.^{57–59} This analytical technique fails to provide information on the relative positions of the different functional groups, and hence, on the structure of the whole molecule.

EPR spectroscopy is a highly sensitive technique and particularly valuable in investigating the structure and bonding of paramagnetic species. It offers exceptional time resolution and can provide detailed information even at low concentrations. EPR spectroscopy has been successfully applied in mechanochemical synthesis to detect paramagnetic metals,^{60,61} explore radical generation,⁶² study single electron transfer,⁶³ investigate conversions of soft materials,⁶⁴ and examine exchange interactions.⁶⁵ However, its applicability is limited to the analysis of paramagnetic species.

NMR spectroscopy, both in solution and solid-state, holds significant potential in the field of mechanochemical synthesis. Solution NMR is traditionally used for analyzing molecular structures of crude or purified products. However, the process of dissolving samples in solution NMR studies can pose challenges as it may alter the composition of the products, leading to potential inaccuracies in the analysis. Solid-state NMR spectroscopy offers a solution to these challenges by allowing direct analysis of solid intermediates and final product mixtures without the need for sample dissolution. This eliminates any ambiguity regarding whether the reactions occur during ball milling, workup and purification, or characterization stages.^{66–69} Solid-state NMR spectroscopy provides an elemental-selective analysis at an atomic level, allows characterization of a broad range of compounds, including amorphous materials, and offers non-destructive analysis. By employing ssNMR spectroscopy, researchers can gain a comprehensive understanding of various aspects of mechanochemical synthesis. It provides insights into reaction mechanisms,⁷⁰ facilitates the study of reaction kinetics,⁷¹ and examines the influence of milling parameters.^{70,72–75}

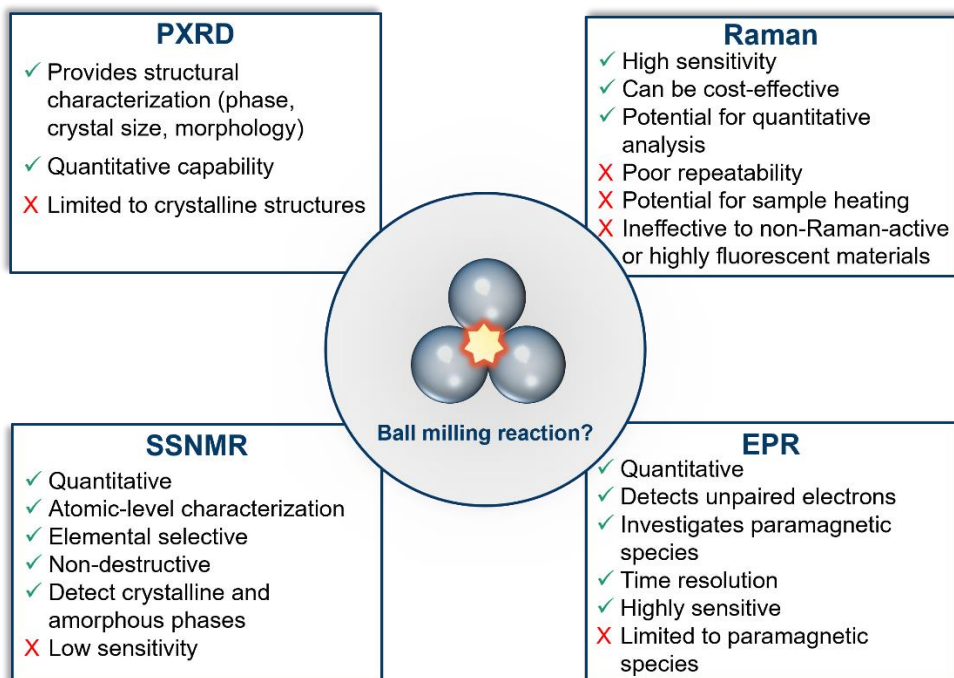


Figure 1.4. Schematic representation highlighting the key advantages and disadvantages associated with analytical techniques commonly utilized for the ex situ monitoring of mechanochemical reactions.

1.3 SSNMR Spectroscopy

1.3.1 Challenges of ssNMR Spectroscopy

Solid-state NMR spectroscopy is a powerful analytical technique that provides a wealth of information, which are not accessible through its solution-state counterpart. However, it has not received the same level of recognition, primarily due to the inherent challenges in achieving comparable resolution in ssNMR experiments. One of the primary challenges arises from the orientational dependence, or anisotropy, of the interactions that influence the dynamics of nuclear spins. These interactions include chemical shielding arising from the interaction with surrounding electrons, as well as the coupling of nuclear spins through bonds (J coupling) and space (dipolar coupling), and quadrupolar coupling, as depicted in **Figure 1.5**. The anisotropic nature of these interactions leads to the broadening of the spectral lineshapes in ssNMR. In contrast, solution-state NMR benefits from the rapid molecular tumbling, effectively averaging out the broadening effects caused by anisotropic interactions, as illustrated in **Figure 1.6**. Nonetheless, it is crucial

to highlight that while anisotropic interactions in ssNMR present challenges, they simultaneously unlock invaluable structural insights, particularly in the investigation of powder samples.

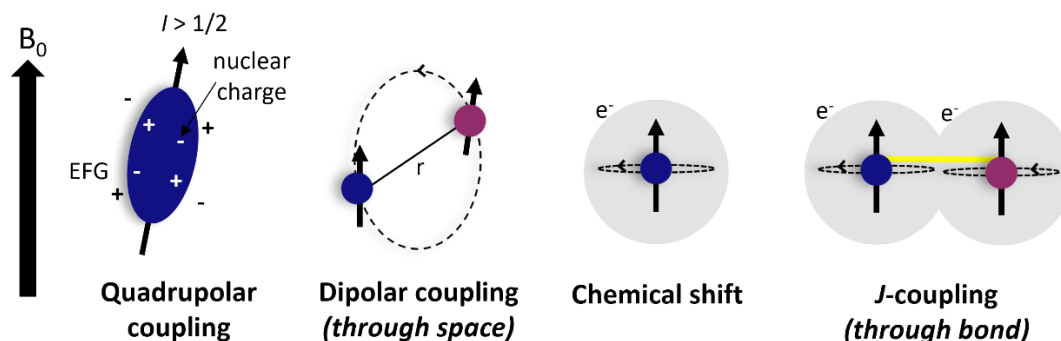


Figure 1.5. Summary of anisotropic interactions in NMR.

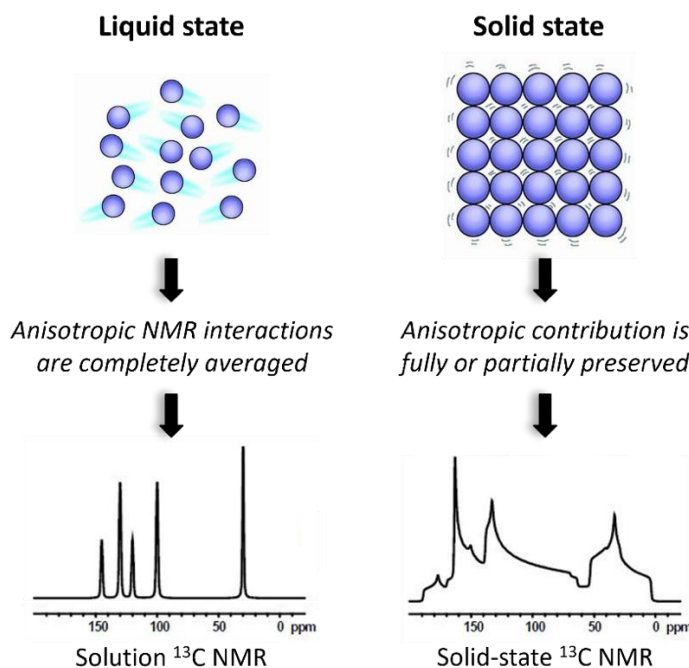


Figure 1.6. Comparison between solution ^{13}C NMR and solid-state ^{13}C NMR spectra

In this context, the orientation dependence of the chemical shift, referred to as chemical shift anisotropy (CSA), gives rise to broad peaks with distinctive line shapes, as exemplified in **Figure 1.7**. The line shape is described by the chemical shift tensor (δ), providing information on the magnitude and the orientation dependence of the chemical shift interaction. The symmetric portion of the chemical shift tensor can be diagonalized into its principal axis system with the set of diagonal elements being referred to as the principal components.⁷⁶ In the Haeberlen-Mehring-

Spiess convention, the principal components are ordered according to their separation from the isotropic value (δ_{iso}), which represents the center of gravity of the line shape.⁷⁷ The isotropic chemical shift is the parameter observed in most NMR experiments on samples in isotropic solvents, due to the averaging of CSA by rapid and random molecular tumbling. The reduced anisotropy (δ_{aniso}) quantifies the magnitude of CSA, indicating the largest separation from the spectral center of gravity. Additionally, the asymmetry parameter η_{CS} provides insights into the degree of divergence from the line shape anticipated for an axially symmetric chemical shift tensor.

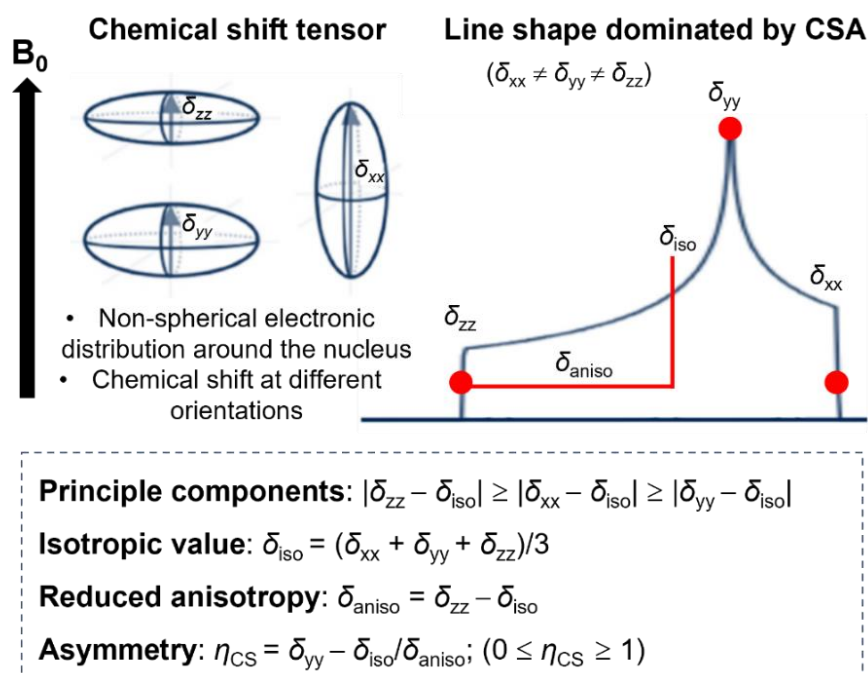


Figure 1.7. Schematic representation of the principal components of chemical shift tensor and line shape dominated by CSA.

Furthermore, the study of quadrupolar nuclei, which have spin quantum numbers greater than $\frac{1}{2}$ and represent over 74% of the NMR-active isotopes, is of significant scientific interest due to the unique quadrupolar interaction resulting from the interplay between their nuclear quadrupolar moment and the electric field gradient (EFG).⁷⁸ This interaction provides valuable insights into molecular structure and local environments. For half-integer spin quadrupolar nuclei, like ^{35}Cl and ^{63}Cu , their NMR spectra are usually dominated by the central transition (CT) between energy levels $m_I = +1/2$ and $-1/2$, which is not broadened by the first-order quadrupolar interaction but only the second-order quadrupolar interaction. The observed lineshapes in these spectra

contain valuable information about the magnitude (C_Q) and asymmetry (η_Q) of the quadrupolar interaction, providing insights into the characteristics of the electric field gradient. The magnitude C_Q is defined as $C_Q = eQV_{zz}/h$ where V_{zz} denotes the largest component of the EFG tensor, Q the nuclear quadrupole moment, e the elementary charge, and h the Planck constant. The asymmetry η_Q is defined as $\eta_Q = (V_{yy} - V_{xx})/V_{zz}$, where $\{V_{xx}, V_{yy}, V_{zz}\}$ are the eigenvalues of the EFG tensor.⁷⁹

1.3.2 Resolution and Sensitivity Enhancement

In the field of organometallic mechanochemical synthesis, ssNMR spectroscopy plays a crucial role in studying spin-1/2 nuclei such as ^1H , ^{13}C , ^{15}N , ^{19}F , and ^{31}P . To gain detailed insights, high-resolution NMR spectra are typically required, which can be achieved using the magic angle spinning (MAS) technique.^{80,81} MAS involves rotating a powdered sample at a fixed angle of 54.74° relative to the static magnetic field B_0 (**Figure 1.8a**). By employing sufficiently fast MAS frequencies (up to 200 kHz),⁸² the interactions affecting spin-1/2 nuclei can be effectively minimized, resulting in improved spectral resolution. Additionally, homo- and heteronuclear decoupling approaches are commonly employed with MAS to further enhance resolution in ssNMR spectra and to extract the relevant information.^{83,84}

Nevertheless, certain spin-1/2 nuclei, such as ^{13}C and ^{15}N , present challenges in ssNMR due to their low natural abundance and small gyromagnetic ratio (γ), which lead to a poor signal-to-noise ratio (SNR). To overcome this limitation, the cross-polarization (CP) technique, is commonly used in combination with MAS and high-power decoupling. CP involves transferring polarization from abundant high- γ nuclei, such as ^1H or ^{19}F , to the less abundant and lower- γ ^{13}C and ^{15}N nuclei through heteronuclear dipolar couplings (**Figure 1.8b**). This polarization transfer enhances the NMR signals and allows for shorter recycle delay times, thus improving the sensitivity.

Another technique to enhance signals from spin-1/2 nuclei, particularly when broadening arises from large chemical shift anisotropy interactions, is the Carr-Purcell-Meiboom-Gill (CPMG) technique.^{85,86} This method applies a train of 180° pulses during data acquisition to refocus the signal, resulting in the recording of multiple spin echoes throughout the entire timescale of transverse relaxation (**Figure 1.8**). Fourier transformation of the resulting echo train produces a spectrum with a series of narrow peaks called spikelets.⁸⁷ These spikelets exhibit significantly improved SNR and accurately represent the line shape of the NMR signal.

In addition to one-dimensional experiments, multidimensional techniques are crucial to probe connectivities and proximities between distinct or identical isotopes. For instance, the two-

dimensional (2D) heteronuclear correlation (HETCOR) experiment based on a single CP transfer (CP-HETCOR) is widely used to probe the proximities between distinct spin-1/2 isotopes.^{88,89} HETCOR correlation involving protons are usually carried under fast MAS to improve the resolution. Under this condition, the sensitivity can be enhanced by exciting and detecting protons using the double CP scheme (DCP), shown in **Figure 1.8c**.⁹⁰ In particular, the DCP experiment with short CP contact time can be used to observe selectively ^1H - ^{13}C covalent bonds in organic moieties.

Furthermore, the study of quadrupolar nuclei presents challenges in practical applications due to the broadening effects associated with second-order quadrupolar interactions, which cannot be averaged out by MAS. To overcome these challenges, researchers have explored various approaches. One effective strategy involves the utilization of high magnetic fields, up to 35.2 T,⁹¹ which significantly reduce the broadening caused by the second-order quadrupolar interaction, leading to a substantial improvement in the spectral resolution.

Moreover, many quadrupolar nuclei suffer from poor sensitivity due to low gyromagnetic ratios, low natural abundances, and large quadrupolar moments, which pose additional challenges for conventional NMR techniques. To overcome these difficulties, the Quadrupolar CPMG (QCPMG) NMR technique,⁹² adapted from CPMG, is commonly employed for signal enhancement (**Figure 1.8d**). It consists of a train of rectangular CT-selective pulses. For patterns with broad widths greater than the excitation bandwidth of the CT-selective pulses, its variant based on WURST (wideband uniform-rate smooth truncation) pulses is commonly employed to achieve efficient broadband excitation.^{93,94} In this sequence, the rectangular pulses used in the QCPMG sequence are replaced with WURST pulses, during which the carrier frequency is swept to broaden the excitation bandwidth (**Figure 1.8e**).

Nevertheless, in certain cases where spectra are extremely broad, it becomes necessary to obtain them in multiple segments. This is achieved by acquiring “sub-spectra” at different offset frequencies and subsequently co-adding them to reconstruct the complete spectrum. This methodology, referred to as piecewise acquisition, frequency stepping, or variable offset cumulative spectroscopy (VOCS),⁹⁵ is commonly used in conjunction with QCPMG or WURST-QCPMG to overcome the challenges associated with extremely broad spectra.^{96,97}

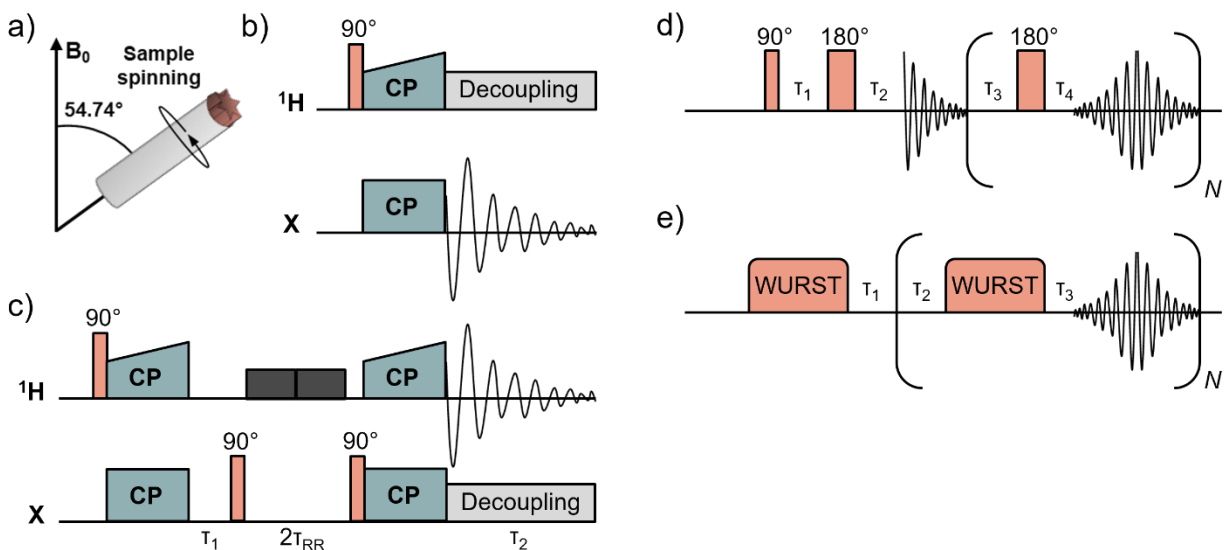


Figure 1.8. (a) Schematic illustration of MAS. Pulse sequences of (b) CP, (c) ^1H detection and indirect detection of X ($^1\text{H}\{X\}$) DCP HETCOR, (d) QCPMG, and (e) WURST-QCPMG. These sequences represent the primary NMR techniques employed in my doctoral research.

1.3.3 Challenges and Advances in Computing NMR Parameters

Despite considerable advancements in improving the resolution and sensitivity of ssNMR techniques, the interpretation and assignment of ssNMR spectra remain notably challenging. Lately, there has been a growing interest among the experimental ssNMR community in utilizing first-principles calculations. These calculations entail computationally predicting NMR parameters, such as chemical shifts, quadrupolar interactions, and indirect J coupling constants, based on specified structural models. This interest is particularly prominent in the realm of organic or organometallic species, where empirical correlations between NMR parameters and atomic-level structure present greater complexities.

Ramsey laid the foundation for computing NMR parameters in the early 1950s.^{98,99} Since then, the quantum chemistry community has developed practical schemes to compute these parameters, attracting interest from experimentalists. There are two main calculation methodologies:

1. Wave Function-based Methods:

Quantum chemistry delves into understanding the behavior of atoms and molecules at the quantum level, primarily governed by the Schrödinger equation, which describes the behavior

within a given system.¹⁰⁰ However, solving this equation becomes highly intricate for systems with numerous electrons, such as larger molecules or solid materials. The commonly used Hartree-Fock method simplifies calculations by approximating electron interactions as an average or mean field interaction. While foundational, this method does not entirely encompass electron-electron correlation, crucial for accurate molecular prediction. Advanced techniques like configuration interaction methods aim to integrate electron correlation effects, allowing more precise predictions of molecular properties. However, their increased accuracy necessitates significantly higher computational resources due to complexity, posing challenges and expenses, especially concerning solid materials or larger molecular systems.

2. Density functional Theory (DFT):

Density Functional Theory (DFT) presents an alternative approach by focusing on electronic density as the core variable. Foundational work by Hohenberg and Kohn established that the energy of a system, comprising electrons and nuclei in their ground state, entirely relies on the system's electron density (ρ).¹⁰¹ Subsequently, Kohn and Sham introduced a practical implementation of DFT, demonstrating how the intricate many-body problem could be reframed using a set of fictitious noninteracting particles that mirror the charge density and, consequently, the total energy of the actual system. The Kohn and Sham (KS) theory illustrates this relationship through an equation:¹⁰²

$$E_{\text{DFT}}[\rho] = T[\rho] + E_{\text{ne}}[\rho] + J[\rho] + E_{\text{xc}}[\rho]$$

Here, T , E_{ne} , J , and E_{xc} represent the kinetic energy of electrons, nuclear-electron attraction energy, electron-electron repulsive energy, and electron-electron exchange-correlation energy, respectively. Each term constitutes a function of the electron density ρ , which is itself a function of three positional coordinates (x , y , and z). The exchange-correlation functional $V_{\text{xc}}[\rho]$, describing exchange and correlation energies among electrons, remains a crucial yet unknown element, posing a challenge in practical computations.

To address this challenge, simplified functional forms have been designed, aligning with established physical principles and constraints. The simplest, known as the local density approximation (LDA),¹⁰² approximates the exchange-correlation energy through a piecewise method, assigning energy at each spatial point equivalent to the exact exchange-correlation energy of a uniform electron gas at the density of that specific point's density. Despite the substantial variation in electron density within a material, this method surprisingly proves

reasonably effective in predicting a solid's energy and structure. To improve accuracy, modifications introduce terms dependent on the gradient of density, known as the generalized gradient approximation (GGA),¹⁰³ enhancing the predictive capability of DFT. Several GGAs have been proposed, among which the Perdew, Bruke, and Ernzerhof (PBE)¹⁰⁴ functional stands out and is widely used in Gauge Including Projector Augmented-Wave (GIPAW) calculations.

Quantum-chemical calculations have traditionally been employed to predict NMR parameters, mainly in discrete systems.^{103,105} However, these methods encountered limitations when applied to extended periodic solids, often treating them as small molecules or atom clusters terminated by hydrogen atoms. This representation failed to accurately mirror the true solid-state structure. The artificial presence of a surface in these models significantly affected the electronic properties within the bulk, with the electric field, typically zero in solids, remaining non-zero in smaller clusters, influencing computed NMR parameters.¹⁰⁶

In 2001, Pickard and Mauri introduced the GIPAW approach,¹⁰⁷ revolutionizing theoretical calculations for solid materials. GIPAW enabled the calculation of magnetic shielding in periodic systems using a plane-wave basis set. Leveraging the inherent periodicity of solids, this method reconstructed the repeating three-dimensional structure from a small-volume unit. This approach facilitated accurate calculations for all atoms within the system simultaneously, significantly reducing time and cost compared to previous methods. Numerous studies have demonstrated the efficacy of GIPAW across diverse material categories, extensively reviewed elsewhere,^{108,109} notably highlighting its effectiveness in analyzing organometallic complexes.¹¹⁰

The GIPAW method has been employed in studying various nuclei. Charpentier's comprehensive review categorized these nuclei into four primary groups, based on their suitability for GIPAW investigations:¹⁰⁹

1. NMR-established nuclei (e.g., ^1H , ^{11}B , ^{13}C , ^{15}N) are renowned for their compatibility with DFT calculations and extensive use in NMR studies.¹¹¹ These are commonly analyzed using the DFT PBE functional, mainly from the first three rows of the periodic table.
2. Less-NMR sensitive nuclei (e.g., ^{33}S , ^{43}Ca , and ^{25}Mg) show reduced NMR sensitivity due to factors like low gyromagnetic ratio and/or natural abundance.^{112,113} Calculations show good agreement with experimental results for quadrupolar coupling constants, and reasonable agreement for isotropic chemical shifts, but only semi-qualitative outcomes for the asymmetry parameter.

3. Quadrupolar halogen nuclei (e.g., $^{35,37}\text{Cl}$, $^{78,81}\text{Br}$, and ^{127}I) possess a significant nuclear quadrupole moment. Recent studies reveal accurate predictions for quadrupolar interaction parameters but potentially overestimated isotropic chemical shifts due to unaccounted relativistic effects in GIPAW implementations.^{114–117} Moreover, the hydration level of compounds notably affects quadrupolar coupling constants, likely influenced by vibrational motions of water molecules affecting NMR parameters.
4. Transition elements (e.g., $^{63/65}\text{Cu}$, ^{51}V , $^{47/49}\text{Ti}$) present challenges in DFT due to semi-core states overlapping with d-valence states. Traditional norm-conserving pseudopotentials (NCP) aim to replicate electronic charge within the core but demand increased basis set size when treating semi-core states as valence.^{118,119} Ultra-soft pseudopotential (USPP) methods relax this constraint by using multiple atom-like pseudo-wave functions, enabling larger cut-off radii.¹²⁰ This advancement has made transition elements compatible with GIPAW.^{110,121–124} Notably, recent DFT calculations for $^{63/65}\text{Cu}$ exhibit impressive agreement with experimental NMR parameters, yet relatively bulky compounds show an underestimation in quadrupolar coupling constants.¹²⁴

Despite advancements, computational complexities persist, particularly in compounds containing heavier elements such as transition metals. Challenges arise from the complexity of generating efficient pseudopotentials crucial for accurate computational modeling in such scenarios. Additionally, the choice of functional, basis set, and geometry optimization procedures significantly influences the accuracy of calculated NMR parameters.^{125,126}

1.3.4 Potential Applications of ssNMR in Mechanochemical Synthesis

Solid-state NMR spectroscopy offers unique capabilities for investigating mechanochemical reactions and understanding the underlying processes. Here are some of the potential applications of ssNMR spectroscopy in this context:

1. Monitoring reaction kinetics:

Solid-state NMR spectra can be recorded at discrete time steps, allowing for the investigation of kinetic information. This has been applied, for example, in studying the mechanochemical synthesis of alane (AlH_3)⁷⁵ and characterizing the mechanochemical properties of $\text{LiBH}_4\text{:AlCl}_3$ mixtures.⁶⁷ Also, ssNMR spectroscopy has been successfully applied to investigate the bromination reaction of a cyclic sulfoximine (1) using N-bromosuccinimide (NBS) within a mixer ball mill.⁷⁴ Ex situ ssNMR spectroscopy allowed the determination of the reaction time required

for the complete conversion of the starting materials. **Figure 1.9** presents the $^1\text{H} \rightarrow ^{13}\text{C}$ CP-MAS spectra of the solid material extracted from the ball mill at different time intervals for the bromination reaction. Analysis of these spectra revealed the presence of small resonances corresponding to the starting material 1 in the initial spectra obtained after 5 and 15 minutes of ball milling. However, after 30 minutes, complete conversion of the starting materials was observed, with no resonances associated with compound 1.

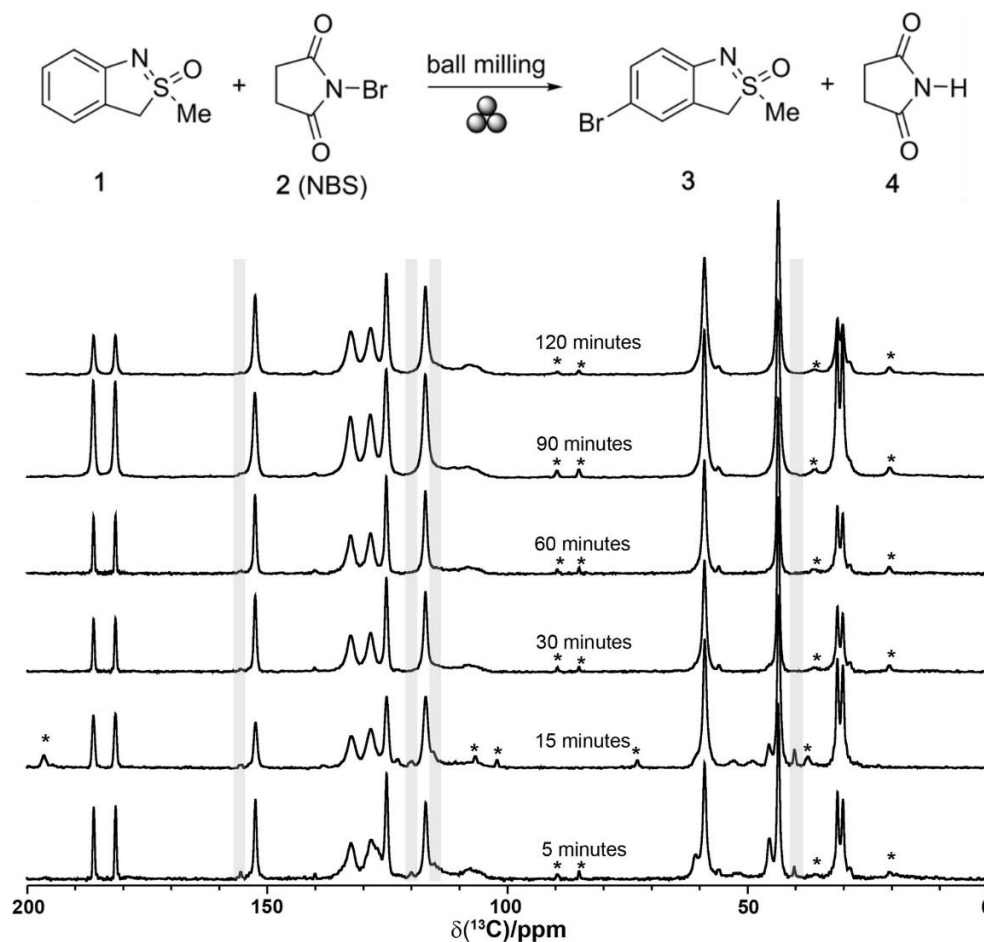


Figure 1.9. 1D $^1\text{H} \rightarrow ^{13}\text{C}$ CP-MAS spectra of samples collected at different time intervals from the milling jar during the bromination reaction of cyclic sulfoximine (shown above the spectra). Resonances associated with the sulfoximine starting material are shaded in grey. Complete conversion of the starting material is observed after 30 minutes of ball milling. The MAS spinning sidebands are denoted by (*).⁷⁴

2. Elucidation of reaction products and intermediates:

Several studies have employed ^{31}P ssNMR spectroscopy to investigate reaction products and characterize mechanochemical processes. These studies have examined the formation of phosphonium salts through the milling of triphenylphosphine with solid organic bromides.¹²⁷ Additionally, the mechanochemical synthesis of Pt-complexes, *cis*-(Ph_3P) $_2\text{PtCl}_2$ and *cis*-(Ph_3P) $_2\text{PtCO}_3$, has been explored by milling polycrystalline PtCl_2 with Ph_3P and *cis*-(Ph_3P) $_2\text{PtCl}_2$ with anhydrous K_2CO_3 , respectively.⁶⁶ The successful formation of these products was confirmed by comparing the ssNMR spectra to their crystalline analogs.

Furthermore, ^{13}C ssNMR spectroscopy has been employed to gain insights into the formation of C-N amide bonds using *N*-(3-(dimethylamino)propyl)-*N'*-ethylcarbodiimide hydrochloride ($\text{EDC}\cdot\text{HCl}$) as a coupling reagent.⁶⁹ This study demonstrated the formation of a stable pseudocyclic intermediate during the reaction of $\text{EDC}\cdot\text{HCl}$ with benzoic acid (**Figure 1.10**).

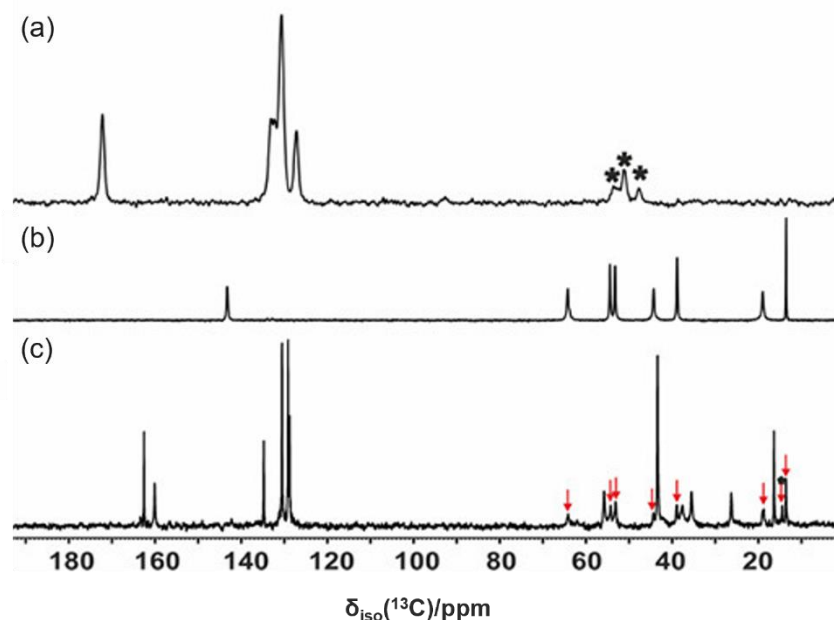


Figure 1.10. 1D $^1\text{H}\rightarrow^{13}\text{C}$ CP-MAS NMR spectra of benzoic acid (a), $\text{EDC}\cdot\text{HCl}$ (b), and crude mixture formed after 1 h grinding (c). The spinning sidebands are denoted by asterisks (*), and the signals of unreacted $\text{EDC}\cdot\text{HCl}$ are indicated by red arrows.

3. Structure determination through NMR crystallography:

Another notable potential lies in the structure determination of reaction products through NMR crystallography. Solid-state NMR offers advantages over PXRD in detecting the formation of amorphous phases, which may not be evident in the powder pattern. This is particularly valuable

when amorphous phases appear as broad backgrounds in XRD. NMR crystallography combines the strengths of XRD and ssNMR spectroscopy, making it valuable in mechanochemistry. In mechanochemistry, novel crystalline materials and polymorphs are often synthesized, which may not be accessible through traditional synthetic methods. NMR crystallography has been successfully applied to various systems, such as multi-component crystals containing urea¹¹⁶ and fluoxetine HCl co-crystals¹¹⁷ leading to the determination of their structures. To investigate these systems, ³⁵Cl ssNMR experiments were specifically conducted. In the case of multi-component crystals containing urea, ³⁵Cl ssNMR experiments provided a unique spectral fingerprint and a distinct set of ³⁵Cl EFG tensor parameters for each system. The structure determination process involved utilizing initial structure models derived from PXRD data, followed by DFT calculations to determine the EFG. However, there was a discrepancy between the experimentally measured EFG tensors and those calculated based on the initial models. To enhance the accuracy of the structural models, plane-wave DFT calculations were performed and the crystal structures were refined by incorporating ssNMR data, particularly the experimental ³⁵Cl EFG tensors.

4. Studying milling products without further post-processing:

Furthermore, ssNMR allows for the direct analysis of product composition without the need for dissolution, which can introduce undesired reactions and alter the product composition. This is in contrast to solution-state NMR, which requires product dissolution in the NMR solvent. Solid-state NMR is particularly useful in preserving polymorphic structural information immediately after mechanochemical formation, as exemplified by the formation of a unique polymorph of Wilkinson's catalyst by ball milling.^{128,129} Additionally, ssNMR has proven valuable in studying compounds with high sublimation tendencies, such as *a*-(trifluoromethyl)-lactic acid (TFL). Direct analysis of TFL mixtures using ssNMR allows for reliable differentiation between optically pure phases and the racemic compound, while solution-based NMR techniques cannot provide distinction and may result in loss of product due to sublimation, thus altering the enantiomer composition.

5. In situ monitoring:

A notable application of in situ ssNMR in mechanochemistry involved the investigation of halogen bond formation between triphenylphosphine oxide (Ph₃PO) and *para*-diiodotetrafluorobenzene (*p*-C₆F₄I₂) using ³¹P MAS NMR (**Figure 1.11**).⁷¹ From the same halogen bond donor (*p*-C₆F₄I₂) and acceptor (Ph₃PO) pair, two distinct halogen-bonded cocrystals

(monoclinic **1** and triclinic **2**) were observed to form, as depicted in **Figure 1.11**. In this study, the researchers analyzed the $^1\text{H} \rightarrow ^{31}\text{P}$ CP-MAS NMR spectra to explore the effects of temperature, MAS frequency, and the presence of a liquid on the co-crystallization process. The normalized peak integrals obtained from the NMR spectra allowed for Johnson-Mehl-Avrami-Yerofeev-Kolmogorov (JMAYK) analysis, revealing that the formation of halogen bonds was primarily controlled by a diffusion-controlled mechanism. This study emphasizes the significance of efficient mixing in initiating the process of halogen bond formation.

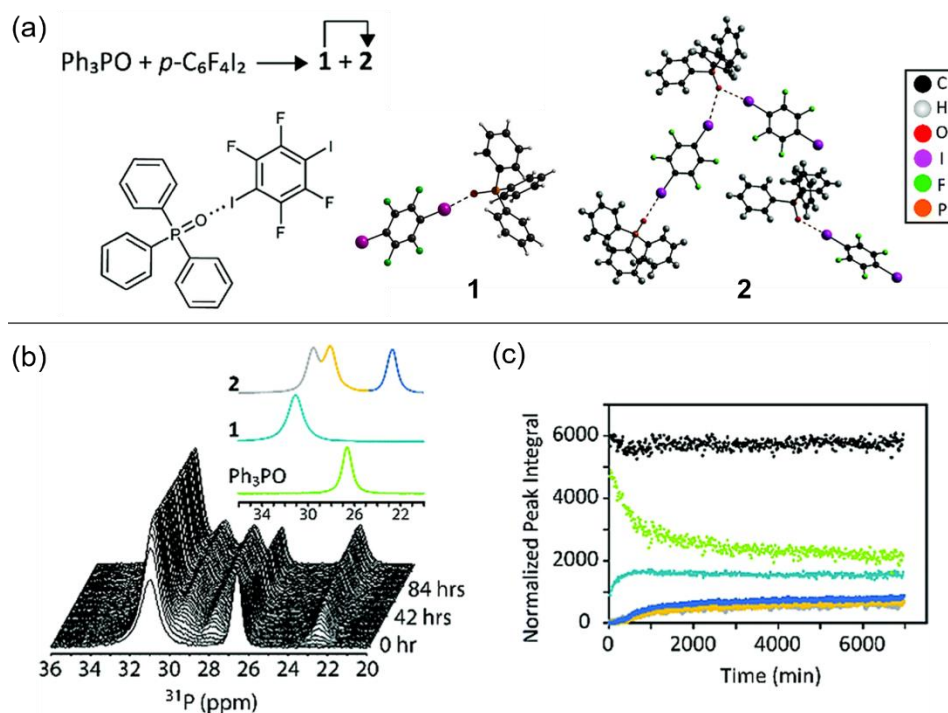


Figure 1.11. Real-time in situ study of co-crystallization between Ph_3PO and $p\text{-C}_6\text{F}_4\text{I}_2$ without milling via 1D $^1\text{H} \rightarrow ^{31}\text{P}$ CP-MAS ssNMR spectroscopy. (a) Chemical structures of the halogen acceptor and donor, along with the crystallographic structures of cocrystals **1**¹³⁰ and **2**. Cocrystal **1** exhibits a single crystallographically identified halogen bond while cocrystal **2** displays three crystallographically distinct halogen bonds. (b) In situ 1D $^1\text{H} \rightarrow ^{31}\text{P}$ CP-MAS NMR spectra conducted at 35 °C, with a magnetic field strength of $B_0 = 9.4$ T, and a MAS frequency, $\nu_R = 10$ kHz. The inset displays isotropic peaks corresponding to Ph_3PO , pure **1**, and pure **2**. (c) Corresponding normalized peak integrals plotted over time. The sum of all peak integrals (black) remains constant, indicating the absence of an amorphous intermediate.⁷¹

In another investigation, the spontaneous co-crystallization of caffeine and malonic acid was examined using ^{13}C MAS NMR spectroscopy (**Figure 1.12**).¹³¹ The kinetics of co-crystallization were assessed by recording $^1\text{H} \rightarrow ^{13}\text{C}$ CP-MAS NMR spectra at regular intervals. Interestingly, the analysis of the time-dependent NMR spectra for both natural-abundant malonic acid and isotope-labeled malonic acid didn't indicate the presence of an intermediate phase during the co-crystallization process. This observation provided valuable insights into the reaction pathway involved in the co-crystallization.

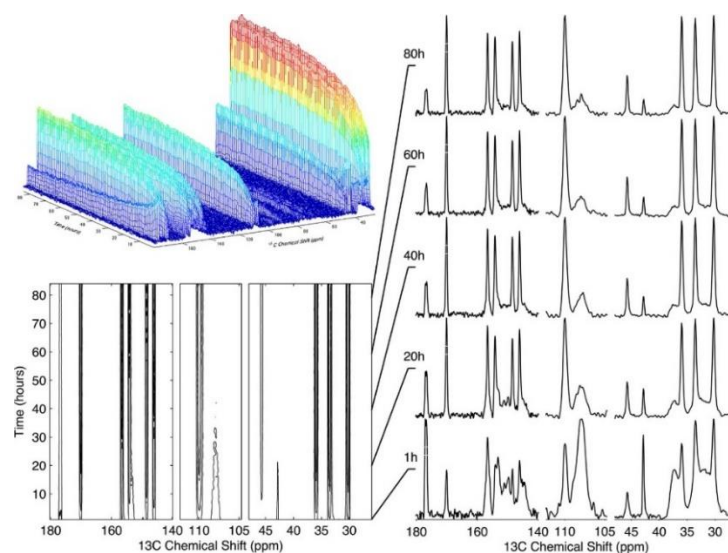


Figure 1.12. In situ ^{13}C MAS NMR spectra of the mechanochemical reaction co-crystallization between caffeine and malonic acid recorded over 84 hours. The ^{13}C NMR spectra as a function of time are displayed as a surface, while the contour maps at the bottom left show the enlargement of regions corresponding to high, moderate, and low isotropic chemical shifts. On the right, five representative spectra display the corresponding regions. Each spectrum was observed after 1 hour.¹³¹

Furthermore, as detailed in the previous section, ssNMR spectroscopy has been successfully applied to investigate the bromination reaction of a cyclic sulfoximine (1) using N-bromosuccinimide (NBS) in a mixer ball mill. The reaction resulted in the formation of brominated sulfoximine (3) and succinimide (4). The authors aimed to extend their ex situ study to an in situ MAS NMR approach (**Figure 1.13**).⁷⁴ The two reagents were mixed together and filled into an NMR rotor, and $^1\text{H} \rightarrow ^{13}\text{C}$ CP-MAS NMR spectra were acquired for 0 to 100 hours. Although only around 20% of product formation was observed, the study highlighted the critical importance of efficient mixing in achieving mechanochemical transformation. By comparing different mixing

techniques (spatula vs. magnetic stirring), insights were gained into the significance of proper mixing for enhancing reaction efficiency.

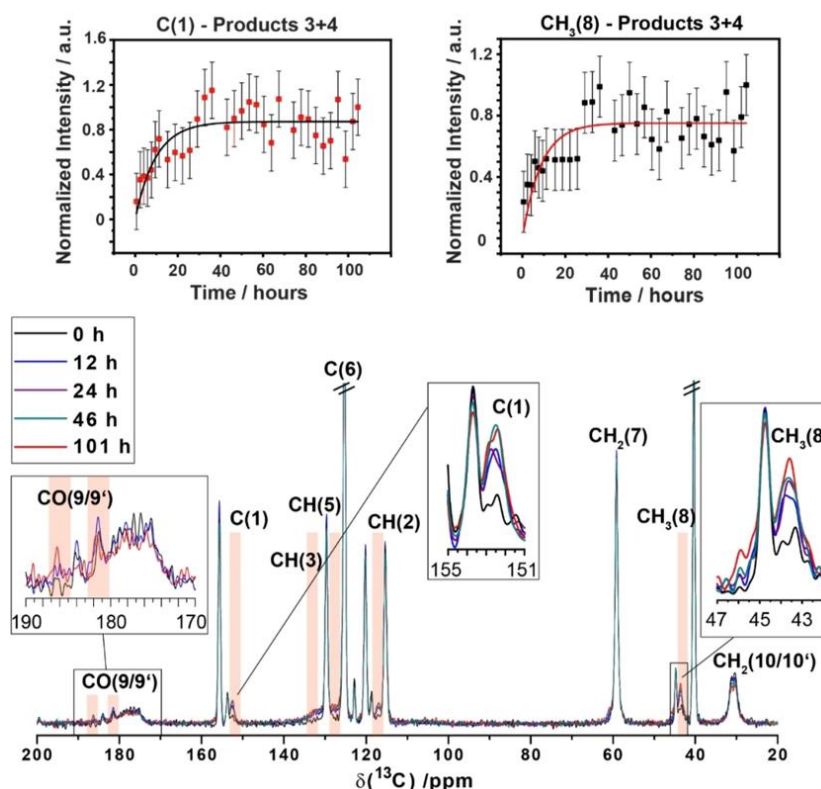


Figure 1.13. In situ $^1\text{H} \rightarrow ^{13}\text{C}$ CP-MAS NMR spectra of the mechanochemical bromination reaction conducted over a time range of 0 to 100 hours (bottom). Resonances attributed to the reaction products are identified using insets and red-colored rectangles. A plot of the normalized intensity of the NMR resonances for the two products as a function of time is presented (top). The solid lines depict a first-order kinetics fit.⁷⁴

Although in situ MAS NMR has demonstrated potential for investigating mechanochemically induced reactions, it is important to consider the drawbacks associated with this method. One limitation is that the effectiveness of mixing effects is primarily observed at the beginning of the MAS experiment when the powder is redistributed within the rotor. As the experiment progresses, the efficiency of mixing diminishes, which can affect the interpretation of the results. Another drawback is the restricted pressure range available with MAS due to the limitations imposed by the rotor's geometry and the maximum spinning frequency as depicted in **Figure 1.14**.

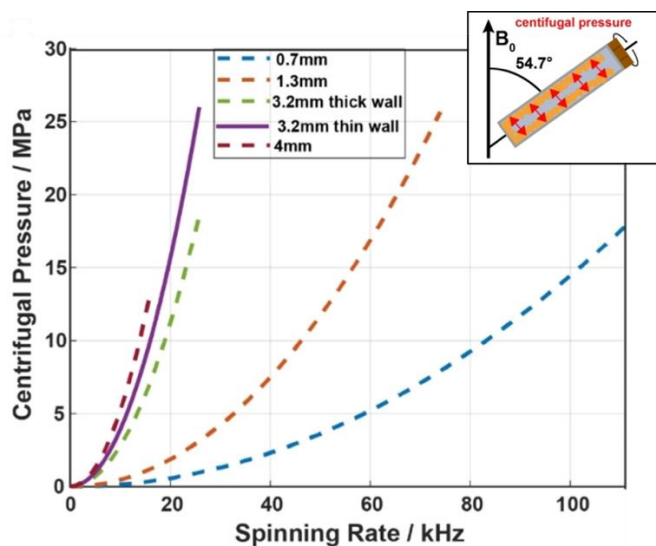


Figure 1.14. Schematic illustration of the centrifugal force exerted on the inner rotor wall is shown as inset. The plot displays the estimated centrifugal pressure as a function of the MAS frequency, taking into account different MAS rotor sizes.⁷⁴

Overall, ssNMR, particularly in its *ex situ* form, offers numerous advantages in investigating mechanochemical reactions, including characterization of reaction products, detection of amorphous phases, atomic-level structural information, preservation of polymorphic structural details, and direct analysis of product composition without the need for dissolution.

1.4 Organometallic Complexes Bearing NHC Ligands

1.4.1 Overview of NHCs

1.4.1.1 Structural properties of NHCs

Carbenes, a class of neutral carbon species, are characterized by the presence of a divalent carbon atom that carries a lone pair of electrons. Unlike typical carbon atoms, the carbene carbon disobeys the octet rule as it possesses only six valence electrons. This electron deficiency renders carbenes highly reactive and inherently unstable. Among the various subclasses of carbenes, NHCs have attracted significant interest. NHCs are heterocyclic compounds that feature a ring structure containing the carbene carbon (C^2) in conjunction with at least one nitrogen atom (**Figure 1.15**).¹³² The presence of neighboring nitrogen donors in NHCs plays a crucial role in electronically stabilizing the carbene carbon, thereby enhancing the overall stability of these compounds.

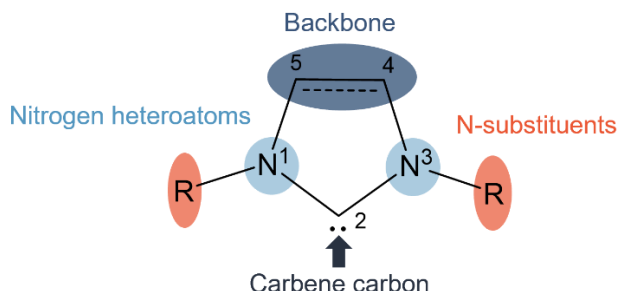


Figure 1.15. General structural features of NHCs.

The reactivity and stability of NHCs were initially investigated by Wanzlick in 1962.¹³³ Subsequently, in 1968, Wanzlick¹³⁴ and Öfele¹³⁵ made a significant breakthrough by demonstrating the first application of NHCs as ligands for metal complexes. They successfully synthesized mercury and chromium complexes bearing NHC ligands. However, despite these groundbreaking discoveries, further exploration of NHCs remained limited for the subsequent two decades. During this period, carbenes, including NHCs, were widely considered too unstable for isolation or effective use in organometallic chemistry.

In 1991, a major milestone was achieved by Arduengo and co-workers, who successfully isolated the first stable and crystalline NHC, known as 1,3-di(adamantly)imidazole-2-ylidene (IAd) (**Figure 1.16**).¹³⁶ Arduengo's groundbreaking discovery provided electronic stabilization through the nitrogen donors and introduced steric hindrance to impede access to the carbene center. This was accomplished by incorporating bulky adamantyl substituents onto the nitrogen atoms, effectively shielding the reactive site and enhancing the stability of NHCs. Arduengo's achievement sparked an explosion of experimental and theoretical studies in the field. Researchers were inspired to synthesize and analyze diverse libraries of novel NHCs, exploring their properties and potential applications. Arduengo's work also stimulated a plethora of investigations into transition metal complexes with NHCs, opening up new avenues in catalysis, medicine, and materials chemistry.^{137–149}

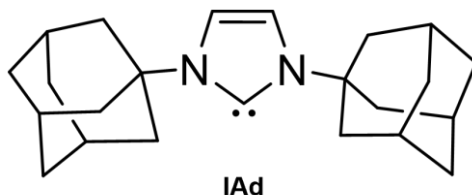


Figure 1.16. The first isolated stable NHC.

1.4.1.2 Stability of NHCs

One prominent characteristic of NHCs is their exceptional stability, which originates from a combination of steric and electronic effects. In the case of IAd, the presence of two bulky adamantyl groups attached to the nitrogen atoms plays a crucial role in stabilizing the compound by hindering its interaction with other molecules. Furthermore, electronic stabilization provided by the nitrogen atoms significantly contributes to the stability of NHCs. Unlike classical carbenes, NHCs exhibit a singlet ground-state electronic configuration. This configuration entails the highest occupied molecular orbital (HOMO) being a sp^2 -hybridized lone pair at the C^2 atom and the lowest unoccupied molecular orbital (LUMO), represented by an unoccupied p -orbital at the C^2 atom. The adjacent nitrogen atoms play a pivotal role in stabilizing this electronic structure. The nitrogen atoms withdraw electrons from the system, resulting in electron-withdrawing effects (σ -electron-withdrawing), while simultaneously donating electrons into the unoccupied p -orbital, leading to electron-donating effects (π -electron-donating) as depicted in **Figure 1.17**. These combined effects contribute to both inductive and mesomeric electronic stabilization, respectively. Additionally, the cyclic nature of NHCs further enhances their stability by favoring the singlet state. This is achieved by imposing a bent arrangement on the C^2 atom, resembling a more sp^2 -like configuration.

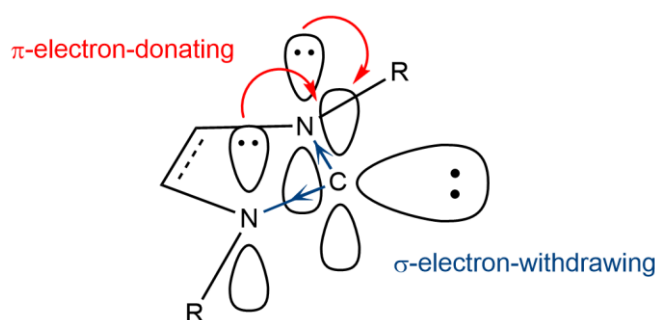


Figure 1.17. Ground state electronic structure of NHCs.

1.4.1.3 Classification of NHCs

NHCs encompass a diverse range of compounds that can be categorized into distinct classes based on variations in the N-substituents, ring sizes, heteroatoms, and ring backbones.¹⁵⁰ Among the different classes, imidazolylidene and imidazolinyliene, which are five-membered NHCs, have emerged as well-established ligands, especially for transition metals (**Figure 1.18**). The

extensive employment of these ligands within the field of organometallic chemistry is widely acknowledged and well-established.

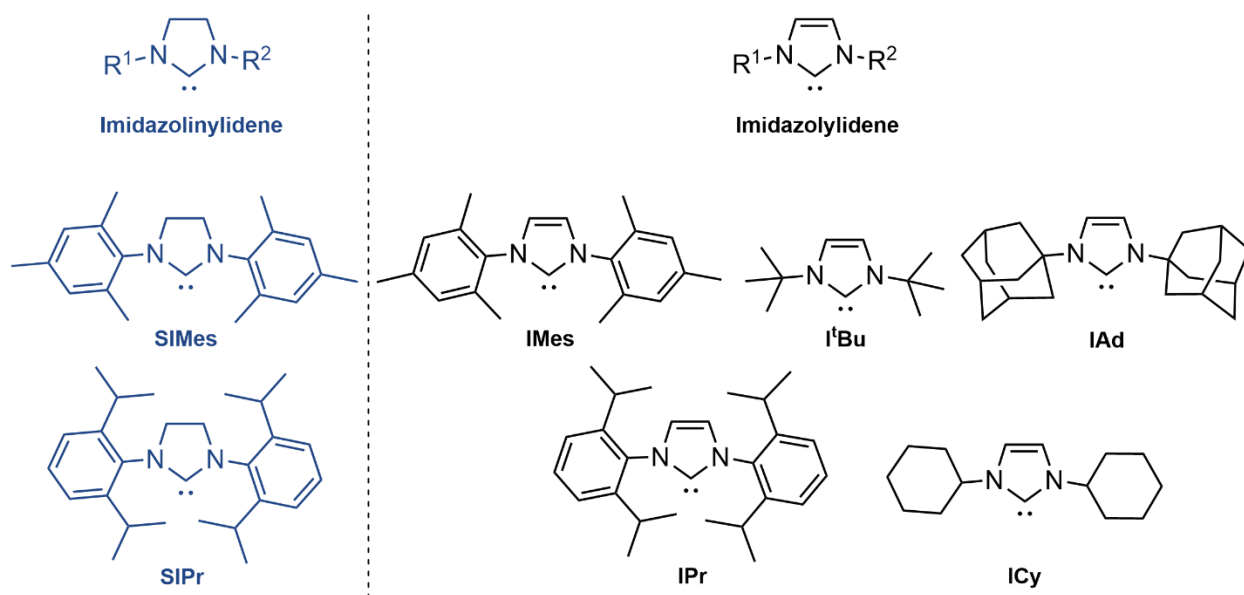


Figure 1.18. Structures of some of the most commonly applied classes of NHCs.

1.4.1.4 Attractive features of NHCs

NHCs have gained remarkable popularity in the field of chemistry due to their array of attractive features. Notably, NHCs offer ease of preparation and handling, making them highly efficient for utilization in both research and industrial settings. NHCs also possess exceptional versatility, enabling their application across a broad range of contexts. Furthermore, NHCs exhibit enhanced stability compared to other ligands making them highly reliable in chemical reactions, while their reduced toxicity ensures a safer working environment. Additionally, NHCs possess high dissociation energies, resulting in stronger bonds with metals, enhancing their catalytic efficiency. Their σ -donor and π -acceptor capabilities, comparable to other ligands, contribute to their broad reactivity.

In terms of their applications, NHCs exhibit diverse uses in modern chemistry, which can be broadly categorized into three main areas (**Figure 1.19**). Firstly, NHCs serve as ligands for transition metals, where they play a crucial role in coordination chemistry, stabilizing and activating metal complexes. Secondly, NHCs exhibit remarkable reactivity upon coordination with *p*-block elements, unlocking unique reactions and facilitating the development of innovative synthetic

approaches. Finally, NHCs function as highly efficient organocatalysts, displaying catalytic efficiency in a range of organic transformations.

1.4.2 Applications of Transition Metal-NHC Complexes

Transition metal-NHC complexes exhibit diverse applications due to their unique properties. One key advantage is their high thermal stability, making them suitable for a wide range of reaction conditions. Additionally, the steric and electronic properties of NHCs can be readily modified, offering flexibility for the development of novel organometallic compounds. These distinctive features have led to the widespread use of transition metal-NHC complexes as both homogeneous and heterogeneous catalysts for various organic transformations.^{151,152} Furthermore, their efficiency in medicinal chemistry has been demonstrated, highlighting their potential in drug development.¹⁵³ Additionally, transition metal-NHC complexes have proven valuable in materials chemistry, contributing to the synthesis of advanced materials. **Figure 1.19** illustrates the significance of transition metal-NHC complexes in these areas.¹⁵⁴

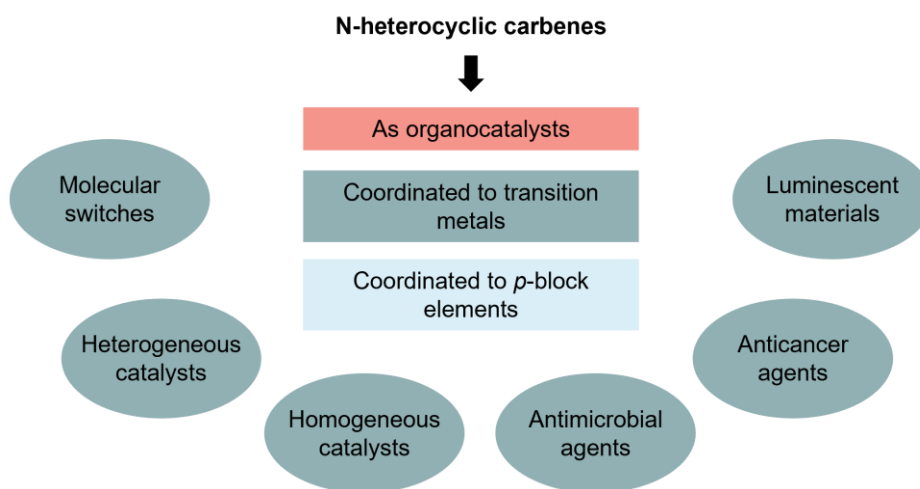
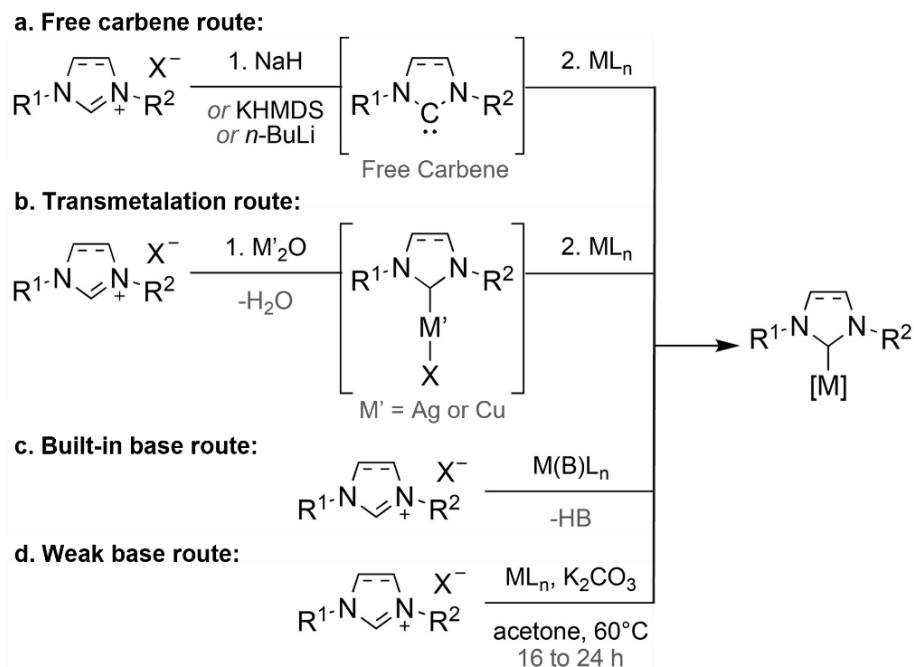


Figure 1.19. Overview of the major applications of NHCs in modern chemistry, categorized into three distinct areas. The figure highlights the diverse applications of transition metal-NHC complexes.

1.4.3 Conventional Synthesis of Transition Metal-NHC Complexes

The synthesis of transition metal-NHC complexes is commonly achieved through several solution-based approaches, each offering distinct advantages and limitations. **Scheme 1.1** displays the commonly employed methods for synthesizing these complexes:¹⁵⁵

1. **Free carbene route:** This approach involves the formation of a free carbene by adding a strong base to an azolium salt, followed by the introduction of a transition metal precursor to the generated NHC. This two-step approach requires strict anhydrous conditions and an inert atmosphere, using potentially hazardous and expensive strong bases.
2. **Transmetallation route:** The transmetallation route involves the reaction between an azolium salt with copper or silver oxides, leading to the formation of Cu- or Ag-NHC complexes. The NHC ligand is then transferred to a desired second transition metal. This approach utilizes air-stable starting materials and generates water as by-product. However, it has limitations in terms of metal availability and requires high temperatures or toxic solvents.
3. **Built-in base route:** The built-in base route requires the prior installation of a ligand with basic properties onto the metal precursor. This ligand can act as a base during the formation of the metal-NHC complex. Some examples utilize commercially available precursors that already possess such ligands. This approach offers a simple one-pot synthetic procedure. However, it is less versatile compared to other approaches.
4. **Weak base route:** Independently introduced by Nolan and Gimeno in 2013, the weak base approach involves the use of weak bases such as K_2CO_3 along with imidazole(in)(ium) salts and transition metal (Au, Ag) precursors. It allows for the one-pot synthesis of metal-NHC complexes under environmentally benign conditions, including the use of aerobic conditions, greener solvents, and less toxic and more cost-efficient weak bases. The weak base approach has demonstrated significant improvements in terms of sustainability, practicability, and reduction in hazardous reagents.



Scheme 1.1. Solution-based synthetic access to transition metal-NHC complexes.¹⁵⁶

1.4.4 Mechanochemical Synthesis of Transition Metal-NHC Complexes

Although synthetic routes to transition metal-NHC complexes traditionally revolve around solution chemistry, over the past eight years several groups have been able to translate the synthetic approaches detailed in the previous section into mechanochemical ones (**Figure 1.20**).¹¹ The pioneering work of Nolan and coworkers paved the way for this transformation by showcasing the feasibility of ligand substitution in $[Au(IPr)(Cl)]$ using organic substrates and KOH by grinding.¹⁵⁷

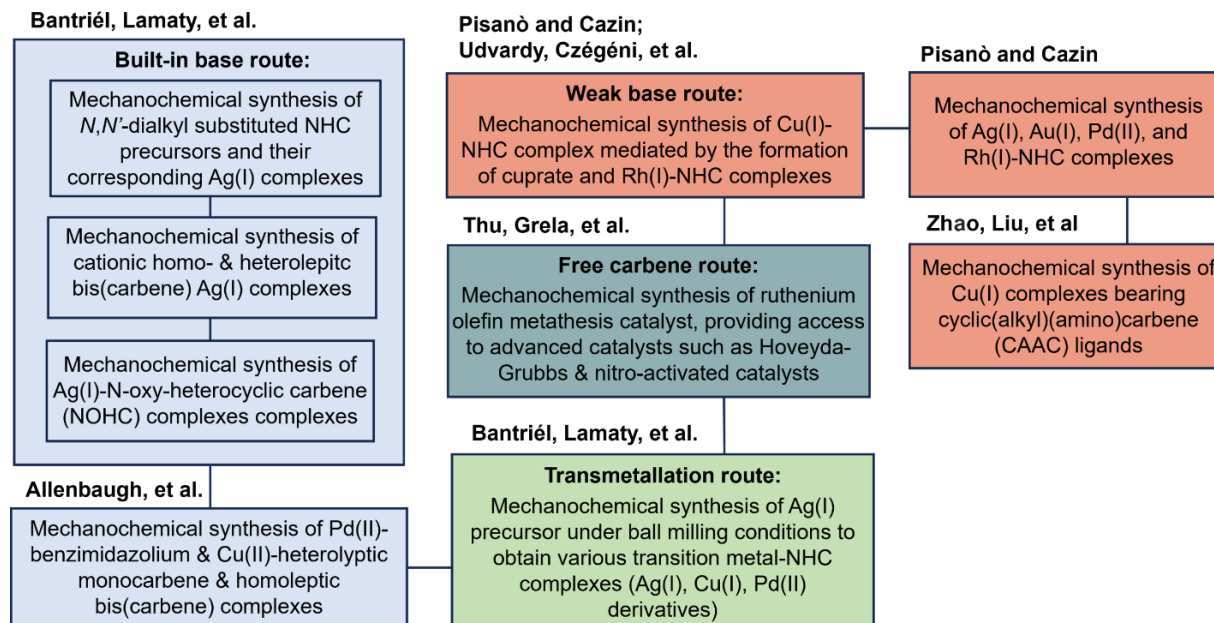
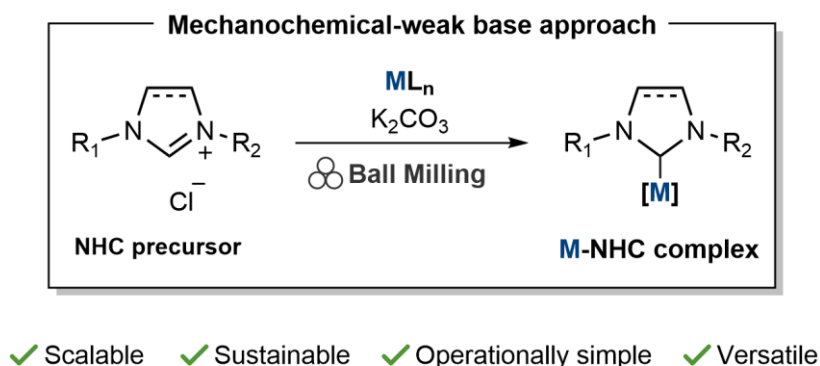


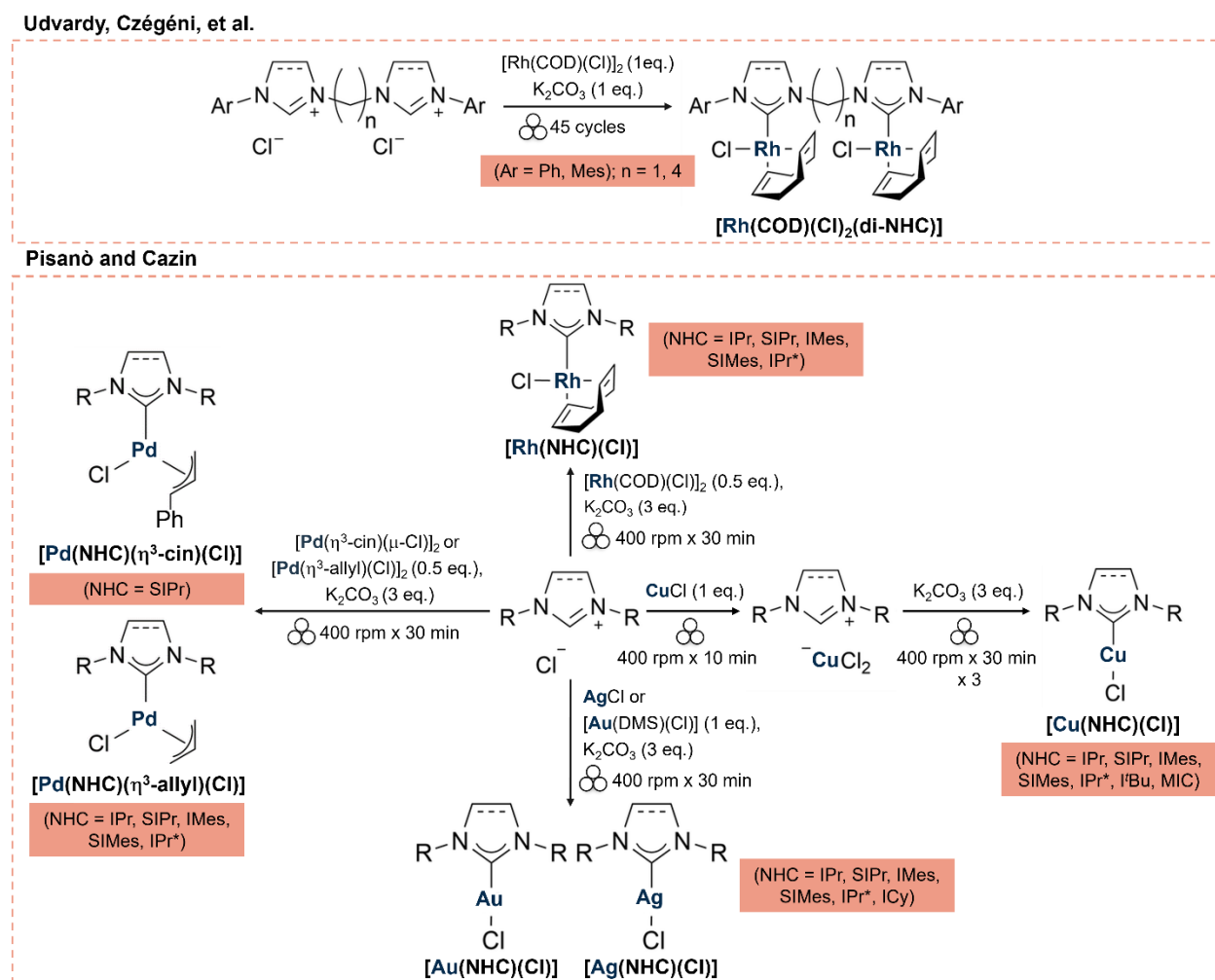
Figure 1.20. Mechanochemical synthesis of transition metal-NHC complexes.^{156,158–169}

The Cazin and Udvardy groups laid the foundation for the mechanochemical realization of one of the most popular synthetic approaches to transition metal-NHC complexes: weak base route (**Scheme 1.2**).^{159,170} In general, the mechanochemical weak base approach involves the application of mild and inexpensive base in conjunction with a variety of metal precursors and azolium chloride salts in order to affix an NHC ligand to a metal center under solvent-free, solid-state mechanochemical conditions.



Scheme 1.2. General weak base approach toward the mechanochemical synthesis of transition metal-NHC complexes.

The mechanochemical weak base approach has garnered significant attention in the scientific community due to its unique characteristics. This method stands out for its use of readily available starting materials and operational simplicity. Moreover, it employs inexpensive bases like K_2CO_3 or Cs_2CO_3 , making it cost-effective. Additionally, this approach is versatile, allowing for the synthesis of various transition metal-NHC complexes, including Cu(I), Ag(I), Au(I), Rh(I), and Pd(II), in combination with different NHC ligands, such as benzimidazolium, imidazole(in)ium, and Cyclic(Alkyl)(Amino)Carbene (CAAC). **Scheme 1.3** represents the main transition metal-NHC complexes synthesized through the mechanochemical weak base approach.



Scheme 1.3. Transition metal-NHC complexes synthesized mechanochemically through the weak base approach. “Ph” and “Mes” denote the phenyl and 2,4,6-trimethylphenyl aromatic groups, respectively. The NHC ligands used are IPr, *N,N'*-bis-[2,6-(di-iso-propyl)phenyl]imidazolidene; SIPr, *N,N'*-bis-[2,6-(di-iso-propyl)phenyl]imidazolinylidene; IMes, *N,N'*-bis-[2,6-(di-iso-propyl)phenyl]imidazolylidene; SIMes, *N,N'*-bis-[2,6-(di-iso-propyl)phenyl]imidazolylidene; I'Bu, *N,N'*-bis-[2,6-(di-iso-propyl)phenyl]imidazolylidene; MIC, *N,N'*-bis-[2,6-(di-iso-propyl)phenyl]imidazolylidene; ICy, *N,N'*-bis-[2,6-(di-iso-propyl)phenyl]imidazolylidene.

N,N'-bis-(2,4,6-trimethylphenyl) imidazolylidene; SIMes, *N,N'*-bis-[2,6-bis(diphenylmethyl)-4-methylphenyl]imidazolinylidene; IPr*, *N,N'*-bis-[2,6-bis(diphenylmethyl)-4-methylphenyl]imidazolylidene; *t*Bu, *N,N'*-bis-(tert-butyl)imidazolylidene; ICy, *N,N'*-bis-(cyclohexyl)imidazolylidene; and MIC, 1-(2,6-diisopropylphenyl)-3-(methyl)-4-(4-tertbutylphenyl)-1,2,3-triazolylidene.

In a pioneering study by Pisanò and Cazin, they successfully developed a solvent-free mechanochemical protocol using a planetary ball mill to synthesize [Cu(NHC)(Cl)] (**Scheme 1.3**).¹⁷⁰ These complexes were synthesized with high yields ranging from good to excellent. Remarkably, the reaction time for these syntheses was impressively short, requiring only 1.5 hours, which is significantly shorter than conventional solution-based methods involving heating or cooling. One of the key advantages of this protocol was the minimized use of solvents, which were limited to the workup phase. Acetone, a commonly preferred solvent in solvent selection guides, was chosen for this purpose. The reaction mechanism involved the formation of a cuprate species, which was then transformed into the desired copper complexes by the addition of an excess amount of K₂CO₃. Furthermore, the scalability of this protocol was demonstrated by achieving a 75% yield of [Cu(IPr)(Cl)] from a reaction mixture containing 5 g of IPr·HCl, CuCl, and K₂CO₃ in just 10 min. The reduction in reaction time was attributed to the elevated temperature within the ball mill vessel, facilitated by an increased number of milling balls. This elevated temperature resulted in more frequent collisions among the reactants, leading to enhanced energy transfer and accelerated reaction rates.

In a separate report, Udvardy, Czégéni and co-workers utilized the mechanochemical weak base approach to synthesize methylene-bridged dinuclear rhodium(I)-NHC complexes of the type [{Rh(Cl)(COD)}₂(μ-di-NHC)].¹⁵⁹ Similar to the Cu(I)-NHC complexes, this approach offered rapid reaction times and limited solvent usage, with solvents being utilized solely during the workup process.

Building upon these findings, Pisanò and Cazin broadened the range of transition metal-NHC complexes synthesized using K₂CO₃ under mechanochemical conditions.¹⁵⁶ They successfully assembled Ag(I)-NHC and Au(I)-NHC complexes using a simple and straightforward protocol that involved combining the NHC salt with the desired metal salt precursor and an excess amount of the base. These assemblies required a milling time of 30 min and consistently yielded complexes with high yields while minimizing solvent use. Only green solvents, acetone and *n*-heptane, were employed during the workup phase. Notably, there was no apparent correlation between the steric

properties of the NHC salt precursors and the reaction time, contrary to what is typically observed in solution-based chemistry. Moreover, the synthesis of the complex $[\text{Au}(\text{SIMes})(\text{Cl})]$ required the use of 6 eq. of K_2CO_3 , whereas the addition of 3 eq. led to the formation of the corresponding aurate intermediate $[\text{IMes}\cdot\text{H}][\text{AuCl}_2]$.

The mechanochemical weak base approach also proved effective in synthesizing Pd(II)-NHC complexes.¹⁵⁶ By using $[\text{Pd}(\eta^3\text{-cin})(\text{Cl})]_2$ and $[\text{Pd}(\eta^3\text{-allyl})(\text{Cl})]_2$, as the metal precursors, $[\text{Pd}(\text{NHC})(\eta^3\text{-cin})(\text{Cl})]$ and $[\text{Pd}(\text{NHC})(\eta^3\text{-allyl})(\text{Cl})]$ complexes were successfully synthesized with excellent yields and a remarkably short reaction time of only 30 min. The versatility and scalability of the approach were demonstrated by easily converting 5 g of $\text{IPr}\cdot\text{HCl}$ into 5.1 g (77%) of $[\text{Pd}(\text{IPr})(\eta^3\text{-allyl})(\text{Cl})]$. Additionally, in the same report, $[\text{Rh}(\text{NHC})(\text{COD})(\text{Cl})]$ complexes were synthesized by adapting the protocol developed by Plenio and co-workers,¹⁷¹ simply substituting the metal salt precursor with $[\text{Rh}(\text{COD})(\text{Cl})]_2$.

Furthermore, Zhao, Lui, and co-workers extended the applicability of the mechanochemical weak base approach to Cu(I) complexes bearing CAAC ligands.¹⁶⁸ By employing this approach, they successfully synthesized Cu(I)-CAAC complexes using Cs_2CO_3 as the weak base and ball milling for three rounds of 30 min.

In summary, the mechanochemical weak base approach has emerged as a significant advancement in the synthesis of transition metal-NHC complexes. This method employs mechanical forces and mild bases, offering several advantages such as reduced solvent consumption, shorter reaction times, and scalability. Its environmentally benign characteristics make it a promising alternative to conventional synthesis techniques. Nevertheless, despite substantial progress, a deeper understanding of the underlying mechanisms driving this approach is crucial.

The goal of my Ph.D. thesis is to harness ssNMR spectroscopy as a powerful tool to unveil the mechanistic aspects involved in the synthesis of transition metal-NHC complexes through the innovative mechanochemical weak base approach. The foundational motivation behind this research stems from the desire to establish sustainable and environmentally friendly routes for chemical synthesis, with a particular emphasis on reducing or eliminating the use of conventional solvents. Throughout my research, I investigated the formation mechanisms of various transition metal-NHC complexes, including $[\text{Cu}(\text{Cl})(\text{NHC})]$, $[\text{Ag}(\text{Cl})(\text{NHC})]$, and $[\text{Rh}(\text{Cl})(\text{NHC})]$, elucidated in Chapter 2, as well as chalcogen-NHC derivatives ($\text{NHC}=\text{Se}$ and $\text{NHC}=\text{S}$), detailed in Chapter 3.

These complexes hold significant potential in catalytic applications and as anti-infective coatings in medical devices. Our investigation encompassed a detailed examination of the role of solvents in driving ligand binding and substitution reactions, thereby highlighting the synergistic interplay between mechanical forces and chemical transformations. Furthermore, we monitored the consumption of the reactants, the intermediates formed, and the final product outcomes across various synthetic routes and workup protocols. Enhanced structural characterization techniques were also employed to provide a more comprehensive understanding of these complexes. In addition, we explored the antimicrobial properties of metal-NHC complexes, particular copper-NHC, across a broad spectrum of resistant microorganisms, thereby expanding the potential applications of these compounds in combating infectious diseases, as detailed in Chapter 4.

1.5 References

- (1) Horie, K.; Barón, M.; Fox, R. B.; He, J.; Hess, M.; Kahovec, J.; Kitayama, T.; Kubisa, P.; Maréchal, E.; Mormann, W.; Stepto, R. F. T.; Tabak, D.; Vohlídal, J.; Wilks, E. S.; Work, W. J. Definitions of Terms Relating to Reactions of Polymers and to Functional Polymeric Materials (IUPAC Recommendations 2003). *Pure Appl. Chem.* **2004**, 76 (4), 889–906. <https://doi.org/10.1351/pac200476040889>.
- (2) Gomollón-Bel, F. Ten Chemical Innovations That Will Change Our World: IUPAC identifies emerging technologies in Chemistry with potential to make our planet more sustainable. *Chem. In.* **2019**, 41 (2), 12–17. <https://doi.org/10.1515/ci-2019-0203>.
- (3) Caley, E. R.; Richards, J. C. *Theophrastus on Stones*; Ohio State University Press, 2015.
- (4) Takacs, L. Quicksilver from Cinnabar: The First Documented Mechanochemical Reaction? *J. Met. Mater. Miner.* **2000**, 52 (1), 12–13. <https://doi.org/10.1007/s11837-000-0106-0>.
- (5) Takacs, L. The Mechanochemical Reduction of AgCl with Metals. *J. Therm. Anal. Calorim.* **2007**, 90 (1), 81–84. <https://doi.org/10.1007/s10973-007-8479-8>.
- (6) Takacs, L. M. Carey Lea, the First Mechanochemist. *J. Mater. Sci.* **2004**, 39 (16), 4987–4993. <https://doi.org/10.1023/B:JMSC.0000039175.73904.93>.
- (7) Ostwald, W.; Drucker, C.; Rudolf, G.; Kuenen, J. P. *Handbuch der allgemeinen Chemie*; Akad. Verlagsges. Leipzig, 1918.

- (8) Takacs, L. M. CAREY LEA, THE FATHER OF MECHANOCHEMISTRY. *Bull. Hist. Chem.* **2003**, 28 (1).
- (9) Petruschke, M. Tribochemistry. von G. HEINICKE. Berlin: Akademie-Verlag 1984. Bestellnummer: 7631993(6746). 495 S., 329 Bilder, 106 Tabellen, 98,– M. *Acta Polym.* **1985**, 36 (7), 400–401. <https://doi.org/10.1002/actp.1985.010360721>.
- (10) Makhaev, V. D.; Borisov, A. P.; Petrova, L. A. Solid-State Mechanochemical Synthesis of Ferrocene. *J. Organomet. Chem.* **1999**, 590 (2), 222–226. [https://doi.org/10.1016/S0022-328X\(99\)00460-X](https://doi.org/10.1016/S0022-328X(99)00460-X).
- (11) Aleksanyan, D. V.; Kozlov, V. A. Mechanochemical Tools in the Synthesis of Organometallic Compounds. *Mendeleev Commun.* **2023**, 33 (3), 287–301. <https://doi.org/10.1016/j.mencom.2023.04.001>.
- (12) Suryanarayana, C. Mechanical Alloying and Milling. *Prog. Mater. Sci.* **2001**, 46 (1), 1–184. [https://doi.org/10.1016/S0079-6425\(99\)00010-9](https://doi.org/10.1016/S0079-6425(99)00010-9).
- (13) Lu Sheng-Yong(陆胜勇), M. Q.-J. Simulation of ball motion and energy transfer in a planetary ball mill. *Chin. Phys. B* **2012**, 21 (7), 78201–078201. <https://doi.org/10.1088/1674-1056/21/7/078201>.
- (14) Burmeister, C. F.; Kwade, A. Process Engineering with Planetary Ball Mills. *Chem. Soc. Rev.* **2013**, 42 (18), 7660–7667. <https://doi.org/10.1039/C3CS35455E>.
- (15) Stolle, A.; Schmidt, R.; Jacob, K. Scale-up of Organic Reactions in Ball Mills: Process Intensification with Regard to Energy Efficiency and Economy of Scale. *Faraday Discuss.* **2014**, 170 (0), 267–286. <https://doi.org/10.1039/C3FD00144J>.
- (16) Štefanić, G.; Krehula, S.; Štefanić, I. The High Impact of a Milling Atmosphere on Steel Contamination. *Chem. Commun.* **2013**, 49 (81), 9245–9247. <https://doi.org/10.1039/C3CC44803G>.
- (17) Andersen, J. M.; Mack, J. Decoupling the Arrhenius Equation via Mechanochemistry. *Chem. Sci.* **2017**, 8 (8), 5447–5453. <https://doi.org/10.1039/C7SC00538E>.

- (18) Baláž, P. *Mechanochemistry in Nanoscience and Minerals Engineering*; Springer: Berlin, 2008.
- (19) Howard, J. L.; Cao, Q.; Browne, D. L. Mechanochemistry as an Emerging Tool for Molecular Synthesis: What Can It Offer? *Chem. Sci.* **2018**, *9* (12), 3080–3094. <https://doi.org/10.1039/C7SC05371A>.
- (20) Andersen, J.; Mack, J. Mechanochemistry and Organic Synthesis: From Mystical to Practical. *Green Chem.* **2018**, *20* (7), 1435–1443. <https://doi.org/10.1039/C7GC03797J>.
- (21) Gečiauskaitė, A. A.; García, F. Main Group Mechanochemistry. *Beilstein J. Org. Chem.* **2017**, *13* (1), 2068–2077. <https://doi.org/10.3762/bjoc.13.204>.
- (22) Rightmire, N. R.; Hanusa, T. P. Advances in Organometallic Synthesis with Mechanochemical Methods. *Dalton Trans.* **2016**, *45* (6), 2352–2362. <https://doi.org/10.1039/C5DT03866A>.
- (23) Hernández, J. G.; Bolm, C. Altering Product Selectivity by Mechanochemistry. *J. Org. Chem.* **2017**, *82* (8), 4007–4019. <https://doi.org/10.1021/acs.joc.6b02887>.
- (24) Seo, T.; Toyoshima, N.; Kubota, K.; Ito, H. Tackling Solubility Issues in Organic Synthesis: Solid-State Cross-Coupling of Insoluble Aryl Halides. *J. Am. Chem. Soc.* **2021**, *143* (16), 6165–6175. <https://doi.org/10.1021/jacs.1c00906>.
- (25) Friščić, T.; Childs, S. L.; Rizvi, S. A. A.; Jones, W. The Role of Solvent in Mechanochemical and Sonochemical Cocrystal Formation: A Solubility-Based Approach for Predicting Cocrystallisation Outcome. *CrystEngComm* **2009**, *11* (3), 418–426. <https://doi.org/10.1039/B815174A>.
- (26) Tan, D.; Friščić, T. Mechanochemistry for Organic Chemists: An Update. *Eur. J. Org. Chem.* **2018**, *2018* (1), 18–33. <https://doi.org/10.1002/ejoc.201700961>.
- (27) Egorov, I. N.; Santra, S.; Kopchuk, D. S.; Kovalev, I. S.; Zyryanov, G. V.; Majee, A.; Ranu, B. C.; Rusinov, V. L.; Chupakhin, O. N. Ball Milling: An Efficient and Green Approach for Asymmetric Organic Syntheses. *Green Chem.* **2020**, *22* (2), 302–315. <https://doi.org/10.1039/C9GC03414E>.

- (28) Do, J.-L.; Friščić, T. Mechanochemistry: A Force of Synthesis. *ACS Cent. Sci.* **2017**, *3* (1), 13–19. <https://doi.org/10.1021/acscentsci.6b00277>.
- (29) Achar, T. K.; Bose, A.; Mal, P. Mechanochemical Synthesis of Small Organic Molecules. *Beilstein J. Org. Chem.* **2017**, *13* (1), 1907–1931. <https://doi.org/10.3762/bjoc.13.186>.
- (30) Šepelák, V.; Düvel, A.; Wilkening, M.; Becker, K.-D.; Heitjans, P. Mechanochemical Reactions and Syntheses of Oxides. *Chem. Soc. Rev.* **2013**, *42* (18), 7507–7520. <https://doi.org/10.1039/C2CS35462D>.
- (31) Tan, D.; García, F. Main Group Mechanochemistry: From Curiosity to Established Protocols. *Chem. Soc. Rev.* **2019**, *48* (8), 2274–2292. <https://doi.org/10.1039/C7CS00813A>.
- (32) Hernández, J. G.; Friščić, T. Metal-Catalyzed Organic Reactions Using Mechanochemistry. *Tetrahedron Letters* **2015**, *56* (29), 4253–4265. <https://doi.org/10.1016/j.tetlet.2015.03.135>.
- (33) Hernández, J. G. C–H Bond Functionalization by Mechanochemistry. *Chem. Eur. J.* **2017**, *23* (68), 17157–17165. <https://doi.org/10.1002/chem.201703605>.
- (34) Beillard, A.; Bantreil, X.; Métro, T.-X.; Martinez, J.; Lamaty, F. Alternative Technologies That Facilitate Access to Discrete Metal Complexes. *Chem. Rev.* **2019**, *119* (12), 7529–7609. <https://doi.org/10.1021/acs.chemrev.8b00479>.
- (35) Krusenbaum, A.; Grätz, S.; Tigineh, G. T.; Borchardt, L.; Kim, J. G. The Mechanochemical Synthesis of Polymers. *Chem. Soc. Rev.* **2022**, *51* (7), 2873–2905. <https://doi.org/10.1039/D1CS01093J>.
- (36) Friščić, T. Supramolecular Concepts and New Techniques in Mechanochemistry: Cocrystals, Cages, Rotaxanes, Open Metal–Organic Frameworks. *Chem. Soc. Rev.* **2012**, *41* (9), 3493–3510. <https://doi.org/10.1039/C2CS15332G>.
- (37) Liu, X.; Li, Y.; Zeng, L.; Li, X.; Chen, N.; Bai, S.; He, H.; Wang, Q.; Zhang, C. A Review on Mechanochemistry: Approaching Advanced Energy Materials with Greener Force. *Adv. Mater.* **2022**, *34* (46), 2108327. <https://doi.org/10.1002/adma.202108327>.

- (38) Szczęśniak, B.; Borysiuk, S.; Choma, J.; Jaroniec, M. Mechanochemical Synthesis of Highly Porous Materials. *Mater. Horiz.* **2020**, *7* (6), 1457–1473. <https://doi.org/10.1039/D0MH00081G>.
- (39) Xu, C.; De, S.; Balu, A. M.; Ojeda, M.; Luque, R. Mechanochemical Synthesis of Advanced Nanomaterials for Catalytic Applications. *Chem. Commun.* **2015**, *51* (31), 6698–6713. <https://doi.org/10.1039/C4CC09876E>.
- (40) Bowden, F. P.; Yoffe, A. D. *Fast Reactions in Solids*; Butterworth's Scientific Publications: London, 1958.
- (41) Takacs, L. The Historical Development of Mechanochemistry. *Chem. Soc. Rev.* **2013**, *42* (18), 7649. <https://doi.org/10.1039/c2cs35442j>.
- (42) Friščić, T.; Halasz, I.; Beldon, P. J.; Belenguer, A. M.; Adams, F.; Kimber, S. A. J.; Honkimäki, V.; Dinnebier, R. E. Real-Time and in Situ Monitoring of Mechanochemical Milling Reactions. *Nat. Chem.* **2013**, *5* (1), 66–73. <https://doi.org/10.1038/nchem.1505>.
- (43) Ardila-Fierro, K. J.; Lukin, S.; Etter, M.; Užarević, K.; Halasz, I.; Bolm, C.; Hernández, J. G. Direct Visualization of a Mechanochemically Induced Molecular Rearrangement. *Angew. Chem. Int. Ed. Engl.* **2020**, *59* (32), 13458–13462. <https://doi.org/10.1002/anie.201914921>.
- (44) Ardila-Fierro, K. J.; Lukin, S.; Etter, M.; Užarević, K.; Halasz, I.; Bolm, C.; Hernández, J. G. Direct Visualization of a Mechanochemically Induced Molecular Rearrangement. *Angew. Chem.* **2020**, *132* (32), 13560–13564. <https://doi.org/10.1002/ange.201914921>.
- (45) Oliveira, P. F. M. de; Michalchuk, A. A. L.; Buzanich, A. G.; Bienert, R.; Torresi, R. M.; Camargo, P. H. C.; Emmerling, F. Tandem X-Ray Absorption Spectroscopy and Scattering for in Situ Time-Resolved Monitoring of Gold Nanoparticle Mechanosynthesis. *Chem. Commun.* **2020**, *56* (71), 10329–10332. <https://doi.org/10.1039/D0CC03862H>.
- (46) Lukin, S.; Germann, L. S.; Friščić, T.; Halasz, I. Toward Mechanistic Understanding of Mechanochemical Reactions Using Real-Time In Situ Monitoring. *Acc. Chem. Res.* **2022**, *55* (9), 1262–1277. <https://doi.org/10.1021/acs.accounts.2c00062>.
- (47) Leroy, C.; Mitteleite, S.; Félix, G.; Fabregue, N.; Špačková, J.; Gaveau, P.; Métro, T.-X.; Laurencin, D. Operando Acoustic Analysis: A Valuable Method for Investigating Reaction

- Mechanisms in Mechanochemistry. *Chem. Sci.* **2022**, *13* (21), 6328–6334. <https://doi.org/10.1039/D2SC01496C>.
- (48) Lukin, S.; Užarević, K.; Halasz, I. Raman Spectroscopy for Real-Time and in Situ Monitoring of Mechanochemical Milling Reactions. *Nat. Protoc.* **2021**, *16* (7), 3492–3521. <https://doi.org/10.1038/s41596-021-00545-x>.
- (49) Haferkamp, S.; Fischer, F.; Kraus, W.; Emmerling, F. Mechanochemical Knoevenagel Condensation Investigated in Situ. *Beilstein J. Org. Chem.* **2017**, *13* (1), 2010–2014. <https://doi.org/10.3762/bjoc.13.197>.
- (50) Julien, P. A.; Germann, L. S.; Titi, H. M.; Etter, M.; Dinnebier, R. E.; Sharma, L.; Baltrusaitis, J.; Friščić, T. In Situ Monitoring of Mechanochemical Synthesis of Calcium Urea Phosphate Fertilizer Cocrystal Reveals Highly Effective Water-Based Autocatalysis. *Chem. Sci.* **2020**, *11* (9), 2350–2355. <https://doi.org/10.1039/C9SC06224F>.
- (51) Batzdorf, L.; Fischer, F.; Wilke, M.; Wenzel, K.-J.; Emmerling, F. Direct In Situ Investigation of Milling Reactions Using Combined X-Ray Diffraction and Raman Spectroscopy. *Angew. Chem. Int. Ed.* **2015**, *54* (6), 1799–1802. <https://doi.org/10.1002/anie.201409834>.
- (52) Silva, I. d'Anciães A.; Bartalucci, E.; Bolm, C.; Wiegand, T. Opportunities And Challenges in Applying Solid-State Nmr Spectroscopy in Organic Mechanochemistry. *Adv. Mater.* **2023**, 2304092. <https://doi.org/10.1002/adma.202304092>.
- (53) Schiffmann, J. G.; Emmerling, F.; Martins, I. C. B.; Van Wüllen, L. In-Situ Reaction Monitoring of a Mechanochemical Ball Mill Reaction with Solid State NMR. *Solid State Nucl. Magn. Reson.* **2020**, *109*, 101687. <https://doi.org/10.1016/j.ssnmr.2020.101687>.
- (54) Užarević, K.; Halasz, I.; Friščić, T. Real-Time and In Situ Monitoring of Mechanochemical Reactions: A New Playground for All Chemists. *J. Phys. Chem. Lett.* **2015**, *6* (20), 4129–4140. <https://doi.org/10.1021/acs.jpcllett.5b01837>.
- (55) Tan, D.; Loots, L.; Friščić, T. Towards Medicinal Mechanochemistry: Evolution of Milling from Pharmaceutical Solid Form Screening to the Synthesis of Active Pharmaceutical Ingredients (APIs). *Chem. Commun.* **2016**, *52* (50), 7760–7781. <https://doi.org/10.1039/C6CC02015A>.

- (56) Ma, X.; Yuan, W.; Bell, S. E. J.; James, S. L. Better Understanding of Mechanochemical Reactions: Raman Monitoring Reveals Surprisingly Simple 'Pseudo-Fluid' Model for a Ball Milling Reaction. *Chem. Commun.* **2014**, 50 (13), 1585–1587. <https://doi.org/10.1039/C3CC47898J>.
- (57) González-González, J. S.; Jiménez-López, R.; Ortégón-Reyna, D.; Gonzalez-Carrillo, G.; Martínez-Martínez, F. J. Mechanochemical Synthesis of the Catechol-Theophylline Cocrystal: Spectroscopic Characterization and Molecular Structure. *Appl. Sci.* **2021**, 11 (9), 3810. <https://doi.org/10.3390/app11093810>.
- (58) Andini, S.; Bolognese, A.; Formisano, D.; Manfra, M.; Montagnaro, F.; Santoro, L. Mechanochemistry of Ibuprofen Pharmaceutical. *Chemosphere* **2012**, 88 (5), 548–553. <https://doi.org/10.1016/j.chemosphere.2012.03.025>.
- (59) Kaiser, R. P.; Krake, E. F.; Backer, L.; Urlaub, J.; Baumann, W.; Handler, N.; Buschmann, H.; Beweries, T.; Holzgrabe, U.; Bolm, C. Ball Milling – a New Concept for Predicting Degradation Profiles in Active Pharmaceutical Ingredients. *Chem. Commun.* **2021**, 57 (90), 11956–11959. <https://doi.org/10.1039/D1CC04716G>.
- (60) Koutavarapu, R.; Reddy, C. V.; Rao, M. C.; Ravikumar, R. V. S. S. N.; Cho, M.; Shim, J. Structural, Optical, and Luminescence Properties of Cu²⁺-Doped Ca-Li Hydroxyapatite Nanopowders Prepared by Mechanochemical Synthesis. *Mater. Res. Express* **2019**, 6 (10), 105046. <https://doi.org/10.1088/2053-1591/ab39ed>.
- (61) Kokorin, A. I.; Streletskii, A. N.; Kolbanev, I. V.; Borunova, A. B.; Degtyarev, Y. N.; Leonov, A. V.; Permenov, D. G.; Konstantinova, E. A. Influence of Aluminum Addition on the Structure and Feathers of V₂O₅ Oxide Prepared by Mechanochemical Activation. *J. Phys. Chem. C* **2019**, 123 (32), 19991–19998. <https://doi.org/10.1021/acs.jpcc.9b05325>.
- (62) Gobindlal, K.; Zujovic, Z.; Yadav, P.; Sperry, J.; Weber, C. C. The Mechanism of Surface-Radical Generation and Amorphization of Crystalline Quartz Sand upon Mechanochemical Grinding. *J. Phys. Chem. C* **2021**, 125 (38), 20877–20886. <https://doi.org/10.1021/acs.jpcc.1c06069>.
- (63) Kuzuya, M.; Kondo, S.; Murase, K. A Novel Single Electron Transfer in Solid-State Organic Compounds: Mechanically Induced Reduction of Dipyridinium Salts. *J. Phys. Chem.* **1993**, 97 (30), 7800–7802. <https://doi.org/10.1021/j100132a003>.

- (64) Balema, V. P.; Hlova, I. Z.; Carnahan, S. L.; Seyed, M.; Dolotko, O.; Rossini, A. J.; Luzinov, I. Correction: Depolymerization of Polystyrene under Ambient Conditions. *New J. Chem.* **2021**, 45 (10), 4867–4867. <https://doi.org/10.1039/D1NJ90029C>.
- (65) Dushkin, A. V.; Troitskaya, I. B.; Boldyrev, V. V.; Grigor'ev, I. A. Solid-Phase Mechanochemical Incorporation of a Spin Label into Cellulose. *Russ. Chem. Bull.* **2005**, 54 (5), 1155–1159. <https://doi.org/10.1007/s11172-005-0374-5>.
- (66) Balema, V. P.; Wiench, J. W.; Pruski, M.; Pecharsky, V. K. Solvent-Free Mechanochemical Synthesis of Two Pt Complexes: Cis-(Ph₃P)₂PtCl₂ and Cis-(Ph₃P)₂PtCO₃. *Chem. Commun.* **2002**, No. 15, 1606–1607. <https://doi.org/10.1039/B203694K>.
- (67) Kobayashi, T.; Dolotko, O.; Gupta, S.; Pecharsky, V. K.; Pruski, M. Mechanochemistry of the LiBH₄–AlCl₃ System: Structural Characterization of the Products by Solid-State NMR. *J. Phys. Chem. C* **2018**, 122 (4), 1955–1962. <https://doi.org/10.1021/acs.jpcc.7b10856>.
- (68) Preishuber-Pflügl, F.; Wilkening, M. Mechanochemically Synthesized Fluorides: Local Structures and Ion Transport. *Dalton Trans.* **2016**, 45 (21), 8675–8687. <https://doi.org/10.1039/C6DT00944A>.
- (69) Wróblewska, A.; Paluch, P.; Wielgus, E.; Bujacz, G.; Dudek, M. K.; Potrzebowski, M. J. Approach toward the Understanding of Coupling Mechanism for EDC Reagent in Solvent-Free Mechanochemistry. *Org. Lett.* **2017**, 19 (19), 5360–5363. <https://doi.org/10.1021/acs.orglett.7b02637>.
- (70) Šepelák, V.; Becker, S. M.; Bergmann, I.; Indris, S.; Scheuermann, M.; Feldhoff, A.; Kübel, C.; Bruns, M.; Stürzl, N.; Ulrich, A. S.; Ghafari, M.; Hahn, H.; Grey, C. P.; Becker, K. D.; Heitjans, P. Nonequilibrium Structure of Zn₂SnO₄ Spinel Nanoparticles. *J. Mater. Chem.* **2012**, 22 (7), 3117–3126. <https://doi.org/10.1039/C2JM15427G>.
- (71) Xu, Y.; Champion, L.; Gabidullin, B.; Bryce, D. L. A Kinetic Study of Mechanochemical Halogen Bond Formation by in situ ³¹P Solid-State NMR Spectroscopy. *Chem. Commun.* **2017**, 53 (71), 9930–9933. <https://doi.org/10.1039/C7CC05051H>.
- (72) Šepelák, V.; Becker, K. D.; Bergmann, I.; Suzuki, S.; Indris, S.; Feldhoff, A.; Heitjans, P.; Grey, C. P. A One-Step Mechanochemical Route to Core–Shell Ca₂SnO₄ Nanoparticles

- Followed by ^{119}Sn MAS NMR and ^{119}Sn Mössbauer Spectroscopy. *Chem. Mater.* **2009**, *21* (12), 2518–2524. <https://doi.org/10.1021/cm900590d>.
- (73) Šepelák, V.; Bergmann, I.; Indris, S.; Feldhoff, A.; Hahn, H.; Becker, K. D.; Grey, C. P.; Heitjans, P. High-Resolution ^{27}Al MAS NMR Spectroscopic Studies of the Response of Spinel Aluminates to Mechanical Action. *J. Mater. Chem.* **2011**, *21* (23), 8332. <https://doi.org/10.1039/c0jm03721d>.
- (74) Bartalucci, E.; Schumacher, C.; Hendrickx, L.; Puccetti, F.; d'Anciães Almeida Silva, I.; Dervişoğlu, R.; Puttreddy, R.; Bolm, C.; Wiegand, T. Disentangling the Effect of Pressure and Mixing on a Mechanochemical Bromination Reaction by Solid-State NMR Spectroscopy**. *Chem. Eur. J.* **2023**, *29* (12), e202203466. <https://doi.org/10.1002/chem.202203466>.
- (75) Gupta, S.; Kobayashi, T.; Hlova, I. Z.; Goldston, J. F.; Pruski, M.; Pecharsky, V. K. Solvent-Free Mechanochemical Synthesis of Alane, AlH_3 : Effect of Pressure on the Reaction Pathway. *Green Chem.* **2014**, *16* (9), 4378–4388. <https://doi.org/10.1039/C4GC00998C>.
- (76) Widdifield, C. M.; Schurko, R. W. Understanding Chemical Shielding Tensors Using Group Theory, MO Analysis, and Modern Density-Functional Theory. *Concepts Magn. Reson.* **2009**, *34A* (2), 91–123. <https://doi.org/10.1002/cmr.a.20136>.
- (77) U. Haeblerlen, In *Advances in Magnetic Resonance*; Suppl. 1; J. S. Waugh, Ed.; Academic Press: New York, 1976.
- (78) Ashbrook, S. E.; Sneddon, S. New Methods and Applications in Solid-State NMR Spectroscopy of Quadrupolar Nuclei. *J. Am. Chem. Soc.* **2014**, *136* (44), 15440–15456. <https://doi.org/10.1021/ja504734p>.
- (79) Autschbach, J.; Zheng, S.; Schurko, R. W. Analysis of Electric Field Gradient Tensors at Quadrupolar Nuclei in Common Structural Motifs. *Concepts Magn. Reson.* **2010**, *36A* (2), 84–126. <https://doi.org/10.1002/cmr.a.20155>.
- (80) Lowe, I. J. Free Induction Decays of Rotating Solids. *Phys. Rev. Lett.* **1959**, *2* (7), 285–287. <https://doi.org/10.1103/PhysRevLett.2.285>.

- (81) Andrew, E. R.; Bradbury, A.; Eades, R. G. Nuclear Magnetic Resonance Spectra from a Crystal Rotated at High Speed. *Nature* **1958**, *182* (4650), 1659–1659. <https://doi.org/10.1038/1821659a0>.
- (82) Nishiyama, Y.; Hou, G.; Agarwal, V.; Su, Y.; Ramamoorthy, A. Ultrafast Magic Angle Spinning Solid-State NMR Spectroscopy: Advances in Methodology and Applications. *Chem. Rev.* **2023**, *123* (3), 918–988. <https://doi.org/10.1021/acs.chemrev.2c00197>.
- (83) Ernst, M. Heteronuclear Spin Decoupling in Solid-State NMR under Magic-Angle Sample Spinning. *J. Magn. Reson.* **2003**, *162* (1), 1–34. [https://doi.org/10.1016/S1090-7807\(03\)00074-0](https://doi.org/10.1016/S1090-7807(03)00074-0).
- (84) Mote, K. R.; Agarwal, V.; Madhu, P. K. Five Decades of Homonuclear Dipolar Decoupling in Solid-State NMR: Status and Outlook. *Prog. Nucl. Magn. Reson. Spectrosc.* **2016**, *97*, 1–39. <https://doi.org/10.1016/j.pnmrs.2016.08.001>.
- (85) Schurko, R. W. Ultra-Wideline Solid-State NMR Spectroscopy. *Acc. Chem. Res.* **2013**, *46* (9), 1985–1995. <https://doi.org/10.1021/ar400045t>.
- (86) MacGregor, A. W.; O'Dell, L. A.; Schurko, R. W. New Methods for the Acquisition of Ultra-Wideline Solid-State NMR Spectra of Spin-1/2 Nuclides. *J. Magn. Reson.* **2011**, *208* (1), 103–113. <https://doi.org/10.1016/j.jmr.2010.10.011>.
- (87) Dey, K. K.; Ash, J. T.; Trease, N. M.; Grandinetti, P. J. Trading Sensitivity for Information: Carr-Purcell-Meiboom-Gill Acquisition in Solid-State NMR. *J. Chem. Phys.* **2010**, *133* (5), 054501. <https://doi.org/10.1063/1.3463653>.
- (88) Caravatti, P.; Bodenhausen, G.; Ernst, R. R. Heteronuclear Solid-State Correlation Spectroscopy. *Chem. Phys. Lett.* **1982**, *89* (5), 363–367. [https://doi.org/10.1016/0009-2614\(82\)80001-8](https://doi.org/10.1016/0009-2614(82)80001-8).
- (89) G.M. Rankin, A.; Pourpoint, F.; Duong, N. T.; Delevoye, L.; Amoureux, J.-P.; Lafon, O. Advances in the Characterization of Inorganic Solids Using NMR Correlation Experiments. In *Comprehensive Inorganic Chemistry III*; Elsevier, 2023; pp 534–582. <https://doi.org/10.1016/B978-0-12-823144-9.00192-8>.

- (90) Wiench, J. W.; Bronnimann, C. E.; Lin, V. S.-Y.; Pruski, M. Chemical Shift Correlation NMR Spectroscopy with Indirect Detection in Fast Rotating Solids: Studies of Organically Functionalized Mesoporous Silicas. *J. Am. Chem. Soc.* **2007**, *129* (40), 12076–12077. <https://doi.org/10.1021/ja074746+>.
- (91) Gan, Z.; Hung, I.; Wang, X.; Paulino, J.; Wu, G.; Litvak, I. M.; Gor'kov, P. L.; Brey, W. W.; Lendi, P.; Schiano, J. L.; Bird, M. D.; Dixon, I. R.; Toth, J.; Boebinger, G. S.; Cross, T. A. NMR Spectroscopy up to 35.2T Using a Series-Connected Hybrid Magnet. *J. Magn. Reson.* **2017**, *284*, 125–136. <https://doi.org/10.1016/j.jmr.2017.08.007>.
- (92) Larsen, F. H.; Jakobsen, H. J.; Ellis, P. D.; Nielsen, N. Chr. Sensitivity-Enhanced Quadrupolar-Echo NMR of Half-Integer Quadrupolar Nuclei. Magnitudes and Relative Orientation of Chemical Shielding and Quadrupolar Coupling Tensors. *J. Phys. Chem. A* **1997**, *101* (46), 8597–8606. <https://doi.org/10.1021/jp971547b>.
- (93) O'Dell, L. A.; Schurko, R. W. QCPMG Using Adiabatic Pulses for Faster Acquisition of Ultra-Wideline NMR Spectra. *Chem. Phys. Lett.* **2008**, *464* (1), 97–102. <https://doi.org/10.1016/j.cplett.2008.08.095>.
- (94) O'Dell, L. A.; Rossini, A. J.; Schurko, R. W. Acquisition of Ultra-Wideline NMR Spectra from Quadrupolar Nuclei by Frequency Stepped WURST–QCPMG. *Chem. Phys. Lett.* **2009**, *468* (4), 330–335. <https://doi.org/10.1016/j.cplett.2008.12.044>.
- (95) Massiot, D.; Farnan, I.; Gautier, N.; Trumeau, D.; Trokiner, A.; Coutures, J. P. ^{71}Ga and ^{69}Ga Nuclear Magnetic Resonance Study of $\beta\text{-Ga}_2\text{O}_3$: Resolution of Four- and Six-Fold Coordinated Ga Sites in Static Conditions. *Solid State Nucl. Magn. Reson.* **1995**, *4* (4), 241–248. [https://doi.org/10.1016/0926-2040\(95\)00002-8](https://doi.org/10.1016/0926-2040(95)00002-8).
- (96) Tang, J. A.; Masuda, J. D.; Boyle, T. J.; Schurko, R. W. Ultra-Wideline ^{27}Al NMR Investigation of Three- and Five-Coordinate Aluminum Environments. *ChemPhysChem* **2006**, *7* (1), 117–130. <https://doi.org/10.1002/cphc.200500343>.
- (97) Schurko, R. W. Ultra-Wideline Solid-State NMR Spectroscopy. *Acc. Chem. Res.* **2013**, *46* (9), 1985–1995. <https://doi.org/10.1021/ar400045t>.

- (98) Ramsey, N. F. The Internal Diamagnetic Field Correction in Measurements of the Proton Magnetic Moment. *Phys. Rev.* **1950**, 77 (4), 567–567. <https://doi.org/10.1103/PhysRev.77.567>.
- (99) Ramsey, N. F. Magnetic Shielding of Nuclei in Molecules. *Phys. Rev.* **1950**, 78 (6), 699–703. <https://doi.org/10.1103/PhysRev.78.699>.
- (100) Martin, R. M. *Electronic Structure: Basic Theory and Practical Methods*; Cambridge University Press: Cambridge, 2004. <https://doi.org/10.1017/CBO9780511805769>.
- (101) Hohenberg, P.; Kohn, W. Inhomogeneous Electron Gas. *Phys. Rev.* **1964**, 136 (3B), B864–B871. <https://doi.org/10.1103/PhysRev.136.B864>.
- (102) Kohn, W.; Sham, L. J. Self-Consistent Equations Including Exchange and Correlation Effects. *Phys. Rev.* **1965**, 140 (4A), A1133–A1138. <https://doi.org/10.1103/PhysRev.140.A1133>.
- (103) Koch, W.; Holthausen, M. C. *A Chemist's Guide to Density Functional Theory*, 1st ed.; Wiley, 2001. <https://doi.org/10.1002/3527600043>.
- (104) Perdew, J. P.; Burke, K.; Ernzerhof, M. Generalized Gradient Approximation Made Simple. *Phys. Rev. Lett.* **1996**, 77 (18), 3865–3868. <https://doi.org/10.1103/PhysRevLett.77.3865>.
- (105) Kaupp, M.; Bühl, M.; Malkin, V. G. Introduction: The Quantum Chemical Calculation of NMR and EPR Parameters. In *Calculation of NMR and EPR Parameters*; John Wiley & Sons, Ltd, 2004; pp 1–5. <https://doi.org/10.1002/3527601678.ch1>.
- (106) Pickard, C. J.; Mauri, F. Calculations of Magnetic Resonance Parameters in Solids and Liquids Using Periodic Boundary Conditions. In *Calculation of NMR and EPR Parameters*; John Wiley & Sons, Ltd, 2004; pp 265–277. <https://doi.org/10.1002/3527601678.ch16>.
- (107) Pickard, C. J.; Mauri, F. All-Electron Magnetic Response with Pseudopotentials: NMR Chemical Shifts. *Phys. Rev. B* **2001**, 63 (24), 245101. <https://doi.org/10.1103/PhysRevB.63.245101>.
- (108) Bonhomme, C.; Gervais, C.; Babonneau, F.; Coelho, C.; Pourpoint, F.; Azaïs, T.; Ashbrook, S. E.; Griffin, J. M.; Yates, J. R.; Mauri, F.; Pickard, C. J. First-Principles Calculation of NMR

- Parameters Using the Gauge Including Projector Augmented Wave Method: A Chemist's Point of View. *Chem. Rev.* **2012**, *112* (11), 5733–5779. <https://doi.org/10.1021/cr300108a>.
- (109) Charpentier, T. The PAW/GIPAW Approach for Computing NMR Parameters: A New Dimension Added to NMR Study of Solids. *Solid State Nucl. Magn. Reson.* **2011**, *40* (1), 1–20. <https://doi.org/10.1016/j.ssnmr.2011.04.006>.
- (110) J. Cramer, C.; G. Truhlar, D. Density Functional Theory for Transition Metals and Transition Metal Chemistry. *Phy. Chem. Chem. Phys.* **2009**, *11* (46), 10757–10816. <https://doi.org/10.1039/B907148B>.
- (111) Szell, P. M. J.; Rehman, Z.; Tatman, B. P.; Hughes, L. P.; Blade, H.; Brown, S. P. Exploring the Potential of Multinuclear Solid-State ^1H , ^{13}C , and ^{35}Cl Magnetic Resonance To Characterize Static and Dynamic Disorder in Pharmaceutical Hydrochlorides. *ChemPhysChem* **2023**, *24* (3), e202200558. <https://doi.org/10.1002/cphc.202200558>.
- (112) Moudrakovski, I.; Lang, S.; Patchkovskii, S.; Ripmeester, J. High Field ^{33}S Solid State NMR and First-Principles Calculations in Potassium Sulfates. *J. Phys. Chem. A* **2010**, *114* (1), 309–316. <https://doi.org/10.1021/jp908206c>.
- (113) Cahill, L. S.; Hanna, J. V.; Wong, A.; Freitas, J. C. C.; Yates, J. R.; Harris, R. K.; Smith, M. E. Natural Abundance ^{25}Mg Solid-State NMR of Mg Oxyanion Systems: A Combined Experimental and Computational Study. *Chem. – Eur. J.* **2009**, *15* (38), 9785–9798. <https://doi.org/10.1002/chem.200900346>.
- (114) Widdifield, C. M.; Bryce, D. L. Solid-State $^{79}/^{81}\text{Br}$ NMR and Gauge-Including Projector-Augmented Wave Study of Structure, Symmetry, and Hydration State in Alkaline Earth Metal Bromides. *J. Phys. Chem. A* **2010**, *114* (5), 2102–2116. <https://doi.org/10.1021/jp909106j>.
- (115) Chapman, R. P.; Bryce, D. L. Application of Multinuclear Magnetic Resonance and Gauge-Including Projector-Augmented-Wave Calculations to the Study of Solid Group 13 Chlorides. *Phys. Chem. Chem. Phys.* **2009**, *11* (32), 6987–6998. <https://doi.org/10.1039/B906627F>.
- (116) Vojvodin, C. S.; Holmes, S. T.; Watanabe, L. K.; Rawson, J. M.; Schurko, R. W. Multi-Component Crystals Containing Urea: Mechanochemical Synthesis and Characterization

- by ^{35}Cl Solid-State NMR Spectroscopy and DFT Calculations. *CrystEngComm* **2022**, *24* (14), 2626–2641. <https://doi.org/10.1039/D1CE01610E>.
- (117) Peach, A. A.; Hirsh, D. A.; Holmes, S. T.; Schurko, R. W. Mechanochemical Syntheses and ^{35}Cl Solid-State NMR Characterization of Fluoxetine HCl Cocrystals. *CrystEngComm* **2018**, *20* (20), 2780–2792. <https://doi.org/10.1039/C8CE00378E>.
- (118) Kleinman, L.; Bylander, D. M. Efficacious Form for Model Pseudopotentials. *Phys. Rev. Lett.* **1982**, *48* (20), 1425–1428. <https://doi.org/10.1103/PhysRevLett.48.1425>.
- (119) Troullier, N.; Martins, J. L. Efficient Pseudopotentials for Plane-Wave Calculations. II. Operators for Fast Iterative Diagonalization. *Phys. Rev. B* **1991**, *43* (11), 8861–8869. <https://doi.org/10.1103/PhysRevB.43.8861>.
- (120) Vanderbilt, D. Soft Self-Consistent Pseudopotentials in a Generalized Eigenvalue Formalism. *Phys. Rev. B* **1990**, *41* (11), 7892–7895. <https://doi.org/10.1103/PhysRevB.41.7892>.
- (121) Truflandier, L.; Paris, M.; Payen, C.; Boucher, F. First-Principles Calculations within Periodic Boundary Conditions of the NMR Shielding Tensor for a Transition Metal Nucleus in a Solid State System: The Example of ^{51}V in AlVO_4 . *J. Phys. Chem. B* **2006**, *110* (43), 21403–21407. <https://doi.org/10.1021/jp0648137>.
- (122) Truflandier, L.; Paris, M.; Boucher, F. DFT Investigation of 3d Transition Metal NMR Shielding Tensors in Diamagnetic Systems Using the Gauge-Including Projector Augmented-Wave Method. *Phys. Rev. B* **2007**, *76* (3), 035102. <https://doi.org/10.1103/PhysRevB.76.035102>.
- (123) Trinité, V.; Vast, N.; Hayoun, M. Effects of Localization of the Semicore Density on the Physical Properties of Transition and Noble Metals. *J. Phys.: Condens. Matter* **2008**, *20* (23), 235239. <https://doi.org/10.1088/0953-8984/20/23/235239>.
- (124) Kaeffer, N.; Mance, D.; Copéret, C. N-Heterocyclic Carbene Coordination to Surface Copper Sites in Selective Semihydrogenation Catalysts from Solid-State NMR Spectroscopy. *Angew. Chem.* **2020**, *132* (45), 20174–20182. <https://doi.org/10.1002/ange.202006209>.

- (125) Ashbrook, S. E.; McKay, D. Combining Solid-State NMR Spectroscopy with First-Principles Calculations – a Guide to NMR Crystallography. *Chem. Commun.* **2016**, 52 (45), 7186–7204. <https://doi.org/10.1039/C6CC02542K>.
- (126) Vasconcelos, F.; Cristol, S.; Paul, J.-F.; Montagne, L.; Mauri, F.; Delevoye, L. First-Principles Calculations of NMR Parameters for Phosphate Materials. *Magn. Reson. Chem. MRC* **2010**, 48 Suppl 1, S142-150. <https://doi.org/10.1002/mrc.2667>.
- (127) Balema, V. P.; Wiench, J. W.; Pruski, M.; Pecharsky, V. K. Solvent-Free Mechanochemical Synthesis of Phosphonium Salts. *Chem. Commun.* **2002**, No. 7, 724–725. <https://doi.org/10.1039/B111515D>.
- (128) Speight, I. R.; Huskić, I.; Arhangelskis, M.; Titi, H. M.; Stein, R. S.; Hanusa, T. P.; Friščić, T. Disappearing Polymorphs in Metal–Organic Framework Chemistry: Unexpected Stabilization of a Layered Polymorph over an Interpenetrated Three-Dimensional Structure in Mercury Imidazolate. *Chem. – Eur. J.* **2020**, 26 (8), 1811–1818. <https://doi.org/10.1002/chem.201905280>.
- (129) Germann, L. S.; Arhangelskis, M.; Stein, R.; Etter, M.; Dinnebier, R. E.; Friscic, T. Profound Effect of the Milling Assembly on Polymorphism in Mechanochemical Cocrystallization. ChemRxiv February 11, 2020. <https://doi.org/10.26434/chemrxiv.11829414.v1>.
- (130) Xu, Y.; Viger-Gravel, J.; Korobkov, I.; Bryce, D. L. Mechanochemical Production of Halogen-Bonded Solids Featuring P=O···I–C Motifs and Characterization via X-Ray Diffraction, Solid-State Multinuclear Magnetic Resonance, and Density Functional Theory. *J. Phys. Chem. C* **2015**, 119 (48), 27104–27117. <https://doi.org/10.1021/acs.jpcc.5b09737>.
- (131) Mandala, V. S.; Loewus, S. J.; Mehta, M. A. Monitoring Cocrystal Formation via In Situ Solid-State NMR. *J. Phys. Chem. Lett.* **2014**, 5 (19), 3340–3344. <https://doi.org/10.1021/jz501699h>.
- (132) de Frémont, P.; Marion, N.; Nolan, S. P. Carbenes: Synthesis, Properties, and Organometallic Chemistry. *Coord. Chem. Rev.* **2009**, 253 (7), 862–892. <https://doi.org/10.1016/j.ccr.2008.05.018>.
- (133) Wanzlick, H. W. Aspects of Nucleophilic Carbene Chemistry. *Angew. Chem. Int. Ed. Engl.* **1962**, 1 (2), 75–80. <https://doi.org/10.1002/anie.196200751>.

- (134) Wanzlick, H.-W.; Schönherr, H.-J. Direct Synthesis of a Mercury Salt-Carbene Complex. *Angew. Chem. Int. Ed. Engl.* **1968**, 7 (2), 141–142. <https://doi.org/10.1002/anie.196801412>.
- (135) Öfele, K. 1,3-Dimethyl-4-imidazolinylden-(2)-pentacarbonylchrom ein neuer übergangsmetall-carben-komplex. *J. Organomet. Chem.* **1968**, 12 (3), P42–P43. [https://doi.org/10.1016/S0022-328X\(00\)88691-X](https://doi.org/10.1016/S0022-328X(00)88691-X).
- (136) Arduengo, A. J. I.; Harlow, R. L.; Kline, M. A Stable Crystalline Carbene. *J. Am. Chem. Soc.* **1991**, 113 (1), 361–363. <https://doi.org/10.1021/ja00001a054>.
- (137) Crudden, C. M.; Allen, D. P. Stability and Reactivity of N-Heterocyclic Carbene Complexes. *Coord. Chem. Rev.* **2004**, 248 (21), 2247–2273. <https://doi.org/10.1016/j.ccr.2004.05.013>.
- (138) Díez-González, S.; Nolan, S. P. Stereoelectronic Parameters Associated with N-Heterocyclic Carbene (NHC) Ligands: A Quest for Understanding. *Coord. Chem. Rev.* **2007**, 251 (5), 874–883. <https://doi.org/10.1016/j.ccr.2006.10.004>.
- (139) Colacino, E.; Martinez, J.; Lamaty, F. Preparation of NHC–Ruthenium Complexes and Their Catalytic Activity in Metathesis Reaction. *Coord. Chem. Rev.* **2007**, 251 (5), 726–764. <https://doi.org/10.1016/j.ccr.2006.07.017>.
- (140) Lee, H. M.; Lee, C.-C.; Cheng, P.-Y. Recent Development of Functionalized N-Heterocyclic Carbene Ligands: Coordination Chemistry and Catalytic Applications. *Curr. Org. Chem.* **2007**, 11 (17), 1491–1524.
- (141) Kühl, O. The Chemistry of Functionalised N-Heterocyclic Carbenes. *Chem. Soc. Rev.* **2007**, 36 (4), 592–607. <https://doi.org/10.1039/B603765H>.
- (142) Lin, I. J. B.; Vasam, C. S. Preparation and Application of N-Heterocyclic Carbene Complexes of Ag(I). *Coord. Chem. Rev.* **2007**, 251 (5), 642–670. <https://doi.org/10.1016/j.ccr.2006.09.004>.
- (143) Cavell, K. N-Heterocyclic Carbenes /Imidazolium Salts as Substrates in Catalysis: The Catalytic 2-Substitution and Annulation of Heterocyclic Compounds. *Dalton Trans.* **2008**, 0 (47), 6676–6685. <https://doi.org/10.1039/B811449H>.

- (144) Marion, N.; Nolan, S. P. Well-Defined N-Heterocyclic Carbenes–Palladium(II) Precatalysts for Cross-Coupling Reactions. *Acc. Chem. Res.* **2008**, *41* (11), 1440–1449. <https://doi.org/10.1021/ar800020y>.
- (145) Jacobsen, H.; Correa, A.; Poater, A.; Costabile, C.; Cavallo, L. Understanding the M(NHC) (NHC=N-Heterocyclic Carbene) Bond. *Coord. Chem. Rev.* **2009**, *253* (5), 687–703. <https://doi.org/10.1016/j.ccr.2008.06.006>.
- (146) Wang, F.; Liu, L.; Wang, W.; Li, S.; Shi, M. Chiral NHC–Metal-Based Asymmetric Catalysis. *Coord. Chem. Rev.* **2012**, *256* (9), 804–853. <https://doi.org/10.1016/j.ccr.2011.11.013>.
- (147) Liu, W.; Gust, R. Metal N -Heterocyclic Carbene Complexes as Potential Antitumor Metallodrugs. *Chem. Soc. Rev.* **2013**, *42* (2), 755–773. <https://doi.org/10.1039/C2CS35314H>.
- (148) Nelson, D. J.; Nolan, S. P. Quantifying and Understanding the Electronic Properties of N-Heterocyclic Carbenes. *Chem. Soc. Rev.* **2013**, *42* (16), 6723–6753. <https://doi.org/10.1039/C3CS60146C>.
- (149) Hu, C.; Li, X.; Wang, W.; Zhang, R.; Deng, L. Metal-N-Heterocyclic Carbene Complexes as Anti-Tumor Agents. *Curr. Med. Chem.* **2014**, *21* (10), 1220–1230.
- (150) Herrmann, W. A.; Köcher, C. N-Heterocyclic Carbenes. *Angew. Chem. Int. Ed. Engl.* **1997**, *36* (20), 2162–2187. <https://doi.org/10.1002/anie.199721621>.
- (151) Velazquez, H. D.; Verpoort, F. N-Heterocyclic Carbene Transition Metal Complexes for Catalysis in Aqueous Media. *Chem. Soc. Rev.* **2012**, *41* (21), 7032–7060. <https://doi.org/10.1039/C2CS35102A>.
- (152) Michalak; Kośnik. Chiral N-Heterocyclic Carbene Gold Complexes: Synthesis and Applications in Catalysis. *Catalysts* **2019**, *9* (11), 890. <https://doi.org/10.3390/catal9110890>.
- (153) Oehninger, L.; Rubbiani, R.; Ott, I. N-Heterocyclic Carbene Metal Complexes in Medicinal Chemistry. *Dalton Trans.* **2013**, *42* (10), 3269–3284. <https://doi.org/10.1039/C2DT32617E>.

- (154) Smith, C. A.; Narouz, M. R.; Lummis, P. A.; Singh, I.; Nazemi, A.; Li, C.-H.; Crudden, C. M. N-Heterocyclic Carbenes in Materials Chemistry. *Chem. Rev.* **2019**, *119* (8), 4986–5056. <https://doi.org/10.1021/acs.chemrev.8b00514>.
- (155) Martynova, E. A.; Tzouras, N. V.; Pisanò, G.; Cazin, C. S. J.; Nolan, S. P. The “Weak Base Route” Leading to Transition Metal–N-Heterocyclic Carbene Complexes. *Chem. Commun.* **2021**, 57 (32), 3836–3856. <https://doi.org/10.1039/D0CC08149C>.
- (156) Pisanò, G.; Cazin, C. S. J. General Mechanochemical Synthetic Protocol to Late Transition Metal–NHC (N-Heterocyclic Carbene) Complexes. *ACS Sustainable Chem. Eng.* **2021**, *9* (29), 9625–9631. <https://doi.org/10.1021/acssuschemeng.1c00556>.
- (157) Egbert, J. D.; Slawin, A. M. Z.; Nolan, S. P. Synthesis of N-Heterocyclic Carbene Gold Complexes Using Solution-Phase and Solid-State Protocols. *Organometallics* **2013**, *32* (7), 2271–2274. <https://doi.org/10.1021/om301187a>.
- (158) Pisanò, G.; J. Cazin, C. S. Mechanochemical Synthesis of Cu(I)-N-Heterocyclic Carbene Complexes. *Green Chem.* **2020**, *22* (16), 5253–5256. <https://doi.org/10.1039/D0GC01923B>.
- (159) De, S.; Joó, F.; Horváth, H.; Udvardy, A.; Czégéni, C. E. Stirring or Milling? First Synthesis of Rh(I)-(Di-N-Heterocyclic Carbene) Complexes Both in Solution and in a Ball Mill. *J. Organomet. Chem.* **2020**, *918*, 121308. <https://doi.org/10.1016/j.jorganchem.2020.121308>.
- (160) Beillard, A.; Golliard, E.; Gillet, V.; Bantreil, X.; Métro, T.-X.; Martinez, J.; Lamaty, F. Expedient Mechanosynthesis of N,N-Dialkyl Imidazoliums and Silver(I)-Carbene Complexes in a Ball-Mill. *Chem. Eur. J.* **2015**, *21* (49), 17614–17617. <https://doi.org/10.1002/chem.201503472>.
- (161) Beillard, A.; Quintin, F.; Gatignol, J.; Retailleau, P.; Renaud, J.-L.; Gaillard, S.; Métro, T.-X.; Lamaty, F.; Bantreil, X. Solving the Challenging Synthesis of Highly Cytotoxic Silver Complexes Bearing Sterically Hindered NHC Ligands with Mechanochemistry. *Dalton Trans* **2020**, 49 (36), 12592–12598. <https://doi.org/10.1039/D0DT00410C>.
- (162) Beillard, A.; Bantreil, X.; Métro, T.-X.; Martinez, J.; Lamaty, F. Mechanochemistry for Facilitated Access to N,N-Diaryl NHC Metal Complexes. *New J. Chem.* **2017**, *41* (3), 1057–1063. <https://doi.org/10.1039/C6NJ02895K>.

- (163) Ryzhakov, D.; Beillard, A.; Le Bideau, F.; Al-Shuaeeb, R. A. A.; Alami, M.; Bantreil, X.; Bonnemoy, A.; Gautier, A.; Lamaty, F.; Messaoudi, S. Azoliums and Ag(I)-N-Heterocyclic Carbene Thioglycosides: Synthesis, Reactivity and Bioactivity. *Eur. J. Org. Chem.* **2022**, 2022 (9), e202101499. <https://doi.org/10.1002/ejoc.202101499>.
- (164) Beillard, A.; Bantreil, X.; Métro, T.-X.; Martinez, J.; Lamaty, F. Unraveling the Synthesis of Homoleptic $[Ag(N,N\text{-Diaryl-NHC})_2]Y$ ($Y = BF_4, PF_6$) Complexes by Ball-Milling. *Dalton Trans.* **2016**, 45 (44), 17859–17866. <https://doi.org/10.1039/C6DT03564G>.
- (165) Wróblewska, A.; Lauriol, G.; Mlostoń, G.; Bantreil, X.; Lamaty, F. Expedient Synthesis of NOxy-Heterocyclic Carbenes (NOHC) Ligands and Metal Complexes Using Mechanochemistry. *J. Organomet. Chem.* **2021**, 949, 121914. <https://doi.org/10.1016/j.jorganchem.2021.121914>.
- (166) Quintin, F.; Pinaud, J.; Lamaty, F.; Bantreil, X. Mechanochemistry of Noels-Type NHC–Ruthenium Complexes and Applications in Ring-Opening Metathesis Polymerization. *Organometallics* **2020**, 39 (5), 636–639. <https://doi.org/10.1021/acs.organomet.0c00013>.
- (167) Mukherjee, N.; Marczyk, A.; Szczepaniak, G.; Sytniczuk, A.; Kajetanowicz, A.; Grela, K. A Gentle Touch: Synthesis of Modern Ruthenium Olefin Metathesis Catalysts Sustained by Mechanical Force. *ChemCatChem* **2019**, 11 (21), 5362–5369. <https://doi.org/10.1002/cctc.201901444>.
- (168) Liao, Q.; Su, K.; Cai, H.; Zhao, T.; Liu, F. Mechanochemical Synthesis of Carbene Copper Complexes for CO₂ Hydrogenation to Formate. *J. CO₂ Util.* **2022**, 59, 101963. <https://doi.org/10.1016/j.jcou.2022.101963>.
- (169) Allenbaugh, R. J.; Zachary, J. R.; Underwood, A. N.; Bryson, J. D.; Williams, J. R.; Shaw, A. Kinetic Analysis of the Complete Mechanochemical Synthesis of a Palladium(II) Carbene Complex. *Inorg. Chem. Commun.* **2020**, 111, 107622. <https://doi.org/10.1016/j.inoche.2019.107622>.
- (170) Pisanò, G.; Cazin, C. S. J. Mechanochemical Synthesis of Cu(I)-N-Heterocyclic Carbene Complexes. *Green Chem.* **2020**, 22 (16), 5253–5256. <https://doi.org/10.1039/D0GC01923B>.

- (171) Savka, R.; Plenio, H. Facile Synthesis of [(NHC)MX(Cod)] and [(NHC)MCl(CO)₂] (M = Rh, Ir; X = Cl, I) Complexes. *Dalton Trans.* **2014**, 44 (3), 891–893. <https://doi.org/10.1039/C4DT03449J>.

CHAPTER 2.

Understanding the Mechanochemical
Synthesis of Transition Metal-NHC
Complexes using ssNMR
Spectroscopy

Chapter 2. Understanding the Mechanochemical Synthesis of Transition Metal-NHC Complexes using ssNMR Spectroscopy

2.1 Introduction

The use of mechanochemical methodologies to drive chemical transformations of solid reactants has witnessed significant advancements,^{1,2} finding applications in diverse chemical science fields, including organic,^{3,4} organometallic,^{5,6} main group,⁷ and supramolecular chemistry,⁸ as well as metal-mediated⁹ and enzymatic-mediated¹⁰ transformations. One of the key advantages of mechanochemistry lies in its ability to create a solvent-free reaction environment, addressing the critical issue of solvent waste management and enhancing environmental efficiency.¹¹ Compared to traditional solution-based methods, mechanochemical conditions generally yield higher product yields in shorter reaction times,¹² even enabling access to products that might be difficult to obtain using solvent-based approaches,¹³ mainly due to solubility issues.¹⁴ Despite the simplicity of using only solid reactants, predicting the outcomes of mechanochemical reactions remains challenging.^{15,16} The lack of consensus on defining a reaction as purely mechanochemical arises from the potential influence of solvent applied during the workup phase of ball milling synthesis, which can alter the final product's structural arrangement.¹⁷ Consequently, the understanding of the mechanochemical reaction mechanism requires the structural characterization of the chemical species in the solid-state before any workup procedure. PXRD and vibrational spectroscopy are commonly employed techniques for this purpose.¹⁸ However, recent studies have shown the potential of ssNMR spectroscopy as an advantageous method for monitoring mechanochemical reactions.^{19,20} Unlike other techniques, ssNMR offers quantitative data and the ability to characterize both crystalline and amorphous structures without the need to dissolve the powder samples in solvents, making it an excellent tool for mechanochemical analysis.

In this chapter, I provide mechanistic insights into the mechanochemical synthesis of transition metal-NHC complexes using ssNMR spectroscopy as the primary analytical technique, complemented by other solid-state analytical methods. Transition metal-NHC complexes are of great interest due to their crucial role in homogeneous catalysis,^{21,22} materials science,²³ and medicinal chemistry.^{24–26} Some research groups have successfully translated traditional synthetic approaches for these complexes into mechanochemical methods.²⁷ Notably, the

mechanochemical weak base approach developed concomitantly by the Cazin and Udvardy groups in 2020 stands out for its simplicity and versatility, using readily available starting materials and an inexpensive base (e.g., K_2CO_3 , Cs_2CO_3).^{28,29} The core concept of this involves co-grinding solid reactants, including the transition metal (i.e., Cu(I), Ag(I), Au(I), Rh(I), Pd(II)) and the NHC ligand (i.e., benzimidazolium, imidazol(in)ium, as well as CAAC precursors), in the presence of a weak base using a ball mill or other suitable milling equipment.³⁰ Despite promising results, concerns arise regarding whether the observed reactions genuinely occur during mechanical processing or result from subsequent treatments involving solvents during workup and purification. Obtaining this crucial information is essential for a deeper understanding of the true source of reactivity in mechanochemical synthetic approaches.

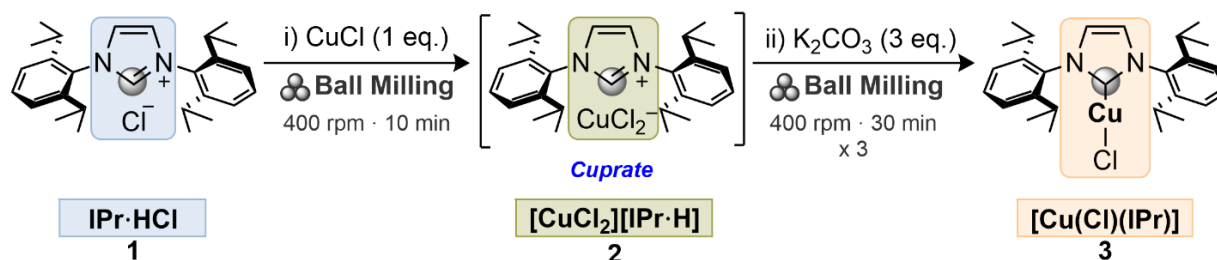
Chapter 2 is structured into three main sections, each dedicated to the investigation of the mechanochemical synthesis of distinct transition metal-NHC complexes.

- Section **2.2** delves into the mechanistic insights of the mechanochemical synthesis of $[\text{Cu}(\text{NHC})(\text{Cl})]$ complexes. This exploration is facilitated through the application of ssNMR spectroscopy and the computation of NMR parameters using DFT.
- Section **2.3** focuses on providing mechanistic insights into the mechanochemical synthesis of $[\text{Ag}(\text{NHC})(\text{Cl})]$ complexes. Our approach in this section centers on the utilization of ssNMR spectroscopy.
- In Section **2.4**, an innovative mechanochemical synthetic approach is investigated and explored to prepare Rh(I)-NHC complexes using a combination of solid-state analytical techniques, including ssNMR spectroscopy, PXRD, and attenuated total reflectance-Fourier transform infrared spectroscopy (ATR-FTIR).

2.2 Cu(I)-NHC Complexes

Here we aimed to elucidate the mechanism involved in the weak base approach applied to the mechanochemical synthesis of $[\text{Cu}(\text{Cl})(\text{NHC})]$ complexes (**Scheme 2.1**) and to investigate whether these complexes and their corresponding cuprate intermediates are formed in the solid-state during the ball milling process or the subsequent workup. To achieve this, we employed ssNMR analysis to monitor the reaction. As a model substrate, we chose the imidazolium salt $\text{IPr}\cdot\text{HCl}$ **1**, and we obtained the corresponding $[\text{Cu}(\text{Cl})(\text{IPr})]$ complex **3** through two different synthetic approaches: i) a one-step one-pot synthesis, and ii) a two-steps one-pot synthesis (as illustrated in **Scheme 2.2**). Multinuclear ssNMR experiments for spin-1/2 (^1H , ^{13}C , ^{15}N) and

quadrupolar (^{35}Cl , ^{63}Cu) nuclei at static magnetic fields of 9.4, 18.8, and 28.2 T were conducted to monitor the consumption of the reactants and the formation of the intermediate and final products for the different synthetic routes and workup protocols (**Scheme 2.2**). We notably leveraged the gain in resolution and sensitivity provided by the 1.2 GHz NMR magnet to observe isotopes subject to large quadrupolar interaction, such as ^{35}Cl and ^{63}Cu . NMR signals were assigned with the help of 2D heteronuclear correlations, and we complemented the analysis with DFT calculations of NMR parameters.



Scheme 2.1. Weak base approach towards the mechanochemical synthesis of $[\text{Cu}(\text{Cl})(\text{IPr})]$.²⁹ The gray sphere denotes the $^{13}\text{C}^2$ carbon of the imidazolyliene moiety in the different compounds.

2.2.1 Results and Discussion

2.2.1.1 Mechanochemical synthesis

The mechanochemical synthesis of $[\text{CuCl}_2][\text{IPr-H}]$ **2** and $[\text{Cu}(\text{Cl})(\text{IPr})]$ **3** was accomplished using a planetary ball mill (Fritsch, Pulverisette 5/4) operating at its maximum milling frequency of 400 rpm.²⁹ The synthesis procedure was conducted within a 12 mL ZrO_2 reactor, loaded with 18 milling bodies ($\varnothing = 5$ mm) made of the same material, and it encompasses two distinct routes: i) a two-steps one-pot (SW) synthesis and ii) a one-step one-pot (OP) synthesis (**Scheme 2.2**).

i) Two-Steps One-Pot (SW) Synthesis:

In this route, the synthesis process occurs in two distinct steps within a single reaction vessel:

- **Step 1:** The reactor was charged with $\text{IPr}\cdot\text{HCl}$ (**1**) (1 eq.) and CuCl (1 eq.) in an air environment. The mixture of these two reactants was subjected to grinding for 30 min at a speed of 400 rpm to produce the reaction mixture **2**.

- **Step 2:** Following the initial grinding, K_2CO_3 (1 eq.) was added to the solid mixture **2** and further subjected to grinding for three repetitions of 30 min each at 400 rpm to form **3^{SW}**.

ii) One-Step One-Pot (OP) Synthesis:

In this approach, the entire synthesis process occurs in a single step within the same reaction vessel:

- Single Step:** The reactor was charged with all the reactants at once - $\text{IPr}\cdot\text{HCl}$ **1** (1 eq.), CuCl (1 eq.), and K_2CO_3 (1 eq.), then subjected to grinding for three repetitions of 30 min each at 400 rpm to form **3^{OP}**.

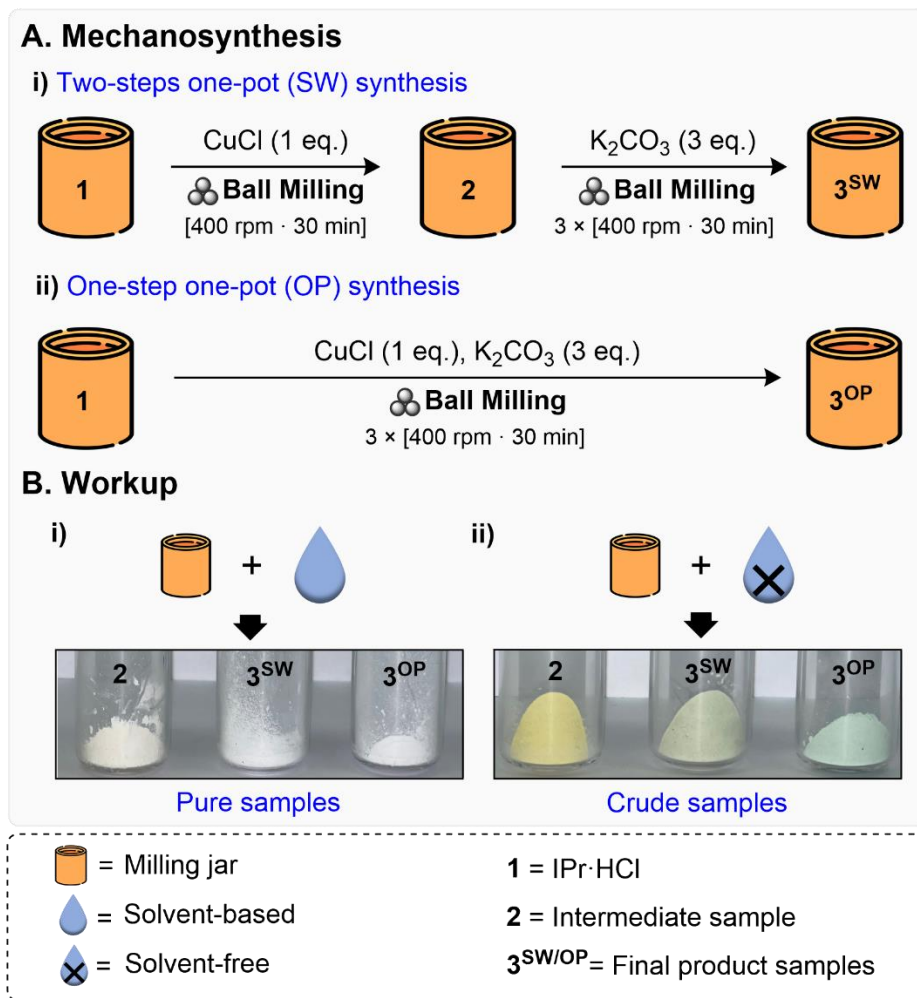
The two distinct mechanochemical synthesis routes were carried out twice to execute two different workup protocols. The chosen approach depended on the presence or absence of solvents:

i) Solvent-Based Workup:

After the milling process, the contents of the reactors (**2**, **3^{OP}**, and **3^{SW}**) were extracted using CH_2Cl_2 . The resulting solution was subsequently filtered through SiO_2 . The SiO_2 pad was rinsed with additional CH_2Cl_2 , followed by concentration via rotatory evaporation to approximately one-quarter of its initial volume. To this concentrated solution, an excess of *n*-pentane was added. The resulting solution was subjected to sonication, and the resulting solids were collected through vacuum filtration. These solids were washed with extra *n*-pentane and finally dried under vacuum conditions for an extended duration. The resulting solids are referred to as pure **2**, **3^{OP}**, and **3^{SW}** samples.

ii) Solvent-Free Workup:

Following the milling process, the contents of the reactors (**2**, **3^{OP}**, and **3^{SW}**) were manually extracted using a spatula. These solids were then transferred into a vial for analysis without further manipulation and referred to as crude **2**, **3^{OP}**, and **3^{SW}** samples.



Scheme 2.2. (A) Schematic outline of the mechanochemistry: (i) two-step one-pot (SW) synthesis and (ii) one-step one-pot (OP) synthesis. (B) Pure and crude samples collected after (i) solvent-based and (ii) solvent-free workup procedures, respectively.

2.2.1.2 ^1H ssNMR spectroscopy

The 1D ^1H ssNMR spectra of compound **1** and both pure and crude forms of **2**, **3^{OP}**, and **3^{SW}** were acquired at a static magnetic field, $B_0 = 18.8$ T with MAS frequency, $\nu_R = 60$ kHz, in order to enhance the spectral resolution (**Figure 2.1**). The ^1H signals observed were assigned based on ^1H isotropic chemical shifts measured in solution and DFT calculations of ^1H isotropic chemical shifts for periodic crystal structures (see **Figure 2.2** and **Table 2.1**), as well as 2D $^1\text{H}\{^{13}\text{C}\}$ DCP HETCOR spectra (see **Figure 2.3**). The imidazolium $^1\text{H}^2$ signal is a good indicator of the reaction progress since, in **Figure 2.1a**, it is shifted from 12.5 ppm in **1** down to 10 ppm in pure **2**, whereas it is no longer observed in the ^1H spectra of **3^{SW/OP}** owing to the deprotonation of this site.

After 10 min ball milling of IPr·HCl in the presence of CuCl, the $^1\text{H}^2$ signal of $[\text{CuCl}_2][\text{IPr}\cdot\text{H}]$ cuprate is detected in the pure sample but not in the crude one (**Figure 2.4**). However, by increasing the ball-milling time to 30 min, the cuprate $^1\text{H}^2$ signal is also detected in the crude sample **2** (**Figure 2.1b**), which confirms the formation of the cuprate in the solid-state during ball milling.

The ^1H spectra of crude samples **2** and $3^{\text{OP/SW}}$, depicted in **Figure 2.1b**, exhibit a $^1\text{H}^2$ signal resonating at 12.5 ppm, indicating the presence of unreacted IPr·HCl in the crude samples. Moreover, an additional ^1H signal at 13.5 ppm, attributed to KHCO_3 , is present in the ^1H spectra of crude $3^{\text{OP/SW}}$.³¹

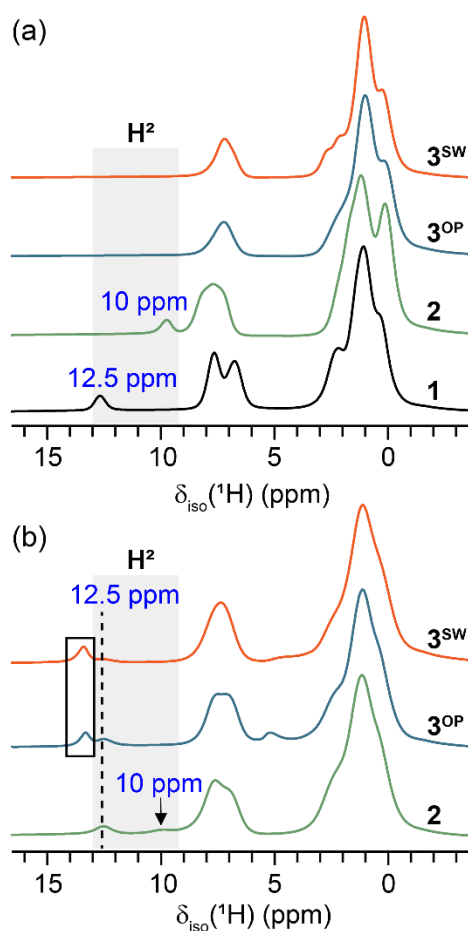


Figure 2.1. 1D ^1H MAS NMR spectra of (a) pure and (b) crude **2** (green), 3^{OP} (blue), and 3^{SW} (orange) acquired at $B_0 = 18.8$ T with a MAS frequency, $\nu_R = 60$ kHz. The spectrum of compound **1** is also shown in black in panel (a) for the sake of comparison. The shaded area denotes the region where the $^1\text{H}^2$ signal of **1** and $[\text{CuCl}_2][\text{IPr}\cdot\text{H}]$ resonates. The ^1H signal denoted by the black

box corresponds to KHCO_3 . The signal resonating near 5 ppm in 1D ^1H NMR spectrum of crude **3^{OP}** and **3^{SW}** is assigned to water.

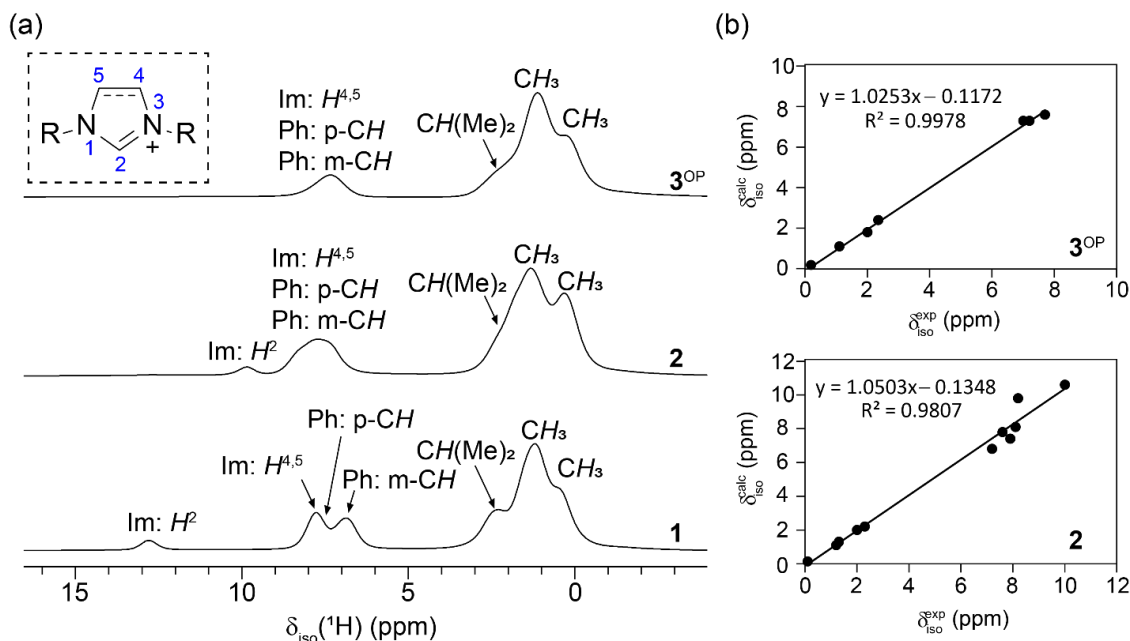


Figure 2.2. (a) 1D ^1H MAS NMR spectra of **1** and pure **2** and **3^{OP}** acquired at $B_0 = 28.2$ T with $\nu_R = 60$ kHz, along with the assignment of the ^1H signals. Im and Ph denote the signals of the imidazole and phenyl ring, respectively. These spectra exhibit slightly higher resolution than those shown in **Figure 2.1a** recorded at $B_0 = 18.8$ T. The atom numbering of the imidazole ring is indicated on the structure shown as an inset. (b) Correlation between DFT-calculated ($\delta_{\text{iso}}^{\text{calc}}$) and experimental ($\delta_{\text{iso}}^{\text{exp}}$) isotropic chemical shifts for the ^1H sites of $[\text{CuCl}_2][\text{IPr-H}]$ and $[\text{Cu}(\text{Cl})(\text{IPr})]$ crystal structures. The $\delta_{\text{iso}}^{\text{exp}}$ values were measured from the 1D ^1H MAS NMR spectra of pure **2** and **3^{OP}** shown in panel (a).

Table 2.1. Experimental and computed $\delta_{\text{iso}}(^1\text{H})$ shifts in ppm for crystal structures (DFT^C) of **1** and pure **2** and **3^{OP}**.

Sample		CH ₃	CH(Me) ₂	Ph: m-CH	Ph: p-CH	Im: H ⁵	Im: H ⁴	Im: H ²
1	Exp.	0.4 1.1	2.3	6.8	7.6	7.8	7.8	12.5
	DFT ^C	–	–	–	–	–	–	–
2	Exp.	0.1	2	7.2	7.6	8.2	8.1	10.0
		1.2	2.3	7.9				
		1.3						
	DFT ^C	0.1 1.1 1.3	2 2.2	6.8 7.4	7.8	9.8	8.1	10.6
3^{OP}	Exp.	0.2	2	7	7.2	7.7	7.7	–
		1.1	2.3					
	DFT ^C	0.2 1.1	1.8 2.1	7.2	7.3	7.6	7.6	–

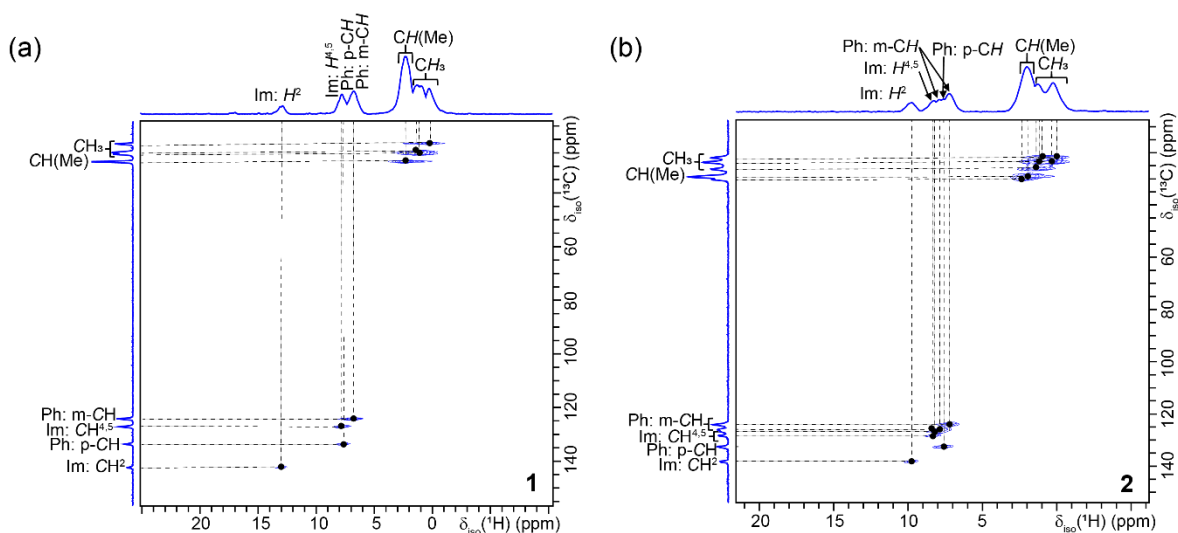


Figure 2.3. 2D $^1\text{H}\{^{13}\text{C}\}$ DCP HETCOR NMR spectra of (a) **1** and (b) pure **2** acquired at $B_0 = 18.8$ T with $\nu_R = 60$ kHz.

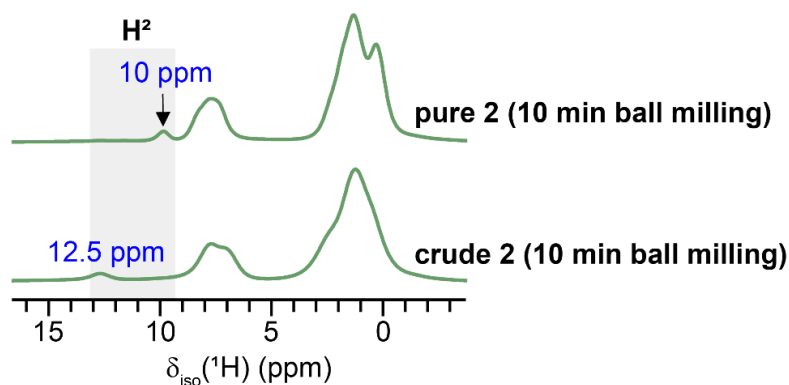


Figure 2.4. 1D ^1H MAS NMR spectra of crude and pure **2** prepared by ball milling IPr·HCl (1 eq.) in the presence of CuCl (1 eq.) for 10 min. The 1D ^1H MAS NMR spectra are acquired at $B_0 = 18.8$ T with $\nu_R = 60$ kHz. The shaded area denotes the region where the $^1\text{H}^2$ signal resonates.

2.2.1.3 ^{13}C ssNMR spectroscopy

To confirm these observations, we also acquired $^1\text{H} \rightarrow ^{13}\text{C}$ CP-MAS spectra of the same samples (**Figure 2.5**). These spectra were assigned (see **Figure 2.6a**) based on ^{13}C isotropic chemical shifts measured in solution,^{32,33} 2D $^1\text{H}\{^{13}\text{C}\}$ DCP HETCOR spectra (see **Figure 2.3**),^{34,35} and DFT calculations of ^{13}C isotropic chemical shifts for periodic crystal structures and isolated molecules (see **Figure 2.6b** and **Table 2.2**). The 2D $^1\text{H}\{^{13}\text{C}\}$ DCP HETCOR spectra were acquired at a high magnetic field ($B_0 = 18.8$ T) and high MAS frequency ($\nu_R = 60$ kHz) to improve the resolution of ^1H dimension and using short contact times for the CP transfers in order to probe selectively the proximities between covalently bonded ^1H and ^{13}C nuclei. In particular, the observation in these 2D spectra of a cross peak between ^1H and ^{13}C signals at 12.5 and 143 ppm for compound **1** and at 10 and 138 ppm for pure compound **2** confirms that these ^{13}C signals are assigned to C^2 atoms. These 2D spectra also facilitate the assignment of ^1H and ^{13}C signals of aromatic and $\text{CH}^{4,5}$ sites. **Figure 2.6b** also shows the good agreement between the experimental and DFT-calculated isotropic chemical shift values for **1** and pure compounds **2** and **3^{OP}**.

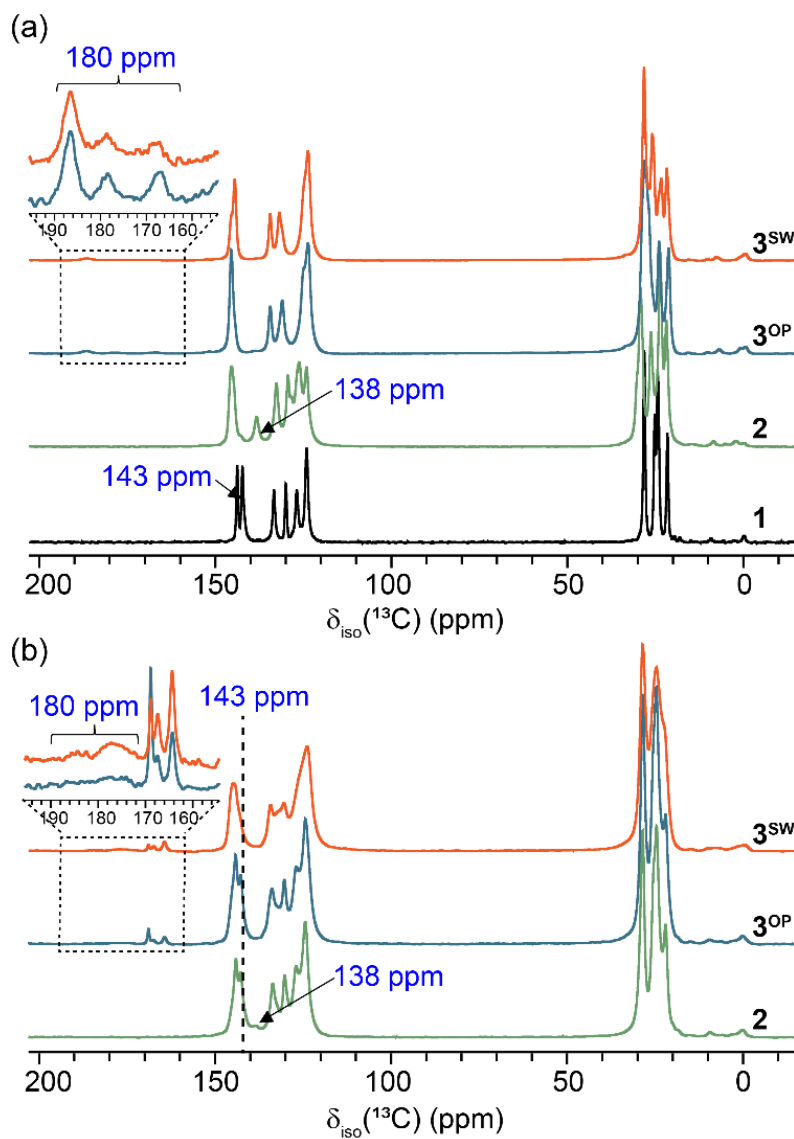


Figure 2.5. $1D\ ^1H \rightarrow\ ^{13}C$ CP-MAS NMR spectra of (a) pure and (b) crude **2** (green), **3^{OP}** (blue), and **3^{SW}** (orange) samples acquired at $B_0 = 9.4$ T with $\nu_R = 12.5$ kHz. The spectrum of compound **1** is also shown in black in panel (a) for the sake of comparison. The multiplet assigned to the $^{13}C^2$ site for samples **3^{OP}** and **3^{SW}** is shown as an inset in panels (a) and (b). The isotropic chemical shifts of the $^{13}C^2$ nucleus are indicated on the spectra. Furthermore, the vertical dashed line in panel (b) denotes the isotropic chemical shift of the $^{13}C^2$ nucleus in compound **1**.

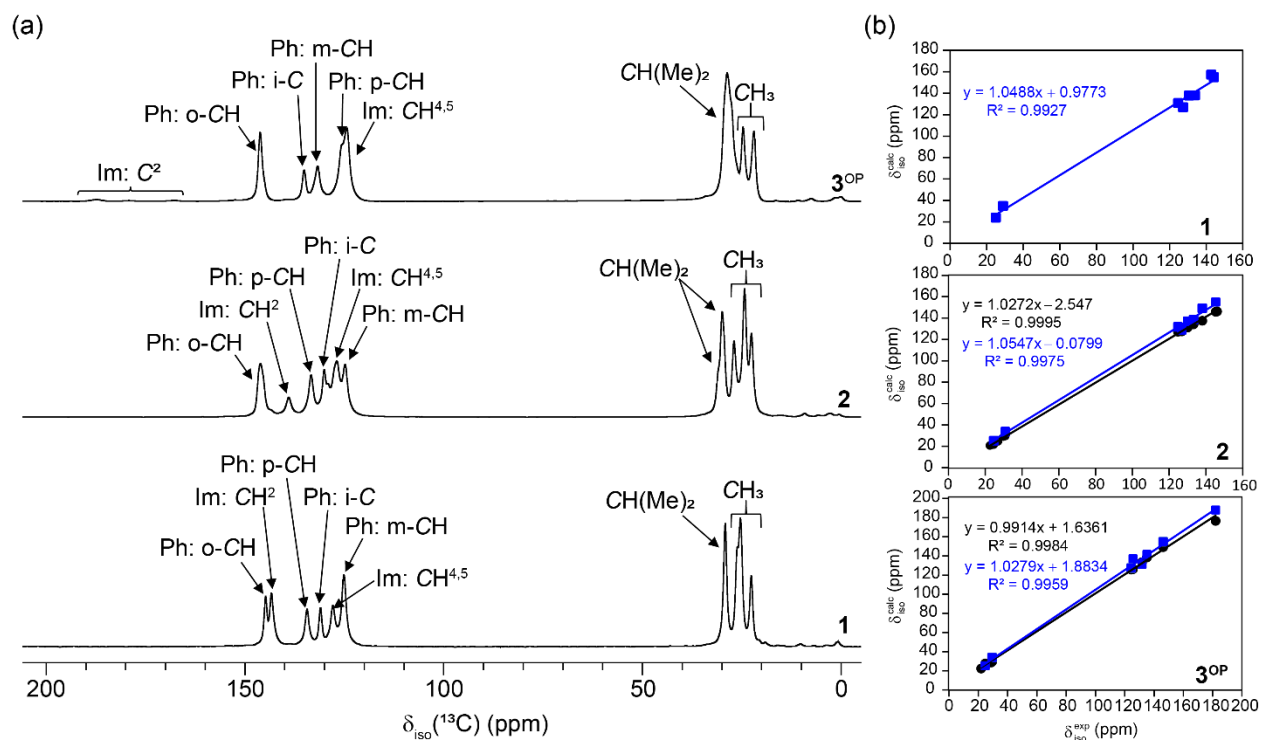


Figure 2.6. (a) 1D $^1\text{H} \rightarrow ^{13}\text{C}$ CP-MAS NMR spectra of **1** and pure **2** and **3^{OP}** acquired at $B_0 = 9.4$ T with $\nu_R = 12.5$ kHz, along with the assignment of the ^{13}C signals. The spectral assignment is based on ^{13}C isotropic chemical shifts measured in solution^{32,33} as well as 2D $^1\text{H}\{^{13}\text{C}\}$ DCP HETCOR NMR spectra and DFT calculations of the isotropic chemical shifts. (b) Correlation between $\delta_{\text{iso}}^{\text{exp}}$ and $\delta_{\text{iso}}^{\text{calc}}$ for the ^{13}C sites of **1** and pure **2** and **3^{OP}** crystals (blue squares) and isolated molecules (black circles). The $\delta_{\text{iso}}^{\text{exp}}$ values were measured from the 1D $^1\text{H} \rightarrow ^{13}\text{C}$ CP-MAS spectra of **1** and pure **2** and **3^{OP}** shown in panel (a).

The 1D $^1\text{H} \rightarrow ^{13}\text{C}$ CP-MAS NMR spectra of pure compounds **3^{OP}** and **3^{SW}** exhibit a multiplet around 180 ppm assigned to $^{13}\text{C}^2$ nuclei in $[\text{Cu}(\text{Cl})(\text{IPr})]$. This multiplet arises from J -coupling and second-order quadrupolar-dipolar cross-terms with $^{63,65}\text{Cu}$ isotopes with spin $I = 3/2$.³⁶ This interpretation is confirmed by smaller splitting at a higher magnetic field, as seen in **Figure 2.7**, since the second-order quadrupolar-dipolar cross-terms are inversely proportional to the B_0 field strength. Assuming that the shortest C-Cu distance is equal to that measured by X-ray diffraction,

1.953 Å,³⁷ the ^{13}C - $^{63,65}\text{Cu}$ dipolar coupling constants are equal to $b(^{13}\text{C}\text{-}^{63}\text{Cu})/(2\pi) = 0.93b(^{13}\text{C}\text{-}^{65}\text{Cu})/(2\pi) = 1.078$ kHz since the ratio of $^{63,65}\text{Cu}$ gyromagnetic ratios is $\gamma(^{63}\text{Cu})/\gamma(^{65}\text{Cu}) = 0.93$. Using these dipolar coupling constants, these spectra can be simulated with $\delta_{\text{iso}} = 180$ ppm, the isotropic value of the indirect ^{13}C - $^{63,65}\text{Cu}$ coupling tensor, $^1J_{\text{iso}}(^{13}\text{C}\text{-}^{63}\text{Cu}) = 0.93 ^1J_{\text{iso}}(^{13}\text{C}\text{-}^{65}\text{Cu}) = 682 \pm 8$ Hz, its anisotropy, $\Delta^1J(^{13}\text{C}\text{-}^{63}\text{Cu}) = 0.93 \Delta^1J(^{13}\text{C}\text{-}^{65}\text{Cu}) = -160 \pm 260$ Hz and quadrupolar coupling constants, $C_Q(^{63}\text{Cu}) = 1.08 C_Q(^{65}\text{Cu}) = 80 \pm 5$ MHz since the ratio of electric quadrupolar moments of $^{63,65}\text{Cu}$ isotopes is $Q(^{63}\text{Cu})/Q(^{65}\text{Cu}) = 1.08$. These parameters are close to those recently measured for $[\text{Cu}(\text{Cl})(\text{NHC})]$ complex, in which the NHC ligand was *N,N*-bis-[2,4,6-trimethylphenyl]imidazol-2-ylidene.³⁸ The best-fit $C_Q(^{63}\text{Cu})$ value agrees well with that calculated using DFT from the periodic crystal structure of $[\text{Cu}(\text{Cl})(\text{IPr})]$ (67 MHz). Its large value stems from a large electric field gradient owing to the highly asymmetric environment of the Cu atom in this compound. The measured $^1J_{\text{iso}}(^{13}\text{C}\text{-}^{63}\text{Cu})$ coupling constant agrees with that calculated using DFT for the isolated $[\text{Cu}(\text{Cl})(\text{IPr})]$ complex (660 Hz).

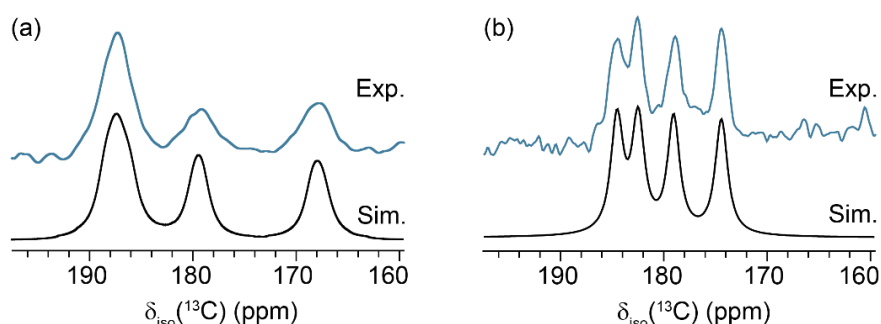


Figure 2.7. 1D $^1\text{H} \rightarrow ^{13}\text{C}$ CP-MAS spectra of pure **3OP** at the $^{13}\text{C}^2$ central line recorded at magnetic fields of (a) 9.4 T (MAS rate, $\nu_R = 12$ kHz) and (b) 18.8 T (MAS rate, $\nu_R = 18$ kHz): experimental (blue) and simulated (black).

As seen in **Figure 2.5b**, the 1D $^1\text{H} \rightarrow ^{13}\text{C}$ CP-MAS spectrum of crude **2** sample exhibits a peak at 138 ppm showing the formation of $[\text{CuCl}_2][\text{IPr}\cdot\text{H}]$ cuprate in the solid-state during the ball milling in agreement with ^1H NMR spectrum. The $^1\text{H} \rightarrow ^{13}\text{C}$ CP-MAS spectra of crude **3OP^{SW}** samples do not exhibit a signal at 138 ppm but a broad signal near 180 ppm. Furthermore, no cross peak between ^1H and ^{13}C signals at 10 and 138 ppm, respectively, is detected in their 2D $^1\text{H}\{^{13}\text{C}\}$ DCP HETCOR spectra shown in **Figure 2.8b** and **c**. This observation shows that during ball milling, the $[\text{Cu}(\text{Cl})(\text{IPr})]$ complex is formed in the solid-state, whereas the cuprate is completely transformed into this complex. The 1D $^1\text{H} \rightarrow ^{13}\text{C}$ CP-MAS spectra of crude **2** and **3OP^{SW}** samples also exhibit an additional signal at 143 ppm indicating the presence of unreacted $\text{IPr}\cdot\text{HCl}$.

Moreover, the signals at 162 and 169 ppm detected in the ^{13}C spectra of crude **3**^{OP/SW} indicate the presence of KHCO_3 and K_2CO_3 , respectively.³¹ The spectra of crude samples exhibit broader signals than those of pure samples owing to the disorder created by ball milling. This broadening is especially large for the C^2 multiplet of $[\text{Cu}(\text{Cl})(\text{IPr})]$ complex since the disorder results in a distribution of $C_Q(^{63,65}\text{Cu})$ values, and hence, splitting due to second-order quadrupolar-dipolar cross-terms.

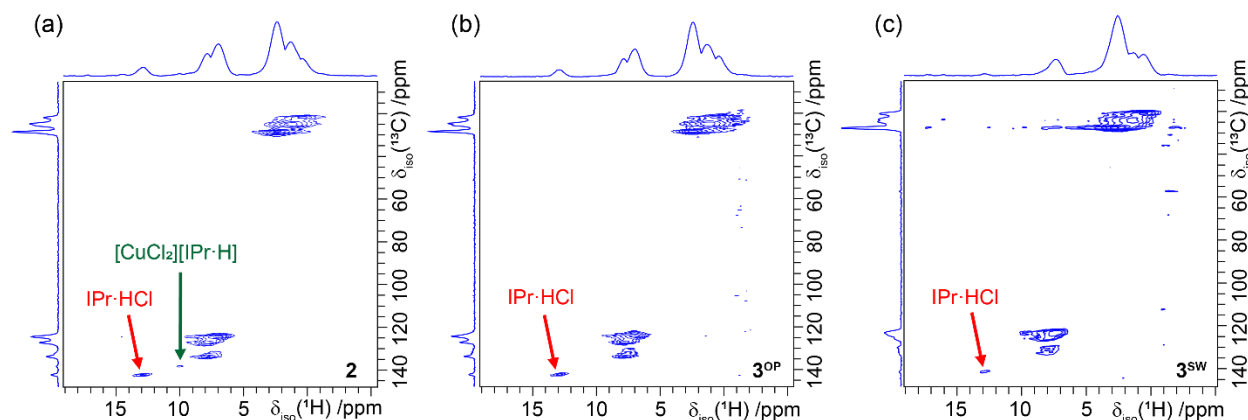


Figure 2.8. 2D $^1\text{H}\{^{13}\text{C}\}$ DCP HETCOR spectra of crude (a) **2**, (b) **3**^{OP}, and (c) **3**^{SW} acquired at $B_0 = 18.8$ T with $\nu_R = 60$ kHz. The cross peak ascribed to the $^{13}\text{C}^2$ site in IPr-HCl and $[\text{CuCl}_2][\text{IPr-H}]$ compounds are denoted by red and green arrows, respectively.

2.2.1.4 ^{15}N ssNMR spectroscopy

Next the 1D $^1\text{H} \rightarrow ^{15}\text{N}$ CP-MAS spectra of these samples were recorded. The spectra of the pure compounds are shown in **Figure 2.9**. The ^{15}N signals were assigned with the help of DFT calculations of $\delta_{\text{iso}}(^{15}\text{N})$ for isolated molecules and periodic crystal structures (**Table 2.3**). Only $[\text{CuCl}_2][\text{IPr-H}]$ cuprate exhibits two distinct ^{15}N signals.

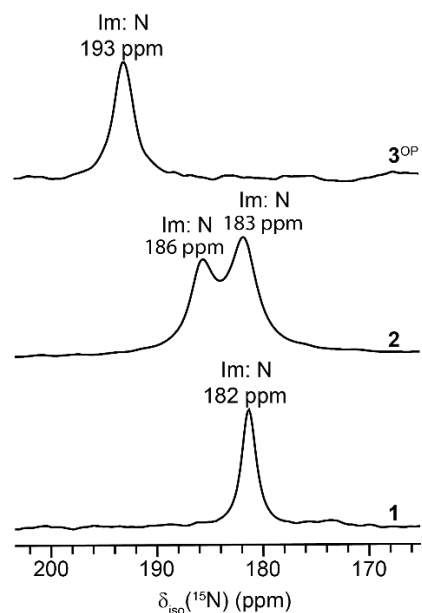


Figure 2.9. 1D $^1\text{H} \rightarrow ^{15}\text{N}$ CP-MAS NMR spectra of **1** and pure **2** and **3^{OP}** acquired at $B_0 = 9.4$ T with $\nu_R = 8$ kHz, along with the assignment of the ^{15}N signals.

Table 2.3. Experimental and computed $\delta_{\text{iso}}(^{15}\text{N})$ shifts in ppm for the crystals (DFT^C) and isolated molecules (DFT^I) of **1** and pure **2** and **3^{OP}**.

Sample		Exp.	DFT ^C	DFT ^I
1		182	–	185
2	Site 1	183	184	183
	Site 2	186	186	186
3^{OP}		193	192	200

The ^{15}N spectrum of crude **2**, shown in **Figure 2.10c**, shows one peak that could not be satisfactorily fitted by a single resonance and requires three-line deconvolution to fully describe the lineshape. The two peaks at 183.0 and 185.0 ppm, represented by green-filled lines, are attributed to $[\text{CuCl}_2][\text{IPr}\cdot\text{H}]$ whereas the peak at 182.7 ppm is attributed to unreacted $\text{IPr}\cdot\text{HCl}$. This spectrum confirms the formation of the cuprate in the solid-state during ball milling. The ^{15}N spectra of crude **3^{OP}** and **3^{SW}** exhibit two signals (**Figure 2.10a** and **b**). The peak at 194 ppm can be deconvoluted into one component, corresponding to the final product, $[\text{Cu}(\text{Cl})(\text{IPr})]$, which confirms the formation of this complex in the solid-state during ball milling. The signal at lower chemical shift can be deconvoluted into one component corresponding to unreacted $\text{IPr}\cdot\text{HCl}$, with no signal corresponding to cuprate observed. This observation confirms that the cuprate is

converted into $[\text{Cu}(\text{Cl})(\text{IPr})]$ in the presence of the K_2CO_3 base. The relative amount of $[\text{Cu}(\text{Cl})(\text{IPr})]$ with respect to unreacted $\text{IPr}\cdot\text{HCl}$ is almost two-fold higher for $\mathbf{3}^{\text{SW}}$ than for $\mathbf{3}^{\text{OP}}$.

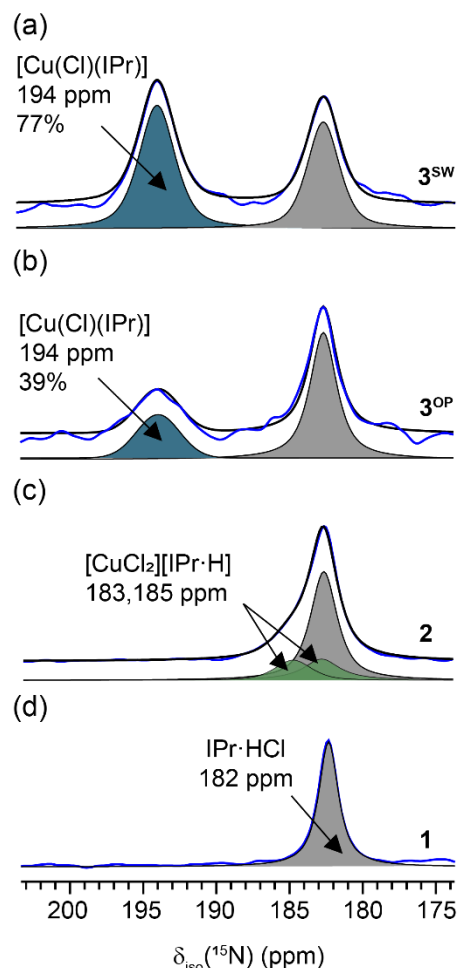


Figure 2.10. Experimental (blue) and simulated (black) 1D $^1\text{H} \rightarrow ^{15}\text{N}$ CP-MAS NMR spectra of crude (a) $\mathbf{3}^{\text{SW}}$, (b) $\mathbf{3}^{\text{OP}}$, and (c) $\mathbf{2}$ and (d) $\mathbf{1}$ acquired at $B_0 = 9.4$ T with $\nu_R = 8$ kHz. The simulated spectra are the sum of up to three components: the blue, green, and gray-filled peaks are ^{15}N components associated with $[\text{Cu}(\text{Cl})(\text{IPr})]$, $[\text{CuCl}_2][\text{IPr}\cdot\text{H}]$, and $\text{IPr}\cdot\text{HCl}$ compounds, respectively. The relative integrated intensity of $[\text{Cu}(\text{Cl})(\text{IPr})]$ signal is indicated in the figure for samples $\mathbf{3}^{\text{SW}}$ and $\mathbf{3}^{\text{OP}}$.

2.2.1.5 ^{63}Cu ssNMR spectroscopy

Copper possesses two naturally occurring NMR-active isotopes: ^{63}Cu and ^{65}Cu , with respective natural abundances of 69.17% and 30.82%. Both of these isotopes exhibit a spin quantum number of $I = 3/2$, which classifies them as quadrupolar nuclei. They are characterized

by nuclear quadrupole moments (eQ) with $Q = -22.0 \text{ fm}^2$ for ^{63}Cu and -20.4 fm^2 for ^{65}Cu , and gyromagnetic ratios (γ) of $7.112 \times 10^7 \text{ rad.s}^{-1}.\text{T}^{-1}$ and $7.604 \times 10^7 \text{ rad.s}^{-1}.\text{T}^{-1}$, respectively.³⁹ The study of copper isotopes in ssNMR spectroscopy is notably intricate due to the interplay between large quadrupolar interactions and CSA.^{40–45} This interplay can result in a CT powder pattern with a breadth on the order of MHz. Despite this complexity, it provides valuable insights into various parameters critical for comprehending the behavior of copper nuclei in various environments. These parameters include the magnitude of the quadrupolar interaction, which is quantified by the quadrupolar coupling constant (C_Q) and its asymmetry (η_Q). Additionally, it includes parameters associated with CSA, such as the reduced anisotropy (δ_{aniso}), its asymmetry η_{CS} , and Euler angles ($\alpha_{\text{CS-Q}}$, $\beta_{\text{CS-Q}}$, $\gamma_{\text{CS-Q}}$) describing the relative orientation of CSA and EFG tensors. To address the challenges associated with ultra-wideline (UW) spectra and to enhance sensitivity and improve resolution, we employed the QCPMG pulse sequence combined with the VOCS technique (VOCS-QCPMG) under static conditions.^{46,47}

In this study, we selected the ^{63}Cu isotope owing to its higher natural abundance. 1D ^{63}Cu QCPMG NMR experiments for both pure and crude forms of **2** and **3**^{OP/SW} at magnetic field strengths of $B_0 = 18.8 \text{ T}$ and 28.2 T were conducted. We also employed a single-pulse sequence, with a spinning speed of $\nu_R = 10 \text{ kHz}$, to detect the signal around 0 ppm associated with CuCl.

The 1D VOCS-QCPMG ^{63}Cu NMR spectrum of the pure sample **2**, depicted in **Figure 2.11d**, exhibits a CT powder pattern with a linewidth of 2.5 MHz at $B_0 = 18.8 \text{ T}$. This pattern necessitates the acquisition of 7 sub-spectra, resulting in a total experimental time of 7 h. Similarly, the pure samples of **3**^{OP} and **3**^{SW} exhibit broader CT linewidth, approximately equal to 4.2 MHz at 18.8 T (**Figure 2.11e** and **f**). This broader pattern requires the acquisition of 11 sub-spectra for each sample, leading to a total experimental time of 15 h. The resulting ^{63}Cu NMR spectra were simulated using the “QUadrupolar Exact SofTware” (QUEST) program,⁴⁸ providing detailed ^{63}Cu NMR parameters, as outlined in **Table 2.4**. Notably, the experimental $C_Q(^{63}\text{Cu})$ values are measured to be 59.5 MHz for $[\text{CuCl}_2][\text{IPr}\cdot\text{H}]$ and 77.4 MHz for $[\text{Cu}(\text{Cl})(\text{IPr})]$. It is noteworthy that these $C_Q(^{63}\text{Cu})$ values rank among the largest observed for ^{63}Cu ssNMR, and they are comparable to those reported for Cu(I) atoms with linear local environment.^{40,41,43} Additionally, the $C_Q(^{63}\text{Cu})$ value of $[\text{Cu}(\text{Cl})(\text{IPr})]$ aligns well with the value obtained from the simulation of $^{13}\text{C}^2$ multiplet of $[\text{Cu}(\text{Cl})(\text{IPr})]$ complex ($80 \pm 5 \text{ MHz}$), as previously described. Moreover, the utilization of high magnetic field strengths facilitates the determination of the CSA parameters, as the effect of CSA scales proportionally with the strength of the magnetic field. We measured large δ_{aniso}

values of -1235 ppm for $[\text{CuCl}_2][\text{IPr}\cdot\text{H}]$ and -1060 ppm for $[\text{Cu}(\text{Cl})(\text{IPr})]$, falling well within the typical chemical shift range exhibited by copper compounds, approximately -790 and -975 ppm.⁴²

To assess the accuracy and reliability of these parameters, 1D ^{63}Cu VOCS-QCPMG spectra were also acquired at a higher magnetic field strength of $B_0 = 28.2$ T, as illustrated in **Figure 2.11a**, **b**, and **c**. As the second-order quadrupolar broadening is inversely proportional to the B_0 field strength, the linewidths are reduced by a factor of $28.2/18.8 = 1.5$ at $B_0 = 28.2$ T with respect to $B_0 = 18.8$ T. These spectra, measured at 18.8 and 28.2 T, were simultaneously simulated to determine the ^{63}Cu NMR parameters. These parameters exhibit good agreement with values calculated for the crystals using DFT, as detailed in **Table 2.4**.

It is noteworthy that the pure samples do not exhibit a ^{63}Cu signal near 0 ppm, indicating the absence of CuCl in those samples.

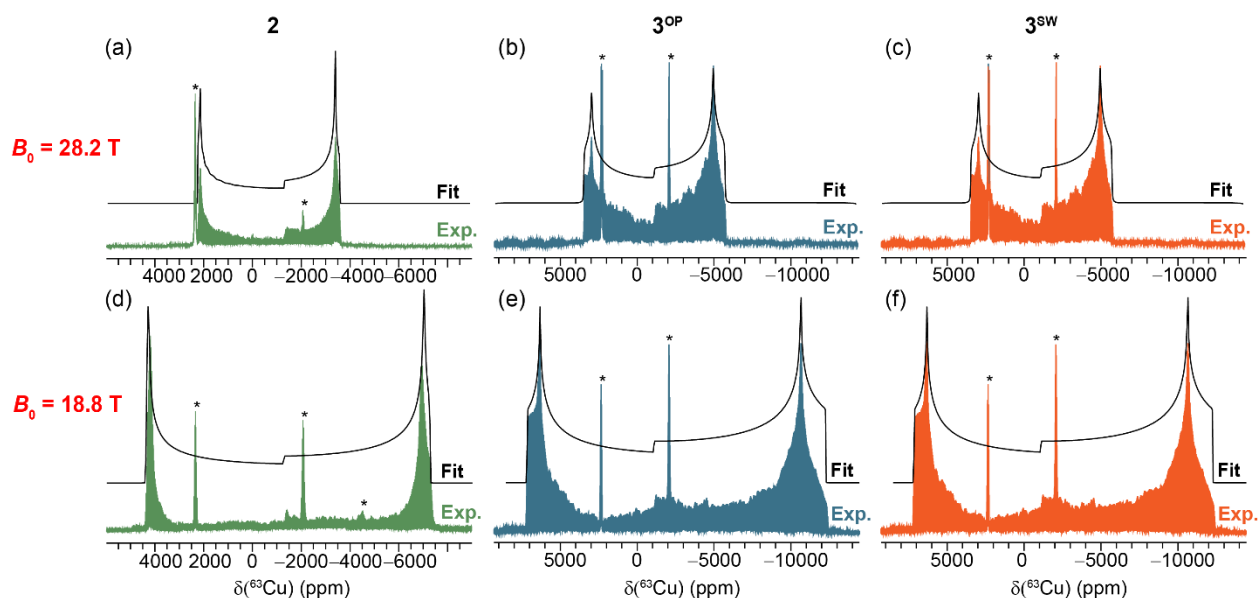


Figure 2.11. Experimental and simulated (black) static 1D ^{63}Cu VOCS-QCPMG NMR spectra of pure (a, d) **2** (green), (b, e) **3^{OP}** (blue), and (c, f) **3^{SW}** (orange) acquired at room temperature and two magnetic field strengths: (a, b, c) $B_0 = 28.2$ T and (d, e, f) $B_0 = 18.8$ T. These spectra are generated by performing a Fourier transform of the sum of QCPMG echoes. The asterisk symbol (*) indicates the NMR signals from copper parts inside the probe including the sample coil (see **Figure 2.13**).

Table 2.4. Experimental and DFT calculated ^{63}Cu NMR parameters for pure forms of **2**, **3^{OP}**, and **3^{SW}** samples.

Samples		$\delta_{\text{iso}}(^{63}\text{Cu})$ /ppm	$C_Q(^{63}\text{Cu})$ /MHz	$\eta_Q(^{63}\text{Cu})$	$\delta_{\text{aniso}}(^{63}\text{Cu})$ /ppm	$\eta_{\text{CS}}(^{63}\text{Cu})$	$(\alpha_{\text{CS-Q}}, \beta_{\text{CS-Q}}, \gamma_{\text{CS-Q}})$
Pure 2	Exp	−80	59.5	0.03	−1235	0.07	(90,1,50)
	DFT	−144	45.2	0.08	−1488	0.07	–
Pure 3^{OP}	Exp	−60	77.4	0.07	−1060	0.24	(0, 0, 0)
	DFT	16	67.3	0.22	−406	0.24	–
Pure 3^{SW}	Exp	−60	77.4	0.07	−1060	0.24	(0, 0, 0)
	DFT	16	67.3	0.22	−406	0.24	–

Our investigation further extended to the crude samples, where the ^{63}Cu NMR spectra in **Figure 2.12** provided valuable insights into the composition of these samples. To expedite the analysis, only two sub-spectra were acquired for each of the crude samples for the sake of time. In **Figure 2.12a**, the 1D ^{63}Cu QCPMG NMR spectrum of crude **2** exhibits two distinct singularities, corresponding to the $[\text{CuCl}_2][\text{IPr}\cdot\text{H}]$ compound. Furthermore, the ^{63}Cu NMR spectra of the crude **3^{OP}** and **3^{SW}** samples display two singularities assigned to $[\text{Cu}(\text{Cl})(\text{IPr})]$. These observations further confirm the synthesis of both $[\text{CuCl}_2][\text{IPr}\cdot\text{H}]$ and $[\text{CuCl}_2][\text{IPr}\cdot\text{H}]$ compounds in the solid-state during the ball milling process. Moreover, an additional signal at 0 ppm is detected in the crude samples, as shown in **Figure 2.12b**, indicating the presence of unreacted CuCl in the crude reaction mixtures.

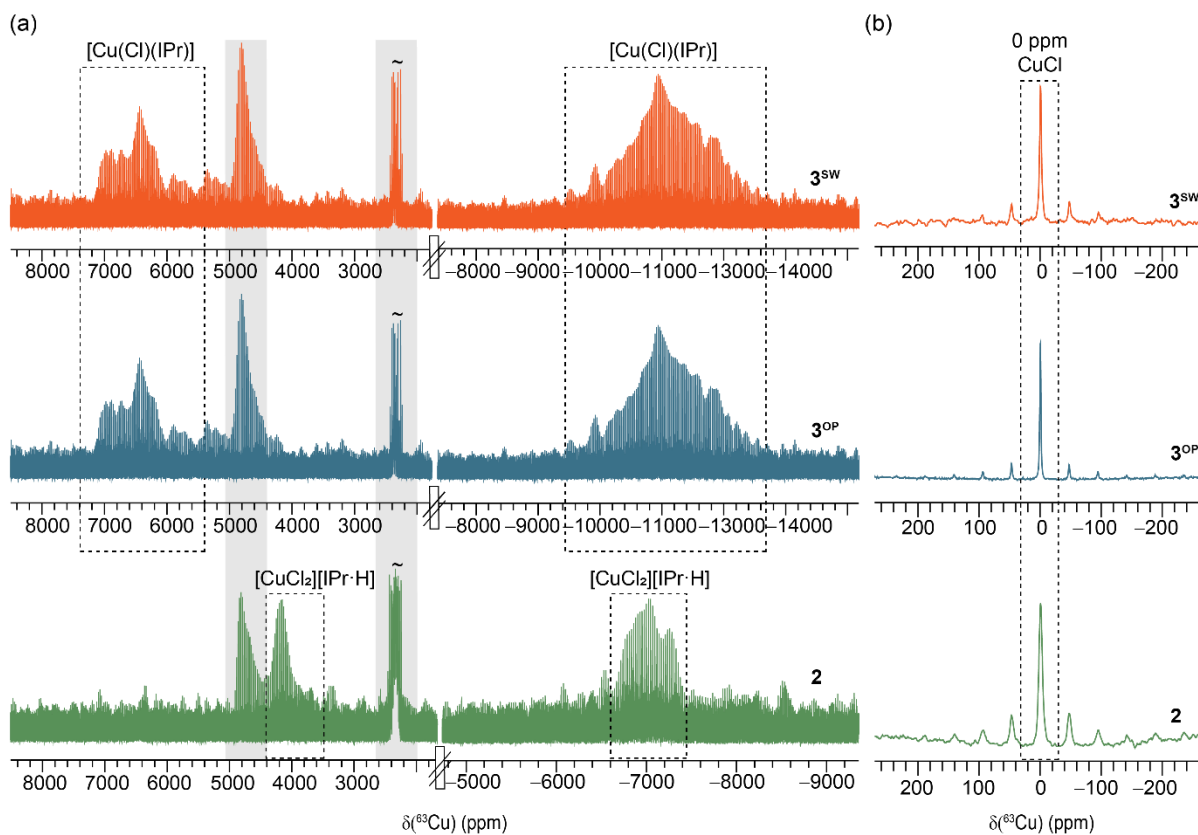


Figure 2.12. (a) Static 1D VOCS-QCPMG and (b) MAS ^{63}Cu NMR spectra of crude **2**, **3^{OP}**, and **3^{SW}** acquired at $B_0 = 18.8$ T and $T = 298$ K. The spectra in panel (a) are reconstructed by the co-addition of two sub-spectra and are the Fourier transform of the sum of QCPMG echoes. The gray-shaded regions denote the ^{63}Cu signals from the probe (see **Figure 2.13**). The spectra in panel (b) are acquired with $\nu_{\text{R}} = 10$ kHz.

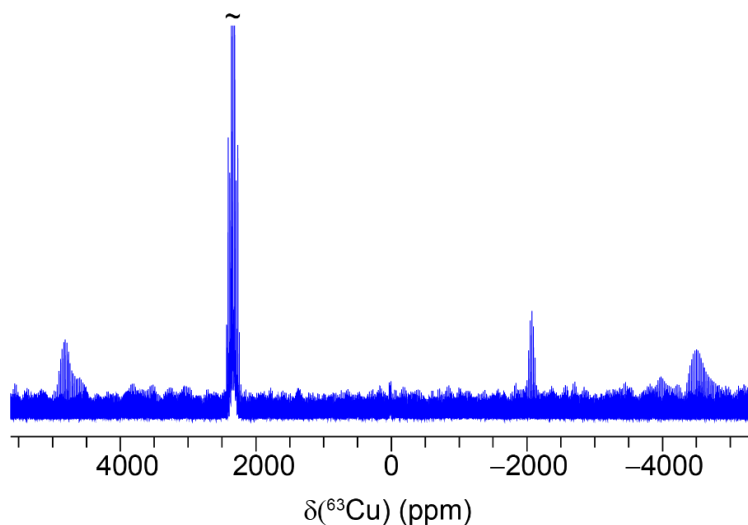


Figure 2.13. Background ^{63}Cu NMR signals from the 4 mm double-resonance HX probe acquired at $B_0 = 18.8$ T. The spectrum is reconstructed by the co-addition of three individual pieces acquired using the QCPMG pulse sequence.

2.2.1.6 ^{35}Cl ssNMR spectroscopy

Chlorine possesses two NMR-active isotopes: ^{35}Cl and ^{37}Cl . These isotopes are quadrupolar nuclei with a spin quantum number of $I = 3/2$. Their relative abundances in nature are 75.78% and 24.22%, respectively. However, their gyromagnetic ratios, $\gamma = 2.624 \times 10^7 \text{ rad.s}^{-1}.\text{T}^{-1}$ for ^{35}Cl and $2.184 \times 10^7 \text{ rad.s}^{-1}.\text{T}^{-1}$ for ^{37}Cl , are lower than those of nitrogen-15 and these isotopes are considered as low- γ nuclei. Additionally, these isotopes exhibit relatively moderate electric quadrupole moments with $Q = -8.16$ and -6.43 fm^2 , respectively.³⁹ Given its higher natural abundance and higher sensitivity, the ^{35}Cl isotope is the preferred choice for NMR investigations.

The 1D WURST-QCPMG ^{35}Cl NMR spectra of **1** and pure **2** and **3**^{OP/SW} are presented in **Figure 2.14**, along with their spectral simulations.⁴⁹ These simulations were carried out using the QUEST program, resulting in the determination of ^{35}Cl NMR parameters presented in **Table 2.5**. To enhance the accuracy of these parameters, the spectra were acquired at two magnetic field strengths ($B_0 = 18.8$ and 28.2 T).

The ^{35}Cl spectra and the best-fit NMR parameters exhibit noticeable differences among the three compounds. The 1D ^{35}Cl ssNMR spectrum of compound **1** shows a single resonance with $\delta_{\text{iso}}(^{35}\text{Cl}) = 50 \text{ ppm}$ and $C_Q(^{35}\text{Cl}) = 3.5 \text{ MHz}$. These NMR parameters are consistent with those previously documented for HCl salts.^{50–53} The ^{35}Cl NMR spectrum of pure **2** was simulated with

two ^{35}Cl sites resonating at $\delta_{\text{iso}}(^{35}\text{Cl}) = -90$ ppm and $\delta_{\text{iso}}(^{35}\text{Cl}) = -110$ ppm. Their $C_Q(^{35}\text{Cl})$ values are in good agreement with those calculated using DFT for the crystal structure. The pure **3^{OP}** and **3^{SW}** samples display similar spectra showing a single ^{35}Cl site with NMR parameters consistent with those reported for terminal Cl sites in group IV transition metal organometallic complexes.⁵⁴ Furthermore, these parameters were validated further by recording the ^{35}Cl spectra at $B_0 = 28.2$ T, taking advantage of the enhanced resolution and sensitivity provided by a higher magnetic field.

The ^{35}Cl NMR spectra of the crude compounds are dominated by a signal with $\delta(^{35}\text{Cl}) = -127$ ppm and $C_Q(^{35}\text{Cl}) = 0.31$ MHz assigned to CuCl. This signal confirms the presence of unreacted CuCl in the crude compounds, in agreement with the ^{63}Cu NMR spectra. Nevertheless, this CuCl signal masks the signal of other species. Hence, ^{35}Cl NMR does not allow probing the formation of cuprate and $[\text{Cu}(\text{Cl})(\text{IPr})]$ complex in the solid-state.

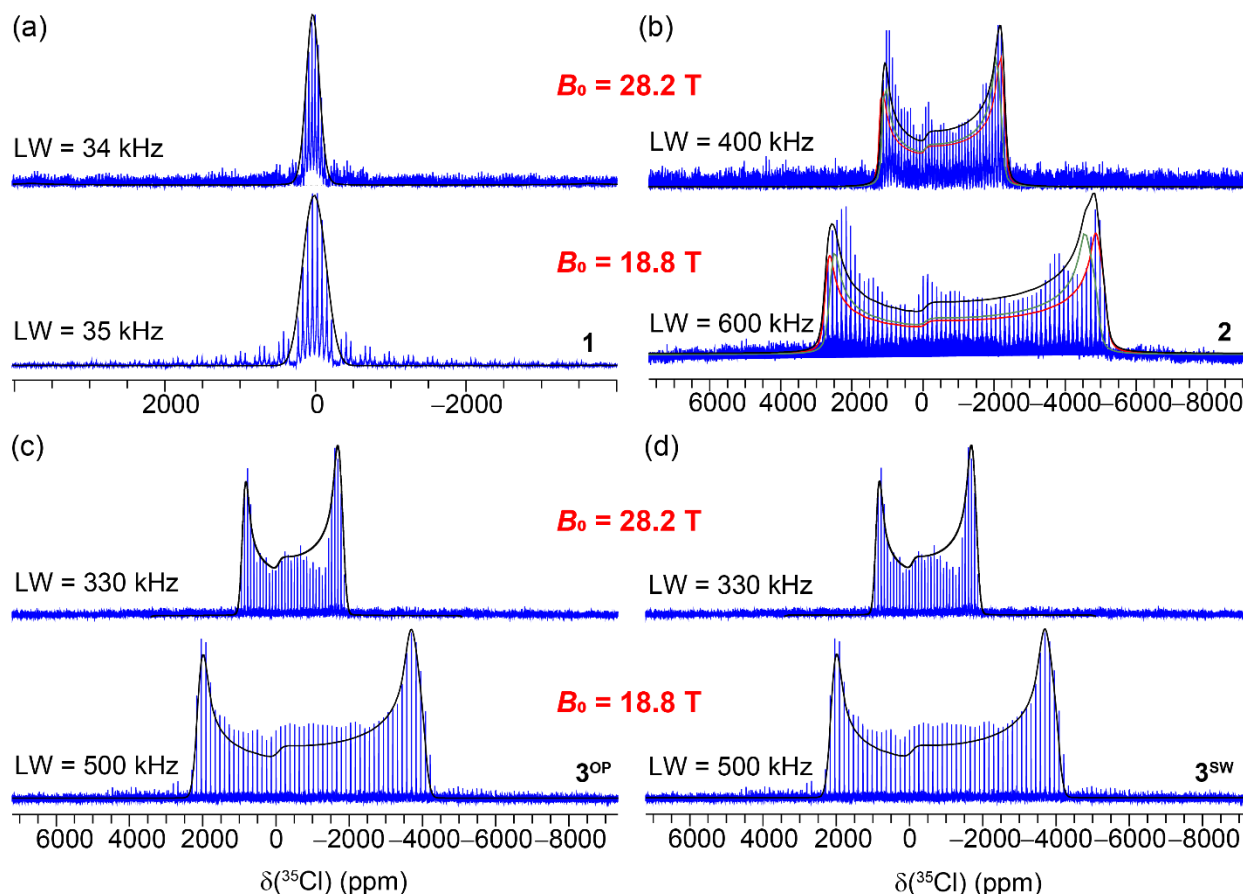


Figure 2.14. Experimental (blue) and simulated (black) 1D WURST-QCPMG ^{35}Cl NMR spectra of (a) **1** and pure (b) **2**, (c) **3^{OP}**, and (d) **3^{SW}** acquired at two magnetic field strengths, $B_0 = 18.8$ T (bottom) and 28.2 T (top), under static conditions at $T = 298$ K. Line width (LW) information is

included. These spectra are generated by performing a Fourier transform of the sum of QCMPPG echoes. VOCS technique was employed to record the ^{35}Cl NMR spectra of pure **2**, **3^{OP}**, and **3^{SW}** at $B_0 = 18.8$ T (see acquisition details in **Table 2.7**).

Table 2.5. ^{35}Cl NMR parameters of **1** and pure **2**, **3^{OP}**, and **3^{SW}** determined by the simulation of the 1D ^{35}Cl NMR spectra of **Figure 2.14** and calculated for the periodic crystal structures using DFT (DFT^C).

Sample			$\delta(^{35}\text{Cl})$ /ppm	$C_Q(^{35}\text{Cl})$ /MHz	$\eta_Q(^{35}\text{Cl})$
1	Exp.		50	3.5	0.50
	DFT ^C		–	–	–
Pure 2	Exp.	Site 1	–90	19.1	0.03
		Site 2	–110	18.6	0.04
	DFT ^C	Site 1	–40	–22.6	0.14
		Site 2	–60	–20.5	0.20
Pure 3^{OP}	Exp.		–80	16.8	0.05
	DFT ^C		–55	–19.3	0.11
Pure 3^{SW}	Exp.		–80	16.8	0.05
	DFT ^C		–55	–19.3	0.11

2.2.2 Experimental Details

2.2.2.1 Samples preparation

All mechanochemical experiments were conducted using a Fritsch Pulverisette 5/4 planetary ball mill. *N,N'*-bis-[2,6-(di-iso-propyl)phenyl]imidazolium chloride (IPr-HCl) was synthesized according to a literature procedure,⁵⁵ while CuCl and K₂CO₃ were purchased from TCI and Carl-Roth, respectively, and used as received.

2.2.2.1.1 Ball milling

Two-Steps One-pot Synthesis: A 12 mL zirconia reactor equipped with 18 balls of the same material (7.52 g, $\varnothing = 5$ mm) was charged in the air with IPr-HCl (150.0 mg, 0.35 mmol) and CuCl (34.9 mg, 0.35 mmol). The mixture of the two reactants was first ground for 30 min at 400 rpm before the addition of K_2CO_3 (146.3 mg, 1.06 mmol). After the addition of the base, the resulting mixture of solids was further ground in 3 repetitions of 30 min at 400 rpm.

One-Step One-Pot Synthesis: A 12 mL zirconia reactor equipped with 18 balls of the same material (7.52 g, $\varnothing = 5$ mm) was charged in the air with IPr-HCl (150.0 mg, 0.35 mmol), CuCl (34.9 mg, 0.35 mmol), and K_2CO_3 (146.3 mg, 1.06 mmol). The mixture of solids was then ground in 3 repetitions of 30 min at 400 rpm.

2.2.2.1.2 Workup

Solvent-Free: At the end of the milling process the content of the reactor was manually extracted with the aid of a spatula, transferred in a vial, and analyzed without any further manipulations.

Solvent-Based: At the end of the milling process, the content of the reactor was extracted with CH_2Cl_2 (3×4 mL), and the resulting solution was filtered over SiO_2 . The SiO_2 pad was rinsed with additional CH_2Cl_2 (3×2 mL) and the filtrate was subsequently concentrated by rotatory evaporation to about $\frac{1}{4}$ of its original volume. To this solution, an excess of *n*-pentane (10 mL) was added and the resulting solution was sonicated for a few minutes to induce the precipitation of the desired product. The solids formed were then collected by vacuum filtration, washed with additional *n*-pentane, and then dried under a high vacuum for several hours.

2.2.2.2 ssNMR spectroscopy

2.2.2.2.1 ssNMR experiments at $B_0 = 9.4$ T

We recorded 1D $^1H \rightarrow ^{13}C$ and $^1H \rightarrow ^{15}N$ CP-MAS NMR experiments at room temperature on a widebore Bruker AVANCE NEO NMR spectrometer at $B_0 = 9.4$ T, i.e., Larmor frequencies of 400.1 MHz for 1H , 100.6 MHz for ^{13}C , and 40.5 MHz for ^{15}N . Powdered samples were packed into 4 mm outer diameter zirconia rotors with Kel-F drive caps and spun at a MAS rate, $\nu_R = 12.5$ kHz in ^{13}C MAS experiments, whereas, for ^{15}N MAS experiments, the samples were spun at $\nu_R = 8$ kHz.

The 1D $^1\text{H} \rightarrow ^{13}\text{C}$ CP-MAS NMR spectra, except that shown in **Figure 2.7b**, were acquired using a Bruker 4 mm triple resonance (HXY) MAS probe operated in double resonance mode. The initial ^1H $\pi/2$ pulse lasted 2.2 μs and employed a nutation frequency $\nu_1 = 114$ kHz and was followed by a CP contact time of 1 ms. During the CP transfer, the nutation frequency on the ^{13}C channel was constant and equal to 55 kHz, while the ^1H nutation frequency was linearly ramped from 90 to 100. SPINAL-64 heteronuclear decoupling with nutation frequency, $\nu_1 = 102$ kHz, was applied on the ^1H channel during the acquisition period.⁵⁶ The 1D $^1\text{H} \rightarrow ^{13}\text{C}$ CP-MAS spectra were recorded using a recovery delay $\tau_{\text{RD}} = 1.3$ s and resulted from averaging 8192 transients, corresponding to a total experimental time of 3 h. The $^{13}\text{C}^2$ multiplet due to J -coupling and quadrupolar-dipolar cross terms with $^{63,65}\text{Cu}$ isotopes was simulated using WSolids1 software.⁵⁷

The 1D $^1\text{H} \rightarrow ^{15}\text{N}$ CP-MAS experiments were performed using a 4 mm double resonance (HX) low- γ MAS probe. The ^1H $\pi/2$ pulse duration and the CP contact time were 3.3 μs ($\nu_1 = 75.8$ kHz) and 4 ms, respectively. During the CP transfer, the nutation frequency on the ^{15}N channel was constant and equal to 34 kHz, whilst, on the ^1H channel, it was linearly ramped from 100 to 50. Swept-frequency TPPM (SW_f -TPPM) heteronuclear decoupling of 49 kHz was employed during the acquisition period.⁵⁸ All 1D $^1\text{H} \rightarrow ^{15}\text{N}$ CP-MAS spectra were recorded with 10500 co-added transients using $\tau_{\text{RD}} = 2$ s, corresponding to a total experimental time of 6 h. The ^{15}N chemical shifts were referenced to liquid NH_3 using α -glycine (32.7 ppm) as a secondary reference. The $^1\text{H} \rightarrow ^{15}\text{N}$ CP-MAS spectra were simulated using the line shape analysis (SOLA) module within TopSpin software.

2.2.2.2 ssNMR experiments at $B_0 = 18.8$ T

The 1D ^1H MAS NMR spectra shown in **Figure 2.1** were recorded on a standard bore Bruker AVANCE NEO NMR spectrometer at $B_0 = 18.8$ T, i.e. a ^1H Larmor frequency of 800.1 MHz with $\nu_{\text{R}} = 60$ kHz using a 1.3 mm double resonance (HX) MAS probe and single-pulse sequence. The ^1H $\pi/2$ pulse lasted 1.13 μs and employed a nutation frequency $\nu_1 = 222$ kHz. The ^1H MAS NMR spectra resulted from the averaging of 64 transients with $\tau_{\text{RD}} = 1.3$ s.

The 1D ^{63}Cu and ^{35}Cl , and 2D $^1\text{H}\{^{13}\text{C}\}$ DCP HETCOR experiments were recorded on a standard bore Bruker AVANCE NEO NMR spectrometer at $B_0 = 18.8$ T, i.e., Larmor frequencies of 212.2 MHz for ^{63}Cu , 201.2 MHz for ^{13}C , and 78.4 MHz for ^{35}Cl . All these spectra were acquired at room temperature. The 1D $^1\text{H} \rightarrow ^{13}\text{C}$ CP-MAS NMR spectrum of pure **3^{OP}** compound was also

acquired at $B_0 = 18.8$ T to check the influence of the static magnetic field on the splitting of $^{13}\text{C}^2$ multiplet due to quadrupolar-dipolar cross terms (see **Figure 2.7b**).

The 1D $^1\text{H} \rightarrow ^{13}\text{C}$ CP-MAS NMR spectrum of pure **3^{OP}** compound was acquired using a 1.3 mm double resonance (HX) MAS probe. The initial ^1H $\pi/2$ pulse lasted 2.25 μs with $\nu_1 = 111.1$ kHz and was followed by a CP contact time of 3 ms. During the CP transfer, the nutation frequency on the ^{13}C channel was constant and equal to 46 kHz, while the ^1H nutation frequency was linearly ramped from 100 to 50. SPINAL-64 heteronuclear decoupling with $\nu_1 = 130$ kHz was applied on the ^1H channel during the acquisition period. The 1D $^1\text{H} \rightarrow ^{13}\text{C}$ CP-MAS spectra were recorded using $T_{\text{RD}} = 1.2$ s and resulted from averaging 7632 transients, corresponding to a total experimental time of 2.5 h.

The 2D $^1\text{H}\{^{13}\text{C}\}$ DCP HETCOR experiments were recorded to correlate ^1H and ^{13}C isotropic chemical shifts.^{34,35} These spectra were acquired using a 1.3 mm double resonance (HX) MAS probe. Short CP contact times of 0.7 ms and 0.15 ms were used during the first and second CP transfers, respectively, to probe selectively the proximities between covalently bonded ^1H and ^{13}C nuclei. The nutation frequencies on the ^1H and ^{13}C channels during ^1H $\pi/2$ pulses and $^1\text{H} \rightarrow ^{13}\text{C}$ and $^{13}\text{C} \rightarrow ^1\text{H}$ CP transfers were the same as those used for the acquisition of the 1D $^1\text{H} \rightarrow ^{13}\text{C}$ CP-MAS NMR spectrum at $B_0 = 18.8$ T. After the $^1\text{H} \rightarrow ^{13}\text{C}$ CP transfer, the ^1H magnetization was destroyed by two saturation pulses lasting 2.25 μs with orthogonal phases and nutation frequencies set to 111 kHz. The 2D spectra were recorded with $\nu_R = 60$ kHz using non-uniform sampling (NUS) with an exponentially biased sampling keeping 40% of the points with respect to uniform sampling. The 2D spectra resulted from 20 transients for each of the 400 t_1 increments with $T_{\text{RD}} = 1.7$ s, corresponding to a total experimental time of 4 h.

The 1D ^{63}Cu and ^{35}Cl ssNMR spectra were recorded using a 4 mm HX probe designed and built by Peter L. Gor'kov from the National High Magnetic Field Laboratory (NHMFL). The powdered samples were packed in 4 mm outer diameter thin-walled zirconia rotors. The ^{63}Cu spectra were acquired under static conditions using the QCPMG pulse sequence.⁴⁶ The QCPMG pulses lasted 1.65 μs with $\nu_1 = 152$ kHz. The refocusing pulses were repeated with a cycle time of 200 μs and 56 echoes were acquired for each transient. SW_r-TPPM heteronuclear decoupling with $\nu_1 = 109$ kHz was applied during the acquisition. To diminish interference from copper metal within the probe head, a hole-burning pulse lasting 50 ms with $\nu_1 = 14$ kHz was applied before the QCPMG scheme. The 1D ^{63}Cu QCPMG spectra under static conditions of crude samples (shown in **Figure 2.12a**) were recorded using $T_{\text{RD}} = 1$ s and resulted from averaging 49056

transients, corresponding to a total experimental time of 13.6 h, for each sub-spectrum. It is worth noting that, to reduce experimental time, only two sub-spectra of each sample were recorded. The acquisition details of the 1D ^{63}Cu VOCS-QCPMG spectra of the pure samples recorded under static conditions (shown in **Figure 2.11**) are detailed in **Table 2.6**. The 1D ^{63}Cu VOCS-QCPMG spectrum showing the background signals from the probe in **Figure 2.13** was recorded using $T_{RD} = 1$ s and resulted from averaging 25,120 transients, corresponding to a total experimental time of 7 h, for each sub-spectrum. The narrow ^{63}Cu signal of CuCl at 0 ppm (**Figure 2.12b**) was acquired under MAS conditions with $\nu_R = 10$ kHz using a single pulse lasting 1 μs with $\nu_1 = 250$ kHz and resulted from averaging 64 transients.

The 1D ^{35}Cl spectra were acquired under static conditions using the WURST-QCPMG pulse sequence.^{59,60} The WURST pulse had a length of 25 μs with $\nu_1 = 39$ kHz and an offset sweep of 100 kHz. During the QCPMG acquisition, the WURST pulses were repeated with a cycle time of 100 μs , and 30 echoes were acquired for each transient. $\text{SW}_T\text{-TPPM}$ heteronuclear decoupling with $\nu_1 = 109$ kHz was applied during the acquisition. The acquisition parameters of the 1D ^{35}Cl WURST-QCPMG spectra under static conditions (shown in **Figure 2.14**) are listed in **Table 2.7**.

2.2.2.2.3 ssNMR experiments at $B_0 = 28.2$ T

To improve spectral resolution, 1D ^1H MAS NMR spectra of **1** and pure **2** and **3^{OP}** (shown in **Figure 2.2**) were also recorded on a standard bore Bruker AVANCE NEO NMR spectrometer at $B_0 = 28.2$ T i.e. a ^1H Larmor frequency of 1200.49 MHz with $\nu_R = 60$ kHz using a 1.3 mm double resonance (HX) MAS probe and DEPTH pulse sequence, for which the ^1H $\pi/2$ pulse lasted 1.48 μs and employed a nutation frequency $\nu_1 = 170$ kHz. The ^1H MAS NMR spectra resulted from the averaging of 64 transients with $T_{RD} = 1.3$ s.

For the accurate determination of the ^{63}Cu and ^{35}Cl NMR parameters, the 1D ^{63}Cu and ^{35}Cl ssNMR of **1** and pure **2** and **3^{OP}** were also recorded on a standard bore Bruker AVANCE NEO NMR spectrometer at $B_0 = 28.2$ T i.e. Larmor frequency of 318.33 MHz for ^{63}Cu and 117.63 MHz for ^{35}Cl . All these spectra were acquired at room temperature using a 3.2 mm double resonance (HX) MAS probe. The powdered samples were packed in 3.2 mm outer diameter thick-walled zirconia rotors.

The 1D ^{63}Cu spectra were acquired under static conditions using the QCPMG pulse sequence.⁴⁶ The QCPMG pulses lasted 1.675 μs with $\nu_1 = 149.3$ kHz. The refocusing pulses were repeated with a cycle time of 200 μs and 56 echoes were acquired for each transient. No ^1H

heteronuclear decoupling was applied during the acquisition since the ^1H channel was out of service. To diminish interference from copper metal within the probe head, a hole-burning pulse lasting 50 ms with $\nu_1 = 3$ kHz was applied before the QCPMG scheme. The acquisition details of the 1D ^{63}Cu VOCS-QCPMG spectra under static conditions (shown in **Figure 2.11**) are listed in **Table 2.6**.

The 1D ^{35}Cl spectra were acquired under static conditions using the WURST-QCPMG pulse sequence.⁵⁹ The WURST pulse had a length of 25 μs with $\nu_1 = 46$ kHz and an offset sweep of 500 kHz. During the QCPMG acquisition, the WURST pulses were repeated with a cycle time of 100 μs , and 50 echoes were acquired for each transient. SW $_T$ -TPPM heteronuclear decoupling with $\nu_1 = 10$ kHz was applied during the acquisition. The acquisition details of the 1D ^{35}Cl WURST-QCPMG spectra under static conditions (shown in **Figure 2.14**) are listed in **Table 2.7**.

The ^1H isotropic chemical shifts were referenced to tetramethylsilane (TMS) using the signal of the CH_2 group of adamantane at 1.735 ppm as a secondary reference.⁶¹ ^{13}C and ^{15}N isotropic chemical shifts were indirectly referenced using the previously published relative NMR frequencies.⁶¹ ^{63}Cu and ^{35}Cl isotropic chemical shifts were referenced to solid CuCl at 0 ppm and -127.23 ppm as secondary references, respectively.

Table 2.6. Experimental NMR details for the static ^{63}Cu QCPMG measurements of the pure samples **2**, **3^{OP}**, and **3^{SW}**.

Sample	B_0 /T	Number of sub-spectra	T_{RD} /s	Transients per sub- spectrum	Total acquisition time /h	VOCS step size /kHz	Spikelet separation /kHz
Pure 2	18.8	7	0.5	6462	7	−400	5
	28.2	7	0.5	6462	7	−300	5
Pure 3^{OP}	18.8	11	1	4992	15	−400	5
	28.2	10	1	4992	14	−300	5
Pure 3^{SW}	18.8	11	1	4992	15	−400	5
	28.2	10	1	4992	14	−300	5

Table 2.7. Experimental NMR details for the static ^{35}Cl WURST-QCPMG measurements of compound **1** and the pure samples **2**, **3^{OP}**, and **3^{SW}**.

Sample	B_0 /T	Number of sub-spectra	T_{RD} /s	Transients per sub-spectrum	Total acquisition time /min	VOCS step size /kHz	Spikelet separation /kHz
1	18.8	1	2	128	4	–	5
	28.2	1	2	640	21	–	5
Pure 2	18.8	13	0.5	512	60	–100	10
	28.2	1	0.5	44000	360	–	10
Pure 3^{OP}	18.8	5	0.5	128	5	–100	10
	28.2	1	0.5	1024	9	–	10
Pure 3^{SW}	18.8	5	0.5	128	5	–100	10
	28.2	1	0.5	1024	9	–	10

2.2.2.3 DFT calculations of NMR parameters

All calculations on the isolated molecules in gas phase have been performed using density DFT with the PBE0 functional,⁶² as implemented in the ADF package,^{63,64} in combination with a fine integration parameter (with a numerical integration parameter set to 5). A triple- ξ basis set with two polarization functions on all atoms (TZ2P) was used. All geometries were optimized without any symmetry constraint. These geometries were used to obtain the chemical shielding properties.

All calculations on the crystals were performed using the Vienna Ab initio Simulation Package (VASP) code,⁶⁴ with the generalized gradient approximation Perdew-Burke-Ernzerhof (PBE) used as exchange-correlation functional for geometry optimization and NMR parameters calculations.⁶⁵

The structural optimization was performed from XRD data (CCDC 234224 and CCDC 620849) considering only ionic coordinates.^{37,66} The plane-wave cut-off energy of 600 eV was set during the optimization process and a k-point density of $3 \times 3 \times 2$ was applied. The NMR shielding tensors were calculated using gauge-included projector augmented wave (GIPAW) formalism as implemented in VASP.^{67,68} In **Figure 2.2b** and **Figure 2.6b**, the chemical shifts were set relative to an unambiguous isolated resonance (H-X for ^1H , C-X for ^{13}C). In the present work, we used $Q(^{63}\text{Cu}) = -22.0 \text{ fm}^2$ and $Q(^{35}\text{Cl}) = -8.16 \text{ fm}^2$ as documented by Pyykkö.³⁹

2.2.3 Conclusion

In conclusion, the potential of multinuclear ssNMR spectroscopy in elucidating the mechanochemical synthesis of $[\text{Cu}(\text{Cl})(\text{NHC})]$ complexes has been demonstrated. The ssNMR spectroscopic data, in conjunction with DFT calculations of NMR parameters, unequivocally reveal that both the cuprate and the desired NHC complex are indeed formed within the solid-state during the ball milling process, rather than not in the solvent as part of the workup protocols. Furthermore, our investigations indicate the absence of the cuprate intermediate in the crude samples of the final product, suggesting a simultaneous conversion of cuprate into $[\text{Cu}(\text{Cl})(\text{NHC})]$. Additionally, we have successfully shown that ssNMR can effectively monitor the presence of unreacted reagents, such as $\text{NHC} \cdot \text{HCl}$, K_2CO_3 , and CuCl , as well as the formation of by-products like KHCO_3 . As a result, the overall reaction outcome is confirmed with all intermediates and products now unequivocally identified.

2.2.4 Statement of Contribution

Section 2.2 of Chapter 2 contains original, unpublished material that will be part of upcoming publication. The article will be authored by myself as the first author, along with the co-authors: Gianmarco Pisanò, Dr. Andrew G. M. Rankin, Dr. Laura Falivene, Dr. Julien Trébosc, Dr. Laurent Delevoye, Prof. Dr. Luigi Cavallo, Prof. Dr. Steven P. Nolan, Prof. Dr. Catherine S. J. Cazin, and Prof. Dr. Olivier Lafon. For this publication, I carried out the ssNMR experiments, analyzed the experimental data, and drafted the original version of the article. G.P. was responsible for synthesizing the $\text{Cu}(\text{I})$ -NHC complexes and assisted in editing the article. A.R. assisted in the ssNMR experiments and contributed to the article's editing. J.T. assisted in the ssNMR experiments. L.F. and L.C. carried out the DFT calculations on isolated structures and L.D. performed DFT calculations on crystal structures and assisted in editing the article. S.N.P. contributed to the analysis and interpretation of the results and assisted in editing the article.

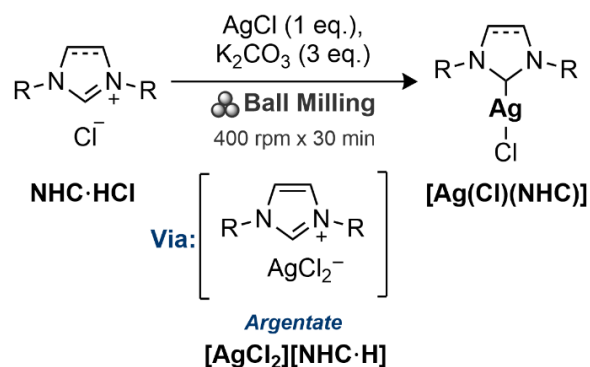
C.S.J.C and O.L. provided supervision, contributed to the analysis and interpretation of the results, and assisted in editing the article.

2.3 Ag(I)-NHC Complexes

In section **2.3**, we delve into the mechanochemical synthesis of Ag(I)-NHC complexes, building upon our prior investigation of [Cu(Cl)(NHC)] complexes. These Ag(I)-NHC complexes are of significant interest due to their versatile applications in synthetic chemistry,⁶⁹ as well as their potential as antimicrobial and antitumoral agents, as demonstrated in numerous research reports.^{24,70,71}

Recent research conducted by Cazin and co-workers has examined the feasibility of using the mechanochemical weak base approach to synthesize [Ag(Cl)(NHC)] complexes, as illustrated in **Scheme 2.3**.⁷² This innovative method involves ball milling an azolium chloride salt with cost-effective silver precursor (AgCl) in the presence of K₂CO₃, resulting in remarkable yields of [Ag(Cl)(NHC)] complexes. Interestingly, this approach was hypothesized to proceed through [AgCl₂][NHC·H] argentate intermediate species, a phenomenon similar to what has previously been observed with the Cu(I)-NHC complexes, where the weak base, K₂CO₃, fails to deprotonate the azolium salt.

In light of these considerations, this section of our research has two primary objectives. Firstly, we aim to determine whether the [Ag(Cl)(NHC)] complex forms during the ball milling process or emerges during subsequent workup procedures. Secondly, we investigate the hypothesis surrounding argentate synthesis. To achieve these goals, we chose imidazolium salt IPr·HCl **1** as our model substrate. We employed one-step one-pot synthesis procedures, which enabled us to successfully isolate both the corresponding [AgCl₂][IPr·H] (**4**) argentate intermediate and [Ag(Cl)(IPr)] (**5**) complex, as illustrated in **Scheme 2.4**. To monitor the formation of these compounds at different stages of the synthesis process, including different workup protocols, we conducted a comprehensive series of multinuclear (¹H, ¹³C, ¹⁵N, and ¹⁰⁹Ag) ssNMR spectroscopy experiments.



Scheme 2.3. Mechanochemical synthesis of [Ag(Cl)(NHC)] complexes through the weak base approach.⁷²

2.3.1 Results and Discussion

2.3.1.1 Mechanochemical synthesis

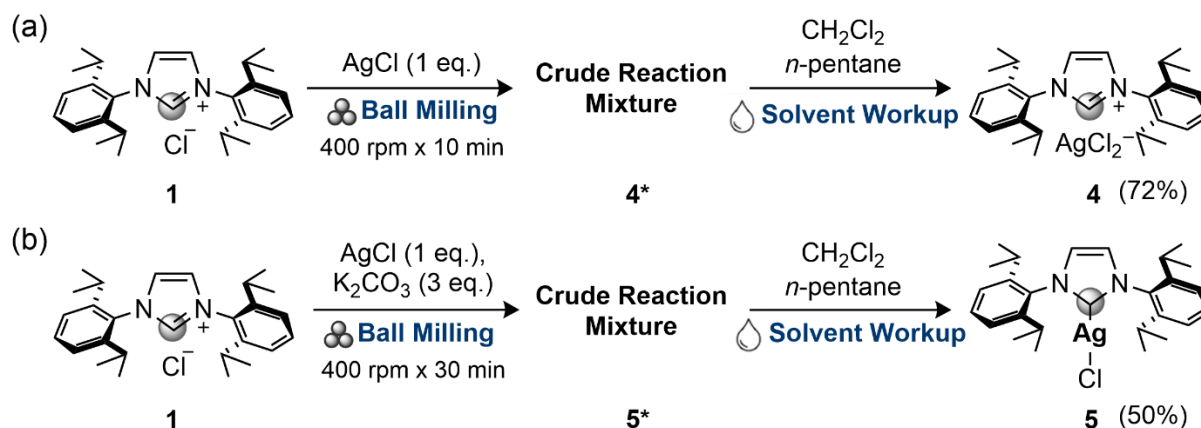
The mechanochemical synthesis of [AgCl₂][IPr·H] (**4**) and [Ag(Cl)(IPr)] (**5**) was carried out using a planetary ball mill (Fritsch, Pulverisette 5/4) operating at its maximum milling frequency of 400 rpm.⁷² The reaction was conducted within a 12 mL ZrO₂ reactor, equipped with 18 milling bodies (Ø = 5 mm), all composed of the same material.

i) Mechanochemical Synthesis of [AgCl₂][IPr·H] (**4**):

The reactor was charged with IPr·HCl (**1**) (1 eq.) and AgCl (1 eq.) in an air environment. The mixture of these two reactants was subjected to grinding for 10 min at a speed of 400 rpm, resulting in the formation of the crude reaction mixture **4*** as the initial product. Subsequent solvent-based workup was employed to process the crude reaction mixture, leading to the isolation and purification of the desired pure compound **4** in a yield of 72%.

ii) Mechanochemical Synthesis of [Ag(Cl)(IPr)] (**5**):

The reactor was charged with IPr·HCl (**1**) (1 eq.), AgCl (1 eq.), and K₂CO₃ (3 eq.) in an air environment. The mixture of these reactants was subjected to grinding for 30 min at a speed of 400 rpm, resulting in the formation of the crude reaction mixture **5*** as the initial product. Subsequent solvent-based workup was employed to process the crude reaction mixture, resulting in the isolation and purification of the desired pure compound **5** in a yield of 50%.



Scheme 2.4. Mechanochemical synthesis of (a) **4** and (b) **5** complexes. The gray circle denotes the $^{13}\text{C}^2$ carbon of the imidazolyidene moiety.

2.3.1.2 ^1H ssNMR spectroscopy

We conducted 1D ^1H ssNMR spectra for both the pure (**4**, **5**) and crude (**4***, **5***) samples with a static magnetic field strength of $B_0 = 9.4$ T and a MAS frequency of $\nu_R = 12.5$ kHz (**Figure 2.15**). To significantly enhance spectral resolution, we implemented a windowed homonuclear dipolar decoupling scheme, called supercycled windowed decoupling using mind-boggling optimization (wDUMBO-S2) pulse sequence.⁷³ The assignment of ^1H signals for compounds **4** and **5** was performed based on the ^1H isotropic chemical shifts measured in solution (see **Figure 2.16**).

In **Figure 2.15a**, the distinctive imidazolium $^1\text{H}^2$ signal shifted from 12.5 ppm in compound **1** to 10 ppm in **4**, signifying the successful synthesis of $[\text{IPr}\cdot\text{H}][\text{AgCl}_2]$. This particular signal was notably absent in the ^1H spectrum of compound **5**, implying the deprotonation of the corresponding site within this compound.

The 1D ^1H MAS NMR spectra of the crude samples, **4*** and **5***, shown in **Figure 2.15b**, exhibit $^1\text{H}^2$ signal resonating at 12.5 ppm, indicating the presence of unreacted $\text{IPr}\cdot\text{HCl}$ in the crude reaction mixtures. Moreover, the $^1\text{H}^2$ signal associated with $[\text{IPr}\cdot\text{H}][\text{AgCl}_2]$ is barely distinguishable in the ^1H spectrum of **4*** at 10 ppm.

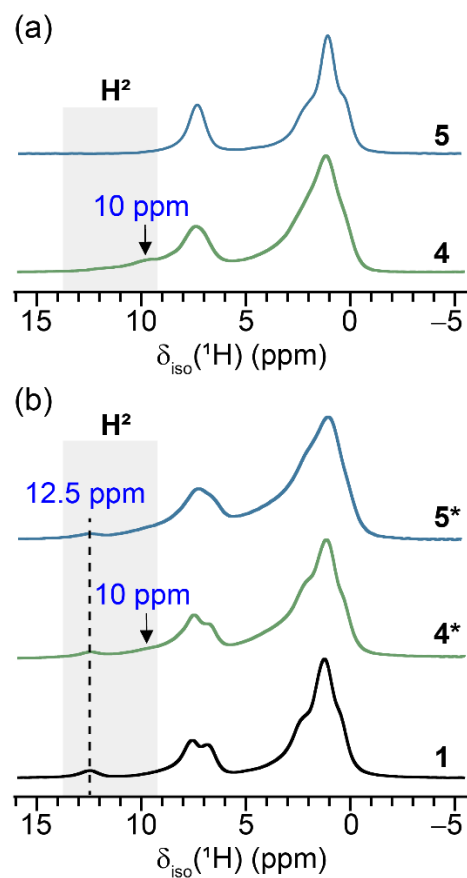


Figure 2.15. 1D ^1H wDUMBO-decoupled MAS NMR spectra of (a) pure (**4**, **5**) and (b) crude (**4***, **5***) samples acquired at $B_0 = 9.4$ T with a MAS frequency, $\nu_R = 12.5$ kHz. The spectrum of compound **1** is also shown in black in panel (b) for the sake of comparison. The shaded area denotes the region where the $^1\text{H}^2$ signal of compounds **1** and **4** resonates.

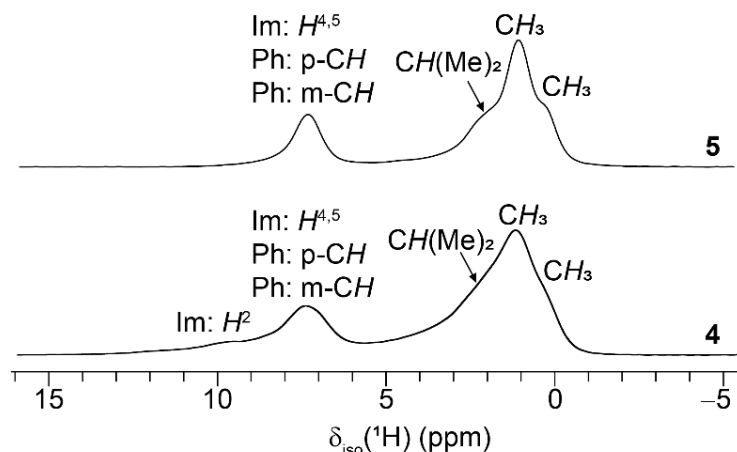


Figure 2.16. 1D ^1H wDUMBO-decoupled MAS NMR spectra of compounds **4** and **5** acquired at $B_0 = 9.4$ T with a MAS frequency, $\nu_R = 12.5$ kHz, along with the assignment of the ^1H signals. Im and Ph denote the signals of the imidazole and phenyl ring, respectively.

2.3.1.3 ^{13}C ssNMR spectroscopy

In order to confirm the presence of the desired compounds in both the pure (**4**, **5**) and crude (**4***, **5***) samples, we conducted 1D $^1\text{H} \rightarrow ^{13}\text{C}$ CP-MAS NMR spectra for these samples (**Figure 2.17**). The assignment of the ^{13}C NMR spectrum of compound **5** is detailed in **Figure 2.18a**, relying on ^{13}C isotropic chemical shifts measured in solution⁷⁴ and the 2D $^1\text{H}\{^{13}\text{C}\}$ DCP HETCOR spectrum shown in **Figure 2.18b**.

Silver possesses two stable isotopes, ^{107}Ag and ^{109}Ag , with natural abundances of 51.8 and 48.2%, low and close gyromagnetic ratios, -1.089×10^7 and -1.252×10^7 $\text{rad.s}^{-1}.\text{T}^{-1}$ and a nuclear spin $I = 1/2$. The 1D $^1\text{H} \rightarrow ^{13}\text{C}$ CP-MAS NMR spectrum of **5** exhibits a doublet centered at 183 ppm with $^1J(^{13}\text{C}^2\text{-}^{107/109}\text{Ag}) = 245$ Hz, attributed to the $^{13}\text{C}^2$ site bonded to the $^{107/109}\text{Ag}$ nuclei within $[\text{Ag}(\text{Cl})(\text{IPr})]$ (**Figure 2.17a**). Owing to the close γ ratios of both silver isotopes, the doublets due to the J -coupling with ^{107}Ag and ^{109}Ag isotopes are not resolved. The isotropic chemical shift of the $^{13}\text{C}^2$ site closely aligns with the values reported in the literature for solution NMR and falls within the expected range for coordinated NHCs.⁷⁴ Moreover, the 1D $^1\text{H} \rightarrow ^{13}\text{C}$ CP-MAS NMR spectrum of compound **4**, exhibits a distinct $^{13}\text{C}^2$ signal at 139 ppm (**Figure 2.17a**). This observation is consistent with the findings from the 1D ^1H ssNMR spectrum of compound **4** and aligns with the results from the ^{13}C ssNMR spectra of the cuprate compound, as depicted in **Figure 2.5** in section 2.2.1.3.

Furthermore, the 1D $^1\text{H} \rightarrow ^{13}\text{C}$ CP-MAS spectrum of **4*** exhibits a $^{13}\text{C}^2$ signal at 139 ppm (Figure 2.17b), thus confirming the solid-state formation of $[\text{AgCl}_2][\text{IPr}\cdot\text{H}]$ during the ball milling process. Additionally, in the $^1\text{H} \rightarrow ^{13}\text{C}$ CP-MAS spectrum of **5***, no signal at 139 ppm is observed, but a doublet centered at 183 ppm are present. This observation indicates that during ball milling, the $[\text{Ag}(\text{Cl})(\text{IPr})]$ complex forms in the solid state, while the argentate is completely transformed into this complex. Moreover, the 1D $^1\text{H} \rightarrow ^{13}\text{C}$ CP-MAS spectra of **4*** and **5*** exhibit an additional signal at 143 ppm, confirming the presence of unreacted $\text{IPr}\cdot\text{HCl}$ in the crude reaction mixtures. Furthermore, signals at 162 and 169 ppm detected in the ^{13}C spectrum of **5*** indicate the presence of KHCO_3 and K_2CO_3 , respectively.³¹ It is important to note that the spectra of crude samples display broader signals compared to those of pure samples, likely attributed to the disorder introduced during the ball milling process.

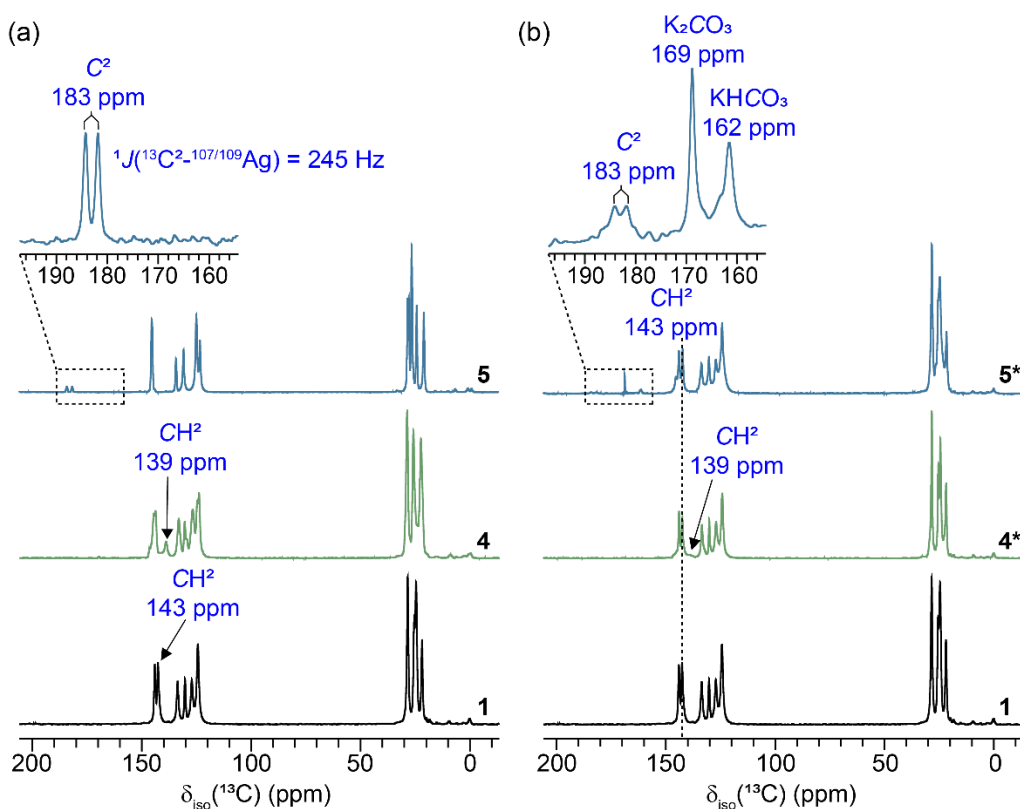


Figure 2.17. 1D $^1\text{H} \rightarrow ^{13}\text{C}$ CP-MAS NMR spectra of (a) pure (**4**, **5**) and (b) crude (**4***, **5***) samples acquired at $B_0 = 9.4 \text{ T}$ with $\nu_R = 12.5 \text{ kHz}$. The spectrum of compound **1** is also shown in black in panels (a) and (b) for the sake of comparison. The signals assigned to the $^{13}\text{C}^2$ site for compound $[\text{Ag}(\text{Cl})(\text{IPr})]$ are shown as an inset in panels (a) and (b). The vertical dashed line in panel (b) denotes the isotropic chemical shift of the $^{13}\text{C}^2$ nucleus in compound **1**.

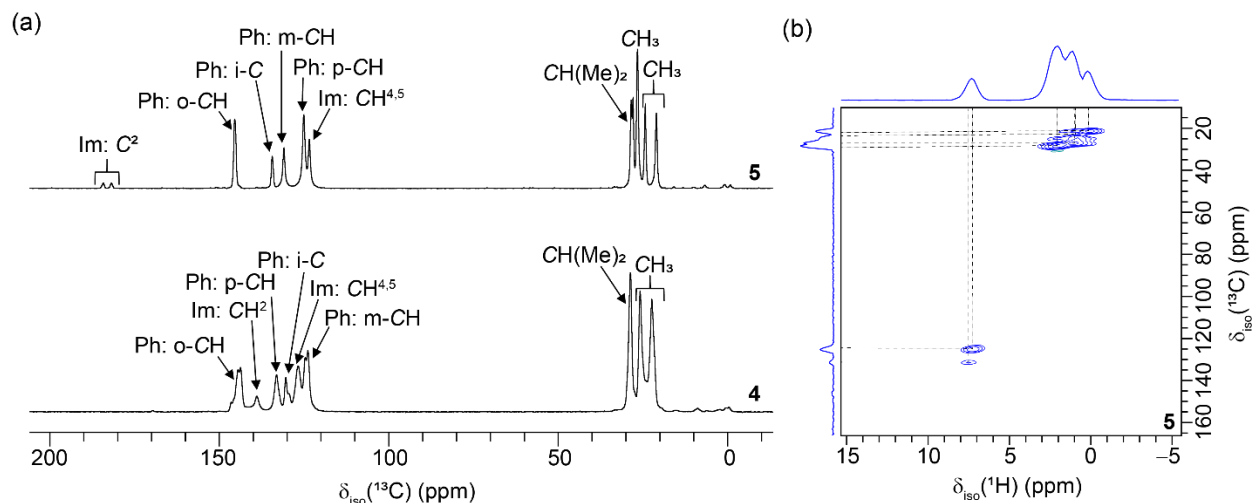


Figure 2.18. (a) 1D $^1\text{H} \rightarrow ^{13}\text{C}$ CP-MAS NMR spectra of compounds **4** and **5** acquired at $B_0 = 9.4$ T with $\nu_R = 12.5$ kHz, along with the assignment of the ^{13}C signals. The spectral assignment of **5** is based on ^{13}C isotropic chemical shifts measured in solution⁷⁴ as well as the 2D $^1\text{H}\{^{13}\text{C}\}$ DCP HETCOR NMR spectrum. (b) 2D $^1\text{H}\{^{13}\text{C}\}$ DCP HETCOR NMR spectrum of **5** acquired at $B_0 = 18.8$ T with $\nu_R = 60$ kHz.

2.3.1.4 ^{15}N ssNMR spectroscopy

Next, the 1D $^1\text{H} \rightarrow ^{15}\text{N}$ CP-MAS spectra of these samples were recorded (**Figure 2.19**). The ^{15}N spectrum of **5** exhibits a single peak at 195 ppm, represented as a blue-filled line. This observation is in agreement with the previously reported crystal structure of $[\text{Ag}(\text{Cl})(\text{IPr})]$ in the literature.⁷⁴ For the ^{15}N NMR spectrum of sample **5***, two distinct signals are observed. The peak at 195 ppm could be deconvoluted into a single component, indicating the presence of $[\text{Ag}(\text{Cl})(\text{IPr})]$, thus confirming its formation in the solid-state during ball milling. The signal at lower chemical shift could be deconvoluted into a single component, attributed to the unreacted $\text{IPr} \cdot \text{HCl}$, with no signal corresponding to argentate observed. This observation provides conclusive evidence of the simultaneous conversion of argentate into $[\text{Ag}(\text{Cl})(\text{IPr})]$ in the presence of the K_2CO_3 base.

The ^{15}N spectrum of compound **4** exhibits two signals (**Figure 2.19c**). One signal, resonating at 186 ppm, could be deconvoluted into a single signal, represented by the green-filled line and attributed to $[\text{AgCl}_2][\text{IPr} \cdot \text{H}]$. The signal at lower chemical shift required two-line deconvolution to fully describe the lineshape. The peaks at 183 and 186 ppm of equal intensities displayed as green-filled lines are attributed to $[\text{AgCl}_2][\text{IPr} \cdot \text{H}]$. They indicate the presence of two

crystallographically inequivalent N sites in this compound, like in $[\text{CuCl}_2][\text{IPr}\cdot\text{H}]$ crystal structure. Furthermore, the peak at 182 ppm is attributed to $\text{IPr}\cdot\text{HCl}$. This indicates that compound **4**, unlike compound **5**, displays instability when exposed to light and air, leading to partial decomposition within a few months. This observation is further corroborated by the ^{109}Ag ssNMR analysis, which will be discussed in the following section. Furthermore, the ^{15}N spectrum of the crude sample **4*** is consistent with the findings from the ^1H and ^{13}C spectra, exhibiting ^{15}N signals corresponding to $[\text{AgCl}_2][\text{IPr}\cdot\text{H}]$ and unreacted $\text{IPr}\cdot\text{HCl}$ (**Figure 2.19d**).

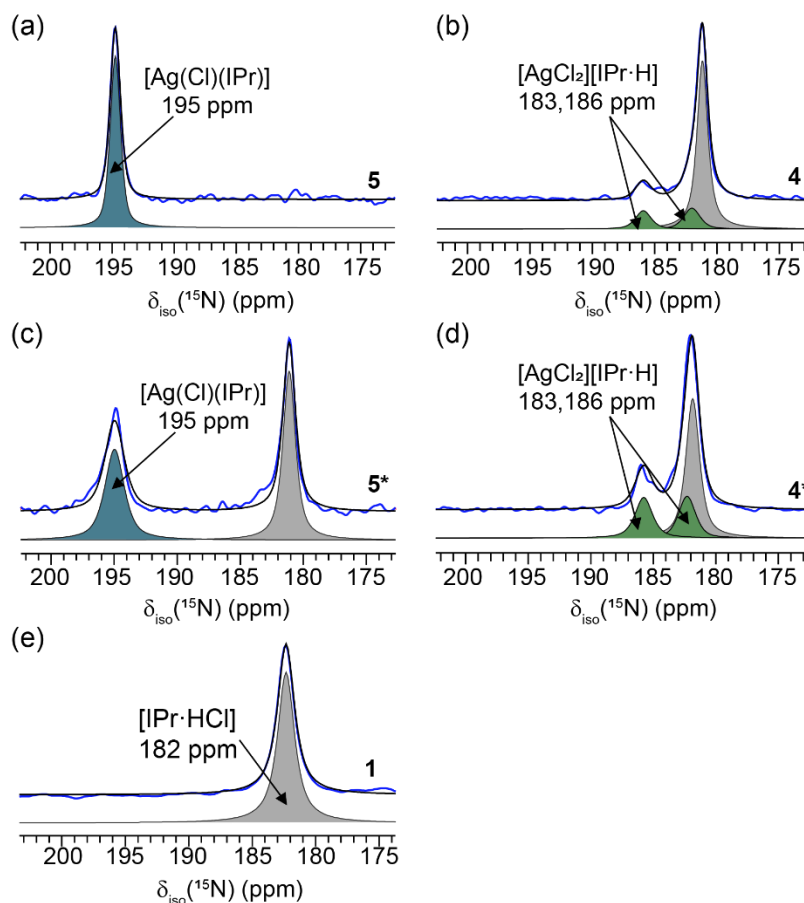


Figure 2.19. Experimental (blue) and simulated (black) 1D $^1\text{H}\rightarrow^{15}\text{N}$ CP-MAS NMR spectra of (a) **5**, (b) **4**, (c) **5***, and (d) **4*** acquired at $B_0 = 9.4$ T with $\nu_R = 8$ kHz. The simulated spectra are the sum of up to three components: the blue, green, and gray-filled peaks are ^{15}N components associated with $[\text{Ag}(\text{Cl})(\text{IPr})]$, $[\text{AgCl}_2][\text{IPr}\cdot\text{H}]$, and $\text{IPr}\cdot\text{HCl}$ compounds, respectively.

2.3.1.5 ^{109}Ag ssNMR spectroscopy

Despite the lower natural abundance of ^{109}Ag isotope (see section 2.3.1.3), its detection is usually preferred for NMR studies owing to its higher gyromagnetic ratio, which results in higher receptivity (relative to ^{13}C): 0.29 for ^{109}Ag instead of 0.20 for ^{107}Ag . Nevertheless, ^{109}Ag NMR experiments often exhibit low sensitivity owing to the low γ ratio of this isotope and its long spin-lattice relaxation time (T_1), necessitating extended experiment times to acquire spectra with satisfactory SNR. To overcome these challenges, we employed 1D $^1\text{H} \rightarrow ^{109}\text{Ag}$ CP-MAS pulse sequence with flip-back recovery,⁷⁵ illustrated in **Figure 2.20**, to detect the ^{109}Ag NMR signals of metal complexes, in which silver atoms are surrounded by protons. The flip-back $\pi/2$ pulse at the end of the spin lock on the ^1H channel returns the residual proton magnetization to the z-axis, which reduces the recovery delay and hence, improves the sensitivity. Moreover, we utilized the CPMG pulse sequence to detect ^{109}Ag signals from the AgCl compound, which does not contain protons and hence, is not detected in $^1\text{H} \rightarrow ^{109}\text{Ag}$ CP-MAS spectra.

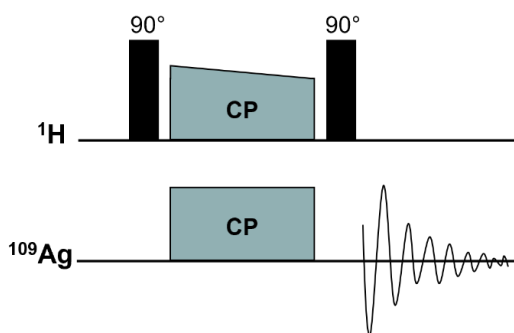


Figure 2.20. The 1D $^1\text{H} \rightarrow ^{109}\text{Ag}$ CP-MAS pulse sequence with flip-back recovery and no ^1H decoupling.

The ^{109}Ag spectrum of sample **4** exhibits ^{109}Ag isotropic resonance at 489 ppm attributed to $[\text{AgCl}_2][\text{IPr}\cdot\text{H}]$ (**Figure 2.21c**). Interestingly, an additional ^{109}Ag signal resonating at 390 ppm corresponding to AgCl is detected in the 1D ^{109}Ag CPMG spectrum (**Figure 2.22c**). These observations align with the ^{15}N NMR findings, suggesting that $[\text{AgCl}_2][\text{IPr}\cdot\text{H}]$ is partially decomposed into $\text{IPr}\cdot\text{HCl}$ and AgCl .

The 1D $^1\text{H} \rightarrow ^{109}\text{Ag}$ CP-MAS spectrum of the crude sample **4*** exhibits higher sensitivity than that of **4**, allowing us to simulate the spinning sidebands and determine the ^{109}Ag NMR parameters for $[\text{AgCl}_2][\text{IPr}\cdot\text{H}]$: $\delta_{\text{iso}} = 489$ ppm, $\delta_{\text{aniso}} = -1400$ ppm, and $\eta_{\text{CS}} = 0$, as illustrated in **Figure 2.21d**.

Furthermore, the ^{109}Ag isotropic signal corresponding to compound **5** resonates at 612 ppm, with $\delta_{\text{aniso}} = -1377$ ppm and $\eta_{\text{CS}} = 0$, as shown in **Figure 2.21a**. These parameters closely match those previously reported for the $[\text{Ag}(\text{Cl})(\text{NHC})]$ complex, where the NHC ligand was *N,N*-bis-[2,4,6-trimethylphenyl]imidazol-2-ylidene.^{76,77} The presence of the ^{109}Ag isotropic peak at 612 ppm in the crude sample **5*** further confirms the synthesis of the $[\text{Ag}(\text{Cl})(\text{IPr})]$ in solid-state during ball milling, as depicted in **Figure 2.21b**. Moreover, an additional signal at 390 ppm is observed in the 1D ^{109}Ag CPMG spectrum of both **4*** and **5***, indicating the presence of unreacted AgCl in the crude reaction mixtures.⁷⁸ This signal is not observed in the pure sample **5**.

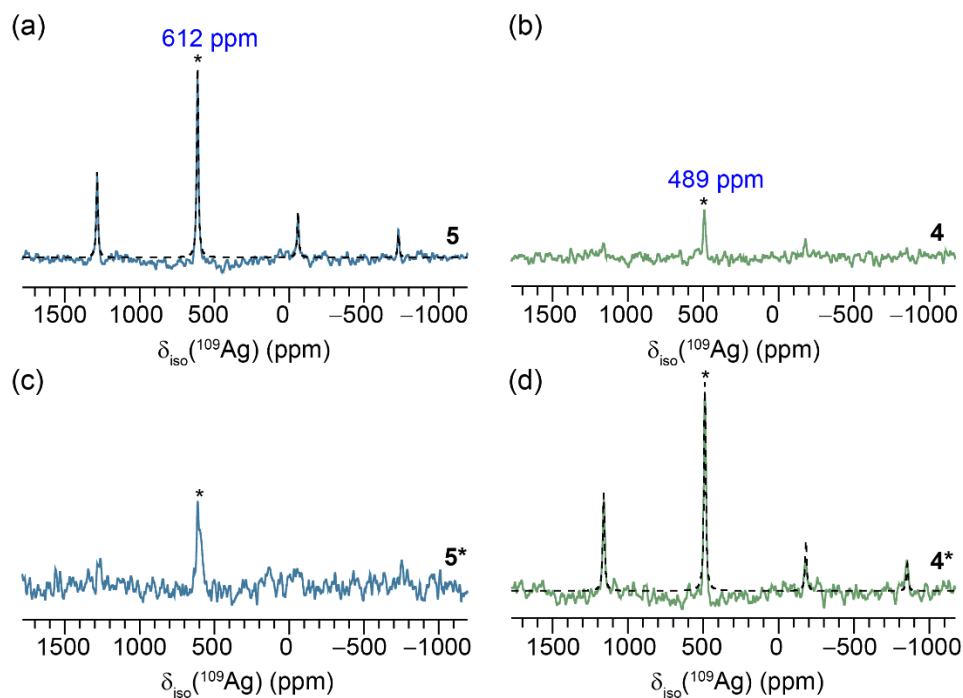


Figure 2.21. 1D $^1\text{H} \rightarrow ^{109}\text{Ag}$ CP-MAS NMR spectra of (a) **5**, (b) **4**, (c) **5***, and (d) **4*** acquired at $B_0 = 9.4$ T with MAS frequency, $\nu_R = 12.5$ kHz. The simulated spectra of **5** and **4*** are represented as black dashed lines. The isotropic resonances are indicated by *.

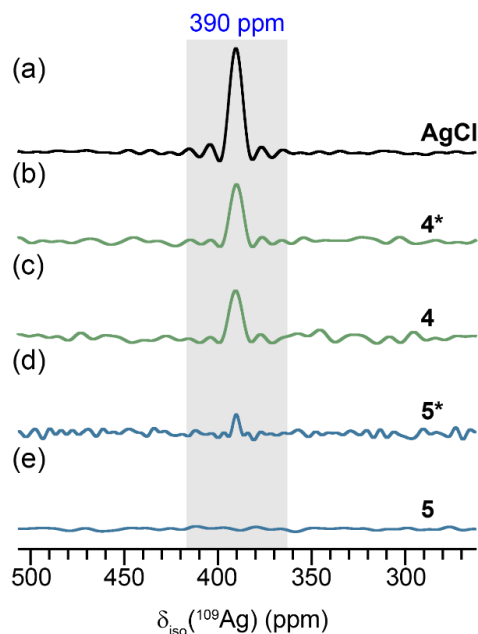


Figure 2.22. 1D static ^{109}Ag CPMG NMR spectra of (a) **AgCl**, (b) **4***, (c) **4**, (d) **5***, and (e) **5** acquired at $B_0 = 9.4$ T with MAS frequency, $\nu_R = 12.5$ kHz. The gray-shaded region denotes the signal corresponding to AgCl resonating at 390 ppm.

2.3.2 Experimental Details

2.3.2.1 Samples preparation

All mechanochemical experiments were conducted using a Fritsch Pulverisette 5/4 planetary ball mill.

2.3.2.1.1 Ball milling

Synthesis of $[\text{AgCl}_2][\text{IPr}\cdot\text{H}]$: A 12 mL zirconia reactor equipped with 18 balls of the same material (7.52 g, $\varnothing = 5$ mm) was charged in the air with IPr·HCl (150.0 mg, 0.35 mmol) and AgCl (50 mg, 0.35 mmol). The mixture of solids was then ground for 10 min at 400 rpm.

Synthesis of $[\text{Ag}(\text{Cl})(\text{IPr})]$: A 12 mL zirconia reactor equipped with 18 balls of the same material (7.52 g, $\varnothing = 5$ mm) was charged in the air with IPr·HCl (150.0 mg, 0.35 mmol), AgCl (50.0 mg, 0.35 mmol), and K_2CO_3 (146.0 mg, 1.06 mmol). The mixture of solids was then ground for 30 min at 400 rpm.

2.3.2.1.2 Workup

Solvent-Free (4*, 5*): At the end of the milling process the content of the reactor was manually extracted with the aid of a spatula, transferred in a vial, and analyzed without any further manipulations.

Solvent-Based (4, 5): At the end of the milling process, the content of the reactor was extracted with CH_2Cl_2 (3×4 mL), and the resulting solution was filtered over SiO_2 . The SiO_2 pad was rinsed with additional CH_2Cl_2 (3×2 mL) and the filtrate was subsequently concentrated by rotatory evaporation to about $\frac{1}{4}$ of its original volume. To this solution, an excess of *n*-pentane (10 mL) was added and the resulting solution was sonicated for a few minutes to induce the precipitation of the desired product. The solids formed were then collected by vacuum filtration, washed with additional *n*-pentane, and then dried under a high vacuum for several hours.

2.3.2.2 ssNMR spectroscopy

All 1D ssNMR experiments were performed at room temperature on a wide-bore Bruker AVANCE NEO NMR spectrometer operating at a static magnetic field of 9.4 T, i.e. Larmor frequencies of 400.1 MHz for ^1H , 100.6 MHz for ^{13}C , 40.5 MHz for ^{15}N , and 18.6 MHz for ^{109}Ag . Powdered samples were packed into 4 mm outer diameter zirconia rotors sealed with Kel-F drive caps and spun at 12.5 kHz.

The 1D ^1H and ^{13}C MAS NMR spectra were acquired with a triple resonance Bruker 4 mm triple-resonance (HXY) MAS probe operated in double resonance mode. 1D ^1H MAS NMR spectra were acquired using wDUMBO-S2 pulse sequence with an overall phase of π between successive DUMBO cycles,⁷³ which was optimized using α -glycine sample. The optimal length of the basic cycle of DUMBO sequence, corresponding approximately to a 6π pulse, was equal to 27 μs . The optimal radiofrequency (rf) field of the DUMBO scheme was 113 kHz. One block of DUMBO cycle was separated from the next cycle by a detection of window of 5 μs . The ^1H DUMBO spectra result from the averaging of 16 transients with a relaxation delay, $T_{\text{RD}} = 1.3$ s.

The 1D $^1\text{H} \rightarrow ^{13}\text{C}$ CP-MAS experiments were performed using a ^1H $\pi/2$ pulse of 2.2 μs followed by a CP contact time of 1 ms. During the CP transfer, the nutation frequency on the ^{13}C channel was constant and equal to 55 kHz, while the ^1H nutation frequency was linearly ramped from 90 to 100. SPINAL-64 heteronuclear decoupling with nutation frequency, $\nu_1 = 102$ kHz, was applied on the ^1H channel during the acquisition period.⁵⁶ The 1D $^1\text{H} \rightarrow ^{13}\text{C}$ CP-MAS spectra were recorded

using a recovery delay $T_{RD} = 1.3$ s and resulted from averaging 8192 transients, corresponding to a total experimental time of 3 h.

The 1D ^{15}N and ^{109}Ag NMR experiments were carried out using a 4 mm double-resonance HX low- γ MAS probe. The 1D $^1\text{H} \rightarrow ^{15}\text{N}$ CP-MAS experiments were performed using a ^1H $\pi/2$ pulse of 2.7 μs followed by a CP contact time of 4 ms. During the CP transfer, the radio frequency (rf) nutation frequency on the ^{15}N channel was constant and equal to 75 kHz, whereas that on the ^1H channel was linearly ramped from 100 to 50. SW_F-TPPM heteronuclear decoupling with an rf nutation frequency of 47 kHz was applied on the ^1H channel during the acquisition.⁵⁸ The 1D $^1\text{H} \rightarrow ^{15}\text{N}$ CP-MAS spectra resulted from averaging 10,500 transients with $T_{RD} = 1.3$ s, corresponding to a total experimental time of 4 h. The experimental 1D $^1\text{H} \rightarrow ^{15}\text{N}$ CP-MAS NMR spectra were simulated using the SOLA module within Bruker TopSpin software.

The 1D $^1\text{H} \rightarrow ^{109}\text{Ag}$ CP-MAS NMR spectra were acquired with flip-back recovery using ^1H $\pi/2$ pulse lengths of 2.9 μs ($\nu_1 = 86$ kHz) and a CP contact time of 10 ms. The nutation frequency on the ^{109}Ag channel was constant at 27.8 kHz, while the ^1H nutation frequency was linearly ramped from 100 to 90 during the CP transfer, whereas no ^1H decoupling was applied during the signal acquisition. The 1D $^1\text{H} \rightarrow ^{109}\text{Ag}$ CP-MAS NMR spectra were recorded with $T_{RD} = 2$ s and resulted from averaging 38240 transients, corresponding to a total experimental time of 21 h. The experimental 1D $^1\text{H} \rightarrow ^{109}\text{Ag}$ CP-MAS NMR spectra were simulated using the SOLA module within Bruker TopSpin software. The 1D ^{109}Ag CPMG NMR spectra were recorded using CPMG pulses with lengths of 11 and 22 μs corresponding to ν_1 of 22.7 and 11.4 kHz, respectively. The refocusing pulses were repeated with a cycle time of 10080 μs , and 400 echoes were acquired for each transient. 1D ^{109}Ag CPMG spectra were obtained with 64 transients separated by $T_{RD} = 200$ s, corresponding to a total experimental time of 3.5 h. The ^{109}Ag chemical shifts were externally referenced to silver *p*-toluenesulfonate ($\text{CH}_3\text{C}_6\text{H}_4\text{SO}_3\text{Ag}$) ($\delta_{\text{iso}}(^{109}\text{Ag}) = 12.45$ ppm).

The 2D $^1\text{H}\{^{13}\text{C}\}$ DCP HETCOR experiment was recorded to correlate ^1H and ^{13}C isotropic chemical shifts.^{34,35} The spectrum was acquired using a 1.3 mm double-resonance (HX) MAS probe and $\nu_R = 60$ kHz. Short CP contact times of 0.7 ms and 0.15 ms were used during the first and second CP transfers, respectively, to probe selectively the proximities between covalently bonded ^1H and ^{13}C nuclei. During the CP transfers, the nutation frequency on the ^{13}C channel was constant and equal to 46 kHz, while the ^1H nutation frequency was linearly ramped from 100 to 50. After the $^1\text{H} \rightarrow ^{13}\text{C}$ CP transfer, the ^1H magnetization was destroyed by two saturation pulses lasting 2.25 μs with orthogonal phases and nutation frequencies set to 111 kHz. The 2D spectrum

was recorded with $\nu_R = 60$ kHz using non-uniform sampling (NUS) with an exponentially biased sampling keeping 40% of the points with respect to uniform sampling. The 2D spectra resulted from 20 transients for each of the 400 t_1 increments with $T_{RD} = 1.7$ s, corresponding to a total experimental time of 4 h.

The ^1H isotropic chemical shifts were referenced to TMS using the signal of the CH_2 group of adamantane at 1.735 ppm as a secondary reference.⁶¹ The ^{13}C and ^{15}N isotropic chemical shifts were indirectly referenced using the previously published relative NMR frequencies.⁶¹

2.3.3 Conclusion

In summary, the application of ssNMR spectroscopy has proven invaluable in unraveling the mechanistic aspects underlying the synthesis of $[\text{Ag}(\text{Cl})(\text{NHC})]$ complexes through the mechanochemical weak base approach. Our investigations have unequivocally confirmed that the formation of the $[\text{AgCl}_2][\text{IPr}\cdot\text{H}]$ argentate and the $[\text{Ag}(\text{Cl})(\text{IPr})]$ complex occur within the solid-state during the ball milling procedure, rather than occurring within the solvent during subsequent workup protocols. Furthermore, our ssNMR spectroscopy data provided clear evidence for the involvement of argentate intermediates in the synthesis of $[\text{Ag}(\text{Cl})(\text{NHC})]$ complexes. Additionally, we have observed the gradual decomposition of $[\text{AgCl}_2][\text{IPr}\cdot\text{H}]$ into $\text{IPr}\cdot\text{HCl}$ and AgCl over time. To strengthen the comprehensiveness of our study, we recommend complementing our findings with computational investigations of NMR parameters and the utilization of other solid-state analytical techniques, such as PXRD. These supplementary analysis will validate the structural characteristics of $[\text{AgCl}_2][\text{IPr}\cdot\text{H}]$, particularly considering that no structural information for this compound is currently available in the literature.

2.3.4 Statement of Contribution

In Chapter 2, section 2.3, my role encompassed the execution of the ssNMR experiments, data analysis, and interpretation of the obtained results. Dr. Julien Trébosc assisted in the execution of the ssNMR experiments. The synthesis of the samples was performed by Gianmarco Pisanò. Prof. Dr. Catherine Cazin and Prof. Dr. Olivier Lafon provided invaluable guidance and expertise.

2.4 Rh(I)-NHC Complexes

Having successfully demonstrated the potential of ssNMR spectroscopy in probing the mechanochemical synthesis of $[\text{Cu}(\text{Cl})(\text{IPr})]$ and $[\text{Ag}(\text{Cl})(\text{IPr})]$ complexes through the weak base

approach, we are now interested in exploring the suitability of this mechanochemical methodology for constructing a series of Rh(I)-NHC complexes of the $[\text{Rh}(\text{acac})(\text{CO})(\text{NHC})]$ type, with a concurrent goal of gaining insights into the underlying mechanism through ssNMR spectroscopy.

Our interest in this particular class of complexes primarily stems from the straightforward synthesis of $[\text{Rh}(\text{acac})(\text{CO})(\text{L})]$ complexes (acac = acetylacetonate), where L denotes a two-electron-donor ligand. This synthetic process involves starting with the Rh precursor $[\text{Rh}(\text{acac})(\text{CO})_2]$ and proceeds via a direct single-step ligand displacement reaction, leading to the removal of one CO ligand. Additionally, Carrow and co-workers have exploited these complexes to evaluate the Tolman electronic parameter (TEP) of newly synthesized phosphine ligands.⁷⁹ This assessment involves a linear correlation analysis linking the carbonyl stretching frequency observed in $[\text{Rh}(\text{acac})(\text{CO})(\text{PR}_3)]$ complexes with the TEP values corresponding to the same set of phosphine ligands. Similarly, Gessner and co-workers have applied a similar linear correlation analysis to determine the TEP value for a di(amino)-substituted carbodiphosphorane (CDP) ligand, utilizing the IR stretching frequency of the corresponding $[\text{Rh}(\text{acac})(\text{CO})(\text{L})]$ complexes.⁸⁰ This positions this class of complexes as an interesting platform for assessing the electronic properties of monodentate ligands. However, it is crucial to note that only a limited number of $[\text{Rh}(\text{acac})(\text{CO})(\text{NHC})]$ complexes have been reported, and these have been synthesized using methods that demand strictly anhydrous conditions.^{81–86} Thus, the establishment of a reliable and simple synthetic protocol for assembling these complexes holds significant practical importance.

Cazin, Nolan, and co-workers have recently disclosed a solvent-based synthetic protocol that allows the assembly of this class of complexes using operationally simple conditions and readily available starting materials.⁸⁶ Nevertheless, this solvent-based synthesis involves relatively long reaction times (ranging from 3 to 18 hours, depending on the nature of the $\text{NHC} \cdot \text{HBF}_4$ salt employed) and requires the application of heat.

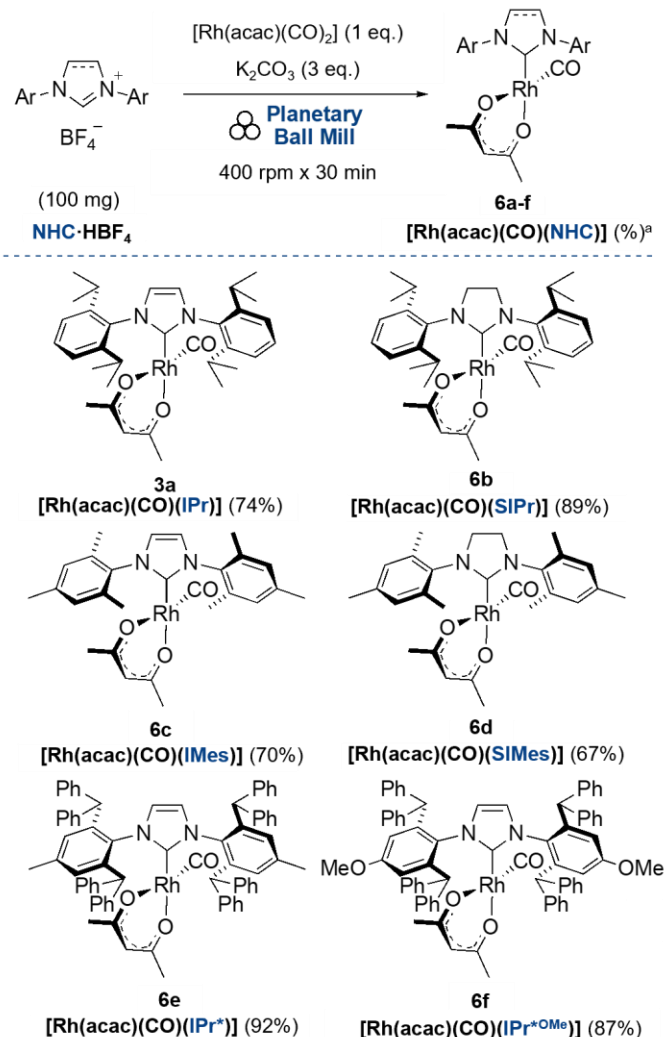
In this context, we present a straightforward mechanochemical synthetic protocol designed to access a series of $[\text{Rh}(\text{acac})(\text{CO})(\text{NHC})]$ complexes bearing *N,N'*-diaryl imidazolyliidene and imidazolinyliidene NHC ligands (**Scheme 2.5**). A comprehensive analysis using ssNMR spectroscopy, complemented by PXRD and ATR-FTIR, provides invaluable insights into the underlying mechanism of this transformation.

2.4.1 Results and Discussion

2.4.1.1 Mechanochemical synthesis

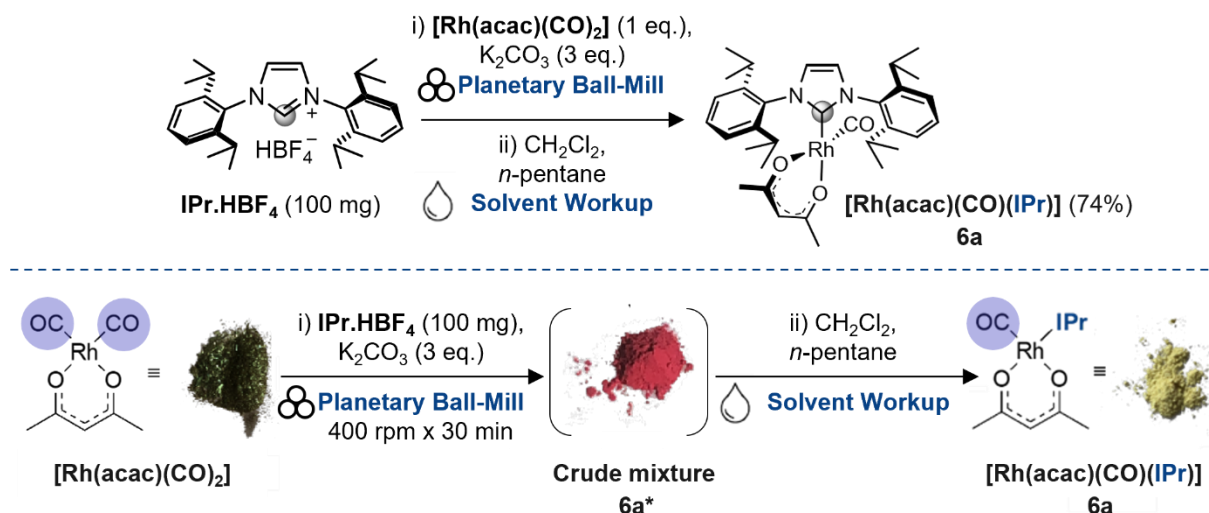
Very recently, Cazin and co-workers^{29,72} and Udvardy, Czégéni, and co-workers,²⁸ have independently demonstrated the viability of utilizing a mild and cost-effective base such as K_2CO_3 along with various metal precursors and azolium chloride salts to affix NHC ligand to Cu(I), Ag(I), Au(I), Pd(II), and Rh(I) metal center under solvent-free, solid-state mechanochemical conditions. Our investigation sought to determine whether a similar approach involving K_2CO_3 , azolium tetrafluoroborate salts ($\text{NHC}\cdot\text{HBF}_4$), and the metal precursor $[\text{Rh}(\text{acac})(\text{CO})_2]$ could successfully yield a series of *N,N'*-diaryl NHC-Rh(I) complexes of the $[\text{Rh}(\text{acac})(\text{CO})(\text{NHC})]$ type under solvent-free, solid-state mechanochemical conditions. Gratifyingly, these conditions resulted in the formation of the desired complexes (as depicted in **Scheme 2.5**).

All reactions were conducted in a planetary ball mill, using a ZrO_2 reactor charged with 28 balls of the same material (10.3 g, $\varnothing = 5$ mm, corresponding to a filling degree for the milling bodies of $\Phi_{\text{MB}} = 0.15$) and on a 100 mg scale of the $\text{NHC}\cdot\text{HBF}_4$ salt precursor. Milling of the reactants for 30 min at 400 rpm, afforded the desired metal complexes (**6a-f**) in good to excellent yields. We were able to appreciate the advantages of conducting synthesis under mechanochemical conditions: all the $\text{NHC}\cdot\text{HBF}_4$ subjected to these reaction conditions were successfully coordinated to the Rh(I)-center in very short reaction times, with final products isolated after a very simple workup consisting of extraction in a 1 : 3 volume mixture of CH_2Cl_2 : *n*-pentane, microfiltration of the resulting solution, solvent removal under reduced pressure and trituration of the resulting solid using *n*-pentane (for details, see **Experimental Details**). The identity of complexes (**6a-f**) was confirmed using ^1H liquid-state NMR spectroscopy.



Scheme 2.5. Mechanochemical synthesis of $[\text{Rh}(\text{acac})(\text{CO})(\text{NHC})]$ (**6a-f**) complexes. Reaction conditions: $\text{NHC}\cdot\text{HBF}_4$ (100 mg), $[\text{Rh}(\text{acac})(\text{CO})_2]$ (1 eq.), and K_2CO_3 (3 eq.) in a planetary ball mill at 400 rpm for 30 min. ^aIsolated yield (%).

To gain insights into the reaction mechanism and determine the stage at which the desired products were formed, multinuclear (^1H , ^{13}C , ^{15}N , ^{19}F , and ^{11}B) ssNMR experiments at a magnetic field strength of 9.4 T were employed in conjunction with PXRD and ATR-FTIR. For this purpose, the NHC salt precursor $\text{IPr}\cdot\text{HBF}_4$ was chosen for its simplicity and ease of characterization. Following the milling process, the crude reaction mixture **6a*** underwent recrystallization, leading to the isolation of pure $[\text{Rh}(\text{acac})(\text{CO})(\text{IPr})]$ (**6a**) complex (**Scheme 2.6**). By comparing the high-resolution ssNMR spectra of the **6a*** with **6a**, we could ascertain the specific stage at which the desired products were formed, whether during the ball milling process or because of the subsequent workup.



Scheme 2.6. Mechanochemical synthesis of $[\text{Rh}(\text{acac})(\text{CO})(\text{IPr})]$ **6a** complex. Reaction conditions: i) A mixture of $\text{IPr} \cdot \text{HBF}_4$ (100 mg, 0.21 mmol), $[\text{Rh}(\text{acac})(\text{CO})_2]$ (54 mg, 0.21 mmol), and K_2CO_3 (87 mg, 0.63 mmol) is subjected to mechanochemical milling in a planetary ball mill at 400 rpm for 30 min, resulting in the formation of the crude reaction mixture **6a*** as the initial product; ii) Subsequent solvent-based workup is employed to process the crude reaction mixture, yielding to the isolation and purification of the desired pure product $[\text{Rh}(\text{acac})(\text{CO})(\text{IPr})]$ **6a** in 74% yield. The gray circle denotes the $^{13}\text{C}^2$ carbon of the imidazolyliidene moiety in both $\text{IPr} \cdot \text{HBF}_4$ and **6a**. The bottom scheme denotes the distinct color of the samples involved. The blue circle depicts the CO ligand and represents the substitution of one CO ligand in $[\text{Rh}(\text{acac})(\text{CO})_2]$ with IPr to form the desired complex.

2.4.1.2 ^1H ssNMR spectroscopy

Initially, 1D ^1H NMR spectra of solids, $\text{IPr} \cdot \text{HBF}_4$, $[\text{Rh}(\text{acac})(\text{CO})_2]$, **6a***, and **6a** were acquired under MAS with the homonuclear dipolar decoupling scheme, wDUMBO-S2,⁷³ to enhance spectral resolution. The resulting spectra are represented in **Figure 2.23** along with their respective assignment. Notably, the ^1H spectrum of the crude reaction mixture **6a*** contains signals of the reactants, $\text{IPr} \cdot \text{HBF}_4$ and $[\text{Rh}(\text{acac})(\text{CO})_2]$, but does not display those of the final product **6a**.

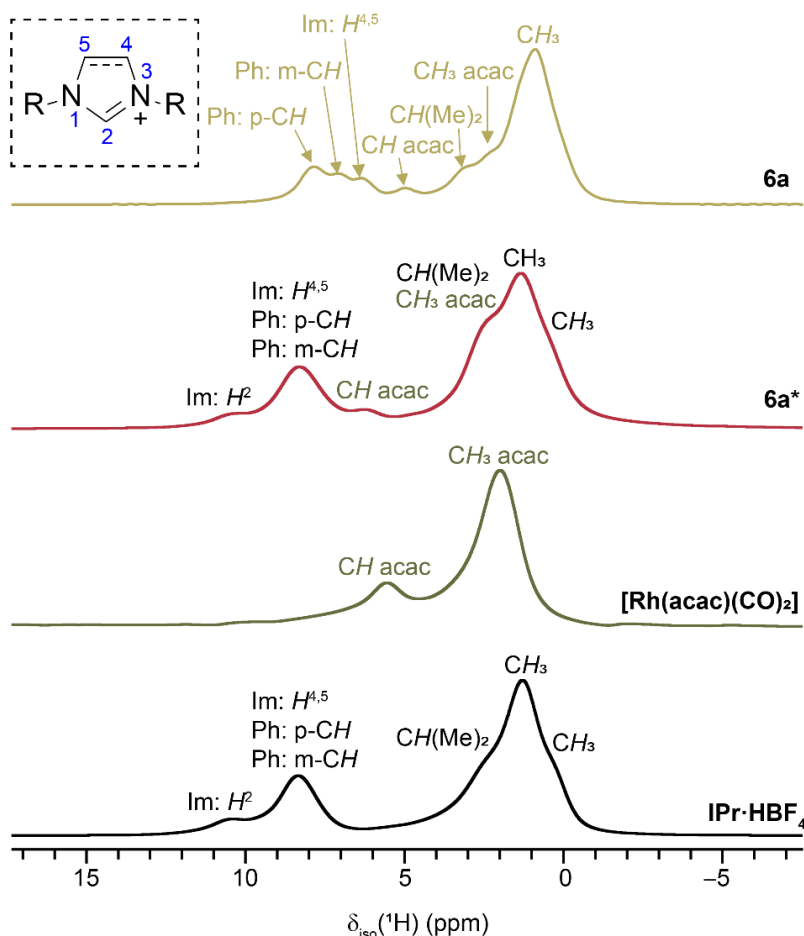


Figure 2.23. 1D ^1H wDUMBO-decoupled MAS NMR spectra of **IPr·HBF₄** (black), **[Rh(acac)(CO)₂]** (green), **6a*** (red), and **6a** (olive), acquired at $B_0 = 9.4$ T with a MAS frequency, $\nu_R = 12.5$ kHz. Peak assignment of the ^1H signals of **IPr·HBF₄**, **[Rh(acac)(CO)₂]**, and **6a** is based on their solvent-based ^1H NMR counterpart.^{33,86} The atom numbering of the imidazole ring is indicated on the structure shown as an inset.

2.4.1.3 ^{13}C ssNMR spectroscopy

Similar conclusions were drawn from the analysis of the 1D $^1\text{H} \rightarrow ^{13}\text{C}$ CP-MAS spectra of these samples (**Figure 2.24**). The ^{13}C signals observed were assigned based on ^{13}C isotropic chemical shifts measured in solution (**Figure 2.25**).^{31,86,87} Notably, the ^{13}C spectrum of **6a*** does not exhibit a doublet at 192 ppm, corresponding to the $^{13}\text{C}^2$ signal of the imidazolylidene moiety within the final product **6a**. Conversely, this spectrum contains a singlet at 140 ppm assigned to the $^{13}\text{C}^2$ signal of **IPr·HBF₄**. Furthermore, the carbonyl ^{13}C signals are similar for **[Rh(acac)(CO)₂]** and **6a*** and differ from those of **6a**. In particular, the ^{13}C signal of the CO ligand of **6a** at 178 ppm is not

observed in the spectrum of **6a**^{*}. Additionally, the presence of a signal at 170 ppm in the ¹³C spectrum of **6a**^{*} indicates the presence of K₂CO₃.³¹ Hence, the crude reaction mixture contains unreacted IPr·HBF₄, [Rh(acac)(CO)₂], and K₂CO₃ but no final product **6a**. This observation was further validated through the ATR-FTIR spectroscopic analysis discussed in the following section.

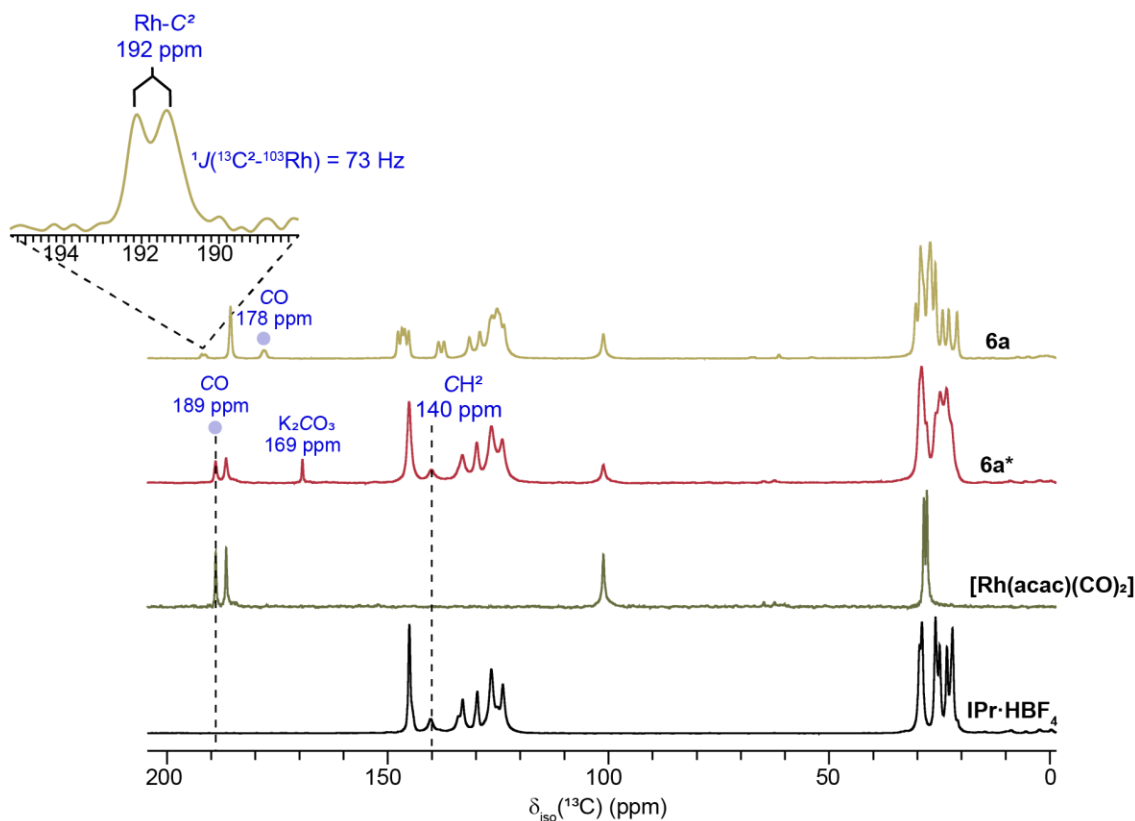


Figure 2.24. 1D ¹H→¹³C CP-MAS of IPr·HBF₄ (black), [Rh(acac)(CO)₂] (green), **6a**^{*} (red), and **6a** complex (olive), acquired at $B_0 = 9.4$ T with a MAS frequency, $\nu_R = 12.5$ kHz. An expansion of the ¹H→¹³C CP-MAS spectrum of **6a**, shown as an inset, displays the doublet assigned to the ¹³C² nucleus of the imidazolyliene ring split by the J -coupling constant $^1J(^{13}\text{C}-^{103}\text{Rh}) = 73$ Hz.

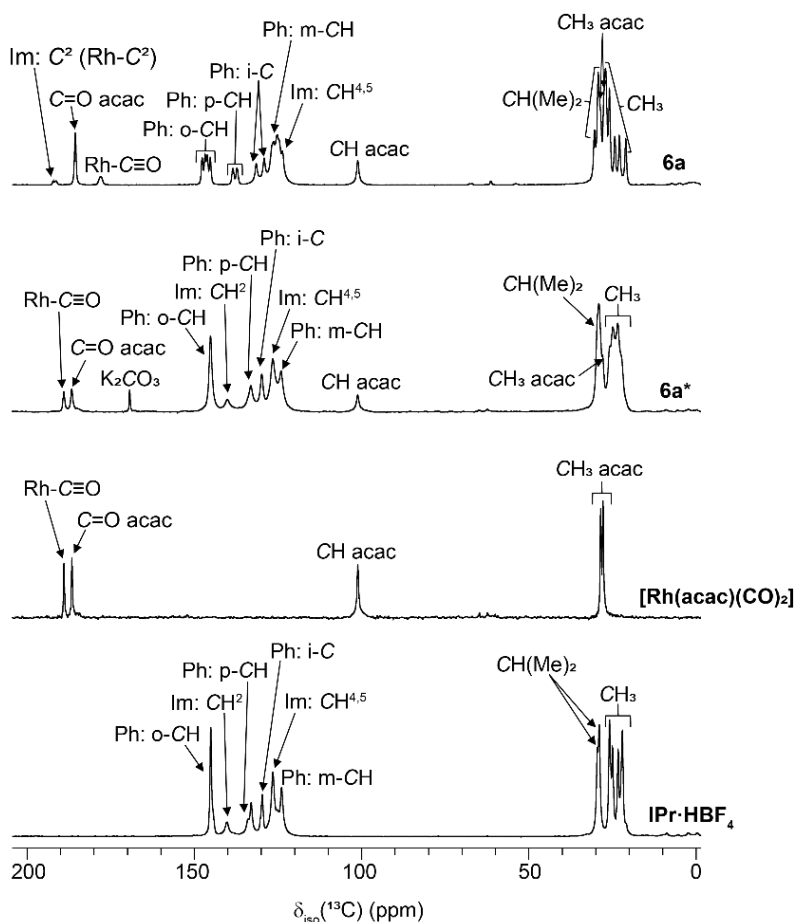


Figure 2.25. 1D $^1\text{H} \rightarrow ^{13}\text{C}$ CP-MAS spectra of $\text{IPr} \cdot \text{HBF}_4$, $[\text{Rh}(\text{acac})(\text{CO})_2]$, **6a***, and **6a**, acquired at $B_0 = 9.4$ T with a MAS frequency, $\nu_R = 12.5$ kHz. Peak assignment of the ^{13}C signals of $\text{IPr} \cdot \text{HBF}_4$, $[\text{Rh}(\text{acac})(\text{CO})_2]$, **6a**, and K_2CO_3 is based on their solvent-based ^{13}C NMR counterpart.^{31,86,87}

2.4.1.4 ^{15}N , ^{19}F , and ^{11}B ssNMR spectroscopy

The 1D $^1\text{H} \rightarrow ^{15}\text{N}$ CP-MAS, as well as 1D ^{11}B and ^{19}F MAS spectra presented in **Figure 2.26**, further confirm the presence of $\text{IPr} \cdot \text{HBF}_4$ and the absence of compound **6a** in the crude reaction mixture **6a***. Notably, the ^{19}F signal of $\text{IPr} \cdot \text{HBF}_4$ is broadened in **6a***, as compared to its appearance in $\text{IPr} \cdot \text{HBF}_4$. This broadening indicates a distribution of the local environment of ^{19}F nuclei in **6a*** mixture arising from the creation of crystallographic defects or reactant mixing by ball milling.

Furthermore, the 1D $^1\text{H} \rightarrow ^{15}\text{N}$ CP-MAS spectrum of **6a*** exhibits a ^{15}N signal at 184 ppm identical to that of $\text{IPr} \cdot \text{HBF}_4$. This result is consistent with the ^1H and ^{13}C data and supports our

observations that compound **6a** is not formed during the ball milling process but is formed only after the workup of the milled solids using solvents.

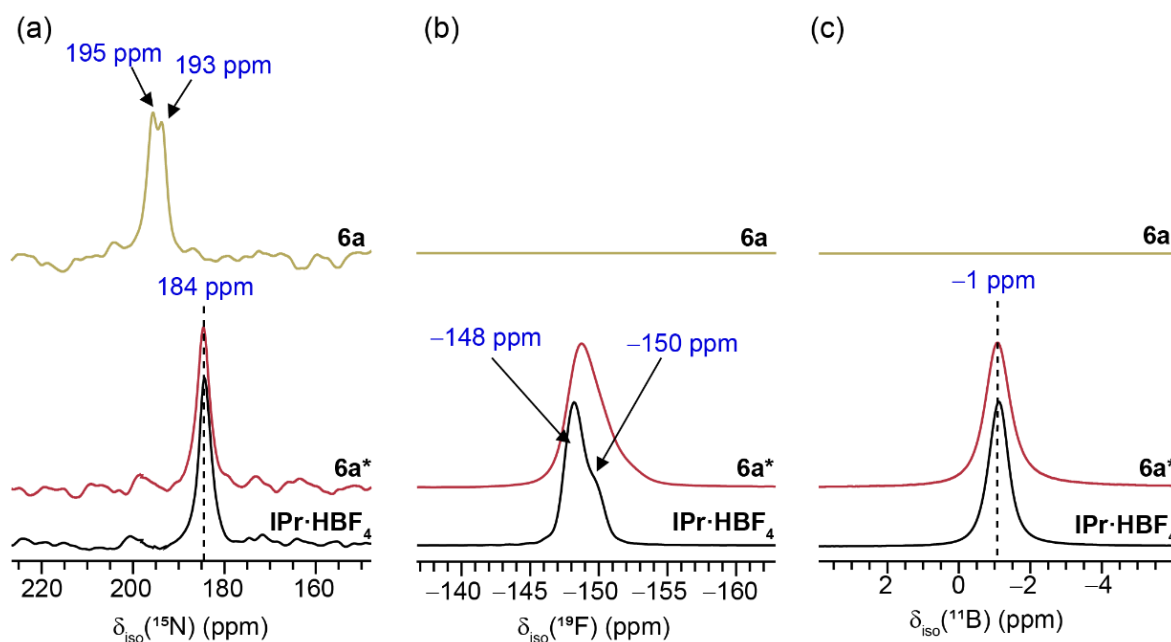


Figure 2.26. 1D (a) $^1\text{H}\rightarrow^{15}\text{N}$ CP-MAS, (b) ^{19}F MAS, and (c) ^{11}B MAS NMR spectra of $\text{IPr}\cdot\text{HBF}_4$ (black), $[\text{Rh}(\text{acac})(\text{CO})_2]$ (green), **6a*** (red), and **6a** (olive) acquired at $B_0 = 9.4$ T with a MAS frequency, $\nu_R = 12.5$ kHz for ^{15}N and ^{11}B and, $\nu_R = 20$ kHz for ^{19}F .

2.4.1.5 ATR-FTIR spectroscopy

To validate our NMR observations, we performed ATR-FTIR spectroscopic analysis on the solids of $[\text{Rh}(\text{acac})(\text{CO})_2]$, **6a***, and **6a** (Figure 2.27). The fingerprint infrared carbonyl region reveals no significant differences between the spectrum of $[\text{Rh}(\text{acac})(\text{CO})_2]$ and **6a***. The CO stretching frequencies are present in both spectra but are slightly shifted. In contrast, the spectrum of **6a** solely exhibited a single CO band at 1958 cm^{-1} .

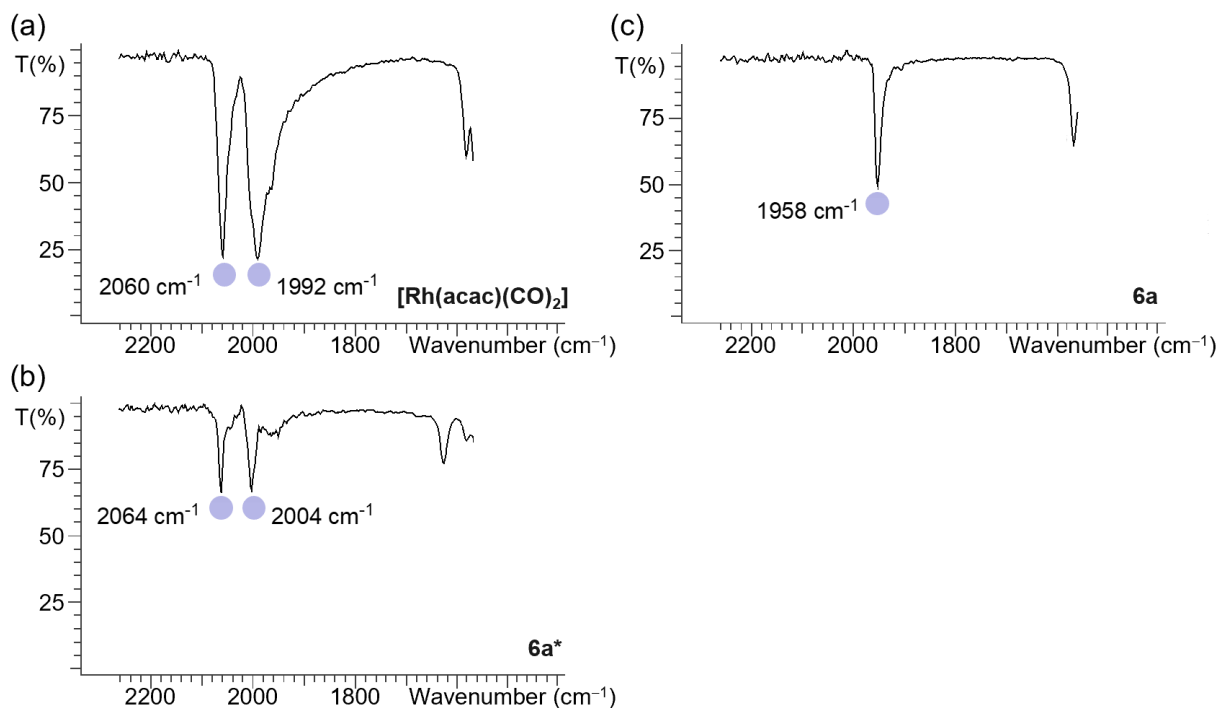


Figure 2.27. ATR-FTIR spectra of the carbonyl stretching region for (a) $[\text{Rh}(\text{acac})(\text{CO})_2]$, (b) 6a^* , and (c) 6a . All spectra were recorded directly on solids.

2.4.1.6 PXRD

The results from PXRD, as depicted in **Figure 2.28a**, further support our findings. The PXRD pattern of 6a^* shows that this mixture contains $\text{IPr}\cdot\text{HBF}_4$, $[\text{Rh}(\text{acac})(\text{CO})_2]$, and K_2CO_3 crystallites. Furthermore, reflections from 6a crystals were not detected in the XRD pattern of 6a^* . This observation confirms that compound 6a is not formed before the addition of the solvent. The reflections observed in the powder pattern of 6a^* are noticeably broader than those originating from the reagents since ball milling reduces the size of the crystallites and results in the formation of crystallographic defects, as illustrated in **Figure 2.28b**.

Therefore, all the experimental data gathered show that 6a^* is a physical mixture of the reagents resulting from mechanical treatment.

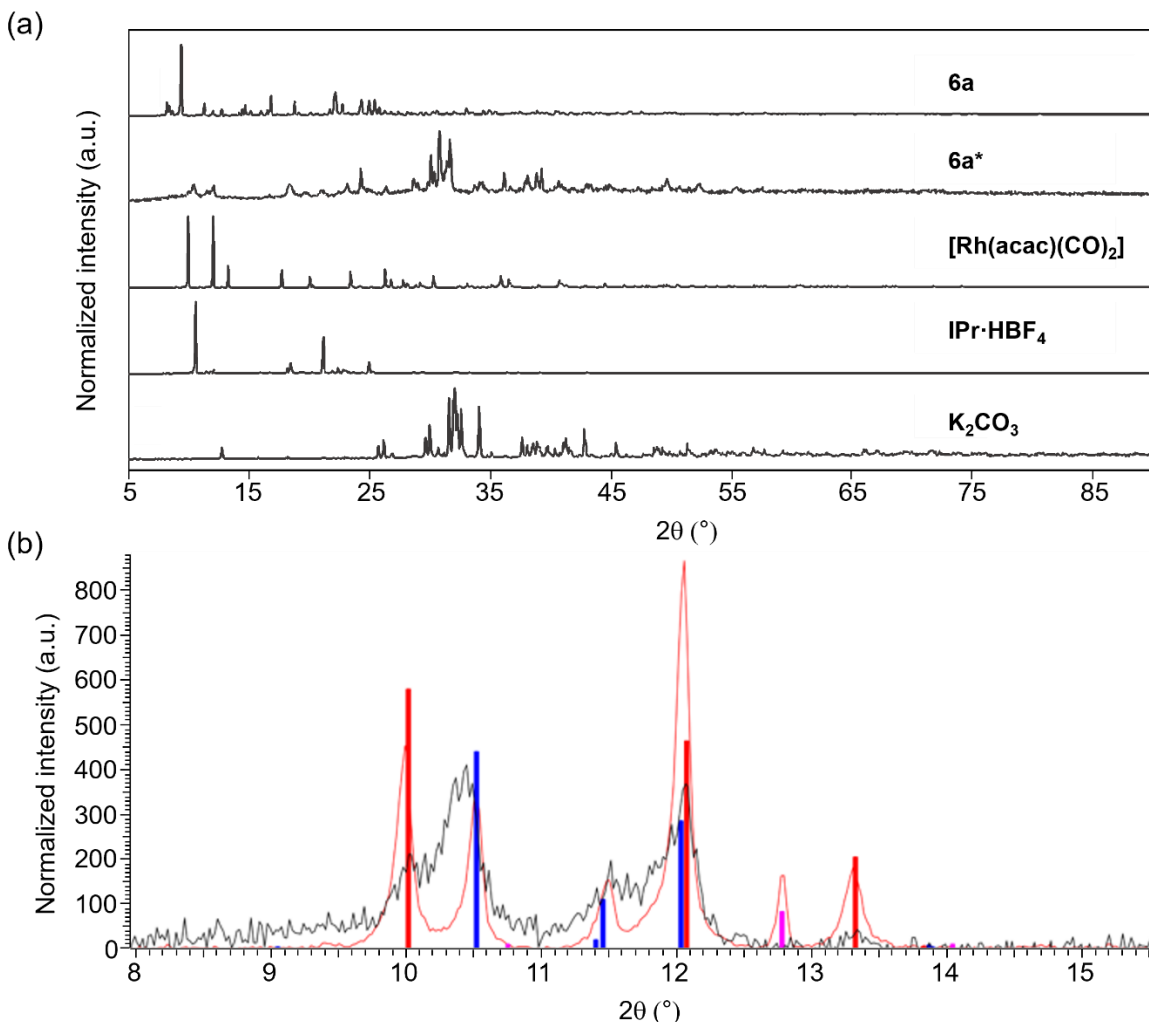


Figure 2.28. (a) PXRd patterns for **6a**, **6a***, [Rh(acac)(CO)₂], IPr·HBF₄, and K₂CO₃. (b) An expansion of the PXRd patterns between 2θ = 8 and 15.5° of **6a*** (black) and physical mixture of the reagents (IPr·HBF₄, [Rh(acac)(CO)₂], and K₂CO₃) (red) with the proportions used for the reaction (see **Scheme 2.6**). The simulated PXRd patterns of IPr·HBF₄ (blue), [Rh(acac)(CO)₂] (red), and K₂CO₃·1.5H₂O (pink) are also displayed. The PXRd pattern of the **6a*** mixture does not exhibit reflection of the **6a** complex, in particular at 2θ = 9°.

2.4.1.7 In situ ATR-FTIR spectroscopy

Considering these findings, the necessity for mechanical treatment before the reaction came into question. To assess this, kinetic profiles were established through in situ ATR-FTIR monitoring of reactions conducted in solution with both the pre-ground solid reactants (**6a***) and the non-pre-ground solid reactants, as illustrated in **Figure 2.29a**. Remarkably, these experiments

demonstrated the significant impact of pre-grinding, resulting in rapid reaction completion within a few minutes. In contrast, the reaction with non-pre-ground starting materials necessitated several hours at room temperature to achieve the same outcome. The corresponding profile is illustrated in **Figure 2.29b**. We then proceeded to explore whether comparable results could be achieved through manual grinding using a simple mortar and pestle. Encouragingly, this approach proved effective. Following the manual pre-grinding of the reaction components for 10 min, subsequent solvent addition and workup yielded a 72% yield of the complex **6a**.

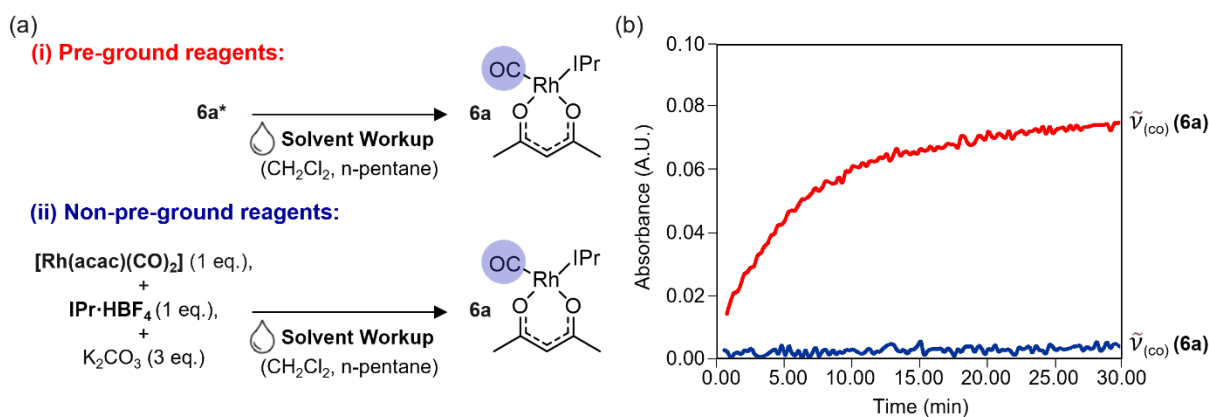


Figure 2.29. (a) Synthesis of compound **6a** involving a solvent-based workup process initiated with (i) pre-ground (**6a***) and (ii) non-pre-ground reagents. (b) Kinetic profiles of reactions with pre-ground (red) and non-pre-ground (blue) reagents. The progress of the reaction was tracked by monitoring the changes in the intensity of absorption of $\tilde{\nu}_{(\text{co})}$ corresponding to compound **6a** at 1961 cm⁻¹ after the addition of solvent for the pre-ground treated solids in comparison to the non-pre-ground solids.

2.4.2 Experimental Details

2.4.2.1 Samples preparation

All azolium tetrafluoroborate (**NHC**·HBF₄) salts used in this study (i.e. *N,N'*-bis-(2,6-diisopropylphenyl)imidazolium tetrafluoroborate or **IPr**·HBF₄, *N,N'*-bis-(2,6-diisopropylphenyl)imidazolinium tetrafluoroborate or **SIPr**·HBF₄, *N,N'*-bis-(2,4,6-trimethylphenyl)imidazolium tetrafluoroborate or **IMes**·HBF₄, *N,N'*-bis-(2,4,6-trimethylphenyl)imidazolinium tetrafluoroborate or **SIMes**·HBF₄, *N,N'*-bis-[2,6-bis(diphenylmethyl)-4-methylphenyl]imidazolium tetrafluoroborate or **IPr***·HBF₄, *N,N'*-bis-[2,6-bis(diphenylmethyl)-4-methoxyphenyl]imidazolium tetrafluoroborate or **IPr*OMe**·HBF₄) were

synthesized according to well-known literature procedures.^{55,88,89} K_2CO_3 was purchased from Carl Roth and used as received. The metal precursor, $[\text{Rh}(\text{acac})(\text{CO})_2]$, was purchased from Umicore and used as received. All solvents employed (i.e., *n*-pentane, CH_2Cl_2) were purchased from Chem-Lab and used without any further purification.

2.4.2.1.1 Mechanosynthesis

Ball Milling Experiments: A 12 mL ZrO_2 reactor was charged in the air with $\text{NHC}\cdot\text{HBF}_4$ (100 mg), $[\text{Rh}(\text{acac})(\text{CO})_2]$ (1 eq.), and K_2CO_3 (3 eq.) along with 28 balls of the same material (10.3 g, $\varnothing = 5$ mm). The reactor was sealed, and placed in a Fritsch Pulverisette 5/4 planetary ball mill, and its content was milled for 30 min at a maximum working frequency of 400 rpm.

Mortar and Pestle Experiments: $\text{IPr}\cdot\text{HBF}_4$ (100 mg, 0.21 mmol), $[\text{Rh}(\text{acac})(\text{CO})_2]$ (54 mg, 0.21 mmol), and K_2CO_3 (87 mg, 0.63 mmol) were manually ground using a ceramic mortar and pestle for approximately 10 min.

2.4.2.1.2 Workup

Solvent-Free (6a*): At the end of the milling process the content of the reactor was manually extracted with the aid of a spatula, transferred in a vial, and analyzed without any further manipulations.

Solvent-Based (6a): The mixture of solids obtained as a red-amaranth powder after ball milling, was extracted using CH_2Cl_2 (2×4 mL) to produce a yellow solution. This solution was first microfiltered in a 25 mL round-bottom flask to remove the excess base and then concentrated on a rotatory evaporator to approximately 1/4 of its original volume. To this solution, *n*-pentane (4 mL) was added and subsequently sonicated in a water bath at room temperature for a few minutes to induce the precipitation of unreacted $\text{NHC}\cdot\text{HBF}_4$ salt. The precipitate was filtered off and the filtrate concentrated to dryness on a rotatory evaporator under reduced pressure to afford a dirty-yellow solid residue. The residue was triturated using *n*-pentane (4 mL) and the suspended solid was subsequently collected by vacuum filtration on a fritted glass funnel (sinter $\varnothing = 5$ mm, porosity 3). Portions of *n*-pentane (3×1 mL) were used to wash the flask and the filter cake. After air was drawn through the filter cake for a few minutes, the product was transferred to a tared vial and then further dried under a high vacuum for several hours.

2.4.2.2 ssNMR spectroscopy

All ssNMR experiments were performed at room temperature on a wide-bore Bruker AVANCE NEO NMR spectrometer operating at a static magnetic field of 9.4 T, i.e. Larmor frequencies of 400.1 MHz for ^1H , 376.5 MHz for ^{19}F , 128.4 MHz for ^{11}B , 100.6 MHz for ^{13}C , and 40.5 MHz for ^{15}N . In ^1H , ^{13}C , ^{15}N , and ^{11}B MAS NMR experiments, powdered samples were packed into 4 mm outer diameter zirconia rotors sealed with Kel-F drive caps and spun at 12.5 kHz, whereas for ^{19}F MAS experiments, the samples were packed into 2.5 mm outer zirconia diameter sealed with Vespel caps and spun at 20 kHz.

The 1D ^1H and ^{13}C MAS NMR spectra were acquired with a triple resonance Bruker 4 mm triple-resonance (HXY) MAS probe operated in double resonance mode. 1D ^1H MAS NMR spectra were acquired using wDUMBO-S2 pulse sequence with an overall phase of π between successive DUMBO cycles,⁷³ which was optimized using α -glycine sample. The optimal length of the basic cycle of DUMBO sequence, corresponding approximately to a 6π pulse, was equal to 27 μs . The optimal rf field of the DUMBO scheme was 113 kHz. One block of DUMBO cycle was separated from the next cycle by a detection of window of 5 μs . The ^1H DUMBO spectra result from the averaging of 16 transients with a relaxation delay, $\tau_{\text{RD}} = 1.3$ s. The ^1H isotropic chemical shifts were referenced to TMS using the signal of the CH_2 group of adamantane at 1.85 ppm as a secondary reference.

The 1D $^1\text{H} \rightarrow ^{13}\text{C}$ CP-MAS experiments were performed using a ^1H $\pi/2$ pulse of 2.7 μs followed by a CP contact time of 1 ms. During the CP transfer, the rf nutation frequency on ^{13}C channel was constant and equal to 79 kHz, whereas that on ^1H channel was linearly ramped from 90 to 100. SPINAL-64 heteronuclear decoupling with rf nutation frequency of 93.5 kHz was applied on ^1H channel during the acquisition.⁵⁶ The 1D $^1\text{H} \rightarrow ^{13}\text{C}$ CP-MAS spectra resulted from averaging 8192 transients $\tau_{\text{RD}} = 1.3$ s, corresponding to an experimental time of 3 h. The ^1H and ^{13}C isotropic chemical shifts were referenced to neat TMS using the deshielded resonance (38.5 ppm) of adamantane as a secondary reference.

The 1D $^1\text{H} \rightarrow ^{15}\text{N}$ CP-MAS experiments were carried out using a 4 mm double-resonance HX low- γ MAS probe. The ^1H $\pi/2$ pulse of 2.7 μs was followed by a CP contact time of 4 ms. During the CP transfer, the rf nutation frequency on ^{15}N channel was constant and equal to 75 kHz, whereas that on ^1H channel was linearly ramped from 100 to 50. SW_F-TPPM heteronuclear decoupling with rf nutation frequency of 47 kHz was applied on ^1H channel during the

acquisition.⁵⁸ The 1D $^1\text{H} \rightarrow ^{15}\text{N}$ CP-MAS spectra resulted from averaging 10,500 transients with $T_{\text{RD}} = 1.3$ s, corresponding to a total experimental time of 4 h. The ^{15}N isotropic chemical shifts were referenced to liquid NH_3 using α -glycine (32.7 ppm) as a secondary reference.

The 1D ^{11}B MAS NMR spectra were acquired using a 4 mm double-resonance HX MAS probe and a Bloch decay sequence with a $\pi/2$ pulse of 2.7 μs employing an rf nutation frequency of 93 kHz. As ^{11}B nuclei in tetrahedral BF_4^- anion is subject to vanishing quadrupolar interaction, this pulse excites both the central transition between energy levels $+1/2 \leftrightarrow -1/2$ and the satellite transitions between levels $\pm 3/2 \leftrightarrow \pm 1/2$. The ^{11}B spectra result from averaging 128 transients with $T_{\text{RD}} = 5$ s, corresponding to a total experimental time of 11 min. The ^{11}B isotropic chemical shifts were referenced to $\text{Et}_2\text{O} \cdot \text{BF}_3$ using NaBH_4 (−42.06 ppm) as a secondary reference.

The 1D ^{19}F MAS NMR spectra were acquired using a 4 mm double-resonance HX MAS probe and a Bloch decay sequence with a $\pi/2$ pulse of 2.6 μs . The ^{19}F NMR spectra result from averaging 64 transients with $T_{\text{RD}} = 10$ s, corresponding to a total experimental time of 11 min. The ^{19}F isotropic chemical shifts were referenced to CFCl_3 using CaF_2 (−108 ppm) as a secondary reference.

2.4.2.3 PXRD

PXRD patterns were obtained at 298 K using a Bruker D8 Avance diffractometer with motorized anti-scatter screen and autochanger, in Bragg-Brentano θ - θ geometry (goniometer radius 280 mm) and using the Cu $K\alpha$ -radiation ($\lambda = 1.54184$ Å). A Bruker LynxEye XE-T silicon stripe line detector with 192 channels was used at the secondary beam side. Measurements were carried out in $4^\circ \leq 2\theta \leq 90^\circ$ range, with a step size of 0.02° and a total scan time of 18 min.

2.4.2.4 ATR-FTIR spectroscopy

ATR-FTIR measurements on powdered samples were obtained at 298 K using a PerkinElmer Spectrum 1000 spectrometer equipped with a PIKE MIRacle single reflection ATR module. Spectra were collected in transmission mode in the spectral range $4000\text{--}600$ cm^{-1} , at 1 cm^{-1} resolution and 8 scans per spectrum.

2.4.2.5 In-Situ ATR-FTIR spectroscopy

All measurements were conducted using a Mettler-Toledo AutoChem Inc. ReactIR 15™ spectrometer equipped with a DS AgX FiberConduit sampler.

Experiments starting with pre-ground reagents: The pre-ground solid **6a*** was transferred into a two-necked round bottom flask equipped with a magnetic stirring bar and one of the two necks fitted with a DS AgX FiberConduit IR probe. Once the solids were introduced in the reaction flask and its headspace purged with argon Ar, the IR recording was started followed by the slow addition of CH₂Cl₂ (5 mL), and the reaction was monitored for 30 min while magnetically stirring the solution at 650 rpm. IR spectra were acquired at 16 scans every 15 s. At the end of the 30 min, the solution was microfiltered in a 25 mL flask to remove all the insoluble, and all volatiles were subsequently removed by rotatory evaporation. The afforded solid was dispersed in *n*-pentane (2 - 4 mL), the resulting solution sonicated for a few minutes, and the precipitate collected by vacuum filtration and then dried under vacuum for several hours. [Rh(acac)(CO)(IPr)] **6a** was obtained as a yellow solid in 86% yield (112.3 mg, 0.18 mmol).

Experiments starting with non-pre-ground reagents: A mixture of IPr·HBF₄ (100.0 mg, 0.21 mmol), [Rh(acac)(CO)₂] (54.2 mg, 0.21 mmol), and K₂CO₃ (87.0 mg, 0.63 mmol) was placed in a two-necked round bottom flask equipped with a magnetic stirring bar and one of the two necks fitted with a DS AgX FiberConduit IR probe. Once the solids were introduced in the reaction flask and its headspace purged with argon Ar, the IR recording was started followed by the slow addition of CH₂Cl₂ (5 mL), and the reaction was monitored for 240 min while magnetically stirring the solution at 650 rpm. IR spectra were acquired at 16 scans every 15 s. At the end of the 240 min, an aliquot (150 μL) of the reaction solution was withdrawn, transferred to an NMR tube, and after all the volatiles were removed and the resulting solid residue dissolved in CDCl₃, analyzed by NMR.

2.4.3 Conclusion

In summary, we have reported the application of mechanochemistry to synthesize a series of [Rh(acac)(CO)(NHC)] complexes using a weak base synthetic route. These complexes were derived from common NHC·HBF₄ salts and a commercially available precursor, [Rh(acac)(CO)₂]. The mechanism leading to the formation of the desired complexes was examined through a combination of ssNMR spectroscopy, ATR-FTIR spectroscopy, and PXRD techniques carried out on solids. The spectroscopic data unequivocally confirm the necessity of a solvent to drive the

ligand binding and substitution reactions to completion, ultimately leading to product formation. While grinding was found to assist the reaction, the primary drive toward product formation was brought about by events occurring during or after solvent addition. We believe that this described method will prove convenient for the synthetic community seeking access to organometallic complexes.

2.4.4 Statement of Contribution

Section **2.4** of Chapter 2 presents original, unpublished material that will be part of the upcoming publication. I am the second author of the paper, along with co-authors: Gianmarco Pisanò, Dr. Julien Trébosc, Dr. Ida Ritacco, Dr. Pascal Roussel, Prof. Dr. Lucia Caporaso, Prof. Dr. Luigi Cavallo, Prof. Dr. Olivier Lafon, Prof. Dr. Steven P. Nolan, and Prof. Dr. Catherine S. J. Cazin. My role involved conducting ssNMR experiments, analyzing results, writing the ssNMR section, and contributing to paper editing. G.P. carried out the synthesis experiments and wrote the original draft of the paper. J.T. assisted in the ssNMR experiments. P.R. conducted PXRD experiments. I.R., L.F., and L.C. performed DFT calculations. S.N.P. contributed to the analysis and interpretation of the results and assisted in editing the article. C.S.J.C and O.L. provided supervision, result analysis, and editing of the article.

2.5 References

- (1) Do, J.-L.; Friščić, T. Mechanochemistry: A Force of Synthesis. *ACS Cent. Sci.* **2017**, *3* (1), 13–19. <https://doi.org/10.1021/acscentsci.6b00277>.
- (2) Friščić, T.; Mottillo, C.; Titi, H. M. Mechanochemistry for Synthesis. *Angew. Chem. Int. Ed.* **2020**, *59* (3), 1018–1029. <https://doi.org/10.1002/anie.201906755>.
- (3) Stolle, A.; Szuppa, T.; Leonhardt, S. E. S.; Ondruschka, B. Ball Milling in Organic Synthesis: Solutions and Challenges. *Chem. Soc. Rev.* **2011**, *40* (5), 2317–2329. <https://doi.org/10.1039/C0CS00195C>.
- (4) Tan, D.; Friščić, T. Mechanochemistry for Organic Chemists: An Update. *Eur. J. Org. Chem.* **2018**, *2018* (1), 18–33. <https://doi.org/10.1002/ejoc.201700961>.
- (5) Rightmire, N. R.; Hanusa, T. P. Advances in Organometallic Synthesis with Mechanochemical Methods. *Dalton Trans.* **2016**, *45* (6), 2352–2362. <https://doi.org/10.1039/C5DT03866A>.

- (6) Beillard, A.; Bantreil, X.; Métro, T.-X.; Martinez, J.; Lamaty, F. Alternative Technologies That Facilitate Access to Discrete Metal Complexes. *Chem. Rev.* **2019**, *119* (12), 7529–7609. <https://doi.org/10.1021/acs.chemrev.8b00479>.
- (7) Tan, D.; García, F. Main Group Mechanochemistry: From Curiosity to Established Protocols. *Chem. Soc. Rev.* **2019**, *48* (8), 2274–2292. <https://doi.org/10.1039/C7CS00813A>.
- (8) Friščić, T. Supramolecular Concepts and New Techniques in Mechanochemistry: Cocrystals, Cages, Rotaxanes, Open Metal–Organic Frameworks. *Chem. Soc. Rev.* **2012**, *41* (9), 3493–3510. <https://doi.org/10.1039/C2CS15332G>.
- (9) Porcheddu, A.; Colacino, E.; De Luca, L.; Delogu, F. Metal-Mediated and Metal-Catalyzed Reactions Under Mechanochemical Conditions. *ACS Catal.* **2020**, *10* (15), 8344–8394. <https://doi.org/10.1021/acscatal.0c00142>.
- (10) Bolm, C.; Hernández, J. G. From Synthesis of Amino Acids and Peptides to Enzymatic Catalysis: A Bottom-Up Approach in Mechanochemistry. *ChemSusChem* **2018**, *11* (9), 1410–1420. <https://doi.org/10.1002/cssc.201800113>.
- (11) Clarke, C. J.; Tu, W.-C.; Levers, O.; Bröhl, A.; Hallett, J. P. Green and Sustainable Solvents in Chemical Processes. *Chem. Rev.* **2018**, *118* (2), 747–800. <https://doi.org/10.1021/acs.chemrev.7b00571>.
- (12) Howard, J. L.; Cao, Q.; Browne, D. L. Mechanochemistry as an Emerging Tool for Molecular Synthesis: What Can It Offer? *Chem. Sci.* **2018**, *9* (12), 3080–3094. <https://doi.org/10.1039/C7SC05371A>.
- (13) Hernández, J. G.; Bolm, C. Altering Product Selectivity by Mechanochemistry. *J. Org. Chem.* **2017**, *82* (8), 4007–4019. <https://doi.org/10.1021/acs.joc.6b02887>.
- (14) Seo, T.; Toyoshima, N.; Kubota, K.; Ito, H. Tackling Solubility Issues in Organic Synthesis: Solid-State Cross-Coupling of Insoluble Aryl Halides. *J. Am. Chem. Soc.* **2021**, *143* (16), 6165–6175. <https://doi.org/10.1021/jacs.1c00906>.
- (15) Kaupp, G. Mechanochemistry: The Varied Applications of Mechanical Bond-Breaking. *CrystEngComm* **2009**, *11* (3), 388–403. <https://doi.org/10.1039/B810822F>.

- (16) Boldyreva, E. Mechanochemistry of Inorganic and Organic Systems: What Is Similar, What Is Different? *Chem. Soc. Rev.* **2013**, 42 (18), 7719–7738. <https://doi.org/10.1039/C3CS60052A>.
- (17) Koby, R. F.; Doerr, A. M.; Rightmire, N. R.; Schley, N. D.; Brennessel, W. W.; Long, B. K.; Hanusa, T. P. Mechanochemical Formation, Solution Rearrangements, and Catalytic Behavior of a Polymorphic Ca/K Allyl Complex. *Chem. Eur. J.* **2021**, 27 (31), 8195–8202. <https://doi.org/10.1002/chem.202100589>.
- (18) Lukin, S.; Germann, L. S.; Frišćić, T.; Halasz, I. Toward Mechanistic Understanding of Mechanochemical Reactions Using Real-Time In Situ Monitoring. *Acc. Chem. Res.* **2022**, 55 (9), 1262–1277. <https://doi.org/10.1021/acs.accounts.2c00062>.
- (19) Silva, I. d'Anciães A.; Bartalucci, E.; Bolm, C.; Wiegand, T. Opportunities And Challenges in Applying Solid-State Nmr Spectroscopy in Organic Mechanochemistry. *Adv. Mater.* **2023**, 2304092. <https://doi.org/10.1002/adma.202304092>.
- (20) Leroy, C.; Métro, T.-X.; Laurencin, D. 9.18 - The Expanding Frontier between Mechanochemistry & Solid State NMR: Special Focus on Inorganic Components of Materials. In *Comprehensive Inorganic Chemistry III (Third Edition)*; Reedijk, J., Poeppelemeier, K. R., Eds.; Elsevier: Oxford, 2023; pp 514–533. <https://doi.org/10.1016/B978-0-12-823144-9.00136-9>.
- (21) Díez-González, S.; Nolan, S. P. Copper, Silver, and Gold Complexes in Hydrosilylation Reactions. *Acc. Chem. Res.* **2008**, 41 (2), 349–358. <https://doi.org/10.1021/ar7001655>.
- (22) Lazreg, F.; Nahra, F.; Cazin, C. S. J. Copper–NHC Complexes in Catalysis. *Coord. Chem. Rev.* **2015**, 293–294, 48–79. <https://doi.org/10.1016/j.ccr.2014.12.019>.
- (23) Mercks, L.; Albrecht, M. Beyond Catalysis: N-Heterocyclic Carbene Complexes as Components for Medicinal, Luminescent, and Functional Materials Applications. *Chem. Soc. Rev.* **2010**, 39 (6), 1903–1912. <https://doi.org/10.1039/B902238B>.
- (24) Nayak, S.; Gaonkar, S. L. Coinage Metal N-Heterocyclic Carbene Complexes: Recent Synthetic Strategies and Medicinal Applications. *ChemMedChem* **2021**, 16 (9), 1360–1390. <https://doi.org/10.1002/cmdc.202000836>.

- (25) Pan, T.; Wang, Y.; Liu, F.-S.; Lin, H.; Zhou, Y. Copper(I)–NHCs Complexes: Synthesis, Characterization and Their Inhibition against the Biofilm Formation of *Streptococcus Mutans*. *Polyhedron* **2021**, *197*, 115033. <https://doi.org/10.1016/j.poly.2021.115033>.
- (26) Ekinci, O.; Akkoç, M.; Khan, S.; Yaşar, S.; Gürses, C.; Noma, S.; Balcıoğlu, S.; Sen, B.; Aygün, M.; Yılmaz, İ. Synthesis and Biological Evaluation of Au-NHC Complexes. *Appl. Organomet. Chem.* **2022**, *36* (9), e6811. <https://doi.org/10.1002/aoc.6811>.
- (27) Aleksanyan, D. V.; Kozlov, V. A. Mechanochemical Tools in the Synthesis of Organometallic Compounds. *Mendeleev Commun.* **2023**, *33* (3), 287–301. <https://doi.org/10.1016/j.mencom.2023.04.001>.
- (28) De, S.; Joó, F.; Horváth, H.; Udvardy, A.; Czégéni, C. E. Stirring or Milling? First Synthesis of Rh(I)–(Di-N-Heterocyclic Carbene) Complexes Both in Solution and in a Ball Mill. *J. Organomet. Chem.* **2020**, *918*, 121308. <https://doi.org/10.1016/j.jorganchem.2020.121308>.
- (29) Pisanò, G.; Cazin, C. S. J. Mechanochemical Synthesis of Cu(I)–N-Heterocyclic Carbene Complexes. *Green Chem.* **2020**, *22* (16), 5253–5256. <https://doi.org/10.1039/D0GC01923B>.
- (30) Martynova, E. A.; Tzouras, N. V.; Pisanò, G.; Cazin, C. S. J.; Nolan, S. P. The “Weak Base Route” Leading to Transition Metal–N-Heterocyclic Carbene Complexes. *Chem. Commun.* **2021**, *57* (32), 3836–3856. <https://doi.org/10.1039/D0CC08149C>.
- (31) Stueber, D.; Patterson, D.; Mayne, C. L.; Orendt, A. M.; Grant, D. M.; Parry, R. W. Carbonates, Thiocarbonates, and the Corresponding Monoalkyl Derivatives. 1. Their Preparation and Isotropic (13)C NMR Chemical Shifts. *Inorg. Chem.* **2001**, *40* (8), 1902–1911. <https://doi.org/10.1021/ic0012266>.
- (32) Santoro, O.; Collado, A.; Slawin, A. M. Z.; Nolan, S. P.; Cazin, C. S. J. A General Synthetic Route to [Cu(X)(NHC)] (NHC = N-Heterocyclic Carbene, X = Cl, Br, I) Complexes. *Chem. Commun.* **2013**, *49* (89), 10483–10485. <https://doi.org/10.1039/C3CC45488F>.
- (33) Beillard, A.; Métro, T.-X.; Bantreil, X.; Martinez, J.; Lamaty, F. Cu(0), O₂ and Mechanical Forces: A Saving Combination for Efficient Production of Cu–NHC Complexes. *Chem. Sci.* **2017**, *8* (2), 1086–1089. <https://doi.org/10.1039/C6SC03182J>.

- (34) Ishii, Y.; Yesinowski, J. P.; Tycko, R. Sensitivity Enhancement in Solid-State ^{13}C NMR of Synthetic Polymers and Biopolymers by ^1H NMR Detection with High-Speed Magic Angle Spinning. *J. Am. Chem. Soc.* **2001**, *123* (12), 2921–2922. <https://doi.org/10.1021/ja015505j>.
- (35) Wiench, J. W.; Bronnimann, C. E.; Lin, V. S.-Y.; Pruski, M. Chemical Shift Correlation NMR Spectroscopy with Indirect Detection in Fast Rotating Solids: Studies of Organically Functionalized Mesoporous Silicas. *J. Am. Chem. Soc.* **2007**, *129* (40), 12076–12077. <https://doi.org/10.1021/ja074746+>.
- (36) Harris, R. K.; Olivieri, A. C. Quadrupolar Effects Transferred to Spin-12 Magic-Angle Spinning Spectra of Solids. *Prog. Nucl. Magn. Reson. Spectrosc.* **1992**, *24* (5), 435–456. [https://doi.org/10.1016/0079-6565\(92\)80004-Y](https://doi.org/10.1016/0079-6565(92)80004-Y).
- (37) Kaur, H.; Zinn, F. K.; Stevens, E. D.; Nolan, S. P. (NHC)Cu^I (NHC = N-Heterocyclic Carbene) Complexes as Efficient Catalysts for the Reduction of Carbonyl Compounds. *Organometallics* **2004**, *23* (5), 1157–1160. <https://doi.org/10.1021/om034285a>.
- (38) Kaeffer, N.; Mance, D.; Copéret, C. N-Heterocyclic Carbene Coordination to Surface Copper Sites in Selective Semihydrogenation Catalysts from Solid-State NMR Spectroscopy. *Angew. Chem.* **2020**, *132* (45), 20174–20182. <https://doi.org/10.1002/ange.202006209>.
- (39) Pyykkö, P. Year-2017 Nuclear Quadrupole Moments. *Mol. Phys.* **2018**, *116* (10), 1328–1338. <https://doi.org/10.1080/00268976.2018.1426131>.
- (40) Kroeker, S.; Hanna, J. V.; Wasylishen, R. E.; Ainscough, E. W.; Brodie, A. M. Anisotropy in The ^{31}P , $^{63/65}\text{Cu}$ Indirect Spin–Spin Coupling And ^{31}P Nuclear Shielding Tensors of Linear Copper(I) Phosphines. *J. Magn. Reson.* **1998**, *135* (1), 208–215. <https://doi.org/10.1006/jmre.1998.1580>.
- (41) Kroeker, S.; Wasylishen, R. E.; Hanna, J. V. The Structure of Solid Copper(I) Cyanide: A Multinuclear Magnetic and Quadrupole Resonance Study. *J. Am. Chem. Soc.* **1999**, *121* (7), 1582–1590. <https://doi.org/10.1021/ja983253p>.
- (42) Tang, J. A.; Ellis, B. D.; Warren, T. H.; Hanna, J. V.; Macdonald, C. L. B.; Schurko, R. W. Solid-State ^{63}Cu and ^{65}Cu NMR Spectroscopy of Inorganic and Organometallic Copper(I)

- Complexes. *J. Am. Chem. Soc.* **2007**, *129* (43), 13049–13065. <https://doi.org/10.1021/ja073238x>.
- (43) Aguiar, P. M.; Kroeker, S. Cyanide Orientational Ordering and Copper Electric Field Gradients in $\text{CuCN}\cdot\text{N}_2\text{H}_4$. *Phys. Chem. Chem. Phys.* **2009**, *11* (5), 834–840. <https://doi.org/10.1039/B808266A>.
- (44) Lucier, B. E. G.; Tang, J. A.; Schurko, R. W.; Bowmaker, G. A.; Healy, P. C.; Hanna, J. V. Solid-State ^{65}Cu and ^{31}P NMR Spectroscopy of Bis(Triphenylphosphine) Copper Species. *J. Phys. Chem. C* **2010**, *114* (17), 7949–7962. <https://doi.org/10.1021/jp907477m>.
- (45) Benito, Q.; Le Goff, X. F.; Nocton, G.; Fargues, A.; Garcia, A.; Berhault, A.; Kahlal, S.; Saillard, J.-Y.; Martineau, C.; Trébosc, J.; Gacoin, T.; Boilot, J.-P.; Perruchas, S. Geometry Flexibility of Copper Iodide Clusters: Variability in Luminescence Thermochromism. *Inorg. Chem.* **2015**, *54* (9), 4483–4494. <https://doi.org/10.1021/acs.inorgchem.5b00321>.
- (46) Larsen, F. H.; Jakobsen, H. J.; Ellis, P. D.; Nielsen, N. Chr. Sensitivity-Enhanced Quadrupolar-Echo NMR of Half-Integer Quadrupolar Nuclei. Magnitudes and Relative Orientation of Chemical Shielding and Quadrupolar Coupling Tensors. *J. Phys. Chem. A* **1997**, *101* (46), 8597–8606. <https://doi.org/10.1021/jp971547b>.
- (47) Massiot, D.; Farnan, I.; Gautier, N.; Trumeau, D.; Trokiner, A.; Coutures, J. P. ^{71}Ga and ^{69}Ga Nuclear Magnetic Resonance Study of $\beta\text{-Ga}_2\text{O}_3$: Resolution of Four- and Six-Fold Coordinated Ga Sites in Static Conditions. *Solid State Nucl. Magn. Reson.* **1995**, *4* (4), 241–248. [https://doi.org/10.1016/0926-2040\(95\)00002-8](https://doi.org/10.1016/0926-2040(95)00002-8).
- (48) Perras, F. A.; Widdifield, C. M.; Bryce, D. L. QUEST-QUadrupolar Exact SoftWare: A Fast Graphical Program for the Exact Simulation of NMR and NQR Spectra for Quadrupolar Nuclei. *Solid State Nucl. Magn. Reson.* **2012**, *45–46*, 36–44. <https://doi.org/10.1016/j.ssnmr.2012.05.002>.
- (49) O'Dell, L. A. The WURST Kind of Pulses in Solid-State NMR. *Solid State Nucl. Magn. Reson.* **2013**, *55–56*, 28–41. <https://doi.org/10.1016/j.ssnmr.2013.10.003>.
- (50) Bryce, D. L.; Gee, M.; Wasylshen, R. E. High-Field Chlorine NMR Spectroscopy of Solid Organic Hydrochloride Salts: A Sensitive Probe of Hydrogen Bonding Environment. *J. Phys. Chem. A* **2001**, *105* (45), 10413–10421. <https://doi.org/10.1021/jp011962a>.

- (51) Bryce, D. L.; Sward, G. D.; Adiga, S. Solid-State $^{35/37}\text{Cl}$ NMR Spectroscopy of Hydrochloride Salts of Amino Acids Implicated in Chloride Ion Transport Channel Selectivity: Opportunities at 900 MHz. *J. Am. Chem. Soc.* **2006**, *128* (6), 2121–2134. <https://doi.org/10.1021/ja057253i>.
- (52) Hamaed, H.; Pawlowski, J. M.; Cooper, B. F. T.; Fu, R.; Eichhorn, S. H.; Schurko, R. W. Application of Solid-State ^{35}Cl NMR to the Structural Characterization of Hydrochloride Pharmaceuticals and Their Polymorphs. *J. Am. Chem. Soc.* **2008**, *130* (33), 11056–11065. <https://doi.org/10.1021/ja802486q>.
- (53) Namespetra, A. M.; Hirsh, D. A.; Hildebrand, M. P.; Sandre, A. R.; Hamaed, H.; Rawson, J. M.; Schurko, R. W. ^{35}Cl Solid-State NMR Spectroscopy of HCl Pharmaceuticals and Their Polymorphs in Bulk and Dosage Forms. *CrystEngComm* **2016**, *18* (33), 6213–6232. <https://doi.org/10.1039/C6CE01069E>.
- (54) Rossini, A. J.; Mills, R. W.; Briscoe, G. A.; Norton, E. L.; Geier, S. J.; Hung, I.; Zheng, S.; Autschbach, J.; Schurko, R. W. Solid-State Chlorine NMR of Group IV Transition Metal Organometallic Complexes. *J. Am. Chem. Soc.* **2009**, *131* (9), 3317–3330. <https://doi.org/10.1021/ja808390a>.
- (55) Bantreil, X.; Nolan, S. P. Synthesis of N-Heterocyclic Carbene Ligands and Derived Ruthenium Olefin Metathesis Catalysts. *Nat. Protoc.* **2011**, *6* (1), 69–77. <https://doi.org/10.1038/nprot.2010.177>.
- (56) Fung, B. M.; Khitrin, A. K.; Ermolaev, K. An Improved Broadband Decoupling Sequence for Liquid Crystals and Solids. *J. Magn. Reson.* **2000**, *142* (1), 97–101. <https://doi.org/10.1006/jmre.1999.1896>.
- (57) WSolids1 1.21.3, K. Eichele, Universität Tübingen 2015.
- (58) Thakur, R. S.; Kurur, N. D.; Madhu, P. K. Swept-Frequency Two-Pulse Phase Modulation for Heteronuclear Dipolar Decoupling in Solid-State NMR. *Chem. Phys. Lett.* **2006**, *426* (4), 459–463. <https://doi.org/10.1016/j.cplett.2006.06.007>.
- (59) Kupce, E.; Freeman, R. Adiabatic Pulses for Wideband Inversion and Broadband Decoupling. *J. Magn. Reson. Ser. A* **1995**, *115* (2), 273–276. <https://doi.org/10.1006/jmra.1995.1179>.

- (60) Bhattacharyya, R.; Frydman, L. Quadrupolar Nuclear Magnetic Resonance Spectroscopy in Solids Using Frequency-Swept Echoing Pulses. *J. Chem. Phys.* **2007**, *127* (19), 194503. <https://doi.org/10.1063/1.2793783>.
- (61) Harris, R. K.; Becker, E. D.; Cabral de Menezes, S. M.; Goodfellow, R.; Granger, P. NMR Nomenclature. Nuclear Spin Properties and Conventions for Chemical Shifts (IUPAC Recommendations 2001). *Pure Appl. Chem.* **2001**, *73* (11), 1795–1818. <https://doi.org/10.1351/pac200173111795>.
- (62) Adamo, C.; Barone, V. Toward Reliable Density Functional Methods without Adjustable Parameters: The PBE0 Model. *J. Chem. Phys.* **1999**, *110* (13), 6158–6170. <https://doi.org/10.1063/1.478522>.
- (63) Fonseca Guerra, C.; Snijders, J. G.; te Velde, G.; Baerends, E. J. Towards an Order-N DFT Method. *Theor. Chem. Acc.* **1998**, *99* (6), 391–403. <https://doi.org/10.1007/s002140050353>.
- (64) Kresse, G.; Hafner, J. Ab Initio Molecular Dynamics for Open-Shell Transition Metals. *Phys. Rev. B* **1993**, *48* (17), 13115–13118. <https://doi.org/10.1103/PhysRevB.48.13115>.
- (65) Perdew, J. P.; Burke, K.; Ernzerhof, M. Generalized Gradient Approximation Made Simple. *Phys. Rev. Lett.* **1996**, *77* (18), 3865–3868. <https://doi.org/10.1103/PhysRevLett.77.3865>.
- (66) Blue, E. D.; Gunnoe, T. B.; Petersen, J. L.; Boyle, P. D. Protonation of N-Heterocyclic Carbene Ligand Coordinated to Copper(I): Coordination Mode of Imidazolium Cation as a Function of Counterion as Determined by Solid-State Structures. *J. Organomet. Chem.* **2006**, *691* (26), 5988–5993. <https://doi.org/10.1016/j.jorganchem.2006.09.051>.
- (67) Pickard, C. J.; Mauri, F. All-Electron Magnetic Response with Pseudopotentials: NMR Chemical Shifts. *Phys. Rev. B* **2001**, *63* (24), 245101. <https://doi.org/10.1103/PhysRevB.63.245101>.
- (68) Yates, J. R.; Pickard, C. J.; Mauri, F. Calculation of NMR Chemical Shifts for Extended Systems Using Ultrasoft Pseudopotentials. *Phys. Rev. B* **2007**, *76* (2), 024401. <https://doi.org/10.1103/PhysRevB.76.024401>.

- (69) Lin, I. J. B.; Vasam, C. S. Preparation and Application of N-Heterocyclic Carbene Complexes of Ag(I). *Coord. Chem. Rev.* **2007**, *251* (5), 642–670. <https://doi.org/10.1016/j.ccr.2006.09.004>.
- (70) Johnson, N. A.; Southerland, M. R.; Youngs, W. J. Recent Developments in the Medicinal Applications of Silver-NHC Complexes and Imidazolium Salts. *Molecules* **2017**, *22* (8), 1263. <https://doi.org/10.3390/molecules22081263>.
- (71) Rojo-Gómez, E. G.; Zuno-Cruz, F. J.; Sánchez-Cabrera, G.; Carpio-Granillo, M.; González-Ábrego, D. O.; Coronel-Olivares, C.; Alvarado-Rodríguez, J. G.; Rosales-Hoz, M. J. Synthesis, Structural Characterization, and Antibacterial Activity of Alkenyl Functionalized Imidazolium N-Heterocyclic Silver(I) and Gold(I) Carbene Complexes. *Inorganica Chim. Acta* **2023**, *555*, 121557. <https://doi.org/10.1016/j.ica.2023.121557>.
- (72) Pisanò, G.; Cazin, C. S. J. General Mechanochemical Synthetic Protocol to Late Transition Metal–NHC (N-Heterocyclic Carbene) Complexes. *ACS Sustain. Chem. Eng.* **2021**, *9* (29), 9625–9631. <https://doi.org/10.1021/acssuschemeng.1c00556>.
- (73) Paul, S.; Thakur, R. S.; Goswami, M.; Sauerwein, A. C.; Mamone, S.; Concistrè, M.; Förster, H.; Levitt, M. H.; Madhu, P. K. Supercycled Homonuclear Dipolar Decoupling Sequences in Solid-State NMR. *J. Magn. Reson.* **2009**, *197* (1), 14–19. <https://doi.org/10.1016/j.jmr.2008.11.011>.
- (74) de Frémont, P.; Scott, N. M.; Stevens, E. D.; Ramnial, T.; Lightbody, O. C.; Macdonald, C. L. B.; Clyburne, J. A. C.; Abernethy, C. D.; Nolan, S. P. Synthesis of Well-Defined N-Heterocyclic Carbene Silver(I) Complexes. *Organometallics* **2005**, *24* (26), 6301–6309. <https://doi.org/10.1021/om050735i>.
- (75) Tegenfeldt, J.; Haeberlen, U. Cross Polarization in Solids with Flip-Back of I-Spin Magnetization. *J. Magn. Reson.* (1969) **1979**, *36* (3), 453–457. [https://doi.org/10.1016/0022-2364\(79\)90124-0](https://doi.org/10.1016/0022-2364(79)90124-0).
- (76) Hansen, C.; Docherty, S. R.; Cao, W.; Yakimov, A. V.; Copéret, C. ¹⁰⁹Ag NMR Chemical Shift as a Descriptor for Brønsted Acidity from Molecules to Materials; preprint; Chemistry, 2023. <https://doi.org/10.26434/chemrxiv-2023-cxlm1-v3>.

- (77) Ramnial, T.; Abernethy, C. D.; Spicer, M. D.; McKenzie, I. D.; Gay, I. D.; Clyburne, J. A. C. A Monomeric Imidazol-2-Ylidene–Silver(I) Chloride Complex: Synthesis, Structure, and Solid State ^{109}Ag and ^{13}C CP/MAS NMR Characterization. *Inorg. Chem.* **2003**, *42* (5), 1391–1393. <https://doi.org/10.1021/ic0262381>.
- (78) Penner, G. H.; Li, W. Silver- ^{109}Ag NMR Spectroscopy of Inorganic Solids. *Inorg. Chem.* **2004**, *43* (18), 5588–5597. <https://doi.org/10.1021/ic0349510>.
- (79) Chen, L.; Ren, P.; Carrow, B. P. Tri(1-Adamantyl)Phosphine: Expanding the Boundary of Electron-Releasing Character Available to Organophosphorus Compounds. *J. Am. Chem. Soc.* **2016**, *138* (20), 6392–6395. <https://doi.org/10.1021/jacs.6b03215>.
- (80) Kroll, A.; Steinert, H.; Scharf, L. T.; Scherpf, T.; Mallick, B.; Gessner, V. H. A Diamino-Substituted Carbodiphosphorane as Strong C-Donor and Weak N-Donor: Isolation of Monomeric Trigonal-Planar $\text{L} \cdot \text{ZnCl}_2$. *Chem. Commun.* **2020**, *56* (58), 8051–8054. <https://doi.org/10.1039/D0CC02496A>.
- (81) Datt, M. S.; Nair, J. J.; Otto, S. Synthesis and Characterisation of Two Novel Rh(I) Carbene Complexes: Crystal Structure of $[\text{Rh}(\text{Acac})(\text{CO})(\text{L}_1)]$. *J. Organomet. Chem.* **2005**, *690* (14), 3422–3426. <https://doi.org/10.1016/j.jorganchem.2005.04.046>.
- (82) Berthon-Gelloz, G.; Siegler, M. A.; Spek, A. L.; Tinant, B.; Reek, J. N. H.; Markó, I. E. IPr^* an Easily Accessible Highly Hindered N-Heterocyclic Carbene. *Dalton Trans.* **2010**, *39* (6), 1444–1446. <https://doi.org/10.1039/B921894G>.
- (83) Iglesias, M.; Beetstra, D. J.; Cavell, K. J.; Dervisi, A.; Fallis, I. A.; Kariuki, B.; Harrington, R. W.; Clegg, W.; Horton, P. N.; Coles, S. J.; Hursthouse, M. B. Expanded-Ring and Backbone-Functionalised N-Heterocyclic Carbenes. *Eur. J. Inorg. Chem.* **2010**, *2010* (11), 1604–1607. <https://doi.org/10.1002/ejic.200901182>.
- (84) Lu, W. Y.; Cavell, K. J.; Wixey, J. S.; Kariuki, B. First Examples of Structurally Imposing Eight-Membered-Ring (Diazocanylidene) N-Heterocyclic Carbenes: Salts, Free Carbenes, and Metal Complexes. *Organometallics* **2011**, *30* (21), 5649–5655. <https://doi.org/10.1021/om200467x>.

- (85) Zhao, Q.; Meng, G.; Li, G.; Flach, C.; Mendelsohn, R.; Lalancette, R.; Szostak, R.; Szostak, M. IPr# – Highly Hindered, Broadly Applicable N-Heterocyclic Carbenes. *Chem. Sci.* **2021**, 12 (31), 10583–10589. <https://doi.org/10.1039/D1SC02619D>.
- (86) Guillet, S. G.; Pisanò, G.; Chakraborty, S.; Müller, B. H.; de Vries, J. G.; Kamer, P. C. J.; Cazin, C. S. J.; Nolan, Steven. P. A Simple Synthetic Route to [Rh(Acac)(CO)(NHC)] Complexes: Ligand Property Diagnostic Tools and Precatalysts. *Eur. J. Inorg. Chem.* **2021**, 2021 (34), 3506–3511. <https://doi.org/10.1002/ejic.202100479>.
- (87) Varshavsky, Yu. S.; Cherkasova, T. G.; Galding, M. R.; Korlyukov, A. A.; Podkorytov, I. S.; Gindin, V. A.; Smirnov, S. N.; Mazur, A. S.; Rubaylo, A. I. ¹³C NMR Spectrum of Crystalline [Rh(Acac)(CO)₂]: A Contribution to the Discussion on [Rh(acac)(CO)₂] Molecular Structure in the Solid State. *J. Organomet. Chem.* **2018**, 874, 70–73. <https://doi.org/10.1016/j.jorganchem.2018.08.009>.
- (88) Gómez-Suárez, A.; Ramón, R. S.; Songis, O.; Slawin, A. M. Z.; Cazin, C. S. J.; Nolan, S. P. Influence of a Very Bulky N-Heterocyclic Carbene in Gold-Mediated Catalysis. *Organometallics* **2011**, 30 (20), 5463–5470. <https://doi.org/10.1021/om200705y>.
- (89) Hans, M.; Lorkowski, J.; Demonceau, A.; Delaude, L. Efficient Synthetic Protocols for the Preparation of Common N-Heterocyclic Carbene Precursors. *Beilstein J. Org. Chem.* **2015**, 11 (1), 2318–2325. <https://doi.org/10.3762/bjoc.11.252>.

CHAPTER 3.

Understanding the Mechanochemical
Synthesis of Chalcogen-NHC
Derivatives using ssNMR
Spectroscopy

Chapter 3. Understanding the Mechanochemical Synthesis of Chalcogen-NHC Derivatives using ssNMR Spectroscopy

3.1 Introduction

We investigated the feasibility of the mechanochemical weak base approach to synthesize chalcogen-NHC derivatives. Additionally, we sought to gain a comprehensive understanding of the underlying reaction mechanism through the utilization of ssNMR spectroscopy.

Chalcogen-NHC derivatives represent a captivating and versatile class of compounds that have gained significant attention in the field of organometallic chemistry.^{1–4} These compounds are characterized by the incorporation of chalcogen atoms, which include sulfur (S), selenium (Se), and tellurium (Te), bonded to NHC ligands. This unique combination of elements gives rise to a wide array of compounds with distinctive properties, reactivity, and application.^{4–8} Thiourea ligands (NHC=S) in particular, are widely favored in coordination and organometallic chemistry due to their strong donating ability, versatile coordination behavior with various transition and main group metals, diverse structural features, and high stability in both air and moisture.⁹ The high polarity of the carbon-sulfur bond confers significant advantages in several palladium-catalyzed reactions.⁹ Moreover, research on transition metal thiourea complexes has revealed potential biological activities, including insecticidal, antimicrobial, antitumor, antitubercular, and antithyroid activities.¹⁰ Selenourea ligands (NHC=Se) have also exhibited noteworthy antitumor and antioxidant activities when coordinated with various p- and d-block metal centers and their exceptional biological properties are attributed to their ability to mimic naturally occurring selenoproteins.^{11,12} Additionally, selenourea derivatives are frequently used as probes to investigate the electronic properties of NHCs, which were previously believed to be solely σ -donors.¹³ Moreover, the electrochemical behavior and reactivity of chalcogen-NHC derivatives have recently been elucidated through cyclic voltammetry measurements, revealing their oxidation potential when reacting with halogens.¹⁴

Recently, an operationally simple solution-based approach for synthesizing chalcogen-NHC derivatives has been reported.¹⁵ Despite its convenience, this method suffers from long reaction times and the necessity of heating. Alternatively, a continuous flow method has been introduced

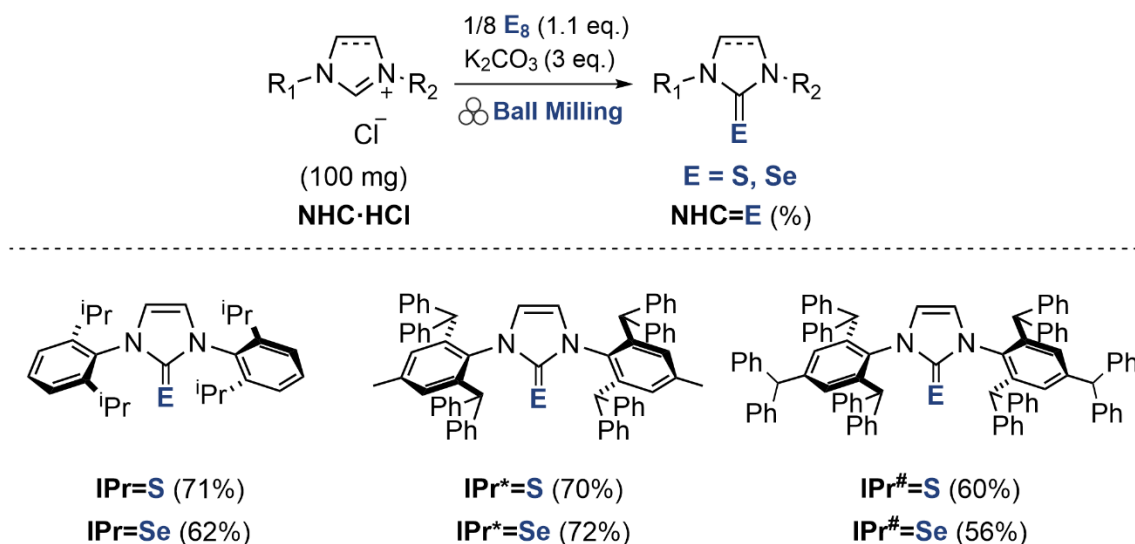
by Nolan and co-workers, which has demonstrated a notable reduction in reaction times compared to conventional batch methodologies.¹⁶ However, this approach is impeded by the excessive utilization of elemental chalcogen and the need for complex equipment, making it challenging to establish and sustain.

In this study, we present a straightforward mechanochemical synthesis of thioureas and selenoureas. The implementation of mechanochemistry has enabled us to circumvent the inherent limitations and drawbacks associated with conventional solution-based methods, rendering our approach a more sustainable, eco-friendly, and practical alternative. To elucidate the underlying mechanism, we conducted a comprehensive ssNMR analysis in conjunction with DFT calculations on NMR parameters. Notably, our investigation encompasses the determination of whether the desired compounds are formed in the solid-state during ball milling or in solution during the subsequent workup protocol.

3.2 Results and Discussion

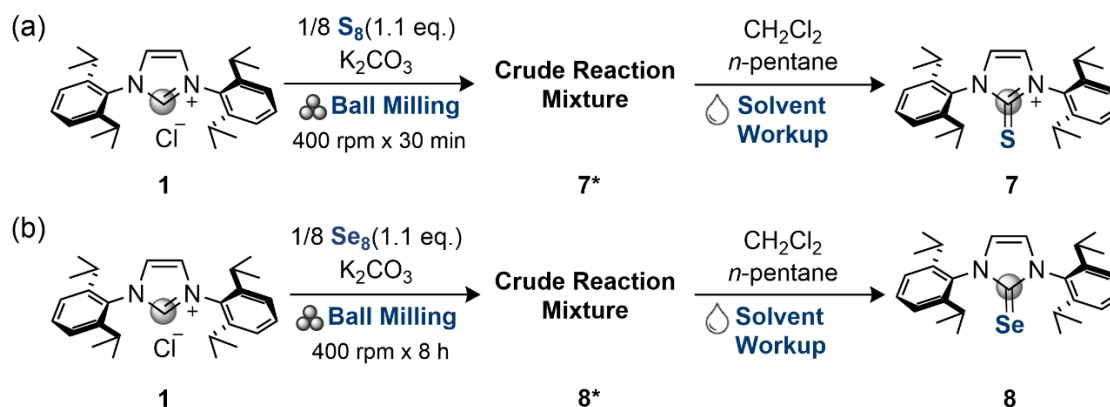
3.2.1 Mechanochemical Synthesis

Building upon the successful mechanochemical synthesis of transition metal-NHC derivatives described in Chapter 2, we aimed to investigate the feasibility of using a mechanochemical weak base approach for synthesizing chalcogen-NHC derivatives. To achieve this, we combined azolium chloride salt (NHC·HCl) with 3 equiv. of weak base K₂CO₃ and 1.1 equiv. of elemental chalcogen (S₈ and Se₈) to synthesize the desired NHC=S and NHC=Se compounds. Remarkably, under these conditions, the desired compounds were successfully synthesized with good yields (**Scheme 3.1**). The reactions were conducted in a planetary ball mill (Fritsch, Pulverisette 5/4) operating at its maximum milling frequency of 400 rpm, using a 12 mL ZrO₂ reactor containing 18 milling bodies (Ø = 5 mm) of the same material, and on a 100 mg scale of the NHC·HCl salt precursor. Following synthesis, the final products were isolated using a straightforward workup protocol. This involved the extraction of the compounds with a 1:3 mixture of CH₂Cl₂ and *n*-pentane, followed by microfiltration. Subsequently, the volatiles were removed under reduced pressure, and the resulting solid was triturated with *n*-pentane. For more details about the synthesis and workup protocol, refer to section **3.3, Experimental Details**. The identity and atom connectivity of the compounds were confirmed through ¹H NMR spectroscopy.



Scheme 3.1. Mechanochemical weak base approach for the synthesis of chalcogen-NHC derivatives. Reaction conditions: NHC·HCl (100 mg), S₈/Se₈ (1.1 equiv.), and K₂CO₃ (3 equiv.), and ball milling time of 30 min (NHC=S) or 8 h (NHC=Se). Isolated yield in parentheses.

To gain insight into the reaction mechanism and determine the stage at which the desired compounds were formed, ssNMR spectroscopy was employed to analyze the composition of the crude mixtures. For this purpose, the NHC salt precursor IPr·HCl (**1**) was chosen for its simplicity and ease of characterization (**Scheme 3.2**). Following the milling process, the crude reaction mixtures **7*** and **8*** underwent recrystallization, leading to the isolation of pure IPr=S (**7**) and IPr=Se (**8**) compounds, respectively. By comparing the high-resolution ssNMR spectra of the crude reaction mixtures **7*** and **8*** with those of the pure products **7** and **8**, respectively, we could ascertain the specific stage at which the desired products were formed, whether during the ball milling process or the subsequent treatment/workup of the crude.



Scheme 3.2. Mechanochemical synthesis of (a) IPr=S (**7**) and (b) IPr=Se (**8**) compounds. The gray circle denotes the C² carbon of the imidazolyliene moiety in the different compounds.

3.2.2 ssNMR Spectroscopy of IPr=S

3.2.2.1 ¹H ssNMR spectroscopy

The 1D ¹H ssNMR spectra of **1**, **7***, and **7** were acquired at a static magnetic field, $B_0 = 9.4$ T, with MAS frequency, $\nu_R = 60$ kHz, to enhance the spectral resolution (**Figure 3.1**). The ¹H signals of compound **7** were assigned based on the ¹H isotropic chemical shifts measured in solution and DFT calculation of the ¹H isotropic chemical shift for the periodic crystal structure of IPr=S (see **Figure 3.2** and **Table 3.1**). The ¹H² signal of compound **1**, resonating at 12.5 ppm, is found to be a useful indicator of the reaction progress. The ¹H spectrum of **7*** exhibits a ¹H² signal at 12.5 ppm, indicating the presence of unreacted IPr·HCl in the crude mixture. In contrast, this signal is not observed in the ¹H spectrum of **7**, indicating successful deprotonation of the site during the reaction. Additionally, the ¹H spectrum of **7*** exhibits a signal at 13.5 ppm, attributed to KHCO_3 .¹⁷

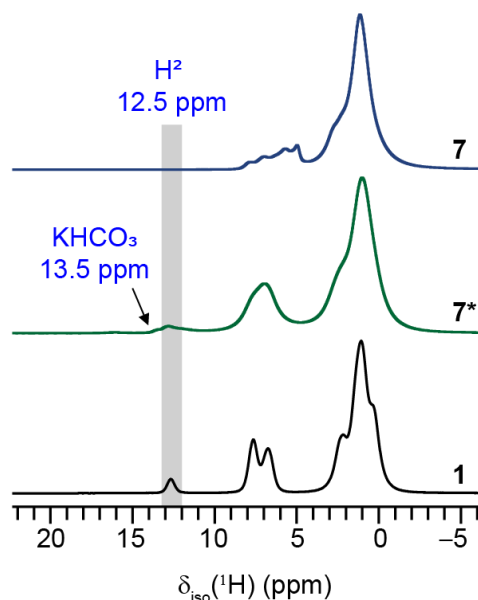


Figure 3.1. 1D ^1H MAS NMR spectra of **1** (black), **7*** (green), and **7** (blue) acquired at $B_0 = 9.4$ T with MAS frequency, $\nu_R = 60$ kHz. The shaded area denotes the region where the imidazolium proton ($^1\text{H}^2$) signal of compound **1** resonates.

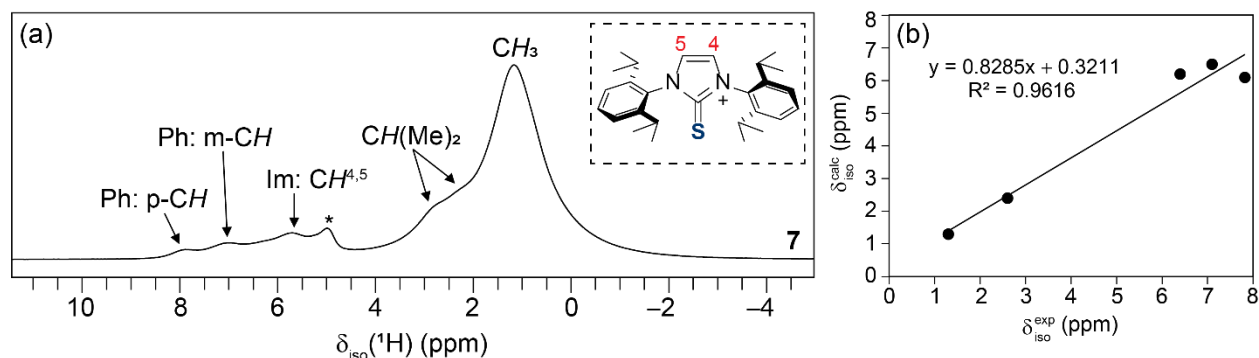


Figure 3.2. 1D ^1H MAS NMR spectra of compound **7**, acquired at $B_0 = 9.4$ T with $\nu_R = 60$ kHz, along with the assignment of the ^1H signals. The signals of the imidazole and phenyl ring are denoted by Im and Ph, respectively. The assignment of the ^1H signals is based on their ^1H solution-state NMR spectra and DFT calculations of the isotropic chemical shifts, as shown in panels (b). The atom numbering of the imidazole ring is indicated on the structure shown as an inset in panel (a). The asterisk symbol (*) denotes the impurity signal from water. (b) Correlation between DFT-calculated ($\delta_{\text{iso}}^{\text{calc}}$) and experimental ($\delta_{\text{iso}}^{\text{exp}}$) isotropic chemical shifts for the ^1H sites of IPr=S crystal structure. The $\delta_{\text{iso}}^{\text{exp}}$ values were measured from the 1D ^1H MAS spectrum of compound **7** shown in panel (a).

Table 3.1. Experimental and calculated $\delta_{\text{iso}}(^1\text{H})$ values of compound **7** measured experimentally and calculated for the periodic crystal structure.

Sample		CH ₃	CH(Me) ₂	Im: CH ^{4,5}	Ph: m-CH	Ph: p-CH
7	Exp.	1.3	2.6	6.4	7.1	7.8
	DFT	1.3	2.4	6.2	6.4	6.1

3.2.2.2 ¹³C ssNMR spectroscopy

To support the conclusion drawn from 1D ¹H MAS NMR spectra and determine whether the IPr=S compound was synthesized in the crude mixture, we performed 1D ¹H→¹³C CP-MAS NMR experiments on the same set of samples, and the resulting spectra are presented in **Figure 3.3**. The assignment of the ¹³C signals of compound **7** was based on the ¹³C isotropic chemical shifts measured in solution¹⁸ and the DFT calculations of ¹³C isotropic chemical shifts for the periodic crystal structure of IPr=S (see **Figure 3.4** and **Table 3.2**). In the 1D ¹H→¹³C CP-MAS spectrum of compound **1**, the characteristic ¹³C² signal of IPr·HCl is observed at 143 ppm. The shift of this signal to 166 ppm in compound **7** indicates the successful synthesis of IPr=S. The ¹³C² signal exhibits a 1:2 asymmetric splitting pattern, which can be attributed to the quadrupolar-dipolar cross-term interaction with the ¹⁴N nucleus ($I = 1$).¹⁹ This signal is broadened in the ¹³C spectrum of ³³S-enriched IPr=S compound, owing to the second-order quadrupolar-dipolar interaction with the ³³S nucleus ($I = 3/2$). This interpretation was validated by a narrower signal observed at higher magnetic field strengths, as shown in **Figure 3.5**, as the second-order quadrupolar-dipolar cross-terms are inversely proportional to the B_0 strength. Assuming the shortest C-S distance to be equal to 1.671 Å, as measured by X-ray diffraction,²⁰ we determined the ¹³C-³³S dipolar coupling constant to be 4.975 kHz. Using this dipolar coupling constant, we simulated the ¹³C² signal with $\delta_{\text{iso}}(^{13}\text{C}) = 166$ ppm, $^1J_{\text{iso}}(^{13}\text{C}-^{33}\text{S}) = 38$ Hz, $\Delta^1J(^{13}\text{C}-^{33}\text{S}) = 950$ Hz, $C_Q(^{33}\text{S}) = -27.4$ MHz, and $\eta_Q(^{33}\text{S}) = 0.12$.

Furthermore, the 1D ¹H→¹³C CP-MAS spectrum of crude mixture **7*** exhibits a signal at 166 ppm, along with a signal at 143 ppm, indicating the presence of IPr=S and unreacted IPr·HCl in the crude mixture, respectively. This observation strongly suggests that the formation IPr=S occurs in the solid-state during the ball milling process. In addition, signals corresponding to KHCO₃ and K₂CO₃ are also detected in the spectrum of **7*** at 162 ppm and 169 ppm, respectively.

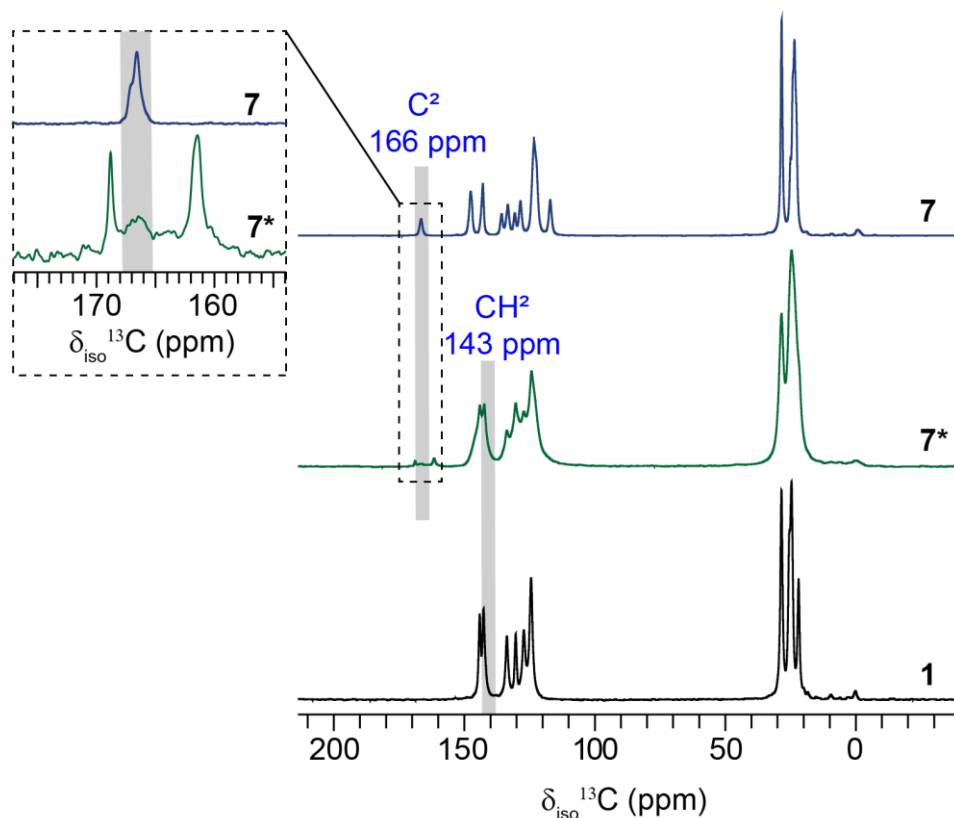


Figure 3.3. 1D $^1\text{H} \rightarrow ^{13}\text{C}$ CP-MAS NMR spectra of **1** (black), **7*** (green), and **7** (blue) samples acquired at $B_0 = 9.4$ T and $T = 298$ K with MAS frequency, $\nu_R = 12.5$ kHz. The isotropic chemical shifts of the C^2 carbon nucleus are indicated by gray shading. A magnified view of the $^{13}\text{C}^2$ signal in **7*** and **7** is presented as an inset.

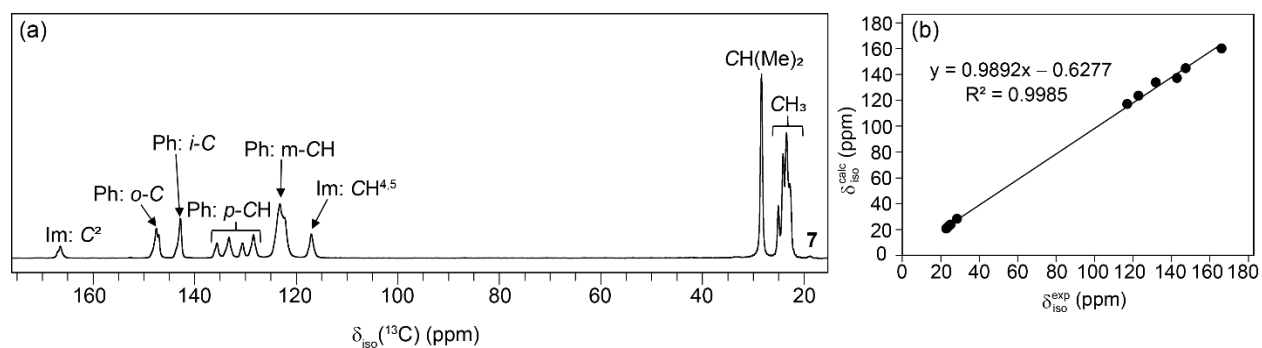


Figure 3.4. 1D $^1\text{H} \rightarrow ^{13}\text{C}$ CP-MAS NMR spectra of compound **7** acquired at $B_0 = 9.4$ T with $\nu_R = 12.5$ kHz, along with the assignment of the ^{13}C signals. The spectral assignment is based on ^{13}C isotropic chemical shifts measured in solution¹⁸ and DFT calculations of the isotropic chemical shifts, as shown in panel (b) and **Table 3.2**. (b) Correlation between DFT-calculated ($\delta_{\text{iso}}^{\text{calc}}$) and

experimental ($\delta_{\text{iso}}^{\text{exp}}$) isotropic chemical shifts for the ^{13}C sites of IPr=S crystal structure. The $\delta_{\text{iso}}^{\text{exp}}$ values were measured from the 1D $^1\text{H} \rightarrow ^{13}\text{C}$ CP-MAS spectrum of compound **7** shown in panel (a).

Table 3.2. $\delta_{\text{iso}}(^{13}\text{C})$ values of compound **7** measured experimentally and calculated for the periodic crystal structure.

Sample		CH_3	$\text{CH}(\text{Me})_2$	Im: $\text{CH}^{4,5}$	Ph: m-CH	Ph: p-CH	Ph: i-C	Ph: o-C	Im: C^2
7	Exp.	22.8							
		23.5							
		24.2	28.4	117.0	122.8	131.8	142.8	147.4	166.0
		25.1							
		20.7							
	DFT	21.8	28.4	117.1	123.6	133.9	137.3	144.9	160.2
		22.9							
		23.8							

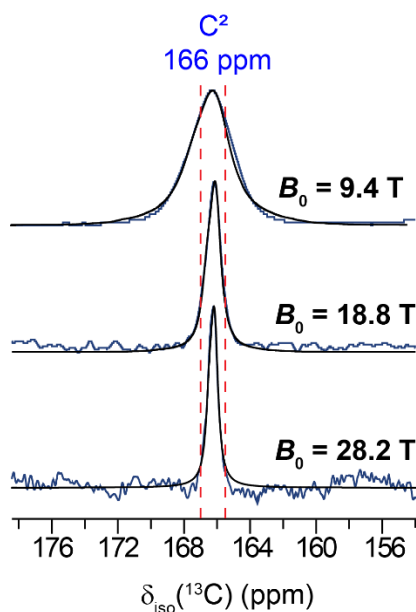


Figure 3.5. Experimental (blue) and simulated (black) 1D $^1\text{H} \rightarrow ^{13}\text{C}$ CP-MAS NMR spectra of ^{33}S -enriched IPr=S at the $^{13}\text{C}^2$ central line recorded at static magnetic fields $B_0 = 9.4$ T (top) (MAS frequency, $\nu_R = 12.5$ kHz), 18.8 T (middle) (MAS frequency, $\nu_R = 12.5$ kHz), and 28.2 T (bottom) (MAS frequency, $\nu_R = 20$ kHz), and $T = 300$ K. The vertical red dotted lines are drawn to highlight the narrowing of the $^{13}\text{C}^2$ as the magnetic field strength increases.

3.2.2.3 ^{15}N ssNMR spectroscopy

Next, 1D $^1\text{H} \rightarrow ^{15}\text{N}$ CP-MAS NMR experiments were performed on **7*** and **7**, as illustrated in **Figure 3.6**. The ^{15}N spectrum of **7** exhibits two distinct ^{15}N signals resonating at 168 and 174 ppm, represented by blue-filled lines, which are attributed to the IPr=S compound. This observation is consistent with the crystal structure of IPr=S reported in the literature,²⁰ and with the DFT calculations of the isotropic chemical shift of ^{15}N for the periodic crystal structure of the IPr=S compound ($\delta_{\text{iso}}^{\text{calc}} = 168$ and 175 ppm). In the ^{15}N spectrum of **7***, the ^{15}N signal is deconvoluted into three signals, two of which are assigned to IPr=S, while the third signal at 182 ppm, represented by a gray-filled line, corresponds to unreacted IPr·HCl. The presence of IPr=S compound, constituting 20% of the mixture relative to unreacted IPr·HCl, further confirms the successful synthesis of IPr=S through the milling process.

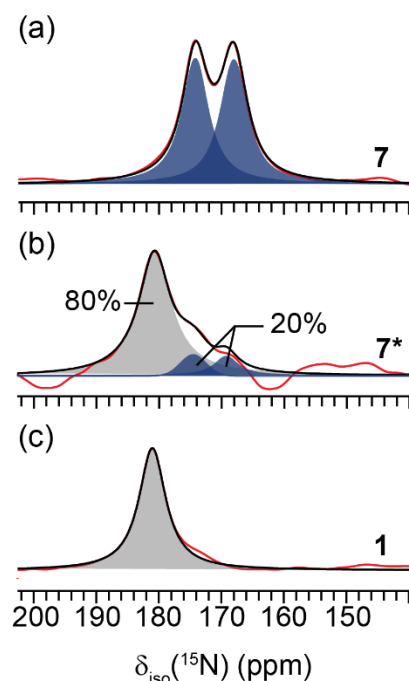


Figure 3.6. Experimental (red) and simulated (black) 1D $^1\text{H} \rightarrow ^{15}\text{N}$ CP-MAS NMR spectra of (a) **7**, (b) **7***, and (c) **1** acquired at a static magnetic field of $B_0 = 9.4$ T with MAS frequency, $\nu_R = 10$ kHz. The simulated spectra are the sum of up to two components: the gray and blue-filled lines are ^{15}N signals associated with IPr·HCl and IPr=S, respectively. The relative integrated intensity of compound IPr=S in the crude mixture is indicated in panel (b).

3.2.2.4 ^{33}S ssNMR spectroscopy

Sulfur-33 is the only naturally occurring NMR-active isotope. This quadrupolar nucleus ($I = 3/2$) with $Q = -6.78 \text{ fm}^2$ is among the most difficult nuclei to study owing to its very low natural abundance (0.76%) and small gyromagnetic ratio ($\gamma = 2.055 \times 10^7 \text{ rad.s}^{-1}.\text{T}^{-1}$). These unfavorable NMR properties result in low receptivity. Furthermore, its NMR signals in solids are broadened by the quadrupolar interaction, which reduces their intensity. As a result of these unfavorable properties, very few ^{33}S ssNMR studies have been reported so far.^{21–25} Furthermore, ^{33}S NMR signal has been mostly detected for inorganic sulfur compounds featuring high molecular symmetry and hence, small quadrupolar broadening,^{24,26–32} whereas ^{33}S nuclei in organosulfur compounds are located in low symmetry environment resulting in large quadrupolar interaction and broad NMR signal.³³

To overcome these challenges, IPr=S compound was enriched in ^{33}S isotope using ^{33}S -enriched S_8 as a sulfur precursor during the mechanosynthesis of IPr=S compound. To increase the sensitivity, ^{33}S NMR spectra of the ^{33}S -enriched IPr=S compound were acquired using the QCPMG pulse sequence at high magnetic field strength.³⁴ Given the large second-order quadrupolar broadening of ^{33}S nuclei in IPr=S compound, their spectra were acquired piecewise using the VOCS technique.

The 1D VOCS-QCPMG ^{33}S NMR spectrum of ^{33}S -enriched IPr=S compound, depicted in **Figure 3.7**, exhibits a CT powder pattern with a linewidth of 1.7 MHz at $B_0 = 18.8 \text{ T}$. This pattern necessitates the acquisition of 11 sub-spectra, resulting in a total experimental time of 20 h. The resulting ^{33}S NMR spectrum was simulated using the QUEST program,³⁵ revealing the following ^{33}S NMR parameters: $\delta_{\text{iso}}(^{33}\text{S}) = 1000 \text{ ppm}$, $C_Q(^{33}\text{S}) = -27.2 \text{ MHz}$, $\eta_Q(^{33}\text{S}) = 0.12$.

DFT calculations of ^{33}S NMR parameters of the periodic crystal structure of IPr=S were also conducted to relate the NMR spectra and the atomic-level structure. While the best-fit $C_Q(^{33}\text{S})$ value agrees with the DFT calculated value (-35.0 MHz), discrepancies were observed in the $\eta_Q(^{33}\text{S})$ (0.56) and $\delta_{\text{iso}}(^{33}\text{S})$ (510 ppm) parameters. We believe that this discrepancy stems from an imperfect structural optimization of this large organic compound.

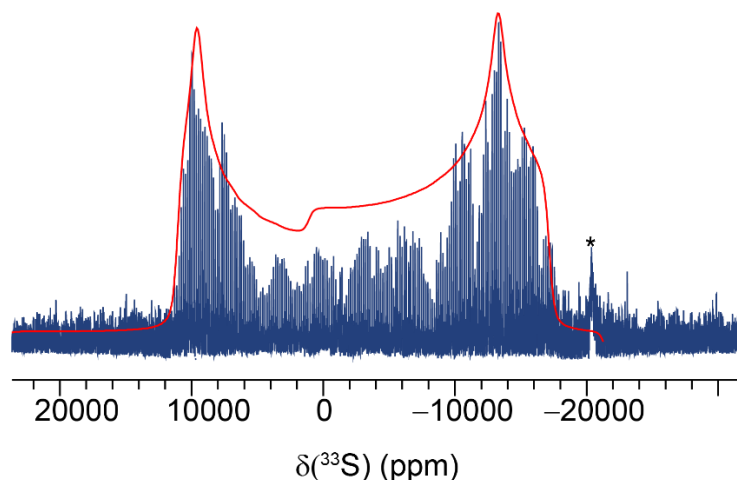


Figure 3.7. Experimental (blue) and simulated (red) 1D ^{33}S VOCS-QCPMG NMR spectrum of ^{33}S -enriched IPr=S acquired at $B_0 = 18.8$ T and $T = 300$ K under static conditions. The spectrum is generated by performing a Fourier transform of the sum of QCMPG echoes. The simulated spectrum was generated using $C_Q(^{33}\text{S}) = -27.4$ MHz and $\eta_Q(^{33}\text{S}) = 0.12$ as the main parameters. The asterisk (*) symbol denotes the NMR signal from the probe.

3.2.3 ssNMR Spectroscopy of IPr=Se

3.2.3.1 ^1H ssNMR spectroscopy

In addition to investigating the mechanochemical synthesis of IPr=S, we studied the mechanistic aspects of IPr=Se mechanochemical synthesis through ssNMR spectroscopy. In this context, 1D ^1H MAS NMR spectra were acquired for the crude mixture **8*** and pure compound **8** at a static magnetic field, $B_0 = 9.4$ T with MAS frequency, $\nu_R = 60$ kHz. The obtained spectra are presented in **Figure 3.8**. The ^1H signals are assigned based on the ^1H isotropic chemical shifts measured in solution (**Figure 3.9**). Notably, the absence of the $^1\text{H}^2$ signal, corresponding to compound **1**, in the 1D ^1H MAS NMR spectrum of **8**, indicates deprotonation. Conversely, the presence of the signal at 12.5 ppm in the ^1H spectrum of **8*** indicates the presence of unreacted IPr·HCl in the crude mixture.

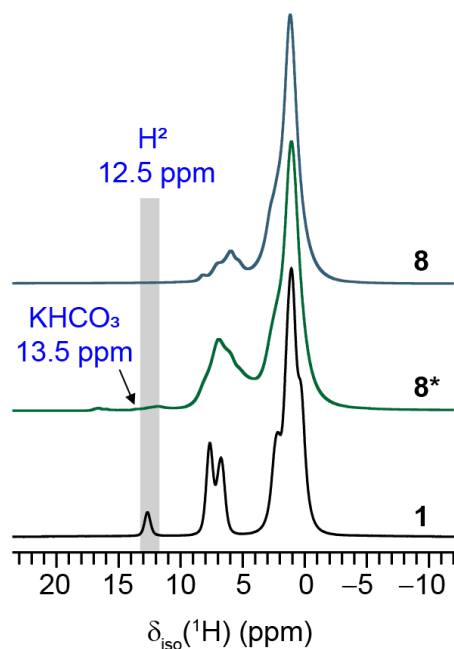


Figure 3.8. 1D ^1H MAS NMR spectra of **8*** (green) and **8** (blue) acquired at $B_0 = 9.4$ T with a MAS frequency, $\nu_R = 60$ kHz. The spectrum of compound **1** is also shown for the sake of comparison. The shaded region indicates the chemical shift region where the imidazolium proton ($^1\text{H}^2$) signal of compound **1** resonates.

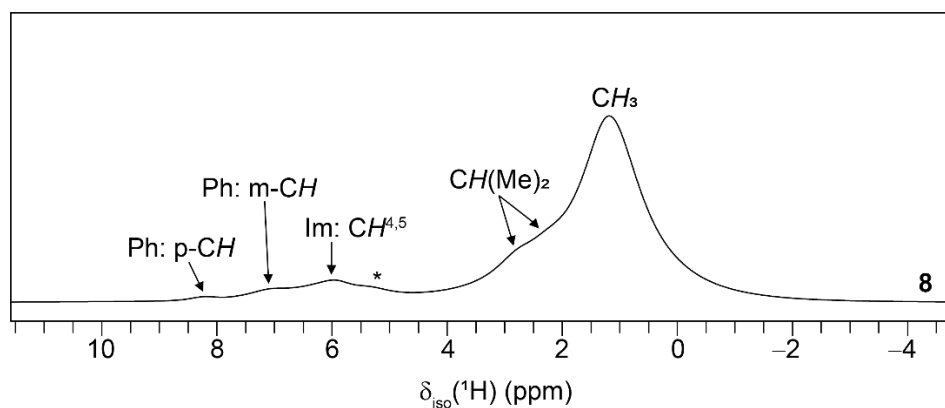


Figure 3.9. 1D ^1H MAS NMR spectra of compound **8**, acquired at $B_0 = 9.4$ T with $\nu_R = 60$ kHz, along with the assignment of the ^1H signals. The assignment of the ^1H signals is based on their ^1H solution-state NMR spectra. The asterisk symbol (*) denotes the impurity signal from water.

3.2.3.2 ^{13}C ssNMR spectroscopy

Furthermore, we conducted 1D $^1\text{H} \rightarrow ^{13}\text{C}$ CP-MAS NMR experiments for **8*** and **8** at a static magnetic field, $B_0 = 9.4$ T with MAS frequency, $\nu_R = 12.5$ kHz (**Figure 3.10**). The ^{13}C signals are assigned (see **Figure 3.11**) based on ^{13}C isotropic chemical shifts measured in solution.³⁶ Notably, the spectra of both **8*** and **8** exhibit a distinctive $^{13}\text{C}^2$ signal at 161.8 ppm, indicating the formation of the $\text{IPr}=\text{Se}$ compound.³⁷ Moreover, in the ^{13}C spectrum of **8***, an additional signal at 143.0 ppm was detected corresponding to unreacted $\text{IPr}\cdot\text{HCl}$. Additionally signals at 161.5 ppm and 169.0 ppm were also observed in the ^{13}C spectrum of **8***, which are attributed to KHCO_3 and K_2CO_3 , respectively. These observations corroborate the successful synthesis of $\text{IPr}=\text{Se}$ in solid-state and signify the presence of unreacted $\text{IPr}\cdot\text{HCl}$, as well as residual K_2CO_3 and KHCO_3 , in the crude mixture.

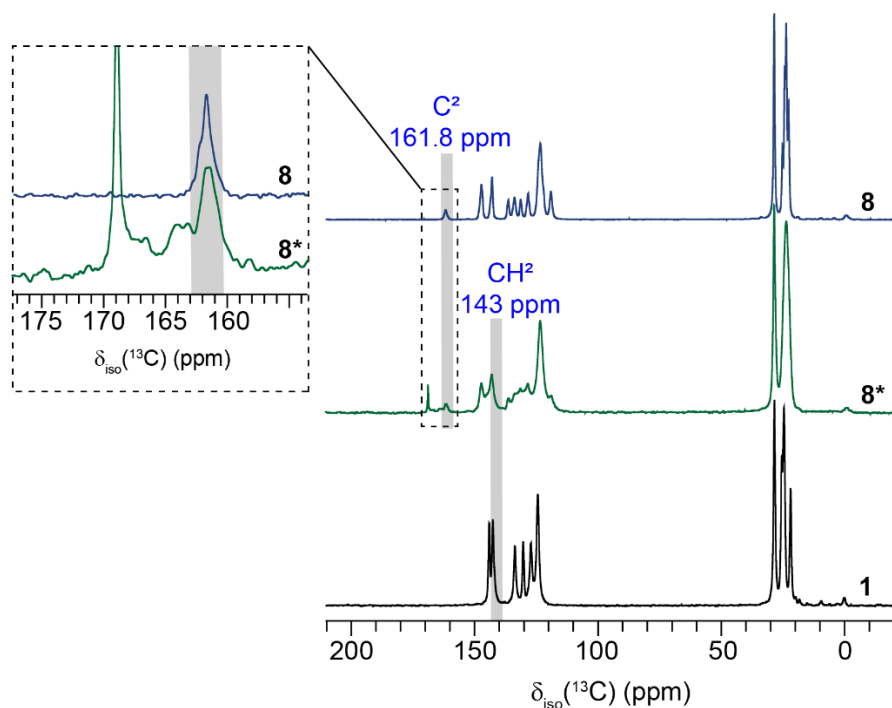


Figure 3.10. 1D $^1\text{H} \rightarrow ^{13}\text{C}$ CP-MAS NMR spectra of **8*** (green) and **8** (blue) acquired at $B_0 = 9.4$ T with a MAS frequency, $\nu_R = 12.5$ kHz. The spectrum of compound **1** is also shown for the sake of comparison. The isotropic chemical shift of the $^{13}\text{C}^2$ site is indicated by gray shading. A magnified view of the $^{13}\text{C}^2$ signal in **8*** and **8** is presented as an inset. In **8**, the $^{13}\text{C}^2$ signal exhibits a 1:2 asymmetric splitting pattern owing to the quadrupolar-dipolar cross-term interaction with the ^{14}N nucleus ($I = 1$). The ^{13}C signals in **8*** at 161.5 ppm and 169.0 ppm are assigned to KHCO_3 and K_2CO_3 , respectively.

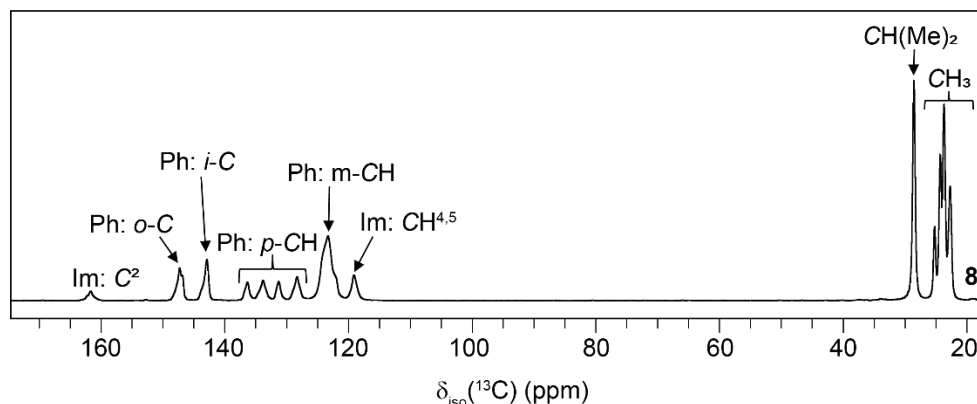


Figure 3.11. 1D $^1\text{H} \rightarrow ^{13}\text{C}$ CP-MAS spectra of compound **8** acquired at $B_0 = 9.4$ T with $\nu_R = 12.5$ kHz, along with the assignment of the ^{13}C signals. The spectral assignment is based on ^{13}C isotropic chemical shifts measured in solution.³⁶

3.2.3.3 ^{77}Se ssNMR spectroscopy

With a natural abundance of 7.63%, ^{77}Se ($I = 1/2$) is the only NMR-active isotope within the selenium element. It serves as a remarkably sensitive tool for investigating molecular structures, primarily owing to its broad chemical shift range, which exceeds 3000 ppm. Nonetheless, the practical application of ^{77}Se ssNMR has encountered specific challenges. These challenges can be attributed, in part, to the frequently encountered extended longitudinal relaxation times (T_1) and the presence of significant CSA in ^{77}Se . These factors can compromise sensitivity and introduce complexity to the acquisition and interpretation of experimental data. However, well-established experimental techniques such as CP-MAS and CPMG have emerged as critical tools in simplifying the acquisition of ^{77}Se ssNMR spectra.^{38–40}

1D ^{77}Se ssNMR spectra of **8*** and **8** were acquired at magnetic field strength of $B_0 = 9.4$ T with MAS frequency, $\nu_R = 10$ kHz. The 1D $^1\text{H} \rightarrow ^{77}\text{Se}$ CP-MAS NMR spectrum of **8**, presented in **Figure 3.12a**, exhibits a spinning sideband pattern associated with a single isotropic resonance at 103 ppm, indicating the presence of a single selenium site. This observation is consistent with the crystal structure of $\text{IPr}=\text{Se}$ reported in the literature,⁴¹ where a single crystallographically distinct selenium site is bonded to the C^2 carbon. Moreover, the observed chemical shift is consistent with the solution-state NMR chemical shift reported in the literature.³⁷ The 1D $^1\text{H} \rightarrow ^{77}\text{Se}$ CP-MAS NMR spectrum is further analyzed by simulation, which reveals that the selenium atom experiences a strong anisotropic environment with an anisotropic chemical shift $\delta_{\text{aniso}}(^{77}\text{Se}) = 399$ ppm and asymmetry of the chemical shift tensor $\eta_{\text{CS}}(^{77}\text{Se}) = 0.24$. Notably, significant broadening

of the ^{77}Se isotropic peak and spinning sidebands is observed, which can be attributed to residual quadrupolar-dipolar ^{77}Se - ^{14}N cross-terms.^{19,39} This observation is in agreement with the splitting of the $^{13}\text{C}^2$ signal, as shown in **Figure 3.10**.

Furthermore, the 1D $^1\text{H} \rightarrow ^{77}\text{Se}$ CP-MAS NMR spectrum of the crude mixture **8***, presented in **Figure 3.12c**, exhibits a broad isotropic resonance at 103 ppm corresponding to the $\text{IPr}=\text{Se}$ compound. The broadening of the ^{77}Se isotropic resonance and the sidebands relative to those of the pure product is attributed to the disorder induced by ball milling during sample preparation. Additionally, the 1D CPMG ^{77}Se NMR spectrum of **8***, presented in **Figure 3.12d**, shows a single ^{77}Se isotropic resonance at 787 ppm, which is assigned to unreacted Se_8 . In contrast, no signal corresponding to Se_8 is observed in the 1D CPMG ^{77}Se NMR spectrum of **8**, indicating the absence of unreacted Se_8 in the pure product. Taken together, these NMR results suggest that the crude mixture **8***, contains the desired $\text{IPr}=\text{Se}$ compound, residual unreacted $\text{IPr}\cdot\text{HCl}$, Se_8 , and K_2CO_3 , and KHCO_3 as a by-product.

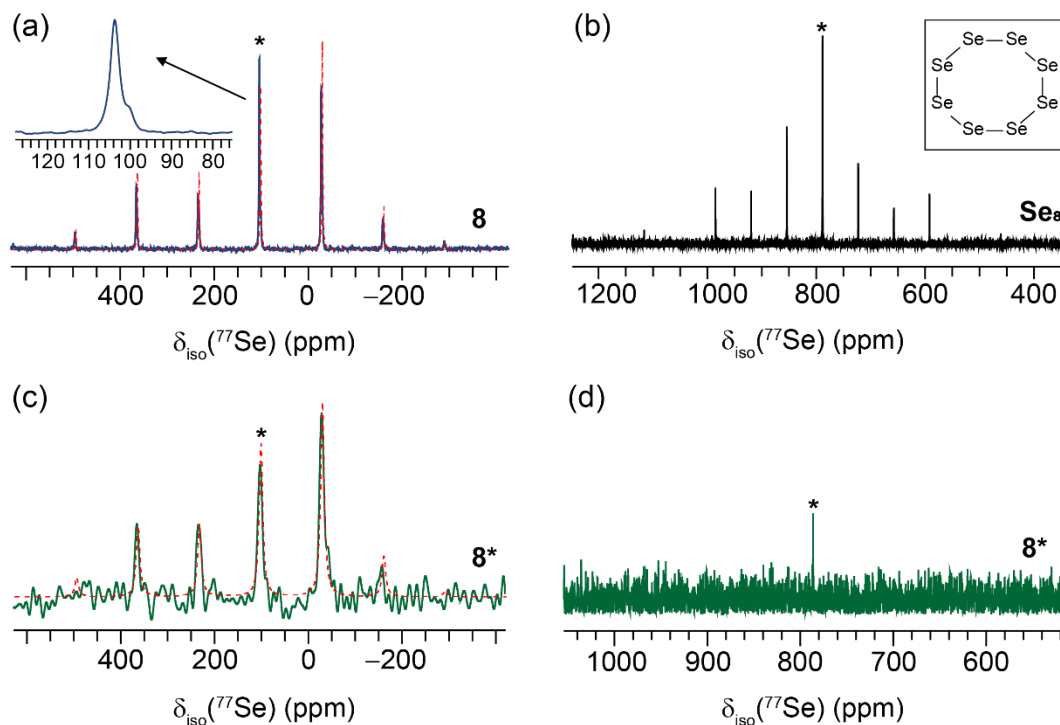


Figure 3.12. 1D ^{77}Se ssNMR spectra of (a) **8**, (b) Se_8 , and (c, d) **8*** acquired at $B_0 = 9.4$ T with MAS frequency, $\nu_R = 10$ kHz, and $T = 298$ K. The spectra are acquired using (a,c) CPMAS and (b, d) CPMG pulse sequences. Isotropic resonances are indicated by *. The inset in panel (a)

shows an expanded view of the isotropic resonance. The structure of compound Se_8 is shown as inset in panel (b).

3.3 Experimental Details

3.3.1 Samples Preparation

3.3.1.1 Materials

The azolium chloride ($\text{NHC}\cdot\text{HCl}$) salts used in this study, namely N,N' -bis-(2,6-diisopropylphenyl)imidazolium chloride ($\text{IPr}\cdot\text{HCl}$), N,N' -bis-[2,6-bis(diphenylmethyl)-4-methylphenyl]imidazolium chloride ($\text{IPr}^*\cdot\text{HCl}$), N,N' -bis-(2,4,6-tribenzhydrylphenyl)imidazolium chloride ($\text{IPr}^\# \cdot\text{HCl}$), were synthesized following a previously published protocol.^{42–44} Chalcogen precursors, elemental sulfur (S_8) and elemental selenium (Se_8), were purchased from Sigma Aldrich, while the 99% ^{33}S -enriched S_8 was purchased from Cortecnet. Potassium carbonate (K_2CO_3) was procured from Carl-Roth. All chemicals were used as received. All solvents employed (i.e., n -pentane, CH_2Cl_2) were purchased from Chem-Lab and used without any further purification.

3.3.1.2 General procedure

All mechanochemical experiments were carried out using a Fritsch Pulverisette 5/4 planetary ball mill operating at its maximum frequency of 400 rpm. Zirconia reactors (12 mL) equipped with 18 balls of the same material (7.52 g, $\varnothing = 5$ mm) were used. The reactor was charged with $\text{NHC}\cdot\text{HCl}$ (100 mg), S_8/Se_8 (1.1 eq.), and K_2CO_3 (3 eq.) under atmospheric conditions, sealed, and then placed in the ball mill for milling the contents of the jar.

3.3.1.3 Synthesis of $\text{IPr}=\text{S}$

The reactor was charged with $\text{IPr}\cdot\text{HCl}$ (**1**) (100 mg, 0.24 mmol), S_8 (8 mg, 0.26 mmol), and K_2CO_3 (98 mg, 0.70 mmol). The mixture of solids was then ground for 30 min at 400 rpm. $\text{IPr}=\text{S}$ (N,N' -bis-(2,6-diisopropylphenyl)imidazol-2-thione) was obtained in 71% yield (70 mg, 0.17 mmol). For ^{33}S -enrichment of $\text{IPr}=\text{S}$, the same procedure was performed, except that ^{33}S -enriched S_8 was used as a sulfur precursor instead of natural abundance S_8 .

3.3.1.4 Synthesis of IPr=Se

The reactor was charged with IPr-HCl (**1**) (100 mg, 0.24 mmol), Se₈ (20 mg, 0.26 mmol), and K₂CO₃ (98 mg, 0.70 mmol). The mixture of solids was then ground in 8 repetitions of 60 min each, for a total duration of 8 h at 400 rpm. IPr=Se (*N,N'*-bis-(2,6-diisopropylphenyl)imidazol-2-selenone) was obtained in 62% yield (68 mg, 0.15 mmol).

3.3.1.5 Workup

Solvent-Free (7*, 8*): At the end of the milling process, the content of the reactor was manually extracted using a spatula and transferred to a vial for analysis without any further manipulations.

Solvent-Based (7, 8): At the end of the milling process, the content of the reactor was extracted with CH₂Cl₂ (3 × 4 mL), and the resulting solution was filtered over SiO₂. The SiO₂ pad was rinsed with additional CH₂Cl₂ (3 × 2 mL), and the filtrate was then concentrated by rotatory evaporation to approximately ¼ of its original volume. An excess of *n*-pentane (10 mL) was added to the concentrated solution, followed by sonication for a few minutes to promote the precipitation of the desired product. The resulting solid was collected by vacuum filtration, washed with additional *n*-pentane, and then dried under a high vacuum for several hours.

3.3.2 ssNMR Spectroscopy

3.3.2.1 ssNMR experiments at $B_0 = 9.4$ T

We recorded the 1D ¹H MAS, ¹H→¹³C and ¹H→¹⁵N CP-MAS, and ⁷⁷Se ssNMR experiments at room temperature on a wide bore Bruker AVANCE NEO NMR spectrometer at a static magnetic field $B_0 = 9.4$ T, corresponding to a Larmor frequency of 400.1 MHz for ¹H, 100.6 MHz for ¹³C, 40.5 MHz for ¹⁵N, and 76.3 MHz for ⁷⁷Se. The powdered samples were packed into 4 mm outer diameter zirconia rotors and sealed with Kel-F drive caps, except for the ¹H experiments in which the samples were packed in 1.3 mm outer diameter zirconia rotors. The samples were spun at a MAS frequency of $\nu_R = 60$ kHz for ¹H MAS experiments, $\nu_R = 12.5$ kHz for ¹³C MAS experiments, and $\nu_R = 10$ kHz for ¹⁵N and ⁷⁷Se MAS experiments.

The 1D ¹H MAS NMR spectra were acquired using a 1.3 mm triple resonance (HXY) MAS probe operated in double resonance mode and employed the DEPTH pulse sequence. The ¹H

$\pi/2$ pulse lasted 2.61 μs and employed a nutation frequency $\nu_1 = 96$ kHz. The ^1H MAS spectra resulted from the averaging of 16 transients with $T_{\text{RD}} = 1.3$ s.

The 1D $^1\text{H} \rightarrow ^{13}\text{C}$ CP-MAS NMR spectra, except for the middle and bottom spectra presented in **Figure 3.5**, were acquired using a Bruker 4 mm triple resonance (HXY) MAS probe, operated in double resonance mode. The initial ^1H $\pi/2$ lasted 2.2 μs with $\nu_1 = 114$ kHz, followed by a CP contact time of 1 ms. During the CP transfer, the nutation frequency on the ^{13}C channel was constant at 71.9 kHz, while the ^1H nutation frequency was linearly ramped from 90 to 100. Heteronuclear decoupling using the SPINAL-64 sequence with $\nu_1 = 101.6$ kHz was applied on the ^1H channel during the acquisition period.⁴⁵ The 1D $^1\text{H} \rightarrow ^{13}\text{C}$ CP-MAS spectra were recorded using $T_{\text{RD}} = 1.3$ s and resulted from averaging 8192 transients, corresponding to a total experimental time of 3 h. The $^{13}\text{C}^2$ signal was simulated using WSolids1 software.⁴⁶

The 1D $^1\text{H} \rightarrow ^{15}\text{N}$ CP-MAS NMR spectra were acquired using a Bruker 4 mm double resonance (HX) low- γ MAS probe. The ^1H $\pi/2$ pulse of 3.3 μs ($\nu_1 = 75.8$ kHz) was followed by a CP contact time of 4 ms. During the CP transfer, the rf nutation frequency on the ^{15}N channel was constant at 34 kHz, while on the ^1H channel, it was linearly ramped from 100 to 50. Heteronuclear decoupling using the SWf-TPPM sequence with an rf nutation frequency of 49 kHz was employed during the acquisition period.⁴⁷ The 1D $^1\text{H} \rightarrow ^{15}\text{N}$ CP-MAS NMR spectra resulted from averaging 20,224 transients with $T_{\text{RD}} = 3$ s, corresponding to a total experimental time of 17 h. The ^{15}N chemical shifts were referenced to liquid NH_3 using α -glycine (32.7 ppm) as a secondary reference. The $^1\text{H} \rightarrow ^{15}\text{N}$ CP-MAS spectra were simulated using the SOLA module within Bruker TopSpin software.

The 1D ^{77}Se ssNMR experiments were conducted using a Bruker 4 mm triple resonance (HXY) MAS probe operating in double resonance mode. The 1D $^1\text{H} \rightarrow ^{77}\text{Se}$ CP-MAS NMR spectra were acquired using an initial ^1H $\pi/2$ pulse of 3.8 μs ($\nu_1 = 92$ kHz) and a CP contact time of 5 ms. The nutation frequency on the ^{77}Se channel was constant at 69 kHz, while the ^1H nutation frequency was linearly ramped from 50 to 100 during the CP transfer. The 1D $^1\text{H} \rightarrow ^{77}\text{Se}$ CP-MAS NMR spectra were recorded with $T_{\text{RD}} = 5$ s and resulted from averaging 4,320 transients, corresponding to a total experimental time of 6 h. SPINAL-64 heteronuclear decoupling sequence with $\nu_1 = 114$ kHz was employed on the ^1H channel in all ^{77}Se ssNMR experiments. The 1D ^{77}Se CPMG NMR spectra were recorded using CPMG pulses with a length of 7 μs and $\nu_1 = 36$ kHz.⁴⁸ The refocusing pulses were repeated with a cycle time of 200 μs , and 240 echoes were acquired for each transient. 1D ^{77}Se CPMG spectra were recorded using $T_{\text{RD}} = 10$ s and resulted from

averaging 2,800 transients, corresponding to a total experimental time of 8 h. The ^{77}Se chemical shifts were externally referenced to H_2SeO_3 ($\delta_{\text{iso}}(^{77}\text{Se}) = 1288.1$ ppm). The experimental ^{77}Se NMR parameters were determined using the SOLA module within Bruker TopSpin software.

3.3.2.2 ssNMR experiments at $B_0 = 18.8$ T

To check the influence of the static magnetic field on the broadening of $^{13}\text{C}^2$ signal due to quadrupolar-dipolar cross terms, the 1D $^1\text{H} \rightarrow ^{13}\text{C}$ CP-MAS NMR spectrum of pure ^{33}S -enriched IPr=S compound, shown in **Figure 3.5**, was also acquired on magnetic field strength of $B_0 = 18.8$ T corresponding to Larmor frequencies of 800.13 MHz for ^1H and 201.19 MHz for ^{13}C . The spectrum was acquired on a standard bore Bruker AVANCE NEO NMR spectrometer using 1.3 mm double resonance (HX) MAS probe, with MAS frequency, $\nu_R = 12.5$ kHz. The temperature was regulated at 300 K. The initial ^1H $\pi/2$ pulse lasted 2.56 μs with $\nu_1 = 98$ kHz, followed by a CP contact time of 3 ms. The nutation frequency on the ^{13}C channel was constant at 63.9 kHz, while the ^1H nutation frequency was linearly ramped from 100 to 50. SPINAL-64 heteronuclear decoupling with $\nu_1 = 62.5$ kHz was applied in the ^1H channel during the acquisition period. The 1D $^1\text{H} \rightarrow ^{13}\text{C}$ CP-MAS spectrum was acquired with $T_{\text{RD}} = 3$ s and by averaging 2,016 transients, with a total experimental time of 1.7 h.

The 1D ^{33}S ssNMR experiments were conducted on a standard bore Bruker AVANCE NEO NMR spectrometer at $B_0 = 18.8$ T, operating at the ^{33}S Larmor frequency of 61.4 MHz, using a Phoenix 4 mm static probe. The experiments were carried out at a regulated temperature of 300 K, with the powdered sample packed in a 4 mm outer diameter thin-walled zirconia rotor. The ^{33}S spectrum was acquired under static conditions using the QCPMG pulse sequence. The QCPMG pulses lasted 4.75 μs with $\nu_1 = 53$ kHz, and the refocusing pulse was repeated with a cycle time of 100 μs and 190 echoes were acquired for each transient. The 11 sub-spectra were recorded using a step size of 100 and 200 kHz, which was a multiplet of the spikelet separation (10 kHz). Each 1D ^{33}S QCPMG sub-spectrum was recorded using $T_{\text{RD}} = 1$ s and resulted from averaging 6,512 transients, corresponding to a total experimental time of 20 h. The ^{33}S chemical shift was referenced to saturated $(\text{NH}_4)_2\text{SO}_4$ in D_2O at $\delta(^{33}\text{S}) = 0$ ppm, and pulse lengths were calibrated against the same reference. Analytical simulation of the 1D ^{33}S ssNMR spectrum was performed using the QUEST program.³⁵

3.3.2.3 ssNMR experiments at $B_0 = 28.2$ T

The 1D $^1\text{H} \rightarrow ^{13}\text{C}$ CP-MAS NMR spectrum of ^{33}S -enriched IPr=S, shown in **Figure 3.5**, was also recorded at $B_0 = 28.2$ T, corresponding to a Larmor frequency of 1200.49 MHz for ^1H and 301.87 MHz for ^{13}C . The spectrum was acquired on a standard bore Bruker AVANCE NEO NMR spectrometer using 3.2 mm double resonance (HX) MAS probe, with MAS frequency, $\nu_R = 20$ kHz. The temperature was regulated at 300 K. The initial ^1H $\pi/2$ pulse lasted 2.59 μs with $\nu_1 = 97$ kHz, followed by a CP contact time of 1 ms. The nutation frequency on the ^{13}C channel was constant at 47 kHz, while the ^1H nutation frequency was linearly ramped from 90 to 100. SPINAL-64 heteronuclear decoupling with $\nu_1 = 3$ kHz was applied in the ^1H channel during the acquisition period. The 1D $^1\text{H} \rightarrow ^{13}\text{C}$ CP-MAS spectrum was acquired with $T_{\text{RD}} = 3$ s and by averaging 186 transients, with a total experimental time of 10 min.

The ^1H isotropic chemical shifts were referenced to tetramethylsilane (TMS) using the signal of the CH_2 group of adamantane at 1.735 ppm as a secondary reference.⁴⁹ ^{13}C isotropic chemical shifts were indirectly referenced using the previously published relative NMR frequencies.⁴⁹

3.3.3 DFT Calculations of NMR Parameters

All calculations on the crystals were performed using the VASP code,⁴² with the generalized gradient approximation PBE used as exchange-correlation functional for geometry optimization and NMR parameters calculations.⁴³ The NMR calculations were performed directly from the XRD data (CCDC 1455043) acquired from monocrystal. The plane-wave cut-off energy of 400 eV was set during the optimization process and a k-point density of $1 \times 3 \times 1$ was applied. The NMR shielding tensors were calculated using GIPAW formalism as implemented in VASP.^{44,45} All calculated chemical shifts were referenced to the experimental ones by determining the average difference between them. In the present work, we used $Q(^{33}\text{S}) = -69.4 \text{ fm}^2$ as documented by Pyykkö.⁴⁶

3.4 Conclusion

In conclusion, we have successfully demonstrated the mechanochemical synthesis of $\text{NHC}=\text{S}$ and $\text{NHC}=\text{Se}$ chalcogen-NHC derivatives using a weak base approach under solvent-free conditions. SSNMR spectroscopy was employed to investigate the mechanism of formation. Our results indicate that the desired compounds are formed in the solid-state during the ball milling process, as evidenced by the formation and identification of IPr=S and IPr=Se compounds in the

crude reaction mixtures. However, the presence of unreacted starting materials in the crude mixtures highlights the need for further optimization of the synthetic route to improve the yield and purity of the final product. Overall, this study highlights the potential of mechanochemistry as an efficient and sustainable approach for the preparation of chalcogen-NHC derivatives, providing a foundation for further research in this field.

3.5 Statement of Contribution

Chapter 3 contains original, unpublished material that will be part of an upcoming publication. The article will be authored by myself as the first author, along with co-authors: Gianmarco Pisanò, Dr. Andrew G. M. Rankin, Dr. Julien Trébosc, Dr. Laurent Delevoye, Prof. Dr. Steven P. Nolan, Prof. Dr. Catherine S. J. Cazin, and Prof. Dr. Olivier Lafon. For this publication, I synthesized the samples, carried out the ssNMR experiments, analyzed the experimental data, and drafted the original version of the article. G.P. assisted in the synthesis of the samples. A.R. and J.T. assisted in the ssNMR experiments. L.D. performed the DFT calculations. S.N.P. contributed to the analysis and interpretation of the results. C.S.J.C and O.L. provided supervision, contributed to the analysis and interpretation of the results, and assisted in editing the article.

3.6 References

- (1) Gonzalez, R.; Azpiroz, R.; Sharma, P.; Villamizar C, C. P.; Anzaldo, B.; Pérez-Flores, F. J.; Toscano, R. A. Ferrocenylated Chalcogen (Se and Te)-Containing N-Heterocyclic Carbenes: Selenones, Silver and Palladium Complexes. *Inorganica Chim. Acta* **2020**, *506*, 119531. <https://doi.org/10.1016/j.ica.2020.119531>.
- (2) Durham, J. L.; Wilson, W. B.; Huh, D. N.; McDonald, R.; Szczepura, L. F. Organometallic Rhenium(III) Chalcogenide Clusters: Coordination of N-Heterocyclic Carbenes. *Chem. Commun.* **2015**, *51* (52), 10536–10538. <https://doi.org/10.1039/C5CC03215F>.
- (3) Ho, L. P.; Tamm, M. Chalcogen-Pnictogen Complexes of Anionic N-Heterocyclic Carbenes with a Weakly Coordinating Borate Moiety. *Eur. J. Inorg. Chem.* **2022**, *2022* (15), e202200090. <https://doi.org/10.1002/ejic.202200090>.
- (4) Doddi, A.; Peters, M.; Tamm, M. N-Heterocyclic Carbene Adducts of Main Group Elements and Their Use as Ligands in Transition Metal Chemistry. *Chem. Rev.* **2019**, *119* (12), 6994–7112. <https://doi.org/10.1021/acs.chemrev.8b00791>.

- (5) Molter, A.; Mohr, F. Gold Complexes Containing Organoselenium and Organotellurium Ligands. *Coord. Chem. Rev.* **2010**, *254* (1), 19–45. <https://doi.org/10.1016/j.ccr.2009.09.017>.
- (6) Aroz, M. T.; Gimeno, M. C.; Kulcsar, M.; Laguna, A.; Lippolis, V. Group 11 Complexes with Imidazoline-2-Thione or Selone Derivatives. *Eur. J. Inorg. Chem.* **2011**, *2011* (18), 2884–2894. <https://doi.org/10.1002/ejic.201100124>.
- (7) Nakata, N.; Kawauchi, F.; Takahashi, S.; Ishii, A. Dicationic Ditelluride Salts Stabilized by N-Heterocyclic Carbene. *New J. Chem.* **2019**, *43* (27), 10894–10898. <https://doi.org/10.1039/C9NJ02138H>.
- (8) McDonough, J. E.; Mendiratta, A.; Curley, J. J.; Fortman, G. C.; Fantasia, S.; Cummins, C. C.; Rybak-Akimova, E. V.; Nolan, S. P.; Hoff, C. D. Thermodynamic, Kinetic, and Computational Study of Heavier Chalcogen (S, Se, and Te) Terminal Multiple Bonds to Molybdenum, Carbon, and Phosphorus. *Inorg. Chem.* **2008**, *47* (6), 2133–2141. <https://doi.org/10.1021/ic701611p>.
- (9) Liu, S.; Lei, Y.; Yang, Z.; Lan, Y. Theoretical Study of the Electron-Donating Effects of Thiourea Ligands in Catalysis. *J. Mol. Struct.* **2014**, *1074*, 527–533. <https://doi.org/10.1016/j.molstruc.2014.06.034>.
- (10) Mohapatra, R. K.; Das, P. K.; Pradhan, M. K.; El-Ajaily, M. M.; Das, D.; Salem, H. F.; Mahanta, U.; Badhei, G.; Parhi, P. K.; Maihub, A. A.; -E-Zahan, Md. K. Recent Advances in Urea- and Thiourea-Based Metal Complexes: Biological, Sensor, Optical, and Corrosion Inhibition Studies. *Comments Inorg. Chem.* **2019**, *39* (3), 127–187. <https://doi.org/10.1080/02603594.2019.1594204>.
- (11) Labunskyy, V. M.; Hatfield, D. L.; Gladyshev, V. N. Selenoproteins: Molecular Pathways and Physiological Roles. *Physiol. Rev.* **2014**, *94* (3), 739–777. <https://doi.org/10.1152/physrev.00039.2013>.
- (12) Nahra, F.; Hecke, K. V.; Kennedy, A. R.; Nelson, D. J. Coinage Metal Complexes of Selenoureas Derived from N-Heterocyclic Carbenes. *Dalton Trans.* **2018**, *47* (31), 10671–10684. <https://doi.org/10.1039/C8DT01506F>.

- (13) Liske, A.; Verlinden, K.; Buhl, H.; Schaper, K.; Ganter, C. Determining the π -Acceptor Properties of N-Heterocyclic Carbenes by Measuring the ^{77}Se NMR Chemical Shifts of Their Selenium Adducts. *Organometallics* **2013**, *32* (19), 5269–5272. <https://doi.org/10.1021/om400858y>.
- (14) Saab, M.; Nelson, D. J.; Leech, M. C.; Lam, K.; Nolan, S. P.; Nahra, F.; Hecke, K. V. Reactions of N-Heterocyclic Carbene-Based Chalcogenoureas with Halogens: A Diverse Range of Outcomes. *Dalton Trans.* **2022**, *51* (9), 3721–3733. <https://doi.org/10.1039/D2DT00010E>.
- (15) Saab, M.; J. Nelson, D.; V. Tzouras, N.; Bayrakdar, T. A. C. A.; P. Nolan, S.; Nahra, F.; Hecke, K. V. Straightforward Access to Chalcogenoureas Derived from N-Heterocyclic Carbenes and Their Coordination Chemistry. *Dalton Trans.* **2020**, *49* (34), 12068–12081. <https://doi.org/10.1039/D0DT02558E>.
- (16) Cauwenbergh, T.; Scattolin, T.; Simoens, A.; Tzouras, N. V.; Stevens, C. V.; Nolan, S. P. Continuous Flow Synthesis of Sulfur- and Selenium–NHC Compounds (NHC=N-Heterocyclic Carbene). *Eur. J. Org. Chem.* **2022**, *2022* (15), e202101296. <https://doi.org/10.1002/ejoc.202101296>.
- (17) Stueber, D.; Patterson, D.; Mayne, C. L.; Orendt, A. M.; Grant, D. M.; Parry, R. W. Carbonates, Thiocarbonates, and the Corresponding Monoalkyl Derivatives. 1. Their Preparation and Isotropic (^{13}C) NMR Chemical Shifts. *Inorg. Chem.* **2001**, *40* (8), 1902–1911. <https://doi.org/10.1021/ic0012266>.
- (18) Wei, S.; Wei, X.-G.; Su, X.; You, J.; Ren, Y. Insight into the Role of the Counteranion of an Imidazolium Salt in Organocatalysis: A Combined Experimental and Computational Study. *Chem. Eur. J.* **2011**, *17* (21), 5965–5971. <https://doi.org/10.1002/chem.201002839>.
- (19) Ashbrook, S. E.; McManus, J.; Thrippleton, M. J.; Wimperis, S. Second-Order Cross-Term Interactions in High-Resolution MAS NMR of Quadrupolar Nuclei. *Prog. Nucl. Magn. Reson. Spectrosc.* **2009**, *55* (2), 160–181. <https://doi.org/10.1016/j.pnmrs.2009.04.002>.
- (20) Zhang, F.; Zhang, J.; Zhou, X. Facile Construction of Yttrium Pentasulfides from Yttrium Alkyl Precursors: Synthesis, Mechanism, and Reactivity. *Inorg. Chem.* **2017**, *56* (4), 2070–2077. <https://doi.org/10.1021/acs.inorgchem.6b02747>.

- (21) Jakobsen, H. J.; Hove, A. R.; Bildsøe, H.; Skibsted, J.; Brorson, M. Advancements in Natural Abundance Solid-State ^{33}S MAS NMR: Characterization of Transition-Metal MS Bonds in Ammonium Tetrathiomallates. *Chem. Commun.* **2007**, No. 16, 1629–1631. <https://doi.org/10.1039/B618497A>.
- (22) O'Dell, L. A.; Klimm, K.; Freitas, J. C. C.; Kohn, S. C.; Smith, M. E. ^{33}S MAS NMR of a Disordered Sulfur-Doped Silicate: Signal Enhancement via RAPT, QCPMG and Adiabatic Pulses. *Appl. Magn. Reson.* **2009**, 35 (2), 247–259. <https://doi.org/10.1007/s00723-008-0159-8>.
- (23) Jakobsen, H. J.; Bildsøe, H.; Skibsted, J.; Brorson, M.; Srinivasan, B. R.; Näther, C.; Bensch, W. New Opportunities in Acquisition and Analysis of Natural Abundance Complex Solid-State ^{33}S MAS NMR Spectra: $(\text{CH}_3\text{NH}_3)_2\text{WS}_4$. *Phys. Chem. Chem. Phys.* **2009**, 11 (32), 6981–6986. <https://doi.org/10.1039/B904841N>.
- (24) Sutrisno, A.; Terskikh, V. V.; Huang, Y. A Natural Abundance ^{33}S Solid-State NMR Study of Layered Transition Metaldisulfides at Ultrahigh Magnetic Field. *Chem. Commun.* **2009**, No. 2, 186–188. <https://doi.org/10.1039/B817017G>.
- (25) Halat, D. M.; Britto, S.; Griffith, K. J.; Jónsson, E.; Grey, C. P. Natural Abundance Solid-State ^{33}S NMR Study of NbS_3 : Applications for Battery Conversion Electrodes. *Chem. Commun.* **2019**, 55 (84), 12687–12690. <https://doi.org/10.1039/C9CC06059F>.
- (26) Haller, M.; Hertler, W. E.; Lutz, O.; Nolle, A. ^{17}Zn and ^{33}S Nuclear Magnetic Shielding in Zinc Chalcogenides. *Solid State Commun.* **1980**, 33 (10), 1051–1053. [https://doi.org/10.1016/0038-1098\(80\)90315-4](https://doi.org/10.1016/0038-1098(80)90315-4).
- (27) Eckert, Hellmut.; Yesinowski, J. P. Sulfur-33 NMR at Natural Abundance in Solids. *J. Am. Chem. Soc.* **1986**, 108 (9), 2140–2146. <https://doi.org/10.1021/ja00269a004>.
- (28) Daunch, W. A.; Rinaldi, P. L. Natural-Abundance Solid-State ^{33}S NMR with High-Speed Magic-Angle Spinning. *J. Magn. Reson. Ser. A* **1996**, 123 (2), 219–221. <https://doi.org/10.1006/jmra.1996.0240>.
- (29) Wagler, T. A.; Daunch, W. A.; Rinaldi, P. L.; Palmer, A. R. Solid State ^{33}S NMR of Inorganic Sulfides. *J. Magn. Reson.* **2003**, 161 (2), 191–197. [https://doi.org/10.1016/S1090-7807\(03\)00046-6](https://doi.org/10.1016/S1090-7807(03)00046-6).

- (30) Couch, S.; Howes, A. P.; Kohn, S. C.; Smith, M. E. ^{33}S Solid State NMR of Sulphur Speciation in Silicate Glasses. *Solid State Nucl. Magn. Reson.* **2004**, 26 (3), 203–208. <https://doi.org/10.1016/j.ssnmr.2004.03.007>.
- (31) Wagler, T. A.; Daunch, W. A.; Panzner, M.; Youngs, W. J.; Rinaldi, P. L. Solid-State ^{33}S MAS NMR of Inorganic Sulfates. *J. Magn. Reson.* **2004**, 170 (2), 336–344. <https://doi.org/10.1016/j.jmr.2004.07.011>.
- (32) Sasaki, A.; Baquerizo Ibarra, L.; Wimperis, S. A High-Resolution Natural Abundance ^{33}S MAS NMR Study of the Cementitious Mineral Ettringite. *Phys. Chem. Chem. Phys.* **2017**, 19 (35), 24082–24089. <https://doi.org/10.1039/C7CP04435F>.
- (33) Yamada, K.; Aoki, D.; Kitagawa, K.; Takata, T. Frequency-Swept Solid-State ^{33}S NMR of an Organosulfur Compound in an Extremely Low Magnetic Field. *Chem. Phys. Lett.* **2015**, 630, 86–90. <https://doi.org/10.1016/j.cplett.2015.04.040>.
- (34) Larsen, F. H.; Jakobsen, H. J.; Ellis, P. D.; Nielsen, N. Chr. Sensitivity-Enhanced Quadrupolar-Echo NMR of Half-Integer Quadrupolar Nuclei. Magnitudes and Relative Orientation of Chemical Shielding and Quadrupolar Coupling Tensors. *J. Phys. Chem. A* **1997**, 101 (46), 8597–8606. <https://doi.org/10.1021/jp971547b>.
- (35) Perras, F. A.; Widdifield, C. M.; Bryce, D. L. QUEST-QUadrupolar Exact SoftWare: A Fast Graphical Program for the Exact Simulation of NMR and NQR Spectra for Quadrupolar Nuclei. *Solid State Nucl. Magn. Reson.* **2012**, 45–46, 36–44. <https://doi.org/10.1016/j.ssnmr.2012.05.002>.
- (36) Abdellah, I.; Cassirame, B.; Sylvie, C.; Nédélec, J.-Y.; Pichon, C. Direct Electrochemical Reduction of Azolium Salts Into N-Heterocyclic Carbenes and Their Subsequent Trapping. *Curr. Top. Electrochem.* **2011**, 16.
- (37) Vummaleti, S. V. C.; Nelson, D. J.; Poater, A.; Gómez-Suárez, A.; Cordes, D. B.; Slawin, A. M. Z.; Nolan, S. P.; Cavallo, L. What Can NMR Spectroscopy of Selenoureas and Phosphinidenes Teach Us about the π -Accepting Abilities of N-Heterocyclic Carbenes? *Chem. Sci.* **2015**, 6 (3), 1895–1904. <https://doi.org/10.1039/C4SC03264K>.

- (38) Wei, D.; Han, M.; Yu, L. Solid-State ^{77}Se NMR of Organoselenium Compounds through Cross Polarization Magic Angle Spinning (CPMAS) Method. *Sci. Rep.* **2017**, *7* (1), 6376. <https://doi.org/10.1038/s41598-017-06892-8>.
- (39) Griffin, J. M.; Knight, F. R.; Hua, G.; Ferrara, J. S.; Hogan, S. W. L.; Woollins, J. D.; Ashbrook, S. E. ^{77}Se Solid-State NMR of Inorganic and Organoselenium Systems: A Combined Experimental and Computational Study. *J. Phys. Chem. C* **2011**, *115* (21), 10859–10872. <https://doi.org/10.1021/jp202550f>.
- (40) Deschamps, M.; Roiland, C.; Bureau, B.; Yang, G.; Le Pollès, L.; Massiot, D. ^{77}Se Solid-State NMR Investigations on $\text{As}_x\text{Se}_{1-x}$ Glasses Using CPMG Acquisition under MAS. *Solid State Nucl. Magn. Reson.* **2011**, *40* (2), 72–77. <https://doi.org/10.1016/j.ssnmr.2011.06.001>.
- (41) Nelson, D. J.; Collado, A.; Manzini, S.; Meiries, S.; Slawin, A. M. Z.; Cordes, D. B.; Nolan, S. P. Methoxy-Functionalized N-Heterocyclic Carbenes. *Organometallics* **2014**, *33* (8), 2048–2058. <https://doi.org/10.1021/om5001919>.
- (42) Bantreil, X.; Nolan, S. P. Synthesis of N-Heterocyclic Carbene Ligands and Derived Ruthenium Olefin Metathesis Catalysts. *Nat. Protoc.* **2011**, *6* (1), 69–77. <https://doi.org/10.1038/nprot.2010.177>.
- (43) Berthon-Gelloz, G.; Siegler, M. A.; Spek, A. L.; Tinant, B.; Reek, J. N. H.; Markó, I. E. IPr* an Easily Accessible Highly Hindered N-Heterocyclic Carbene. *Dalton Trans.* **2010**, *39* (6), 1444–1446. <https://doi.org/10.1039/B921894G>.
- (44) Zhao, Q.; Meng, G.; Li, G.; Flach, C.; Mendelsohn, R.; Lalancette, R.; Szostak, R.; Szostak, M. IPr# – Highly Hindered, Broadly Applicable N-Heterocyclic Carbenes. *Chem. Sci.* **2021**, *12* (31), 10583–10589. <https://doi.org/10.1039/D1SC02619D>.
- (45) Fung, B. M.; Khitrin, A. K.; Ermolaev, K. An Improved Broadband Decoupling Sequence for Liquid Crystals and Solids. *J. Magn. Reson.* **2000**, *142* (1), 97–101. <https://doi.org/10.1006/jmre.1999.1896>.
- (34) WSolids1 1.21.3, K. Eichele, Universität Tübingen 2015.

- (47) Thakur, R. S.; Kurur, N. D.; Madhu, P. K. Swept-Frequency Two-Pulse Phase Modulation for Heteronuclear Dipolar Decoupling in Solid-State NMR. *Chem. Phys. Lett.* **2006**, 426 (4), 459–463. <https://doi.org/10.1016/j.cplett.2006.06.007>.
- (48) Lefort, R.; Wiench, J. W.; Pruski, M.; Amoureux, J.-P. Optimization of Data Acquisition and Processing in Carr–Purcell–Meiboom–Gill Multiple Quantum Magic Angle Spinning Nuclear Magnetic Resonance. *J. Chem. Phys.* **2002**, 116 (6), 2493–2501. <https://doi.org/10.1063/1.1433000>.
- (49) Harris, R. K.; Becker, E. D.; Cabral de Menezes, S. M.; Goodfellow, R.; Granger, P. NMR Nomenclature. Nuclear Spin Properties and Conventions for Chemical Shifts (IUPAC Recommendations 2001). *Pure Appl. Chem.* **2001**, 73 (11), 1795–1818. <https://doi.org/10.1351/pac200173111795>.

CHAPTER 4.

Antimicrobial Activity of Cu(I)-NHC
Complexes against Catheter-
Associated Pathogens

Chapter 4. Antimicrobial Activity of Cu(I)-NHC Complexes against Catheter-Associated Pathogens

4.1 Introduction

In the past few years, transition metal-NHC complexes have garnered significant interest in medicinal chemistry.^{1–3} The key characteristic of NHC ligands lies in their strong σ -electron donation and weak π -electron acceptance within the carbene carbon, establishing a robust metal-carbon (M-C) bond. As a result, the exceptional stability of these metal complexes impedes M-C bond breakage, thereby diminishing the high cytotoxicity typically associated with metal ions. Additionally, the ease of access to NHC ligands and metal complexes through straightforward synthetic pathways facilitates the fine-tuning of their biological properties.⁴

The majority of studies on transition metal-NHCs, including mechanochemically synthesized ones,^{5,6} have focused on their antitumor activities, employing various metals such as silver, gold, and copper.^{7–9} However, investigations into the antimicrobial activity of metal-NHCs have been limited primarily to silver-NHCs.¹⁰ The antibacterial properties of silver complexes rely on silver release, yet silver-NHCs are susceptible to deactivation when exposed to light due to their relatively unstable silver-NHC bonds.¹¹ Hence, it is crucial to develop metal-NHCs with strong coordination abilities to ensure the stability of these complexes.

Conversely, despite the exceptional stability of copper-NHCs against environmental factors like air, moisture, and light, their exploration has remained relatively limited.^{12–14} Copper, a well-established antimicrobial agent in drinking water treatment and transportation, notably catalyzes organic processes within mammalian cells with low toxicity.¹⁵ Ronald's recent work highlighted the potential of copper-NHC complexes as potent antibacterial agents, exhibiting remarkable inhibitory activity against *Listeria*, *Pseudomonas*, *Staphylococcus*, and *Escherichia*.¹⁶ Comparative analyses even suggest that copper-NHCs could rival silver-NHCs in their antimicrobial potential. Additionally, Hamdi's research unveiled the inhibitory activity of benzimidazole-based copper-NHCs against food-borne pathogens and clinical microorganisms.¹⁷ Furthermore, Lin and Zhou recently demonstrated the effectiveness of copper-NHC complexes against a diverse array of oral pathogens, particularly *Streptococcus*.¹⁸ Building upon these promising findings, our study delves into assessing the antimicrobial efficacy of Cu(I)-NHC

complexes against bacterial and fungal strains commonly associated with catheter-related urinary tract infections.

Implanted medical devices, such as catheters and artificial prosthetics, significantly enhance treatment efficacy and patient comfort in modern healthcare. However, their susceptibility to microbial infections poses a significant challenge, particularly intensified by the escalating prevalence of antimicrobial resistance. This issue has been highlighted by the World Health Organization (WHO) as one of the paramount threats to public health, contributing to millions of annual deaths.^{19,20} In the United States, approximately a quarter of hospitalized patients undergo urinary catheterization, exposing them to a daily 5% risk of bacteriuria. Catheter-related urinary tract infections account for 40% of hospital infections, with up to 4% progressing to bacteremia, resulting in extended hospital stays by 1 to 3.8 days per patient and an annual increase in healthcare costs exceeding 500 million dollars.^{21–26} Recent studies propose that incorporating metal complexes, such as silver alloy hydrogel, as coatings on these medical devices effectively combat infections.²⁶ However, the intricate preparation of these antimicrobial metal complexes remains a significant hurdle to their widespread application.

Motivated by the exceptional antimicrobial activity demonstrated by metal-NHCs in prior studies and our earlier research involving the synthesis of metal-NHC complexes via a straightforward, environmentally sustainable, scalable, and solvent-free method, our study aims at investigating the antimicrobial potential of Cu(I)-NHC complexes against a broad spectrum of bacterial and fungal strains associated with catheter-related urinary tract infections.²⁶ Notably, these strains encompass *Escherichia coli*, *Klebsiella* species, *Pseudomonas* species, *Enterobacter* species, various strains of *Staphylococcus*, as well as *Candida* species.

4.2 Results and Discussion

4.2.1 Synthesis of the Cu(I)-NHC Complexes

The Cu(I)-NHC complexes, depicted in **Figure 4.1**, were readily synthesized following the mechanochemical weak base approach reported by the Cazin group.²⁷ These complexes exhibit remarkable stability towards air and moisture. Their structures were confirmed using solution-state ¹H and ¹H-decoupled ¹³C NMR.

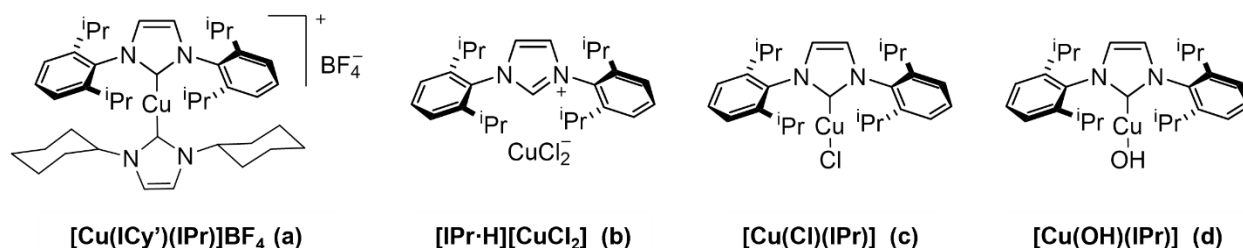


Figure 4.1. The chemical structure of the investigated copper-NHC complexes.

4.2.2 Antimicrobial Properties of the Cu(I)-NHC Complexes

The antimicrobial activity of the synthesized complexes was evaluated by determining the minimum inhibitory concentration (MIC) values against twenty-two different bacterial and fungal strains associated with catheter-related urinary tract infections.²⁸ The MIC is defined as the lowest concentration of an antimicrobial agent that inhibits the visible growth of a microorganism after an overnight incubation.²⁹

As depicted in **Table 4.1**, the complexes tested did not demonstrate effectiveness against gram-negative bacterial strains (*E. coli*, *P. aeruginosa*, *E. aerogenes*, *K. pneumoniae*, *K. oxytoca*) with a MIC of $\geq 64 \mu\text{g/mL}$. Conversely, the MIC range of these complexes against the gram-positive bacteria, *St. aureus*, indicated significant effectiveness. Notably, complex (c) exhibited superior inhibition compared to gentamicin (GEN) in three *St. aureus* strains, ATCC 6538, 08238, and 08239, with MIC values of 0.06, 0.25, and 0.06 $\mu\text{g/mL}$, respectively, lower than the MIC shown by gentamicin of 0.125 $\mu\text{g/mL}$ (**Table 4.1**). Similarly, complexes (b) and (d) showed higher effectiveness than amoxicillin and augmentin antibiotics against *St. aureus* 08239, with MIC values of 1 $\mu\text{g/mL}$, lower than the 2 $\mu\text{g/mL}$ MIC of amoxicillin (AMX) and augmentin (**Table 4.1**). Among the four synthesized complexes, complex (c) exhibited the strongest inhibitory potency against the tested gram-positive strain.

Regarding antifungal activity, the four synthesized complexes demonstrated effectiveness against *Candida* species (*C. tropicalis* 13197, *C. albicans* 10286, and *C. parapsilosis* 13200) with MIC values ranging between 16 – 128 $\mu\text{g/mL}$, <0.03 – 2 $\mu\text{g/mL}$, and <0.03 – 8 $\mu\text{g/mL}$, respectively. Notably, the antifungal inhibition of these complexes surpassed the control antibiotics, amoxicillin, augmentin, and gentamicin with MIC values exceeding 128 $\mu\text{g/mL}$ (**Table 4.1**). The particularly low MIC value of complexes (c) and (d) of $<0.03 \mu\text{g/mL}$ against *C. albicans* 10286 is noteworthy.

Table 4.1. In vitro minimum inhibitory concentration assessment of the mechanochemically synthesized Cu(I)-NHC complexes (**a-d**) against catheter-associated microorganisms.

N°	Reference	Name	Minimum Inhibitory Concentrations (MIC) (µg/mL)						
			a	b	c	d	AMX	Augmentin	GEN
1	ATCC 25922	<i>E. coli</i>	>128	>128	>128	>128	8	8	0.25
2	ATCC 9027	<i>P. aeruginosa</i>	64	>128	>128	>128	>128	>128	1
3	ATCC 6538	<i>St. aureus</i>	8	1	0.06	4	0.25	0.25	0.125
4	08238	<i>St. aureus</i>	8	1	0.125	4	0.5	0.5	0.125
5	08157	<i>E. coli</i>	>128	>128	>128	>128	>128	32	1
6	09003	<i>E. coli</i>	64	>28	>128	>128	28	32	0.25
7	09004	<i>E. aerogenes</i>	>128	>128	>128	>128	>128	>128	5
8	08151	<i>E. coli</i>	>128	>128	>128	>128	8	8	0.25
9	10270	<i>K. pneumoniae</i>	>128	>128	>128	>128	>128	>128	8
10	08129	<i>P. aeruginosa</i>	64	>128	>128	>128	>128	>128	<0.03
11	08131	<i>P. aeruginosa</i>	64	>128	>128	>128	>128	>128	1
12	08136	<i>P. aeruginosa</i>	64	>128	128	128	>128	>128	16
13	08143	<i>St. aureus</i>	16	4	16	8	2	0.25	0.125
14	08146	<i>St. aureus</i>	8	4	16	8	2	2	0.5
15	08148	<i>St. aureus</i>	16	4	32	8	16	2	0.125
16	08239	<i>St. aureus</i>	4	1	0.06	1	2	2	0.125
17	08240	<i>St. aureus</i>	4	4	16	8	16	8	0.125
18	08241	<i>St. aureus</i>	4	4	16	8	16	4	0.25
19	13197	<i>C. tropicalis</i>	16	128	128	32	>128	>128	>128
20	10286	<i>C. albicans</i>	2	0.06	<0.03	<0.03	>128	>128	>128
21	13200	<i>C. parapsilosis</i>	<0.03	0.125	8	0.5	>128	>128	>128
22	11049	<i>K. oxytoca</i>	>128	>128	>128	>128	>128	4	0.25

4.3 Experimental Details

4.3.1 Microorganism Strains

A total of twenty-two catheter-associated pathogens were tested, including eleven gram-negative bacteria, eight gram-positive, and three fungi. The gram-negative bacteria included

Escherichia coli (*E. coli* ATCC 25922, 08157, 09003, 08151), *Pseudomonas aeruginosa* (*P. aeruginosa* ATCC 9027), *Enterobacter aerogenes* (*E. aerogenes* 09004), *Klebsiella pneumoniae* (*K. pneumoniae* 10270), *Pseudomonas aeruginosa* (*P. aeruginosa* 08129, 08131, 08136), and *Klebsiella oxytoca* (*K. oxytoca* 11040). The gram-positive bacteria comprised *Staphylococcus aureus* (*St. aureus* ATCC 6538, 08238, 08143, 08146, 08148, 08239, 08240, 08241). The fungi tested were *Candida tropicalis* (*C. tropicalis* 13197), *Candida albicans* (*C. albicans* 10286), and *Candida parapsilosis* (*C. parapsilosis* 13200).

4.3.2 Minimum Inhibitory Concentration of the Microorganisms

The MICs of the complexes against the twenty-two microorganisms were determined using the agar dilution method following the protocols outlined by the Clinical and Laboratory Standards Institute.³⁰ Each microorganism was grown for 24 h at 37 °C until reaching the mid-logarithmic phase. The complexes, initially dissolved in 10 mL DMSO, were mixed with Mueller Hinton Agar (HMA) and then poured into Petri dishes. Concentrations tested ranged from 128 to 0.03 µg/mL in a serial dilution format (128, 64, 32, 16, 8, 4, 2, 1, 0.5, 0.25, 0.125, 0.06, and 0.03 µg/mL). The Petri dishes containing the HMA-complex mixture were inoculated with the microorganisms using an inoculum replicator, followed by incubation for 24 h at 37 °C. Visual assessment of activity was conducted based on the presence or absence of culture growth. Negative controls were established using solvents. Additionally, three antibiotics, amoxicillin (AMX), augmentin, and gentamicin (GEN), were used as positive controls.

4.4 Conclusion

This study sought to ascertain the potential applicability of Cu(I)-NHC complexes in mitigating infections associated with the utilization of urinary catheters. The significant antibacterial and antifungal activities observed suggest that these mechanochemically synthesized complexes could be further explored as potential candidates for antibacterial and antifungal treatments against catheter-related urinary tract infections. This is particularly notable due to their efficacy against *St. aureus* strains and *Candida* strains. Nonetheless, comprehensive studies, including time-kill assay, scanning electron microscopy, toxicity profiles, and vivo testing, are crucial to thoroughly assess their effectiveness, mode of action, and safety.

4.5 Statement of Contribution

In Chapter 4, my responsibilities encompassed conducting biological tests, analyzing data, and interpreting the results. Séverine Mahieux offered crucial assistance in carrying out the biological experiments, while Gianmarco Pisanò carried out the synthesis of the complexes. Dr. Christel Neut, my co-supervisor, provided supervision and made significant contributions to result analysis and interpretation. Regrettably, her unexpected passing prevented the completion of this section within my PhD thesis. Prof. Dr. Catherine Cazin and Prof. Dr. Olivier Lafon provided invaluable guidance and expertise throughout the entire process.

4.6 References

- (1) Teyssot, M.-L.; Jarrousse, A.-S.; Manin, M.; Chevy, A.; Roche, S.; Norre, F.; Beaudoin, C.; Morel, L.; Boyer, D.; Mahiou, R.; Gautier, A. Metal-NHC Complexes: A Survey of Anti-Cancer Properties. *Dalton Trans.* **2009**, No. 35, 6894–6902. <https://doi.org/10.1039/B906308K>.
- (2) Liu, W.; Gust, R. Metal N-Heterocyclic Carbene Complexes as Potential Antitumor Metallodrugs. *Chem. Soc. Rev.* **2012**, 42 (2), 755–773. <https://doi.org/10.1039/C2CS35314H>.
- (3) Aher, S. B.; Muskawar, P. N.; Thenmozhi, K.; Bhagat, P. R. Recent Developments of Metal N-Heterocyclic Carbenes as Anticancer Agents. *Eur. J. Med. Chem.* **2014**, 81, 408–419. <https://doi.org/10.1016/j.ejmech.2014.05.036>.
- (4) Hussaini, S. Y.; Haque, R. A.; Razali, M. R. Recent Progress in Silver(I)-, Gold(I)/(III)- and Palladium(II)-N-Heterocyclic Carbene Complexes: A Review towards Biological Perspectives. *J. Organomet. Chem.* **2019**, 882, 96–111. <https://doi.org/10.1016/j.jorganchem.2019.01.003>.
- (5) Beillard, A.; Quintin, F.; Gatignol, J.; Retailleau, P.; Renaud, J.-L.; Gaillard, S.; Métro, T.-X.; Lamaty, F.; Bantreil, X. Solving the Challenging Synthesis of Highly Cytotoxic Silver Complexes Bearing Sterically Hindered NHC Ligands with Mechanochemistry. *Dalton Trans.* **2020**, 49 (36), 12592–12598. <https://doi.org/10.1039/D0DT00410C>.

- (6) Bento, O.; Luttringer, F.; Dine, T.; Pétry, N.; Bantreil, X.; Lamaty, F. Sustainable Mechanosynthesis of Biologically Active Molecules. *Eur. J. Org. Chem.* **2022**, 2022. <https://doi.org/10.1002/ejoc.202101516>.
- (7) Karaca, Ö.; Meier-Menches, S. M.; Casini, A.; Kühn, F. E. On the Binding Modes of Metal NHC Complexes with DNA Secondary Structures: Implications for Therapy and Imaging. *Chem. Commun.* **2017**, 53 (59), 8249–8260. <https://doi.org/10.1039/C7CC03074F>.
- (8) Streciwilk, W.; Hackenberg, F.; Müller-Bunz, H.; Tacke, M. Synthesis and Cytotoxicity Studies of P-Benzyl Substituted NHC–Copper(I) Bromide Derivatives. *Polyhedron* **2014**, 80, 3–9. <https://doi.org/10.1016/j.poly.2013.11.039>.
- (9) Elie, M.; Mahoro, G. U.; Duverger, E.; Renaud, J.-L.; Daniellou, R.; Gaillard, S. Cytotoxicity of Cationic NHC Copper(I) Complexes Coordinated to 2,2'-Bis-Pyridyl Ligands. *J. Organomet. Chem.* **2019**, 893, 21–31. <https://doi.org/10.1016/j.jorganchem.2019.04.003>.
- (10) Ronga, L.; Varcamonti, M.; Tesauro, D. Structure-Activity Relationships in NHC-Silver Complexes as Antimicrobial Agents. *Mol. Basel Switz.* **2023**, 28 (11), 4435. <https://doi.org/10.3390/molecules28114435>.
- (11) Garner, M. E.; Niu, W.; Chen, X.; Ghiviriga, I.; Abboud, K. A.; Tan, W.; Veige, A. S. N-Heterocyclic Carbene Gold(I) and Silver(I) Complexes Bearing Functional Groups for Bio-Conjugation. *Dalton Trans.* **2014**, 44 (4), 1914–1923. <https://doi.org/10.1039/C4DT02850C>.
- (12) Bertrand, B.; Gontard, G.; Botuha, C.; Salmain, M. Pincer-Based Heterobimetallic Pt(II)/Ru(II), Pt(II)/Ir(III), and Pt(II)/Cu(I) Complexes: Synthesis and Evaluation of Antiproliferative Properties. *Eur. J. Inorg. Chem.* **2020**, 2020 (35), 3370–3377. <https://doi.org/10.1002/ejic.202000717>.
- (13) Lazreg, F.; Cazin, C. S. J. Medical Applications of NHC–Gold and –Copper Complexes. In *N-Heterocyclic Carbenes*; John Wiley & Sons, Ltd, 2014; pp 173–198. <https://doi.org/10.1002/9783527671229.ch07>.
- (14) Teyssot, M.-L.; Jarrousse, A.-S.; Chevy, A.; De Haze, A.; Beaudoin, C.; Manin, M.; Nolan, S. P.; Díez-González, S.; Morel, L.; Gautier, A. Toxicity of Copper(I)–NHC Complexes

- Against Human Tumor Cells: Induction of Cell Cycle Arrest, Apoptosis, and DNA Cleavage. *Chem. – Eur. J.* **2009**, *15* (2), 314–318. <https://doi.org/10.1002/chem.200801992>.
- (15) Mitra, D.; Li, M.; Kang, E.-T.; Neoh, K. G. Transparent Copper-Based Antibacterial Coatings with Enhanced Efficacy against *Pseudomonas Aeruginosa*. *ACS Appl. Mater. Interfaces* **2019**, *11* (1), 73–83. <https://doi.org/10.1021/acsami.8b09640>.
- (16) Bernardi, T.; Badel, S.; Mayer, P.; Groelly, J.; de Frémont, P.; Jacques, B.; Braunstein, P.; Teyssot, M.-L.; Gaulier, C.; Cisnetti, F.; Gautier, A.; Roland, S. High-Throughput Screening of Metal-N-Heterocyclic Carbene Complexes against Biofilm Formation by Pathogenic Bacteria. *ChemMedChem* **2014**, *9* (6), 1140–1144. <https://doi.org/10.1002/cmdc.201402012>.
- (17) Touj, N.; Chakchouk-Mtibaa, A.; Mansour, L.; Harrath, A. H.; Al-Tamimi, J.; Mellouli, L.; Özdemir, I.; Yasar, S.; Hamdi, N. Synthesis, Spectroscopic Properties and Biological Activity of New Cu(I) N-Heterocyclic Carbene Complexes. *J. Mol. Struct.* **2019**, *1181*, 209–219. <https://doi.org/10.1016/j.molstruc.2018.12.093>.
- (18) Pan, T.; Wang, Y.; Liu, F.-S.; Lin, H.; Zhou, Y. Copper(I)–NHCs Complexes: Synthesis, Characterization and Their Inhibition against the Biofilm Formation of *Streptococcus Mutans*. *Polyhedron* **2021**, *197*, 115033. <https://doi.org/10.1016/j.poly.2021.115033>.
- (19) Aminov, R. History of Antimicrobial Drug Discovery: Major Classes and Health Impact. *Biochem. Pharmacol.* **2017**, *133*, 4–19. <https://doi.org/10.1016/j.bcp.2016.10.001>.
- (20) Aubert-Viard, F.; Mogrovejo-Valdivia, A.; Tabary, N.; Maton, M.; Chai, F.; Neut, C.; Martel, B.; Blanchemain, N. Evaluation of Antibacterial Textile Covered by Layer-by-Layer Coating and Loaded with Chlorhexidine for Wound Dressing Application. *Mater. Sci. Eng. C Mater. Biol. Appl.* **2019**, *100*, 554–563. <https://doi.org/10.1016/j.msec.2019.03.044>.
- (21) Haley, R. W.; Culver, D. H.; White, J. W.; Morgan, W. M.; Emori, T. G. The Nationwide Nosocomial Infection Rate: A New Need For Vital Statistics. *Am. J. Epidemiol.* **1985**, *121* (2), 159–167. <https://doi.org/10.1093/oxfordjournals.aje.a113988>.
- (22) Karchmer, T. B.; Giannetta, E. T.; Muto, C. A.; Strain, B. A.; Farr, B. M. A Randomized Crossover Study of Silver-Coated Urinary Catheters in Hospitalized Patients. *Arch. Intern. Med.* **2000**, *160* (21), 3294–3298. <https://doi.org/10.1001/archinte.160.21.3294>.

- (23) Rupp, M. E. Prevention and Control of Noscomial Infections, 4th Edition. *Shock* **2003**, 20 (6), 586.
- (24) National Nosocomial Infections Surveillance (NNIS) Report, Data Summary from October 1986-April 1996, Issued May 1996. A Report from the National Nosocomial Infections Surveillance (NNIS) System. *Am. J. Infect. Control* **1996**, 24 (5), 380–388.
- (25) Centers for Disease Control (CDC). Public Health Focus: Surveillance, Prevention, and Control of Nosocomial Infections. *MMWR Morb. Mortal. Wkly. Rep.* **1992**, 41 (42), 783–787.
- (26) Rupp, M. E.; Fitzgerald, T.; Marion, N.; Helget, V.; Puumala, S.; Anderson, J. R.; Fey, P. D. Effect of Silver-Coated Urinary Catheters: Efficacy, Cost-Effectiveness, and Antimicrobial Resistance. *Am. J. Infect. Control* **2004**, 32 (8), 445–450. <https://doi.org/10.1016/j.ajic.2004.05.002>.
- (27) Pisanò, G.; Cazin, C. S. J. Mechanochemical Synthesis of Cu(I)-N-Heterocyclic Carbene Complexes. *Green Chem.* **2020**, 22 (16), 5253–5256. <https://doi.org/10.1039/D0GC01923B>.
- (28) Oliveira, J.; Reygaert, W. C. Gram-Negative Bacteria. In *StatPearls*; StatPearls Publishing: Treasure Island (FL), 2023.
- (29) Andrews, J. M. Determination of Minimum Inhibitory Concentrations. *J. Antimicrob. Chemother.* **2001**, 48 Suppl 1. https://doi.org/10.1093/jac/48.suppl_1.5.
- (30) *M100Ed33 | Performance Standards for Antimicrobial Susceptibility Testing, 33rd Edition*. Clinical & Laboratory Standards Institute. <https://clsi.org/standards/products/microbiology/documents/m100/> (accessed 2023-12-22).

GENERAL CONCLUSION

General Conclusion

In conclusion, this doctoral thesis embarks on a profound exploration of the realm of mechanochemistry, driven by the pressing need to address the environmental and economic challenges arising from the extensive use of solvents in modern chemical processes. Within the field of mechanochemical synthesis, a paramount challenge lies in unraveling the intricate mechanisms that underlie these reactions. The influence exerted by solvents during workup procedures can induce alteration in product structures, necessitating comprehensive structural characterization in the solid state before the workup phase. To address this challenge, we harnessed the power of ssNMR spectroscopy as a potent method for monitoring mechanochemical reactions.

Our investigations have delved into the mechanochemical synthesis of transition metal-NHC complexes, with a particular focus on the weak base approach. Notably, our findings regarding the $[\text{Cu}(\text{Cl})(\text{NHC})]$ complexes unequivocally demonstrate that both the cuprate intermediate and the $[\text{Cu}(\text{Cl})(\text{IPr})]$ complex form within the solid-state during ball milling, rather than in solvent during the workup phase. Moreover, the absence of the cuprate intermediate in the final product suggests a simultaneous conversion process. Additionally, ssNMR spectroscopy effectively monitors the presence of reagents and by-products, providing a comprehensive understanding of the overall reaction.

Similarly, our exploration of $[\text{Ag}(\text{Cl})(\text{NHC})]$ complex synthesis through the mechanochemical weak base approach has yielded critical insights. The ssNMR spectroscopy data firmly establish that the argentate intermediate and $[\text{Ag}(\text{Cl})(\text{IPr})]$ complex are both generated within the solid-state during ball milling. We have also observed the gradual decomposition of $[\text{AgCl}_2][\text{IPr}\cdot\text{H}]$ into $\text{IPr}\cdot\text{HCl}$ and AgCl . To further enhance the comprehensiveness of this study, we recommend integrating computational investigations and employing additional solid-state analytical techniques, such as PXRD, in future studies.

Furthermore, our investigations into the synthesis of $[\text{Rh}(\text{acac})(\text{CO})(\text{NHC})]$ complexes using a mechanochemical weak base approach have highlighted the role of solvents in driving ligand binding and substitution reactions. While grinding assists the reaction, our spectroscopic data unequivocally confirm that solvent addition during the workup procedure significantly influences

product formation. This insight is valuable for researchers interested in utilizing mechanochemistry for the synthesis of organometallic complexes.

Extending our horizons, we delved into the mechanochemical synthesis of chalcogen-NHC derivatives, including NHC=S and NHC=Se, through the weak base approach. ssNMR spectroscopy has revealed that IPr=S and IPr=Se form in the solid-state during ball milling, although the presence of unreacted starting materials in the crude mixtures suggests the need for optimization. This study provides a solid foundation for the future development of chalcogen-NHC derivatives through mechanochemistry.

In essence, unveiling universal mechanisms in mechanochemistry remains elusive. Yet, this study provides valuable insights for optimizing these reactions, offering a critical perspective for researchers in this field.

Furthermore, addressing the pressing demand for innovative antimicrobial agents within the rising threat of antimicrobial resistance, our exploration into mechanochemically synthesized Cu(I)-NHC complexes reveals their promising antimicrobial effectiveness against bacterial and fungal strains associated with catheter-related urinary tract infections. Their substantial effectiveness against gram-positive *Staphylococcus aureus* and notable antifungal activity against *Candida* species signify a potential straightforward and eco-friendly strategy for addressing infections associated with urinary catheter use. This thesis not only significantly advances the realm of mechanochemistry but also paves the way for practical applications of transition metal-NHC complexes in addressing urgent healthcare challenges in environmentally sustainable manner.

In summary, this research contributes to the development of environmentally friendly and economically viable methods for chemical synthesis, addressing the pressing challenges posed by solvent usage in modern chemistry. Moreover, the observed antimicrobial activity signifies a promising advancement in combating antimicrobial resistance. As we conclude this research, we are left with a profound appreciation for the potential of mechanochemistry as a sustainable and efficient tool for chemical synthesis, paving the way for further exploration and innovation in this exciting field.

Perspectives

Looking ahead, this research opens several avenues for further exploration and development. Performing in situ ssNMR experiments directly during the mechanochemical process can provide real-time information on reaction intermediates and pathways, enhancing our understanding of reaction mechanisms and kinetics under milling conditions. Additionally, future research can focus on implementing quantitative ssNMR methodologies for mechanochemical systems, enabling accurate determination of reaction yields, quantification of by-products, and tracking the evolution of chemical species during milling. The application of quantitative ssNMR can provide invaluable data for optimizing processes. These efforts will contribute to a deeper understanding of mechanochemical reactions and expand the potential of ssNMR spectroscopy.

Furthermore, investigating the antimicrobial potential of the synthesized organometallic complexes was a pivotal aspect of this research. The initial findings, depicted in Chapter 4. Sadly, Dr. Christel Neut, my co-supervisor who held responsibility for supervising this part of the research, passed away before the project could be completed. I wish to express my sincere gratitude to Dr. Christel Neut for her invaluable guidance and expertise during the initial stages of the antimicrobial activity testing. Regrettably, due to these circumstances, a comprehensive analysis of the findings was not possible. Consequently, these results should be considered preliminary, and their comprehended antimicrobial potential necessitates future study and validation.

Curriculum Vitae

Lama HAMDOUNA

Nationality: Lebanese

Date of birth: 29 November 1994

Université de Lille, CNRS UMR 8181, UCCS, 59652 Villeneuve d'Ascq, France

Hamdouna.lama@gmail.com

Education

2020-2023: PhD in Materials Chemistry/ Chemistry, University of Lille and Ghent University

2019-2020: Master 2 in Biorefinery, University of Lille

2018-2019: Master 1 in Biochemistry, Lebanese University

2012-2015: B.Sc. Biochemistry, Lebanese University

Professional Experience

2020-2023: PhD in Materials Chemistry/ Chemistry, CNRS, Lille, Ghent

2020 (6 months): Research Intern, University of Lille, Lille

Oral Communications

Oral Presentations:

September 2023: Alpine Conference on Magnetic Resonance in Solids, Chamonix-Mont-Blanc

November 2021: Réunion RMN Grand Bassin Parisien, Paris

June 2021: 9 èmes Rencontres RMN-RPE-IRM, Lille

Poster Presentations:

September 2022: Italian-French International Conference on Magnetic Resonance, Milan

July 2022: Rocky Mountain Conference on Magnetic Resonance (RMCMR), Colorado

June 2022, 3i University Network first meeting, Lille

Publications

1) **L. Hamdouna**, G. Pisanò, A. G. M. Rankin, L. Falivene, J. Trébosc, L. Delevoye, L. Cavallo, S. P. Nolan, C. S. J. Cazin, O. Lafon, Understanding the mechanochemical synthesis of [Cu(Cl)(NHC)] complexes using solid-state NMR spectroscopy (in preparation).

2) **L. Hamdouna**, G. Pisanò, A. G. M. Rankin, J. Trébosc, L. Delevoye, S. P. Nolan, C. S. J. Cazin, O. Lafon, Mechanistic insights into the mechanochemical synthesis of chalcogen-NHC derivatives: solid-state NMR spectroscopy studies (in preparation).

- 3) G. Pisanò, **L. Hamdouna**, J. Trébosc, I. Ritacco, P. Roussel, L. Caporaso, L. Cavallo, O. Lafon, S. P. Nolan, C. S. J. Cazin, Mechanistic insights into the mechanosynthesis of [Rh(acac)(CO)(NHC)] complexes (submitted to Green Chemistry Journal).
- 4) P. Raval, N. Thomas, **L. Hamdouna**, L. Delevoye, O. Lafon, G. N. M. Reddy, Boron adsorption kinetics of microcrystalline cellulose and polymer resin, *Langmuir* **2023**, 39, 15, 5384–5395.
- 5) B. Maliszewski, T. Bayrakdar, P. Lambert, **L. Hamdouna**, X. Trivelli, L. Cavallo, A. Poater, M. Beliš, O. Lafon, K. V. Hecke, D. Ormerod, C. Cazin, F. Nagra, S. P. Nolan, Structural and spectroscopic studies of Pt(II)-N-heterocyclic carbene complexes and their use in solvent-free alkene hydrosilylation *Chem. Eur. J.* **2023**, e202301259.